Author:
Bempong-Manful, Emmanuel

Title:
The bases of extragalactic radio jets

The bases of extragalactic radio jets

By

EMMANUEL KWAME BEMPONG-MANFUL

School of Physics
UNIVERSITY OF BRISTOL

A dissertation submitted to the University of Bristol in accordance with the requirements for award of the degree of DOCTOR OF PHILOSOPHY in the Faculty of Science.

SEPTEMBER 2022

Word count: forty-seven thousand, nine hundred and fifty-eight

The bases of extragalactic radio jets

Author:
Emmanuel Kwame BEMPONG-MANFUL

Supervised by:
Prof. Mark BIRKINSHAW (Bristol)
Prof. Martin J. HARDCASTLE (Hertfordshire)

School of Physics, HH Wills Physics Laboratory, University of Bristol,
Bristol BS8 1TL, United Kingdom

Abstract

Extragalactic relativistic plasma jets ejected from SMBHs lurking at the centres of massive galaxies are known to play a key role in the AGN feedback cycle, and consequently the formation and evolution of structure in the Universe. However, the physics driving the observed jet structure in these cosmic outflows remains an open question. In this thesis, I present high resolution and high sensitivity studies of the jet bases in a sample of six extragalactic radio sources, using *deep transverse resolved* radio observations of these objects from the *e*-MERLIN and LOFAR telescopes, and with complementary observations from the VLA along with optical (HST) and X-ray (Chandra) data. These observations provide unique probes of the dynamics and energetics of the inner jets. Physical parameters that can be derived from spectral data, along with relations between the observed quantities for a beamed radio jet, such as intrinsic velocity and orientation angle ($\beta_{\rm jet}$, θ), are investigated. The mapped objects are representative of the range of FR I morphological types in a low-redshift ($z \lesssim 0.05$) flux-limited survey, but we also include a nearby BL Lac object because such objects are usually related to FR I sources by unification schemes. This work forms part of ongoing efforts by the *e*-MERLIN Jets Legacy programme to "resolve key questions in extragalactic jet physics."

This thesis begins with a review of existing literature relevant to the study and the scientific motivation for undertaking the present inquiry (Chapter 1). I then present the data and instruments in Chapter 2, and provide a detailed description of the observations and methods employed in the present work in Chapter 3.

Next I present results (Chapter 4) from 144 MHz LOFAR HBA observations of the kpc-scale jets in our sample. These high dynamic range ($DR \gtrsim 10^5$:1) LOFAR HBA images allow us to characterize the source morphological properties with high precision, and draw conclusions on the host galaxies and their environment. We also detect special features such as loops, and report for the first time the detection of a compact lobe (blob) at the bend in the main jet in the radio galaxy 3C 264. Our derived $\sim$ 150-MHz radio luminosities are consistent with the six sources lying close to the FR I/FR II luminosity break, and show that the physical scales of some of the sources in our sample have been underestimated by a factor of a few in previous studies. I then present results on the energetics of the jet bases for three sources 3C 83.1B, 3C 264 and 3C 371 (Chapters 5, 6 and 7) from multifrequency radio observations. The inner jets in these sources are well resolved and there is good correspondence between features of

the jet observed at all three frequencies. We estimate mildly relativistic speeds ($\beta_{\rm jet}$ = 0.2c) for the inner jets in 3C 83.1B and infer bulk deceleration of the flow at the jet base, most likely by entrainment. The value we find for synchrotron lifetime, $\tau_{\rm syn}$ = 4.2$\times$10^7 years, suggest that relativistic electrons created in and around the central engine could travel the entire $\sim$ 25 kpc length of the inner jets within their lifetime for bulk velocities of $v_{\rm bulk} > 0.05c$ if there is no reacceleration or adiabatic losses. The transverse intensity distribution of the inner structure in 3C 264 suggests plausible velocity stratification within the inner relativistic jet as reported in previous studies. We measure an intrinsic speed of 0.42c ($\Gamma_{\rm jet}$ = 1.1) which constrains the jet viewing angle θ to assume relatively large values (52° $\lesssim$ θ $\lesssim$ 74°), and when compared with the higher initial VLBI jet velocities of $\sim$ 0.99c (Γ = 7) for the inner 300–400 pc, a deceleration of the order of a factor 2 from the initial parsec-scale jet can be inferred. The radiative lifetime of electrons emitting at all three frequencies are very similar, at about 3 Myr. Our observations are consistent with 3C 371 being core-dominated, with the central core emitting $\gtrsim$ 50% of the total flux across all three frequencies and we find evidence of double asymmetric radio knots located 1.3$''$–1.8$''$ away from the compact core. We infer highly relativistic speeds, $\beta_{\rm jet}$ = 0.81c and an orientation angle, θ = 35° for the inner jets in 3C 371. The values we find for the radiative lifetime of electrons emitting at GHz frequencies is of the order of a few 10^5 years, consistent with previous works and suggests that the jets in 3C 371 are relatively young compared with the other sources studied here. Future work suggested on this sample is described in Chapter 8.

Dedication

This work is dedicated to my father Samuel Koranteng Bempong-Manful of blessed memory, my mother Mercy Oparebea Akuffo, my godmother Elizabeth Lartey, my wife and children, my siblings and entire family.

"Gye Nyame!"

Acknowledgements

First, I thank my supervisors, Prof. Mark Birkinshaw (Bristol) and Prof. Martin Hardcastle (Hertfordshire), without whose valuable input this research would not have reached a conclusion. It has been a wonderful experience working under your supervisions, and I have enjoyed our regular discussions on the research over the past years. And not to forget all the exciting experiences and achievements during this period – from organising international conferences to successfully bidding for grants and telescope observing time. Thank you very much for your mentorship and for assisting me with this inspiring work.

My sincere thank you also to Prof. Melvin Hoare (Leeds; PI – DARA Project), and to members of both the *e*-MERLIN Jets Legacy collaboration and the LOFAR VLBI working group for your support in diverse ways – I particluarly found discussions during our periodic telecons over the years very useful. I have also benefited from the great working environment within the Bristol Astrophysics Group, and I want to say thank you to all the staff and postgraduate students working there. Most importantly, I want to thank Dr. Andy Young, Dr. Rhys Morris, Johannes Allotey and former postdoc Dr. Ryan Duffy for their assistance whenever I have had to call on them. Finally, my deepest thanks to my family for their love and support during my studies. This research was undertaken with a studentship through a Newton Fund project, DARA (Development in Africa with Radio Astronomy), and awarded by the UK's Science and Technology Facilities Council (STFC) – grant reference ST/R001103/1.

Declaration

I declare that the work in this dissertation was carried out in accordance with the requirements of the University's Regulations and Code of Practice for Research Degree Programmes and that it has not been submitted for any other academic award. Except where indicated by specific reference in the text, the work is the candidate's own work. Work done in collaboration with, or with the assistance of, others, is indicated as such. Any views expressed in the dissertation are those of the author. The following parts of this submission have been published previously and/or undertaken as part of a previous degree or research programme:

1. **Bempong-Manful E.K.**, Hardcastle M.J., Birkinshaw M., Laing R.A., Leahy J.P., and Worrall D.M., 2020, *A high-resolution view of the jets in 3C 465*, MNRAS, 496, 676.
2. **Bempong-Manful E.K.**, Birkinshaw M., Hardcastle M.J., Worrall D.M., Shimwell T.W. and Orrù E., *LOFAR observations of selected FR I radio sources from the 3CRR catalogue* [MNRAS, submitted].
3. **Bempong-Manful E.K.**, Birkinshaw M. and Hardcastle M.J., *Dynamical age estimates of the extended lobes of FR I radio galaxies* [MNRAS, in prep].
4. **Chapter 1**: an earlier version of this chapter was submitted as part of my thesis for the degree of Master of Science by Research.
5. **Chapters 5, 6 and 7**: this will be published as Bempong-Manful et al., *New constraints on extragalactic jet physics: I–III* [ApJ, in prep].

SIGNED: Emmanuel K. Bempong-Manful DATE: 27 September 2022

Contents

List of Figures

List of Tables

1

Introduction

1.1 Background

The jets in powerful radio galaxies are thought to be highly relativistic outflows consisting mostly of electron-positron plasma (e.g. Wardle et al. 1998; Kundt 2014). However, our in-depth understanding of these jets, including what we are actually seeing in radio emission – whether or not this comes from the whole jet or just a small region, the nature of jet particle acceleration, and the role of magnetic fields among others – is very incomplete. Against this backdrop, our aim in the present study will involve construction of the highest resolution and sensitivity maps to date for a sample of known powerful jet sources, and thus will attempt to resolve the physics driving the observed jet structure.

1.1.1 A historical perspective

The study of celestial objects at radio wavelengths dates back to the early decades of the 20th century, notably with the discovery of some radio signals from very distant objects by Karl Jansky – the results of which was published in his famous 1930s paper *"Electrical Disturbances Apparently of Extraterrestrial Origin"* (Jansky, 1933). Subsequently, radio observations have evolved into an unrivalled means of probing the frontiers of both the local and distant universe and today serve as an exceptional tool in resolving many of the mysteries of the cosmos, from the physics of star births to the formation and evolution of massive galaxies and large scale structures over cosmic time.

Since the first observation of astrophysical jets by Curtis (1918), countless jets of high-energy particles have been observed and studied across a broad spectrum of cosmological scales with radio synthesis maps of hundreds of Active Galactic Nuclei (AGNs; the bright central regions of some galaxies which can be more luminous than the remaining galaxy light) in the last few decades revealing jets, in the ranges of sub-parsec to mega-parsec scales (e.g. Ghisellini et al. 1993). In addition to energy, momentum and mass transport from the host galaxy, these cosmic outflows serve as diagnostic parameters for probing the role of highly energetic processes in the formation and evolution of large scale structure in the Universe and thus, form the foundation for scientific inquiry of many current and future key science projects and cosmological surveys.

1.1.2 Organisation of the thesis

This thesis will comprise eight chapters.

Chapter 1: This is the current chapter, and here I provide a background and introduction to the present study, and discuss the exisiting literature on extragalactic radio sources with a focus on relativistic plasma "jets" produced from the central Supermassive Black Holes (SMBHs) in active galaxies. Key highlights of the chapter include; AGNs (with a focus on radio-loud AGNs) and how their nuclear activity drives feedback, structure formation and black hole growth. I also provide an overview of astrophysical jets with emphasis on extragalactic relativistic jets and discuss the FR I and FR II jet dichotomy. The philosophy of radio interferometry and synthesis imaging in radio astronomy is also presented. Finally, I discuss the scientific motivation/rationale for undertaking the present study and offer an insight into the parameter space we seek to probe as well as the key science goals we aim to address in the present study.

Chapter 2: In chapter two, I present and describe in detail the sample under study, along with the instruments (telescopes and/or interferometry elements) employed in the present work. Emphasis is laid on the technical capabilities of each instrument, and how, from observations (multiwavelength perspective) they complement each other in resolving the physics driving the observed jet structure in extragalactic radio sources.

Chapter 3: This chapter is dedicated to the detailed description of the observations and methods and/or analysis employed in the present study. A comprehensive description of the methods – data calibration and imaging techniques used for constructing total intensity, spectral index (α, defined in the sense $S \propto \nu^{\alpha}$), polarisation and Rotation Measure synthesis maps for our target sample from each instrument is presented. I further provide insight into the interferometry data

combination strategy adopted to combine the L-band *e*-MERLIN and Very Large Array (VLA) datasets to construct the highest-resolution and sensitivity images at GHz frequencies in our sample. An overview of the `FLASH` Magneto(-Hydrodynamic) code is also presented, and with this, I shed some insights into how numerical MHD simulations that incorporate particle acceleration and synchrotron losses (derived from our observations) should allow for modelling the jet kinematics, and from conservation-law analysis (e.g. Laing & Bridle 2002a) taking external pressure and density profiles from X-ray observations – for testing evolutionary models of radio jet propagation in the dense ICM/IGM[1].

Chapters 4, 5, 6 & 7: Chapters four to seven highlight the key results from our analysis in the present study. In Chapter 4, I present and discuss results from analysis of the kpc-scale jets obtained from the first Low Frequency Array High Band Antenna (LOFAR HBA) observations of our target sample and use the data to characterize the source morphological properties with high precision, and draw conclusions on the host galaxies and their environment. Chapters 5 to 7 discuss the energetics of the jet bases. Here, I present and discuss our new high sensitivity, high-resolution multifrequency radio observations, and optical and X-ray images in our sample, and use these data to examine jet physics, orientation effects and energetics in the individual radio sources. We also estimate the jet velocities, mass fluxes, and entrainment rates for our science targets and as well test models of jet deceleration in Fanaroff-Riley Type-Is from relativistic to sub-relativistic speeds on kpc scales. Most of this is done for 3C 83.1B, 3C 264 and 3C 371 in the present work.

Chapter 8: Finally, in chapter eight I bring it all together by providing a summary of our key findings along with relevant conclusions from the main results obtained in the present study in relation to our key science goals. Also, I present prospects for future work and/or extension of the current study which due to time and/or other constraints were not covered in the present study.

1.2 Fundamentals of radio interferometry and synthesis imaging

The single most important factor in the study of celestial bodies at radio frequencies is the ability to generate an accurate image of the observed source from a collection of radio signals. In times past however, this was a daunting task as radio astronomers were limited by several

[1]The intra-cluster or inter-galactic medium (ICM/IGM) is the region of hot and highly ionised X-ray emitting gas that exists between galaxies within the cluster environment.

factors as far as reconstruction of this true sky brightness distribution of celestial objects was concerned. This consequentially resulted in a trade-off between sensitivity (where focus is solely on mapping out extended or large scale structure at the expense of fine details) or resolution (in which fine details of astronomical maps are prioritized at the expense of coarse structure). Today, thanks to radio interferometry, these limitations are increasingly becoming a thing of the past, allowing us to conduct observations at high spatial resolutions without compromising the large scale structures of such celestial sources. The underlying philosophy of radio interferometry and synthesis imaging resides in the fact that through combination of signals from different antennas, one can create a very large effective aperture of the observable sky which can be used as powerful diagnostic tool to reproduce the true properties of the extraterrestrial radio source. The first notable application of interferometric observations was performed on the sun dating as far back as the mid-20th century (McCready, Pawsey & Payne-Scott, 1947). Inspired by the rather low resolution of single-dish radio telescopes, interferometry has evolved into what is now known as Very Long Baseline Interferometry (VLBI) in which radio telescopes are connected in *real time* across different districts and countries (e.g. *e*-MERLIN, EVN, VLBA, Global VLBI, etc.) – a technique which has been influential in large area and deep cosmological surveys in the last few decades. The results of this are evident in the ability to resolve on milliarcsecond spatial scales the effect of high energetic particles from the nuclear regions of distant massive galaxies through to accurate definition of the Celestial Reference Frame among others (e.g. Trimble 2015).

The key parameter measured in interferometry is the spatial coherence function (e.g. Clark 1999) and the primary assumption here is that the rather incoherent spatial intensity distribution of EM waves emitted by a celestial object at a particular frequency, I_v can be reconstructed from the spatial coherence function measured at two points with the interferometer elements, $V_v(r_1, r_2)$ (e.g. Middelberg & Bach 2008). Samples are collected in the so called Fourier Transform plane (u-v plane) of the astronomical image with each point in the u-v plane corresponding to a discrete position and physical separation (baseline) of the interferometer elements. As Trimble (2015) wrote, the development of radio astronomy "has not been free of competition and controversy, at least partly because it is just a little difficult to understand how earth-rotation, aperture-synthesis interferometry works." Figure 1.1 below shows a two-element interferometer.

The interferometer elements primarily produce two distinct quantities; the signal in real

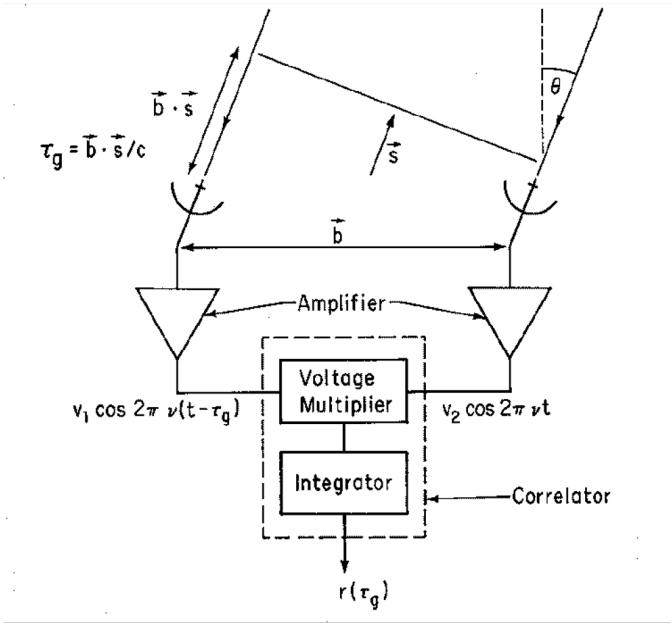

Figure 1.1: A simplified schematic diagram of a two-element interferometer. The projection of the station coordinates onto the (u, v) plane, which is perpendicular to the line-of-sight vector, $\vec{s}$, yields the (u, v) coordinates of the antennas, measured in units of the observing wavelength. The correlator cross-correlates and Fourier transforms the signals from each pair of antennas to generate visibilities for reconstruction of the true brightness distribution of the sky (Adapted from Taylor, Carilli & Perley 1999).

channel (V_r),

$$V_r = \int\int I_v\,(x,y)\,cos\{2\pi\,(ux+vy)\}dxdy \tag{1.1}$$

and the signal in imaginary (V_i),

$$V_i = \int\int I_v\,(x,y)\,sin\{2\pi\,(ux+vy)\}dxdy \tag{1.2}$$

The combination of Equations 1.1 and 1.2 above yields the so called complex visibility function $V_v(u,v)$ which is simply a Fourier Transform of the spatial intensity distribution $I(x,y)$ of emitted EM radiation from the radio source evaluated at a given u-v distance from the projected baseline coordinates and is given by:

$$V_{(u,v)} = \int\int I_v\,(x,y)\,exp\{-2\pi\,i\,(ux+vy)\}dxdy \tag{1.3}$$

Equation 1.3 above denotes the Van Cittert–Zernike theorem (see Zernike 1938 for review). The coordinates (u, v) are vector components from the origin of the (u, v) plane to a point in the plane and measured in wavelengths; and (x, y) are direction cosines towards the radio emitting source. All pairs of interferometer elements measure the visibility function. However, to account for the sensitivity of individual elements in the interferometry (i.e., the antenna response), a factor, $A_{\rm v}$, is often introduced. Equation 1.3 then becomes;

$$V_{(u,v)} = \int\int A_v\,(x,y)\,I_v\,(x,y)\,exp\{-2\pi\,i\,(ux+vy)\}dxdy \tag{1.4}$$

After a typical interferometric observation, the goal then is to recover the true sky brightness distribution from the sampled visibilities which contain characteristic information on both amplitude and phase of the correlated radio signal observed. However, to achieve this one needs to first remove bad data and correct for amplitude and phase errors which commonly result from glitches in the receiver and/or external factors. This procedure also known as data reduction in radio astronomy involves; (1) Flagging – inspecting the visibilities and removing all bad data; (2) Calibration – correcting the phase and amplitudes of the visibilities between the interferometry elements; (3) Deconvolution – recovering the true sky brightness distribution (real image) from the corrected visibilities (dirty image); (4) Self-calibration – using a model for the sky obtained in the deconvolution stage to further correct the phase and amplitudes of the visibilities in order to obtain an improved image.

The fact that radio interferometry samples astrophysical signals through incomplete Fourier measurements (e.g. Wiaux et al. 2009), has led to a great number of researchers developing several algorithms for optimum reconstruction of the true sky brightness distribution. These include: CLEAN (Högbom, 1974); the Maximum Entropy Method (Ables, 1974); Compressed Sensing (Wiaux et al. 2009); WIPE (Lannes, Anterrieu & Bouyoucef, 1994); Smear Fitting technique (Reid, 2006) among others. It is important here to bring to the attention of the reader that almost all of these deconvolution algorithms seek to either simplify and/or improve rather than invalidate an existing one. In the current study we have employed the classical radio astronomy deconvolution method – the "CLEAN" algorithm – a non-linear iterative process which eliminates artefacts from the sampled u-v plane by interpolating the visibilities to empty regions of the u-v plane. For a comprehensive review on interferometry and synthesis imaging in radio astronomy the reader is referred to the latest edition on the subject by Thompson, Moran & Swenson (2017) and references therein.

In spite of the evolution of radio interferometry and advances in deconvolution algorithms, the technique still has its obstructions. The major problem in this field is interference from other objects (natural and manmade) also emitting at radio frequencies during observations – the so called Radio Frequency Interference (RFI). In particular our civilization revolves around radio frequencies – from mobile phone usage through to satellite technology; and the upshot of this is the characteristic mixing of these man-made radio waves with astronomical observations of the transient sky at radio wavelengths. With modern interferometers becoming increasingly more sensitive and powerful, and with the attendant huge volumes of data sets, Peck & Fenech (2013) concludes that creating a robust RFI mitigation technique has become indispensable. Indeed considerable efforts have been made in this regard at both the pre-correlation stage (e.g. Weber et al. 1997; Baan, Fridman & Millenaar 2004) and post-correlation stage (e.g. Briggs, Bell & Kesteven 2000; Athreya 2009) of the data calibration process, and it is worth mentioning here that efforts to automate these RFI mitigation techniques to ease the data cleaning process are already underway. Notable examples includes the Scripted E-MERLIN RFI mitigation PypelinE for iNTerferometry (SERPent; Peck & Fenech 2013) and the André Offringa pipeline (AOFlagger; Offringa et al. 2010a) – both of which have been employed in the present study. In the next section I present and discuss the primary emission mechanisms that govern extragalactic radio sources.

1.3 Radiative processes

Extragalactic radio sources emit over the whole EM spectrum, from the radio to X-rays and often γ-rays. The emission has its origin in various physical mechanisms, with the bulk of the radiation produced through high-energy non-thermal processes; these serve as diagnostic tools in characterising the broadband emission mechanism in radio sources. In particular, three distinct processes – *bremsstrahlung*, *synchrotron* and *inverse-Compton* – are responsible for generating continuum emission in radio sources, with observational evidence suggesting synchrotron and inverse-Compton as the main emission mechanisms at play in extragalactic radio jets. In the following, I present and discuss the basic theories governing these non-thermal radiative processes. For a detailed review on the subject, see Rybicki & Lightman (2008).

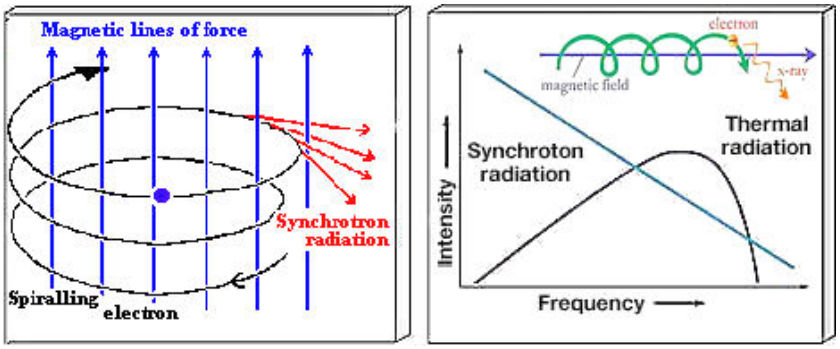

Figure 1.2: Synchrotron radiation is emitted by charged particles, usually electrons, moving at relativistic speeds in magnetic fields. The magnetic field will cause the charged particle to circle around the field line in a helical path. As the charged particle accelerates, it emits electromagnetic radiation that is radiated along the direction in which the particle is moving. A large population of relativistic particles moving in a magnetic field will radiate over a wide range of frequencies and has a high degree of polarisation – (Credit: NASA & University of Hertfordshire).

1.3.1 Synchrotron radiation

Synchrotron radiation is the primary mechanism by which extragalactic radio sources – the objects of interest in the present study – radiate their energy. They are produced when highly relativistic charged particles are accelerated within a magnetic field, $\vec{B}$. Here, the charged particle, usually an electron, is forced to spiral around the field lines and emits electromagnetic radiation that is radiated along the direction in which the particle is moving (see Figure 1.2). The emission mechanism is non-thermal and can occur over a broad frequency range (from radio to X-rays) across the EM spectrum. The phenomenon can easily be observed in many classes of astrophysical systems including jets of radio galaxies, supernova remnants, galaxies and cluster halos, etc. The spectrum of synchrotron emission contains important information about the physical processes governing the emitting regions, such as the source age and energetics, magnetic field, which give significant insights into the interplay between jet and intracluster medium.

The synchrotron power radiated is a function of the particle energy, $E \propto \gamma$, where $\gamma = 1/\sqrt{1 - v^2/c^2}$ with a peak corresponding to the characteristic frequency;

$$\nu \propto (B\sin\theta)\,\varepsilon^2 \propto B\gamma^2 \tag{1.5}$$

where θ is the pitch angle between the particle velocity and the magnetic field direction, and γ

is the Lorentz factor. Thus, the total power radiated by an electron of Lorentz factor γ and pitch angle θ is related to its frequency and is dependent on its magnetic field, the velocity and energy of the electrons. The frequency dependence of the emitted electron power (in cgs units) is given by Rybicki & Lightman (1986);

$$P(\nu) = \sqrt{3}\frac{e^3 B\sin(\theta)}{m_e c^2} F\left(\frac{\nu}{\nu_c}\right) \quad \text{in cgs units} \tag{1.6}$$

The average power is obtained by averaging over all the pitch angles. F is dimensionless and denote the synchrotron spectral function, ν is the frequency of the radiation and ν_c is the critical frequency. F and ν_c are respectively given by,

$$F\left(\frac{\nu}{\nu_c}\right) = \frac{\nu}{\nu_c}\int_{\nu/\nu_c}^{\infty} K_{5/3}(\eta)d\eta \tag{1.7}$$

$$\nu_c = \frac{3\gamma^2 eB\sin(\theta)}{4\pi m_e c^2} = \frac{3}{2}\gamma^2 \nu_G \sin\theta \tag{1.8}$$

where $\nu_G = eB/2\pi m_e c^2$ (in cgs units) is the relativistic gyration frequency and η is some arbitrary integration variable. It is well established that the number density of the electron population in a typical astrophysical source behaves like a power-law,

$$N(E)dE = kE^{-p}dE \tag{1.9}$$

where k is some constant with units of energy to the power $-p$ per volume, p is some power law index of the particle energy distribution and dE is the energy range under investigation. The spectrum of a purely synchrotron emitting electron population follows such a power-law distribution, and the synchrotron total intensity spectrum (energy radiated at a certain frequency) can be described by:

$$S(\nu) \propto \nu^{(1-p)/2} = \nu^{\alpha} \tag{1.10}$$

for $\nu \ll \nu_{max}$ (the broad maximum frequency of emission), $\alpha = (1-p)/2$ is the radio spectral index and ν is the characteristic frequency of the emitted electron population. Over the electron population lifetime, the energy distribution is modified due to energy losses resulting in deviations from the simple power-law. Thus, the slope of the synchrotron spectrum can change, becoming steeper after a certain break frequency and from that change, the so called *radiative* lifetime "age" of the electron population could be estimated.

1.3.2 Inverse-Compton radiation

Inverse-Compton emission mechanism involves the up-scattering of ambient photons to higher energies by electrons. Here, relativistic electrons transfer energy to *low-energy* photons after collisions, boosting them even to gamma-ray energies. For an isotropic distribution of photons, the power emitted (energy loss) in the rest frame by a single electron from inverse-Compton scattering can be described by:

$$P_{iC} = -\left(\frac{dE}{dt}\right) = \frac{4}{3}\sigma_T c \frac{v^2}{c^2}\gamma^2 U'_{rad} \tag{1.11}$$

where v is the velocity of electrons, σ_T is the Thomson cross-section which describes the probability of scattering between the photons and the electrons, and U'_{rad} is the energy density of the photon field in the rest frame of the electron and is given by;

$$U'_{rad} = U_{rad}\int_0^{\pi} \gamma^2 \left(1 + \beta cos\theta\right)^2 \frac{1}{2}\sin\theta d\theta = \frac{4}{3}U_{rad}\left(\gamma^2 - \frac{1}{4}\right) \tag{1.12}$$

Comparing Equation 1.11 with the expression for synchrotron power (Equation 1.6) we see that they both have the same electron-energy dependence – the photon number density is conserved in the scattering whereas the energies are boosted by a factor γ^2. Thus, the spectral shape depends mostly on the energy distribution of the electrons. For a power-law distribution with index p, it follows that the inverse-Compton spectrum is a power-law, and can be described by Equation 1.10.

The ratio of the total amount of energy liberated by relativistic electrons subjected to both a radiation and magnetic field and therefore emitting photons by both the inverse-Compton and synchrotron mechanism, is given by;

$$\frac{P_{syn}}{U_{iC}} = \frac{U_B}{U_{rad}} = \frac{B^2}{8\pi U_{rad}} \quad \text{in cgs units} \tag{1.13}$$

It is noteworthy here that, in radio-loud AGNs where the most powerful "relativistic" jets are produced, the synchrotron photons that characterise the jet emission can be up-scattered by the very electron population that produced them, giving rise to the so called *synchrotron self-Compton* phenomenon – this has the tendency to critically limit the brightness temperature (the power per unit solid angle per unit bandwidth in terms of the Rayleigh-Jeans approximation) that a self-absorbed[2] synchrotron emitting source can reach.

[2]Synchrotron self-absorption occurs when photons propagating through plasma on its way out of a source are

1.3.3 Bremsstrahlung radiation

Bremsstrahlung (or "free-free radiation") is a major part of the radio spectrum and can easily be observed from HII regions. It is emitted by a charged particle that is deflected (i.e., accelerated or decelerated) in a series of Coulomb interactions with ions. In principle, the deflection results in energy loss (i.e., a reduction in kinetic energy) of the electron through the emission of energy in the form of a photon. If the electron energy distribution of the emitted radiation (for optically thick region) follows the well-known Maxwellian distribution (i.e., in thermal equilibrium at a given temperature), the emission is termed *thermal* bremsstrahlung. Here, the emissivity of an electron of charge Z at a frequency ν can be described by the relation;

$$\epsilon_b(\nu) = \frac{2^5\pi e^6}{3m_e c^3}\left(\frac{2\pi}{3m_e k}\right)^{1/2} Z^2 n_e n_i g(Z,T,\nu) T^{-1/2} \exp\left(-\frac{h\nu}{kT}\right) \quad \text{in cgs units} \qquad (1.14)$$

where e and m_e are the charge and mass of the electron; n_e and n_i are the number density of electrons and ions; and k and h are the Boltzmann's and Planck's constant respectively. The term $g(Z,T,\nu)$ is the Gaunt factor which accounts for quantum mechanical effects, and is both frequency and temperature dependent (Rybicki & Lightman, 1986). It follows from Equation 1.14 that, at lower frequencies, the spectrum flattens – with an exponential cutoff at $\nu_{cutoff} \simeq kT/h$. In the case of relativistic electrons with energy distribution that follows a power-law, *relativistic* bremsstrahlung radiation is produced which is also of power-law shape with the same energy index as the emitting electrons.

Of astrophysical interest in the low frequency regime is the so called *free-free absorption* in which the charged particles gain energy during deflection, through absorption of a photon. At a given frequency, this *free-free absorption* which is responsible for a strong turnover of the radio spectrum is given by;

$$S_{ffa}(\nu) = S_0\ (\nu/\nu_0)^{\alpha}\ \exp\Big(-\tau_0\,(\nu/\nu_0)^{-2.1}\Big) \qquad (1.15)$$

where ν_0 is a scale frequency, τ_0 is the optical depth at ν = ν_0, and S_0 is a scale flux density. At ν = ν_0 the flux density is then $S_0\ \exp(-\tau_0)$. In radio-loud AGNs, the steep turnover observed in the lower frequency regions of compact steep-spectrum sources has been argued to arise predominantly from a thick gas- and dust-disk, and interpreted as the presence of "cold

scattered off one of the synchrotron electrons. In this scenario, the total flux seen by the observer will be much smaller than if all the synchrotron photons escaped the source.

dense plasma" around the lobes of GHz Peaked Spectrum (GPS) radio sources – these have the potential to smother expansion of jets and lobes in AGNs (e.g. Kameno et al. 2003). This notwithstanding, *synchrotron self-absorption* is generally favoured over *free-free absorption* as the dominant phenomenon responsible for spectrum turnover due to the non-thermal nature of the emission mechanism at play in extragalactic radio sources and the high density of ionised gas required for free-free absorption to dominate (e.g. see the case of NGC 7385; Birkinshaw, Rawes & Worrall 2020).

1.4 The Active Galactic Nuclei (AGNs)

Active Galactic Nuclei (AGNs) are bright compact regions at the centres of a relatively small minority ($\sim$ 10 – 15 %) of galaxies (e.g. Ho, Filippenko & Sargent 1997), driven by the accretion of infalling material onto the galactic-centre supermassive black hole (central engine). Originally discovered by Carl Seyfert in the 1940s, the physics and environments of these peculiar class of galaxies have progressively become a subject of interest in the field of astrophysical research and are among the most studied entities of the cosmos today. The distinctive characteristic of such galaxies as observed by Seyfert in the optical band was their characteristic bright, semi-stellar nucleus and broad emission lines with gas speeds up to 8500 km/s (Seyfert, 1943). Compelling as the discovery was, the rather poor angular resolution of telescopes at the time made characterization of these objects a daunting task. However, thanks to advances in astronomical instrumentation in the years leading up to the present decade, composite observational evidence particularly at radio frequencies has considerably opened up the hidden Universe and allowed for a more comprehensive mapping of these celestial objects at extreme spatial resolutions (e.g. Grupe 2004). This has greatly broadened our understanding of these extraordinary cosmic species – from the then moderate conclusion drawn that radio-loud quasars, for example were simply strong radio emitting galactic stars (e.g. Schmidt 1963) to rather more complex conclusions today which suggest that these AGNs are powered by the conversion of gravitational energy (of accreted material) into mechanical and electromagnetic energy inside their central engine (e.g. Silk & Rees 1998; Krolik 1999). Today, it is a well-known fact that all massive galaxies contain massive BHs at their centre – the activities of which account for some of the observational characteristics of the host galaxy. These unusual activities within their nuclei coupled with the intense conditions characterizing their environment, earmark them as key

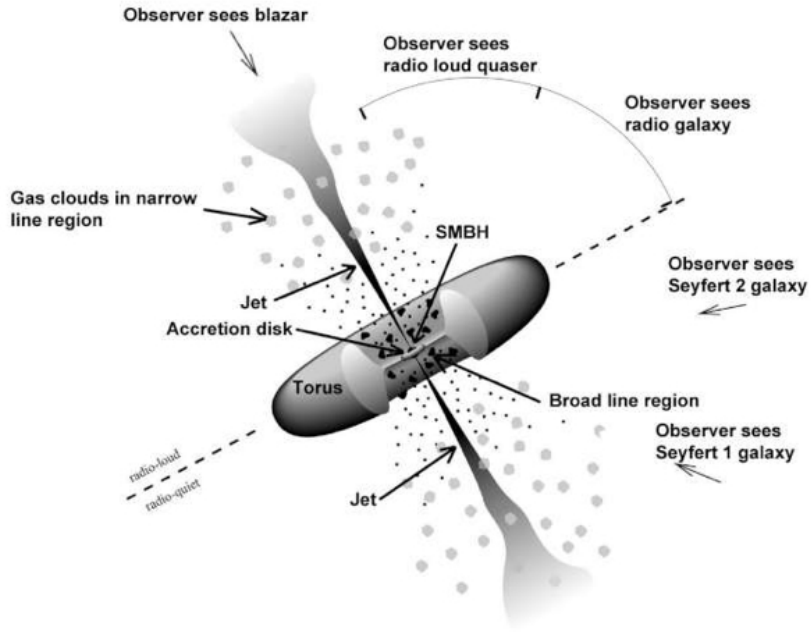

Figure 1.3: Schematic illustration of the standard AGN-unification model as posited by Urry & Padovani (1995). A central accreting supermassive black hole is surrounded by fast moving line-emitting clouds and an obscuring torus. Classification of the different types of AGN discussed in the text and labelled here is dependent on the viewing angle of the observer and jet beaming effects – (Image credit: Robert Findlay).

laboratories for exploring the frontiers of high energy astrophysical processes in the Universe. Figure 1.3 shows the basic building blocks of AGNs; although for many radio AGNs (e.g. 3C 465 and 3C 83.1B), these features are not immediately obvious.

Table 1.1 presents a statistical comparison of the components of a standard AGN model. The gravitational potential energy of the supermassive black hole at the centre is the ultimate source of the AGN luminosity and it is surrounded by an accretion disk which occupies the centre of a geometrically thin and optically thick dusty torus. Orbiting clouds of gas at different distances from the nucleus produce two distinct emission-line regions: (a) the broad-line region (BLR) which predominantly resides under the black hole's gravitational influence and (b) the narrow-line regions (NLR) which spreads over much larger scales. These emission lines according to Popović (2005) are both produced under a broad range of physical and kinematical conditions and serve as powerful diagnostic parameters for emitting gas in the different emitting regions of AGNs. Finally, twin radio jets of relativistic particles (which are the objects of interest in the

Table 1.1: Comparison of the components of a standard AGN model

	Black Hole	Accretion Disk	Emission Lines		Torus
			BLR	NLR	
r (pc)	10^{-6} – 10^{-5}	$\sim 10^{-3}$	~ 0.01 – 0.1	~ 100 – 1000	~ 1 – 100
n_e (cm^{-3})	—	$\sim 10^{15}$	$\sim 10^{10}$	$\sim 10^3$ – 10^6	$\sim 10^3$ – 10^6
v (km s^{-1})	$\sim c$	$\sim 0.3c$	$\sim$ few $\times 10^3$	$\sim$ few $\times 100$	~ 50 – 100

Notes: Demographics of the main constituents of an active galactic nuclei showing their respective sizes, r; number density, n_e; and gas velocity FWHM, v – (Adapted from Bianchi, Maiolino & Risaliti (2012) and references therein).

present study) can also be seen launched from close to the accretion disk in opposite directions. It is worthwhile to mention here that several efforts have been made in the recent past on both the observational (e.g. Pérez et al. 2000; Márquez et al. 2004) and theoretical (e.g. Gutcke et al. 2015) front to elucidate our understanding of the jet activities associated with the central engine – which serves as fuelling mechanism that powers the AGN in order to constrain the morphology and large scale kinematics of these group of galaxies.

1.4.1 Towards a unification theory: the AGN paradigm

As illustrated in Figure 1.3 above, the whole AGN paradigm consists of a central supermassive black hole (e.g. Peterson 2014), whose gravitational potential energy is the ultimate source of the AGN luminosity; a circumnuclear accretion disk (e.g. Narayan & Yi 1994), that provides the means for converting gravitational potential energy into radiation; optically-thick emission line clouds (e.g. Cackett & Horne 2006); an obscuring torus (e.g. Tadhunter 2008), that obstructs the continuum and broad-line emission in some directions; and in some cases bipolar outflows of relativistic plasma which power massive radio sources. However, an intriguing challenge resulting from this paradigm is the fact that different AGN types arises depending on the viewing angle of an observer – i.e. strongly orientation dependent. This prompted researchers to hypothesize that perhaps some different physical conditions might be at play and ultimately led to the concept of constructing a standard model to describe the structure of these cosmic species. Notwithstanding the complexity of host galaxy morphology, environments, and cosmic evolution among others (see Urry & Padovani 1995), several attempts have been made in the past to unify AGNs (e.g. Antonucci 1993; Urry & Padovani 1995; Falcke, Körding & Markoff 2004). For in-depth discussions and review on the subject, the reader is referred to the seminal work

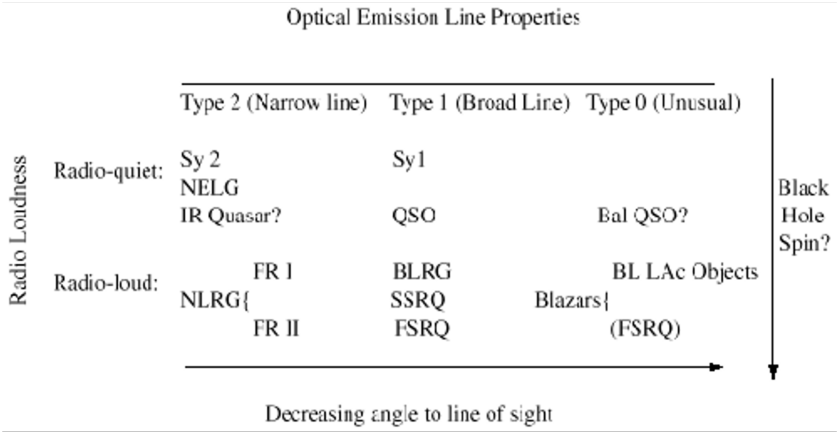

Figure 1.4: An empirical division of AGN according to their observed radio and optical/ultraviolet properties. All AGN-type are the same with the observed differences due to angle of line of sight of the observer. It is important to note here that this proposition dates back to, at least, Rowan-Robinson (1977), and became famous in the mid-80s with subsequent reviews by Lawrence (1987); Antonucci (1993); Urry & Padovani (1995); Goodrich (2001).

of Urry & Padovani (1995) whose effort to unify AGNs about two decades ago has to date proven to be robust and most favoured unified scheme – except that it does not work for most radio galaxies.

Characterisation of AGNs is commonly based on their optical spectra and radio-loudness into; Type 1 – those with bright continua and broad emission lines; and Type 2 – those with weak continua and narrow emission lines. However, the evidence of two forms of strongly anisotropic radiation patterns from radio-loud AGN – (1) obscuration by optically thick matter and (2) relativistic beaming of radio emission primarily stimulates the different classes of AGN unification schemes (Urry, Padovani & Stickel, 1991). Substantial evidence which has motivated unification schemes have predominantly originated from:

1. Apparent Hidden Emission Lines – in which some Seyfert 2s have been observed to show broad emission lines in polarised light due to scattering of photons by hot electrons near the central engine and thereby appearing as Seyfert 1s (e.g. Capetti et al. 1995). Conversely, some narrow line radio galaxies (NLRG) have been observed to have hidden broad lines (e.g. Goodrich 2001).
2. Statistical Tests – where all Seyfert galaxies have been shown to have narrow line regions

with very similar properties (e.g. Cohen 1983). Indeed Lawrence (1987) found the continuum of Seyfert 1s to be stronger compared to their Seyfert 2 counterparts, however, it was not until a decade later that HST observations revealed that the size of Seyfert 1 continuum emitting regions was smaller than those of Seyfert 2s (e.g. Nelson et al. 1996).

Additional evidence for unified schemes has also come from host galaxy properties, environment, and number counts (e.g. Lin, Ostriker & Miller 2010).

The explanation by Miller & Antonucci (1983) of the observed weak polarized broad emission lines which was unexpectedly hidden by strong narrow lines in the Seyfert 2 nucleus of NGC 1068 set the foundations for current unified models. Although at present an inexact construction of AGN unified schemes exists, a great deal of the underlying physics driving these schemes is still work in progress due to the observed strongly anisotropic radiation patterns. With the exception of the presence or absence of a jet, the current most favoured AGN unified models lean towards classification schemes which are largely dependent on the orientation of the dusty torus and the luminosity of the nucleus and can be grouped as:

- Type 1 – Nucleus can be seen face on. Broad and narrow emission lines originating in a high density medium ($n_e \geq 10^9$ cm^{-3}) and low density medium ($n_e \approx 10^3$ – 10^6 cm^{-3}) respectively. Strong continuum emission spectra.
- Type 2 – Nucleus can be seen edge-on. Narrow emission lines due to obscuration of broad lines by dusty torus. Medium is compton thick suppressing X-rays (e.g. Bassani et al. 1999).
- Intermediate – Observational properties lie between Type 1 and 2. Fractional obscuration of nucleus due to orientation of torus.

The luminosity of the galactic nuclei additionally divides radio AGN population into:

- Seyferts – Galaxies (usually a spiral) with a high surface brightness nucleus that reveals unusual emission-lines (e.g. Seyfert 1943; Kraemer & Crenshaw 2000).
- Quasi Stellar Objects (QSOs) – Extremely luminous, high redshift sources (e.g. Mortlock et al. 2011). Further classified into radio-loud and radio-quiet objects.

Despite notable progress in constructing these relatively simple classification schemes, a number of significant problems exist (see Urry, Padovani & Stickel 1991; Urry & Padovani 1995). In particular, the complexity of AGN systems allow researchers to further speculate about the potential existence of fundamentally different objects altogether. The work of Bianchi, Maiolino & Risaliti (2012) in which some objects identified as Type 2 were found to miss broad line regions; and Panessa & Bassani (2002) who also found no clear evidence for the presence of a

dusty disk in a number of low power sources, among others are basis for such speculations and may eventually turn out to be true with more sophisticated astronomical instrumentations on the horizon. Figure 1.4 above shows the taxonomy of AGNs as posited by current most favoured models.

1.5 Radio AGNs

1.5.1 A morphological review

The term 'Radio AGNs' primarily refers to bright radio sources whose strong synchrotron emission allows their detection even at high redshifts. Historically, they have been dichotomized into the radio-loud (RL) and radio-quiet (RQ) galaxies with difference in radio luminosity (which results in the observed differences in host galaxy properties and environments) as the criterion (e.g. Lin, Ostriker & Miller 2010). Radio-quiet AGNs have relatively low luminosity and make up approximately 90 % of all active galaxies. They include; radio-quiet quasars, Seyfert galaxies and LINERs (e.g. Mushotzky 1982). The remaining 10 % are radio-loud AGNs and these include; radio-loud quasars, BL Lac Objects, Optically Violent Variables (OVV) and the two morphologically distinct types: FR I (jet/plume dominated) and FR II (lobe dominated) radio galaxies (Fanaroff & Riley, 1974) which I discuss further in the next section.

In spite of the variances in host galaxy properties and environments, Sanders et al. (1989) reported similar spectral energy distribution at infrared wavelengths for both the radio-quiet and radio-loud AGNs. In a related study, Xu, Sulentic & Tuffs (1999) essentially observed a significant overlap in their emission line luminosities despite separations in their radio luminosities with the work of Cirasuolo et al. (2003) further confirming some continuity of properties among selected radio AGN samples. Additionally, more recent observations have even revealed compelling evidence that a radio-loud/radio-quiet double AGN system may co-exist (see Tadhunter et al. 2012) pointing to a rather sharp contrast to earlier conclusions of Kellermann et al. (1989) and Miller, Peacock & Mead (1990) that there is a big gap in radio power between radio-loud and radio-quiet varieties of QSOs. Furthermore in contrast to previously held assertion that radio-quiet objects lie in disk-dominated hosts compared to bulge-dominated hosts for their radio-loud counterparts (e.g. Smith et al. 1986) evidence suggests that luminous radio-quiet quasars may also exist in bulge-dominated hosts (e.g. Taylor et al. 1996; Bahcall et al. (1997)). Rather than

resolving the complexity of radio AGN classification, these associations of host galaxy properties and environment among the different classes seemingly complicates our quest to classify these objects into unique groups as evident in the unified schemes. In the section to follow, I focus the discussions on a review of the Fanaroff and Riley class of radio galaxies which has indeed proven remarkably robust in our understanding of the morphology of radio-loud AGNs over the last five decades.

1.5.2 The Fanaroff-Riley class I and II dichotomy

The Fanaroff and Riley types are predominantly a classification scheme based on the degree of correlation between the high and low surface brightness in the lobes of extragalactic radio sources with their radio luminosity. The classification is intrinsically linked to the degree of brightening near either the core (the central region of the galaxy) or at the extended regions and can be quantitatively defined as a measure of the ratio of the distance between the two brightest spots and the overall size of the radio galaxy image (Fanaroff & Riley, 1974). Later observations by Birkinshaw et al. (1978) showed that the linear separation between regions of enhanced emission tends to increase with radio luminosity in weak radio galaxies.

1. Fanaroff-Riley Type I (FR I): Their high brightness regions are associated with the central galaxy and are often observed with double-sided radio jets. Luminosities are typically below 10^{25} W Hz^{-1} at 1.4 GHz and they show extended structures which interact with the external environment at large distances ($\sim$ kpc scales) from the galactic centre. Wide and narrow angle tail radio galaxies are within this class.
2. Fanaroff-Riley Type II (FR II): They are edge-brightened with often one-sided highly collimated radio jets which terminate in large radio lobes with visible hot spots. Luminosities are typically above 10^{25} W Hz^{-1} at 1.4 GHz. They include classical doubles – "powerful" radio sources with huge lobed jets extending hundreds of kpc into the intergalactic medium.

While on the one hand there exist fundamental debates about the link between accretion mode and jet morphology (e.g. Best & Heckman 2012; Ineson et al. 2015), the FR morphological divide as described above has long been thought to be fundamentally linked to the interplay of jet power and host galaxy environment (e.g. Bicknell 1995;Laing & Bridle 2002; Hardcastle & Croston 2020). Such morphological difference implies that jets of the same power will disrupt (and thus become FR I) more easily in a high density environment compared to a low one (e.g. Bicknell 1995; Kaiser & Best 2007). Observational evidence in support of such conclusions

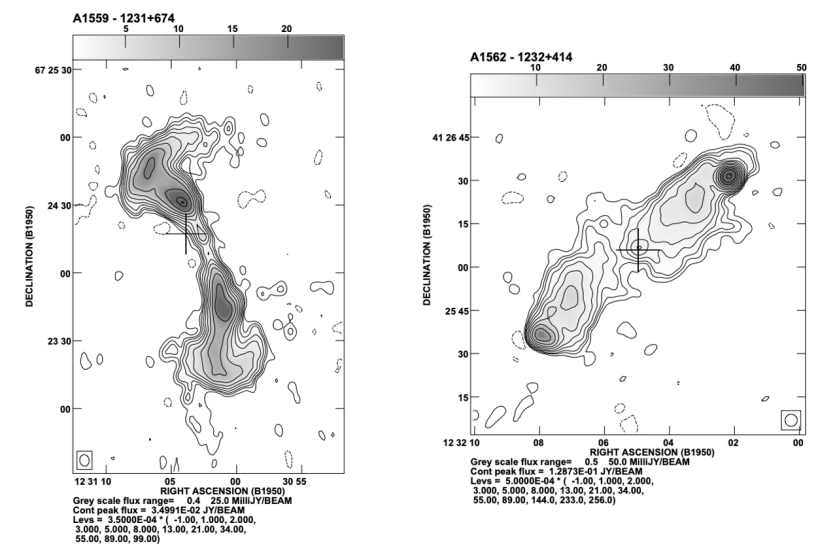

Figure 1.5: Radio maps of the two distinct Fanaroff and Riley class of radio galaxies. Left: a low luminosity (FR I) radio source with diffuse structures and symmetric jets originating from the core. Right: a classical double (FR II) radio source with huge radio lobes and bright hot spots, jets are often too faint to see – (Adapted from Owen & Ledlow 1997).

has come from the discovery by Ledlow & Owen (1996) that the FR I/II luminosity break is dependent on host-galaxy magnitude. Although Urry & Padovani (1995) argue that construction of a physical relation between FR Is and FR IIs is key to resolving AGN unification schemes; differences in the observed radio jets (e.g. Bicknell 2002), luminosity differences (e.g. Heckman et al. 1994), and morphological differences (e.g. Parma et al. 1992) among others makes reconciliation of these two classes a nearly impossible task and Marscher (2005) notes that nothing short of a multi-waveband approach across the EM spectrum would be required to achieve this feat.

The observed variations in the radio jet properties of both classes are directly associated with the differences in host galaxy properties and environment, with typical FR Is found to lie at the centre of optically bright galaxy clusters whereas the FR II counterparts live in isolation or poor groups. Nonetheless, observational evidence have shown that at higher redshifts ($z \gtrsim 0.5$), both classes do live in rich cluster environments (e.g. Hill & Lilly 1991). Similarly, the luminosity ranges for both classes have been observed to overlap at higher radio frequencies by two orders of magnitude (e.g. Laing, Riley & Longair 1983; Morganti, Killeen & Tadhunter 1993). Recent observational studies by Mingo et al. (2019) have also found large populations of low-luminosity

FR IIs, extending three orders of magnitude below the traditional FR break, suggesting the jet power/environment paradigm as a more reliable measure for the FR break. Except for these fractional overlaps, the classification of radio loud sources into two distinct morphological groups (i.e., FR Is & FR IIs – see Figure 1.5) by Fanaroff and Riley has proven remarkably robust and underpins many of the current studies of radio-loud AGNs. It is of interest to mention here that more recently attempts have also been made by researchers to further classify a new group of Fanaroff and Riley class of radio galaxies – the so called FR 0s – which in spite of sharing typical FR I characteristics are more core dominated (by a factor of ~ 30) than FR Is and exhibit a clear deficit of extended radio emission (see Baldi, Capetti & Giovannini 2016 for review).

1.5.3 Low and High excitation radio galaxies

In addition to the spectroscopic classification of radio galaxies into NLRGs (including: Seyfert 2s, FR Is and FR IIs) and BLRGs (Seyfert 1s and FR IIs), these objects can broadly be divided into low-excitation radio galaxies (LERGs) and high-excitation radio galaxies (HERGs) (e.g. Hine & Longair 1979) and, as noted by Laing et al. (1994), the division is primarily based on the strength of excitation in their emission line (e.g., [OIII]) spectra. Low-excitation radio galaxies are almost entirely FR Is with a significant population of low-luminosity FR IIs, while HERGs are almost exclusively FR IIs and encompass all NLRGs and BLRGs. Compared with HERGs, LERGs have accretion of $\lesssim 1$ % Eddington rate, are quiescent, associated with massive galaxies, richer environments, and have a broad range of integrated degrees of polarisation (e.g. Hardcastle 2004; Smolčić 2009; Best & Heckman 2012; Hardcastle et al. 2013; O'Sullivan et al. 2015).

Early works on unified schemes of radio-loud AGNs (e.g. Scheuer 1987; Barthel 1989) posited that physical properties of these objects including their clustering environments must be identical. However, these conclusions have been found in later studies to favour only high-z radio sources (e.g. Singal 1993). At low-z, there exist a fundamental problem in reconciling radio sources with the clustering environments in which they live, and as noted by Hardcastle (2004), the simple unified model of Barthel (1989) breaks down, for example due to the absence of low-z FR II quasars. In line with this observation, Laing et al. (1994) conclude that LERGs – which are predominant at low-z and low FR II luminosities must form a separate population of radio sources. In a related study, Hardcastle, Birkinshaw & Worrall (1998) provides a succinct conclusion on the subject by stating that, treating LERGs as a separate non-unified population

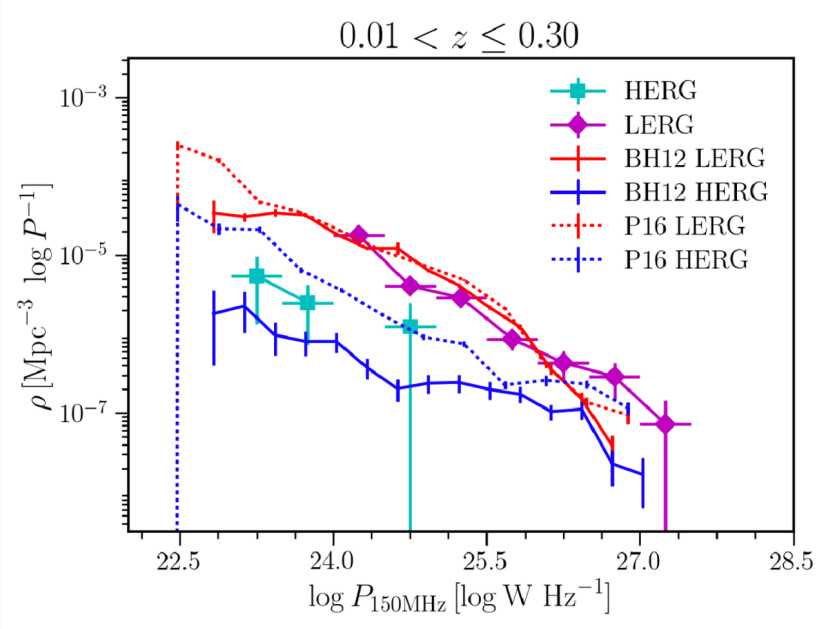

Figure 1.6: The radio luminosity functions for low redshift, $0.01 < z < 0.30$ sample, separated into Star-Forming (SF), and AGN accretion modes – LERGs and HERGs. For comparison, the luminosity functions of Pracy et al. (2016), labelled P16, are included (scaled from 1.4 GHz and to the same units) – (Adapted from Williams et al. 2018).

and BLRGs as low-luminosity quasars could potentially solve the low-z problems for radio-loud unification models. Figure 1.6 shows the radio luminosity functions for a low redshift ($0.01 < z < 0.30$) sample of LERGs and HERGs.

One of the fundamental requirements for the so called LERG/HERG dichotomy can be linked to the works of Laing et al. (1994); Jackson & Rawlings (1997); Hardcastle, Evans & Croston (2006), in which they observed that many low-power radio sources with powerful ($\gtrsim 10^{44}$ erg s^{-1}) jets do not have noticeable accretion disc, torus, BLR, or NLR; suggesting that their optical and X-ray nuclear emission originate entirely from the jet. Additional evidence for this sub-division has also come from systematic differences in their respective accretion mode, and Best & Heckman (2012), highlights this argument by concluding that a simple scenario for the LERG/HERG dichotomy could potentially be linked with accretion rate in both classes. Hardcastle, Evans & Croston (2006) and Smolčić (2009) have further shown that LERGs and HERGs exhibit differences in the way they accrete material onto their respective central SMBH; with LERGs having radiatively inefficient accretion compared with their HERGs counterparts

(e.g. Evans et al. 2006; Best & Heckman 2012). Consequently, Croton et al. (2006) note that, these two distinct radio population may provide feedback in different ways. Indeed these observed differences between the isotropic properties of LERGs and HERGs, supports earlier conclusions by Hardcastle, Birkinshaw & Worrall (1998), that these two classes are physically different populations of radio sources. For further reviews on the LERG/HERG dichotomy, the reader is referred to works of Hardcastle, Birkinshaw & Worrall (1998); Hardcastle (2004); Hardcastle, Evans & Croston (2006); Hardcastle et al. (2013); Ching et al. (2017) and Williams et al. 2018.

1.5.4 The radio AGN duty cycle

The birth, life, death and rebirth of radio galaxies is in many facets analogous to our own human existence and directly points to the universality of re-creation across all cosmic scales and time. In the 1950's the identification and emission mechanism in radio sources were the key questions among researchers (e.g. Baade & Minkowski 1954), however, by the 90's focus had been shifted from these early questions to rather obtaining an understanding of the life-cycle and evolution of radio galaxies (e.g. Dunlop 1999; Tadhunter 2006; Sun et al. 2015). These duty cycles (see Figure 1.7) which are intrinsically powered by outflows of relativistic jets from the central SMBH have direct consequence on feedback, structure formation and black hole growth (cf. Section 1.6). To resolve this however will require an answer to the question of *"what actually fuels radio AGNs in the first place?"*

One of the earliest attempt to resolve the fuelling issue can be traced back to the work of Shlosman, Frank & Begelman (1989); and later conclusions that starburst always accompanies the inception of AGN activity (see Kaufman et al. 1999) have been found to be empirically consistent with the mathematical relation:

$$\dot{M}_t \simeq \left(1.4 \times 10^{11} \mathrm{g\,sec^{-1}}\right) \left(\frac{M}{M_\otimes}\right)^2 \left(\frac{\rho_\infty}{10^{-24} \mathrm{g\,cm^{-3}}}\right) \left(\frac{C_s}{10\,\mathrm{km\,s^{-1}}}\right)^{-3} \tag{1.16}$$

which suggests that SMBHs at the centres of active galaxies accrete material from the interstellar medium via the Bondi accretion. Note that Equation 1.16 above is a numerically scaled solution of the *Bondi accretion* for AGNs (See Bondi 1952 for original derivation). $\dot{M}_\mathrm{t}$ is the rate of accretion onto the galactic SMBH, ρ_∞ is the density of the interstellar medium and C_s the velocity

of infalling material or *sound speed* in the surrounding medium if the infalling material has velocity lower than the sound speed. Note however that, the fuelling mechanism at play may not necessarily be same in all AGNs. For example, the conclusion that FR Is have weaker accretion disks due to their faint nuclear X-ray and UV emission at a given radio power raises the question of whether or not there is a different accretion mode at work in these class of radio AGNs (e.g. Fabian & Rees 1995). Best & Heckman (2012) further argue that high excitation radio galaxies (HERGs) are fuelled at high rates through radiative accretion disks by cold gas, while their low excitation counterparts are fuelled via radiatively inefficient flows at low accretion rates, often by gas associated with the hot X-ray haloes of their host galaxy/cluster. In spite of the absence of a simple AGN fuelling mechanism to date, there is overarching certainty that at later stages of their life cycle the accretion rate is significantly reduced for a number of reasons (see Sanders et al. 1988 for review).

Perhaps the single most important question in the radio AGN duty cycle paradigm rather would be what the active phase (lifetimes) of the central engine of these radio sources are. Schmidt (1966) offered a way for statistically estimating these lifetimes as:

$$t_{RG} \simeq \left(\frac{N_{RG}}{N_E}\right)(t_E) \approx 10^8 \ \ yrs \tag{1.17}$$

where $t_{\rm RG}$ is the harmonic-mean lifetime of a radio galaxy (may include episodic activities), $N_{\rm RG}$ and $N_{\rm E}$ are number densities of radio galaxies and their parent population elliptical galaxies, respectively, and $t_{\rm E}$ is the lifetime of an elliptical galaxy. The physical interpretation of Equation 1.17 above is that the fractional representation of an AGN population gives its lifetime.

Recent observational evidence of longer (more frequent) duty cycles in massive galaxies suggests that these galaxies are capable of sustaining cooling flows[3] which provide fuel to their central SMBHs. This long sustained feedback is known to correlate with the observed galaxy luminosity function in massive galaxies (see Benson et al. 2003 and references therein) and a direct consequence of the so called *episodic activity* which points to a "birth-death-rebirth" concept in radio AGNs (e.g. Baum et al. 1990; Schoenmakers 2001; Saikia & Jamrozy 2009). These repetitive activities are often characterised by a diffuse remnant or lobe of the radio source from an earlier active phase, with a younger lobe or jet within it, as observed by

[3]In nearly a third of all galaxy clusters, the central density of the ICM is thought to be high enough, and the central temperature low enough that it ought to cool in a few 10^6 yr. This rapidly cooling region occupies $\sim 10\%$ of the virial radius and is centered on the brightest cluster galaxy (BCG).

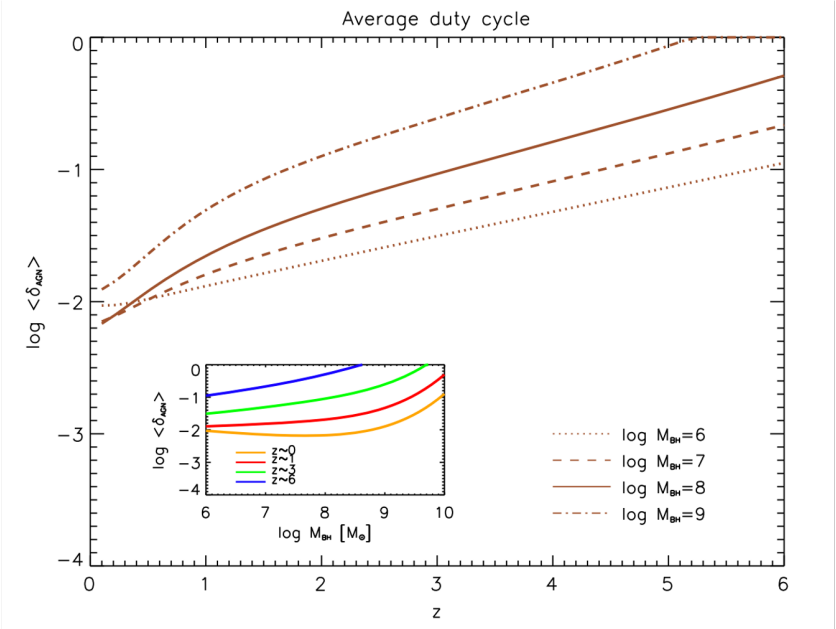

Figure 1.7: Theoretical prediction for the average AGN duty cycle $\langle \delta_{\rm AGN} \rangle$ as a function of redshift z, for different BH masses; $M_{\rm BH}$ = 10^6 (dotted), 10^7 (dashed), 10^8 (solid), and 10^9 $M_\odot$ (dot-dashed). The inset illustrates the AGN duty cycle as a function of BH mass at different redshifts; z=0 (orange), z=1 (red), z=3 (green), and z=6 (blue) – (Source: Aversa et al. 2015).

Schoenmakers et al. (2000). The plausible explanation for this occurrence is that the radio galaxy turned off at some point in its lifetime and turned back on. The concept of lifetime estimation has further prompted the use of both dynamical (e.g. Capetti et al. 1999) and spectral (e.g. Murgia et al. 2011) age estimates to constrain duty cycles, with low and high power radio sources currently thought to have ages of ($\sim 10^{7-8}$ years) and ($\sim 10^{6-7}$ years) respectively.

Obviously there remain more questions than answers at present regarding the duty cycles of radio AGNs, but what we do know is that activity is triggered once infalling material reaches the central accretion disk with the resultant activity dependent on the fuelling rate and black hole mass and spin (e.g. O'Dea 2001). The jets or collimated outflows of electron-positron plasma from the host galaxy central engine, which are emitted in the active phase form the foundations of the present study. In the section to follow, I discuss the context within which these radio AGN activities play a leading role.

1.6 Feedback, structure formation and black hole growth

Understanding how galaxies and large scale structures form and evolve over cosmic time is one of the main challenges for present day astronomy and among the key drivers for many of the current and future large area surveys and instrumentation. To achieve this goal however will require studying the *relevant* comic species across all cosmic time and scale. In line with this, Urry & Padovani (1995) argue that understanding radio AGNs is essential to our understanding of the formation and evolution of structure in the universe.

By virtue of their efficient coupling with both the ISM and IGM (e.g. Tadhunter 2008), suitably-tuned feedback of energy and momentum (e.g. Bîrzan et al. 2008) from AGN activity is thought to be responsible for regulating the properties of structures we see today in the observable universe, as well as the relationship between galaxy bulge and central SMBH masses (e.g. Ferrarese & Merritt 2000). Tadhunter et al. (2012) shed further light on this argument by concluding that gaining insight into triggered radio-loud AGN activity is vital since relativistic outflows and lobes of such AGN provide one of the most important forms of AGN induced feedback. This notwithstanding, Morganti (2010) also draws attention to the fact that such AGN feedback activity can have both constructive and destructive effects. More recently, in an attempt to develop a simple model for AGN feedback in nearby early-type galaxies, Kaviraj et al. (2011) observed that the coupling between AGN energy and the cold gas reservoir can be estimated by a 'feedback function' ($f_{\rm t}$), which relates the observed bolometric luminosity, $L_{\rm B}$ of the AGN as:

$$f_t.L_B.\delta t = G.M.\delta M_g/R \tag{1.18}$$

where G is the gravitational constant, R and M are radius and mass of the galaxy respectively, $\delta M_{\rm g}$ is the cold gas mass removed from the reservoir, and δt is the size of the timestep being considered. Although not the main subject of this study, it is important to note that to date, two modes of AGN feedback have been proposed; (1) the kinetic or radio-mode feedback which primarily occurs in cool core clusters and groups where energy input from AGN jets resulting from activities in the central engine heat up the ICM and regulates accretion and star formation; and (2) the radiative or quasar-mode feedback which occurs in very luminous AGNs and characterized by slower winds of both ionized, neutral atomic, and molecular matter (e.g. Fabian 2012; Voit & Donahue 2015; Fiore et al. 2017).

In the case of structure formation, observational evidence suggest that starburst activity is

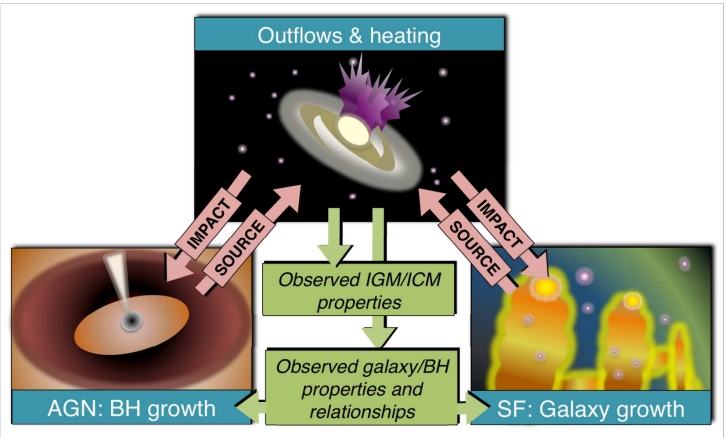

Figure 1.8: A schematic illustration of the possible connection between AGN induced feedback, structure formation and black hole growth. The enhancement or suppression of structure formation is heavily dependent on the total energy and momentum injected into the ISM/ICM through feedback induced activities and this consequently serves as fuel for the accreting SMBH growth. The ultimate result of all these feedback induced activities is evident in the observed variations in bulge properties of host galaxies – (Image credit: Christopher M. Harrison).

closely linked with AGN activity (exception; radio-loud AGNs), with much of the observed emission line spectrum and the UV-optical spectral energy distribution being contributions from the starburst (e.g. Terlevich et al. 1992; Lawrence 1999). In connection to this, Sanders et al. (1988) had previously posited a plausible sequence of galaxy interactions in which starbursts precede AGN activity. Furthermore, quantitative estimates of the power inferred from cavities also shows a correlation with cooling luminosity suggesting that the energy input from the radio AGN feedback mechanism has the potential of resupplying cooling gas on large scales (e.g. Fabian 2012); with jets driving shocks and outflows in the warm gas on scales of $\sim$ 1–10 kpc (e.g. Holt, Tadhunter & Morganti 2008), influencing the star formation histories of the galaxy bulges.

In spite of the controversy that surrounded the correlation between the evolution of galaxies and their SMBHs in the recent past (e.g. Peng et al. 2006), current simulations and observational evidence seemingly allay this debate. As illustrated in Figure 1.8, there exists strong evidence of a tight correlation between SMBH mass ($M_{\rm BH}$) and host bulge mass ($M_{\rm Bul}$) properties (e.g. Fabian 2012; Kormendy & Ho 2013) with winds and outflows from the central engine either

heating or blowing cold gas out of the ISM of the host galaxy which results in either the formation or quenching of stars respectively (e.g. Schawinski et al. 2009). In relation to this, Hopkins et al. (2006) concludes that such coupled AGN feedback-induced activity of star formation could account for the observed $M_{\rm BH}$ – $M_{\rm Bul}$ relation. Zubovas & King (2016) provide a succinct conclusion on the issue by recounting how AGN induced feedback has been included in current galaxy evolution models in order to – (1) explain the drop-off in the galaxy mass function compared with the expected halo mass function above $M_\star \simeq 10^{11} M_\odot$; (2) prevent the cooling catastrophe in galaxy clusters; and (3) as well produce the scaling relations between galaxies and their central SMBH.

To this end, we can conclude that feedback, structure formation and black hole growth, which are a direct consequence of radio AGN activity and intrinsically powered by outflows of relativistic plasma from the host galaxy central engine, are essential components of the evolution of structure in the Universe. The sections to follow will therefore be dedicated to the review of the dynamics and kinematics of these cosmic outflows which are the subject of the present study.

1.7 Astrophysical jets

Astrophysical jets are fast, collimated outflows of plasma from compact celestial objects. They are intrinsically bipolar with a jet-counterjet structure originating from the compact object and serve as conduits for mass, momentum, energy and magnetic flux transport (e.g. Das 1999) to the surrounding medium. The ubiquity of this cosmic phenomenon is evident across a wide range of physical systems and scales – from less collimated outflows in Young Stellar Objects (YSOs) to highly collimated relativistic jets in AGNs hosting the most massive BHs at their centres (e.g. Blandford 2001), as well as intermediate scales between these two extremes. Indeed Shibata & Aoki (2003) observe that recent space observations of our sun reveal spectrum and time variability of emitted EM waves from the solar corona that are very much comparable to cosmic jets. Notwithstanding the vast range of physical systems from which they are produced, cosmic jets and outflows are thought to be driven by essentially similar physical mechanisms (e.g. Wiita 2001). The first direct observations is credited to Curtis (1918) in relation to his detection of a streak of light from the nearby radio galaxy M 87, however, the invention of the term *jet* as applied to these cosmic outflows was not until the 1950s when Baade & Minkowski (1954) in an observational study of the same galactic candidate (M 87) likened the "protrusion"

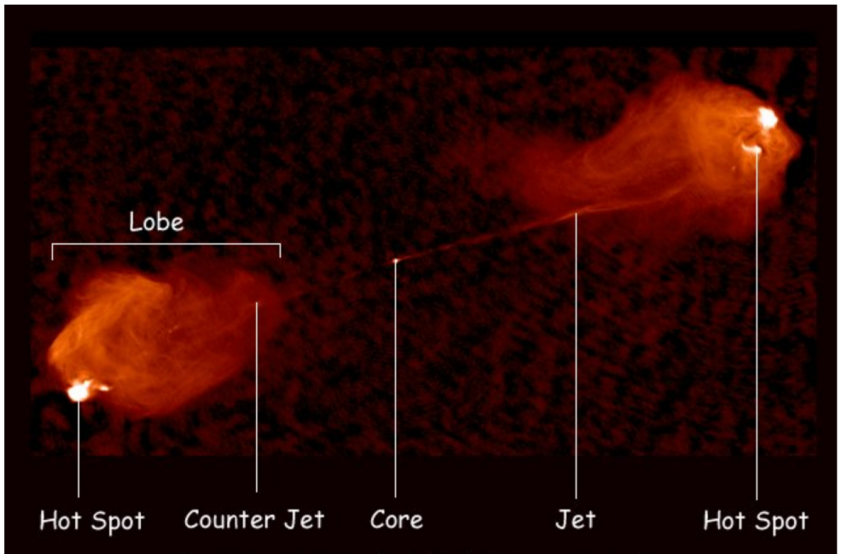

Figure 1.9: A false colour image of the powerful radio galaxy 3C 405 (Cygnus A) at 1.4 and 5 GHz showing the galactic core, and the brightest radio emitting regions (hotspots and lobes) on either side of the core that are connected by collimated jets which can be seen as long narrow bands from the central engine – (Image credit: NRAO/AUI; radio observations by Perley, Dreher & Cowan 1984).

from the galactic core to a jet. Indeed by the late 80s, Clarke et al. (2008) note that extensive study of dozens of extragalactic radio jets had already been conducted.

In the case of radio-loud AGNs – the objects of interest in the present study, the importance of these cosmic outflows stretches beyond their being primary channel of energy loss from accreting SMBHs to the major impact they have on their environment, with related particle acceleration producing the most energetic observable photons and hadrons in the Universe (Aab et al. 2018). Although a great deal of progress has been made in the recent past to elucidate our understanding of these objects, their formation, collimation and acceleration still remain long standing questions in the field of astrophysical research (e.g. Urry & Padovani 1995; Sikora et al. 2005). In the sections to follow, I discuss the framework within which these outflows from AGNs have been studied to constrain their dynamics and kinematics across cosmological scales.

1.8 Extragalactic radio jets in context

The jets in radio-loud AGNs otherwise known as extragalactic relativistic jets (ERJs) are thought to form by a combination of accretion, rotation and magnetic mechanisms (e.g. Pudritz et al. 2007). In addition to offering insight into the role of radio sources in the evolution of structure in the universe, ERJs are thought to be responsible for the production of the most energetic photons and hadrons in the observable Universe, with results from the Pierre Auger Observatory (Aab et al. 2018) indicating that cosmic rays with energies in excess of 6×10^{19} eV originate from radio AGNs. Figure 1.9 shows the typical relativistic jets launched from the central engine of the powerful radio galaxy Cygnus A as observed with the Very Large Array. The significance of these relativistic outflows as discussed in preceding sections is their distinctive role as cosmic vents for suitably-tuned feedback of energy and momentum from dense to diffuse phases of matter. Notwithstanding their cosmic significance, the quantitative study of these objects is extremely difficult, due primarily to their characteristic emission mechanisms – notably broad-band synchrotron (e.g. Hardcastle 2006) and inverse Compton processes at high energies (e.g. Celotti 2001). Major advancements in understanding the physics of these outflows on large scales have thus come from a multi-waveband approach (e.g. Worrall 2005).

1.8.1 Formation, collimation and acceleration

The formation of ERJs is known to primarily occur on approximately $\lesssim 100\,\mathrm{R_G}$[4] ($\lesssim 1$ milliarc-sec) scales by the so called Magneto-Hydrodynamic (MHD) processes (Blandford & Znajek 1977) within the central engine of their host galaxies. Originally developed by Alfvén (1942), MHD includes a magnetic stress term and connects the plasma mass density, ρ; plasma velocity, $\mathbf{v}$; the thermodynamic pressure, P; and the magnetic field, $\mathbf{B}$. Here the plasma is considered as an electrically conducting fluid and is governed by equations of fluid dynamics and Maxwell's equations. However, in the framework of relativistic jet physics, derivation of a self-consistent set of MHD equations are often based on the simplified assumption that the fluid is in steady-state and thermal effects are negligible. Under these conditions, the system can be respectively

[4]The Schwarzschild (gravitational) radius, $\mathrm{R_G}$ is defined as the radius below which the gravitational attraction between the particles of a body must cause it to undergo irreversible gravitational collapse. For an object of mass M, $\mathrm{R_G} = 2GM/c^2$.

described by the relativistic (mass) continuity equation:

$$(\mathbf{v} \cdot \nabla)(\Gamma_\rho) + \Gamma_\rho \nabla \cdot \mathbf{v} = 0 \ , \tag{1.19}$$

and momentum conservation (Euler) equation:

$$\Gamma_\rho (\mathbf{v} \cdot \nabla)(\Gamma_\mathbf{v}) = \frac{1}{c} \left(j^0 \mathbf{E} + \mathbf{j} \times \mathbf{B} \right) \tag{1.20}$$

where Γ is the Lorentz factor, $\mathbf{j}$ and j^0 are the current and charge density respectively, and $\mathbf{E}$ is the electric field. Addition of the Maxwell's equations and the equation of state, $P \propto \rho^{\frac{4}{3}}$ to the two fundamental Equations 1.19 and 1.20 above yields a complete description of the system. A general description and application of MHD to relativistic jets is provided elsewhere (e.g. Meier, Koide & Uchida 2001; Spruit 2013; Vlahakis 2015 and references therein).

In spite of the complexity of plasma physics, not least in an astrophysical context, Blandford & Payne (1982) successfully demonstrated that relativistic jets can be launched magneto-centrifugally from the surface of an accretion disc (cf. Figure 1.10), analogous to the outward spiral motion of a bead on a wire that is tilted enough and whirled about. In this scenario, some magnetic flux is assumed to be in open field lines at a certain angle of inclination with the disk's surface. These lines are fixed in the disk and rotate with it and as a result, ionised plasma is centrifugally accelerated along the field lines like the "bead" on the wire (e.g. Spruit 1996). The ionised material is in principle forced to follow the field lines since it cannot cross them (because of high conductivity of a plasma) resulting in collimation of the outflows (e.g. Clarke et al. 2008).

Kadler et al. (2005) notes that only in radio-loud AGNs does the production, collimation, and acceleration of powerful relativistic jets take place; and these are thought to primarily consist of electron-positron plasma (e.g. Wardle et al. 1998; Kundt 2014). Thus in a classical sense, MHD describes how gravity, magnetic field and pressure gradients influence plasma outflows from the compact core of radio-loud AGNs. Camenzind (2005) highlights this by drawing essentially similar conclusions, that ERJs are powered by conversion of rotational energy (of accretion disk or BH) into kinetic energy of outflows by a combination of strong electromagnetic field in the central engine and differential rotation mechanisms.

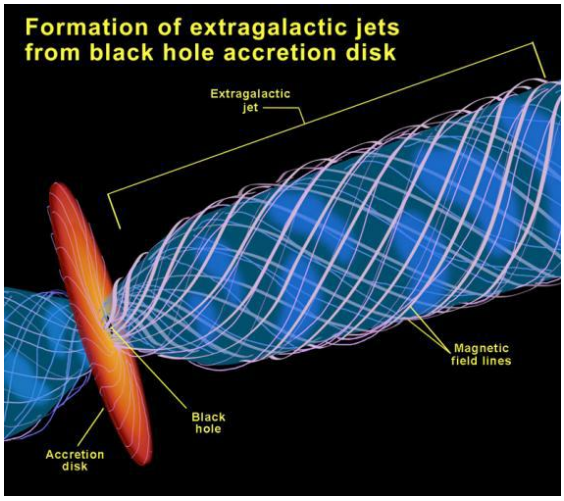

Figure 1.10: An artist impression of ERJ launching from a typical AGN as postulated by Blandford & Znajek (1977). Magnetic field lines are threaded into helical patterns by the spinning BH and/or (rotating accretion disk – Blandford & Payne 1982). These clearly defined field lines serve as funnels along which relativistic jets are launched and collimated from the surface of the disc – (Image credit: NASA/ESA & Ann Field, STScI).

Although the work of Blandford & Znajek (1977) has stood the test of time, and remains the current most favoured model for the launching, collimation and acceleration of ERJs (e.g. Koide et al. 2002); it can be considered as an approximation rather than a true picture of the actual mechanism underlying relativistic jet formation due simply to the fact that MHD describes the large scale slow dynamics of plasma and thus valid for plasma speeds $\ll c$. Thus, the basic assumptions of MHD as well as assumptions of infinite conductivity likely break down when we consider relativistic speeds as in the case of ERJs. The concept of magnetic confinement (e.g. Eichler 1993) once the jets are launched from the central engine, however makes the theory rather attractive. The inability to resolve this formation mechanism is largely due to insufficient resolution of previous and existing telescopes which has in practice placed limitations on the direct observations of the central engine. It is noteworthy here that, in the recent past, our understanding of the origin of relativistic jets have greatly improved, thanks to recent observational results from the Event Horizon Telescope Collaboration (2019) for the central SMBH in M 87 and advances in numerical General Relativistic MHD (GRMHD) codes that have been developed and applied to model relativistic jet formation in various astrophysical conditions (see Mizuno 2022 and references therein).

1.8.2 Magnetic field structure in jets

It is clear from Section 1.8.1 above that models of jet acceleration and collimation rely heavily on a rotating accretion disk threaded by a perpendicular large scale magnetic field (e.g. Pudritz et al. 2007). The jet power $Q_{\rm jet}$ resulting from these magnetic launching regimes depends on the angular velocity Ω of the central object and on the accumulated magnetic flux Ψ as:

$$Q_{\rm jet} \propto \Psi^2 \Omega^2 \tag{1.21}$$

It follows from Equation 1.21 that the likelihood of accumulating a certain large scale magnetic field in the disk is strictly related to the very origin of the field and to the underlying physics driving its propagation and dissipation through the accretion disk. Rothstein & Lovelace (2008) investigated this problem and found that indeed the field accretion can be successful (i.e., stable and highly ordered), particularly for a field that is strong enough where turbulence can be effectively dumped.

An important characteristic of radio synchrotron emission is its polarisation which can be described by the so called Stokes parameters ($IQUV$; Stokes 1852). In cartesian coordinates, the Stokes parameters relate the intensity and polarisation ellipse parameters as:

$$\begin{aligned} S_0 &= I = S \\ S_1 &= Q = I_p \cos 2\psi \cos 2\chi \\ S_2 &= U = I_p \sin 2\psi \cos 2\chi \\ S_3 &= V = I_p \sin 2\chi \end{aligned} \tag{1.22}$$

where S is the total intensity, and I_p, 2ψ and 2χ represent the spherical coordinates in the "Poincaré sphere" of the 3-dimensional vector of cartesian coordinates (S_1, S_2, S_3) that define these Stokes parameters (see Figure 1.11–[left panel]). The factor of two before ψ represents the fact that any polarisation ellipse is indistinguishable from one rotated by 180°, while the factor of two before χ indicates that an ellipse is indistinguishable from one with the semi-axis lengths swapped by a 90° rotation. From an observational point of view, the Stokes parameter V is typically $\lesssim 1\%$ and therefore negligible for the case of radio-loud AGNs. It follows that the

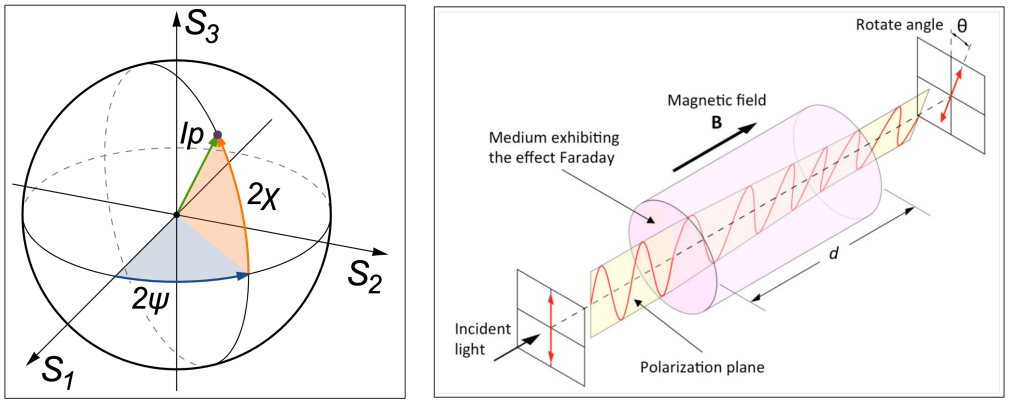

Figure 1.11: Left: An illustration of the Poincaré sphere – a parameterisation of the Stokes ($IQUV$) parameters for polarised light in the form of spherical coordinates. Right: An illustration of polarisation rotation due to the effect of Faraday rotation – (Adapted from Collett 2005).

observable Stokes parameters IQU are instead used to determine the total linear polarisation quantity as:

$$S_{\rm pol} = \sqrt{Q^2 + U^2} \tag{1.23}$$

The fractional linear polarisation $\pi_{\rm pol} = (S_{\rm pol}/I)$ is therefore defined as the ratio between the linearly polarised flux density $S_{\rm pol}$ and the total intensity I flux density. However, for an ideal astrophysical case with a homogeneous magnetic field, the fractional polarisation is independent of the observed frequency and can be determined only by the spectral index from the relation:

$$\pi_{\rm pol} = \frac{3\alpha + 3}{3\alpha + 5} \tag{1.24}$$

It follows from Equation 1.24 that for radio synchrotron observation with values of the spectral index between -0.5 and -1.0, fractional polarisation of between 70 and 75% would be expected, however, typical values inferred from observations are much lower ($\lesssim 5\%$ around VLBI cores, and 20–30% at larger distances from the jet base – e.g. Lister & Homan 2005). From these physical quantities of the linear polarisation, it is possible to investigate the Faraday rotation[5] – an important parameter which probes the magnetic field strength and orientation of both the

[5]The Faraday rotation is a phenomenon whereby the polarisation plane of radio waves rotates due to magnetic flux lines and electrons in the ionosphere, resulting in different phase velocities for left- and right-hand circularly polarised waves. The rotation angle is inversely proportional to the square of the frequency, and the effect is strongest in linearly polarised waves (Iida & Wakana 2003).

interstellar medium (ISM) and host galaxy, as well as distribution of the relativistic and thermal electron populations. For a radiation traveling through a magneto-ionic medium, the complex polarisation vector, $P(\lambda^2) = pIe^{2i\chi}$ can be modified by Faraday rotation effect (see Figure 1.11–[right panel]) via:

$$\chi(\lambda) = \chi(0) + RM\lambda^2 \quad \text{in units of radian} \tag{1.25}$$

where λ is the wavelength of the radiation, p and χ are the degree and angle of polarisation respectively, and RM is the Faraday rotation measure, which in the simplest case of a homogeneous medium, can be described by:

$$RM = \frac{e^3}{2\pi m_e^2 c^4} \int_d^0 n_e B_{\parallel} dl \quad \text{in cgs units} \tag{1.26}$$

where n_e (cm^{-3}) is the electron density of the medium, $B_{\parallel}$ (μG) is the component of the magnetic field along the line of sight, and l (pc) is the geometrical depth of the medium along the line of sight. Conventionally, most polarisation studies have determined RM by fitting Equation 1.25 (e.g. Brentjens & de Bruyn 2005; Taylor & Zavala 2010; Kravchenko, Cotton & Kovalev 2015;). Of astrophysical interests also are effects which produce a frequency-dependent depolarisation due to changes in the fractional polarisation by the magneto-ionic medium with the observed wavelength. The origin of such effect can be *internal* – where the Faraday rotating component is intermixed with the radio emitting region, or *external* – where several Faraday screens are observed somewhere between the radio source and the observer. Several models to interpret these effects have been put forward in the literature (e.g. Burn 1966; Tribble 1991; Homan et al. 2002; Hovatta et al. 2012).

As can be deduced from the above discussions, radio polarimetry provides a powerful tool for deriving fundamental constraints on jet physics and properties of the magneto-ionic medium. Indeed, linear polarisation and RM studies of several hundreds of AGNs have been pursued intensively over the years in the literature. One particular monitoring observations of interest is the MOJAVE programme (e.g. Pushkarev et al. 2017 and references therein) in which systematic VLBA study of Faraday rotation (covering 2 decades; 1996–2016) in several hundreds of radio-loud AGN jets found that; (i) for all classes fractional polarisation increased with core separation, (ii) increase of polarisation fraction towards the edge of the jet – a consequence of Faraday depolarisation, (iii) 40% of jet cores have a preferred Electric Vector Polarisation Angle (EVPA) direction from epoch to epoch, and (iv) compared with quasars and radio galaxies,

BLL cores and jets have more stable EVPAs and tend to be aligned with the initial jet direction. Observations of well resolved jets (typically the jet bases in FR Is) also reveal high linear polarisation with magnetic fields that are at least partially ordered along the jet axes (e.g. Laing & Bridle 2014). Jets with longitudinal magnetic fields have also been interpreted as carrying helical fields with relatively large or small pitch angles whereas evidence of "spine-sheath" polarisation structures are explained as jets carrying a helical magnetic field, with the azimuthal component dominating near the central axis of the jet and the longitudinal component becoming dominant near the edges (e.g. Attridge, Roberts & Wardle 1999). It is noteworthy here that at cm-wavelengths, the effect of Faraday rotation is usually modest outside the AGN core regions, leading to polarisation rotations of around $\lesssim 15^{\circ}$. For further reading, see recent reviews by Blandford, Meier & Readhead 2019; Park & Algaba 2022 and references therein.

1.8.3 Jet velocities and superluminal motion

The question of jet velocities is widely researched in the literature (e.g. O'Donoghue, Owen & Eilek 1990; Jetha, Hardcastle & Sakelliou 2006; Laing & Bridle 2014). Their knowledge is useful not only for understanding the brightness evolution of the jets but is also important for probing the physical processes governing the flow dynamics and energy losses. It is convenient to say that often jets are not channels of uniform brightness. They display compact features of enhanced surface brightness along their path, generally termed as jet knots (cf. Section 1.8.5). In radio-loud AGNs where the jets are relativistic with small inclination angle, these components may exhibit apparent transverse superluminal (greater than the speed of light, c) speeds from one position to another over a period of observation; and efforts towards understanding this unique phenomenon on both the observational (e.g. Cheung, Harris & Stawarz 2007) and numerical (e.g. Komissarov & Falle 1997) fronts are widely pursued in the literature.

While monitoring the motion of knots or similar compact features in large-scale jets is usually difficult, on milliarcsec scales VLBI observations of the parsec-scale jet structure in powerful radio galaxies has now routinely allowed for these remarkable features to be extensively studied (e.g. Polatidis & Wilkinson 1998; Kellermann et al. 2007; Lister et al. 2009; Lister et al. 2013; Snios et al. 2019). In particular, estimates of jet flow speeds through modelling of their asymmetries have provided the direct measurement of proper motions in several dozens of radio-loud AGNs (e.g. Cheung, Harris & Stawarz 2007; Frey et al. 2015; Zhang et al. 2022). Observations of such compact features in jets have yielded velocities greater than that of light –

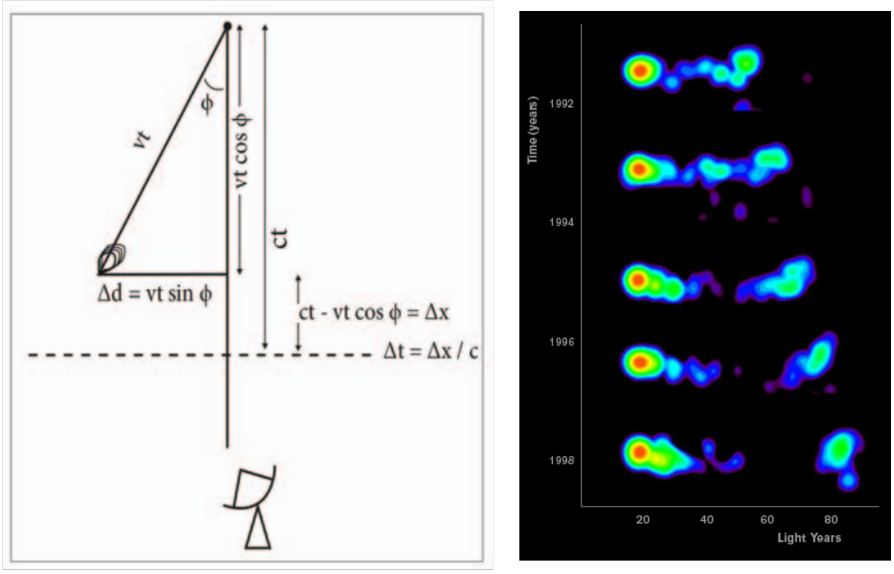

Figure 1.12: Left: Illustration of superluminal motion where the apparent velocity of the knot travelling towards the observer $v_{\rm app}$ = $\beta_{\rm app}c$ is given by $\Delta{\rm d}/\Delta{\rm t}$. Right: Observed superluminal motion in the core-dominated quasar 3C 279. The collage of five images shown here are from a larger set of images obtained with the Very Long Baseline Array and other telescopes by Wehrle and her collaborators. The bright red spot is the stationary core, and the blue-green spot on the extreme right is part of a jet that is moving almost towards us at nearly the speed of light giving rise to apparent velocities greater than that of light – (Adapted from D.J. Saikia (NCRA, Tata); Image credit: NRAO/AUI).

a phenomenon first proposed by Rees (1966) and termed *superluminal motion*. We note here that although relativistic speeds are required, superluminal motion is not strictly a relativistic effect, because no Lorentz transformations are involved. The phenomenon could be understood in terms of jets traversing at velocities close to the speed of light at small angles to the line of sight, and can be quantitatively explained using simple geometric arguments.

As shown in Figure 1.12–[left panel], a jet component emitting a photon at time t, which travels to the observer in a time Δt will travel at a true speed v from one position to another in the same time Δt. Here, the distance between the emitted component and stationary core, $\Delta{\rm d}$ = $v\Delta{\rm t}\sin\phi$ will appear contracted to the observer due to projection effects, whereas difference between the arrival times of the photons, $\Delta{\rm t}_{\rm obs}$ = $\Delta{\rm x}/c$ will be measured by the observer. Simply put, the observer will record motion across the plane of the sky given by $\Delta{\rm d}/\Delta{\rm t}$. Thus, the observed velocity of the component can be approximated by:

$$v_{\rm obs} = \frac{\Delta {\rm d}}{\Delta {\rm t}_{\rm obs}} = \frac{v \Delta {\rm t} \sin \phi}{\left(c \Delta {\rm t} - v \Delta {\rm t} \cos \phi\right) / c} \tag{1.27}$$

For a jet that is inclined at a large enough angle from the plane of the sky, the observed apparent velocity of the compact feature in the jet, $v_{\rm app}$ = $\beta_{\rm app} c$ therefore reduces Equation 1.27 to:

$$\beta_{\rm app} = \frac{\beta \sin \phi}{(1 - \beta \cos \phi)} \tag{1.28}$$

where v = βc is the intrinsic velocity of the knot in the jet and ϕ is the angle of inclination of the jet axis to the line of sight. It follows from Equation 1.27 that, for small viewing angles and large intrinsic speeds, $\beta_{\rm app} \gg 1$, consistent with observations (cf. Figure 1.12–[right panel]). Thus, for a compact knot traversing at speed v = 0.99c in a jet that is inclined at θ = 5° to the line of sight, $\beta_{\rm app}$ = 1.37c. This implies that for sources inclined at small angles to the line of sight and moving at relativistic velocities, the flux density will also appear boosted as a result of the superposition of different relativistic effects. Here, the observed flux emitted by the radio source is affected by special relativistic effects (the so called *relativistic beaming* effects) – i.e., the observed flux will be boosted relative to the actual emission in the rest frame by a factor:

$$\delta = \frac{1}{\Gamma \left(1 - \beta \cos \phi\right)} \tag{1.29}$$

where δ is the relativistic Doppler factor and Γ is the Lorentz factor. Since the solid angle subtended by the radiation is different in the observed and emitted frames, the Doppler factor, δ can boost the emission from a relativistic blob from a jet inclined towards the observer line of sight. For an assumed spectral index of -0.7 for the compact knot in the approaching jet, the observed flux density will be boosted by a factor of $\sim$ 530. It follows that for a blob of emission from the counter jet which is receding, its observed flux will be reduced by the same factor. It is noteworthy here that the so called "Laing-Garrington effect" (Laing 1988; Garrington et al. 1988) in which the lobe containing the (brighter/approaching) jet is found to be less depolarised is generally considered as good evidence for beaming and orientation models, particularly in FR Is which often exhibit considerable brightness asymmetry at the bases of the jets (e.g. Parma, de Ruiter & Fanti 1996). For a detailed review on the subject of jet velocities, see Blandford, Meier & Readhead (2019) and references therein.

1.8.4 The FR I versus FR II jet paradigm

It is widely established that both FR I and FR II radio galaxies to a certain extent, tend to have pairs of jets (e.g. Urry & Padovani 1995); with the less collimated jets in FR Is terminating nearer to the launch point whereas the highly collimated FR II jets terminate at bright hotspots at great distance away from the central region of the galaxy. However, in spite of the similar underlying physical mechanisms, the morphology, kinematics and dynamics of these jets is heavily influenced by variabilities in host galaxy properties and environment, and efforts to constrain the physics driving the observed jet structure (as in the present study) is of ongoing importance.

a) FR I jets

These are relatively low power radio sources with twin jets (cf. Figure 1.13–[left panel]) that are initially relativistic on parsec scales, but decelerate from relativistic to sub-relativistic speeds on kpc scales. The jets exhibit considerable brightness asymmetry at their base (e.g. Parma, de Ruiter & Fanti 1996), are subsonic or transonic (i.e., no strong shocks are observed at their termination points) on kpc-scale velocities, and are both easily observed on large scales due to the absence of strong Doppler boosting effects (e.g. Worrall & Birkinshaw 2006). Laing (1993) also notes that the orientation of the magnetic field configuration relative to the jets in these sources changes from longitudinal to transverse as the jet propagates. It is important here to draw the reader's attention to the fact that these characteristics may not be exact in some cases, particularly in the most powerful FR I sources. The rather turbulent environments within which these radio sources find themselves complicate the dynamics and kinematics of their emitted radio jets – with the so called observed tail-bending phenomenon as the jets propagate through the ISM/ICM (e.g. Owen & Rudnick 1976).

b) FR II jets

FR IIs (cf. Figure 1.13–[right panel]) are the more powerful radio galaxies with jets that remain relativistic on all scales up to the hotspot. The jets are supersonic (i.e., strong shocks are usually inferred at their termination points) and often seen to display a one-sided jet (favouritism) or occasionally with no jets observed at all (Doppler de-boosting) usually on kpc scales (e.g. Bridle et al. 1994; Bicknell 2002). The jets have shallow opening angles (< 4 deg) with knotty structures and magnetic fields that are predominantly parallel to the jet axis (e.g.

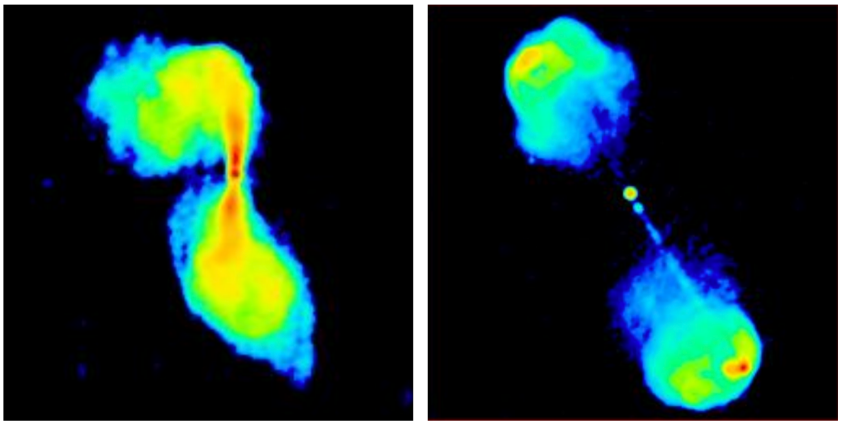

Figure 1.13: VLA maps of the archetype FR I radio source 3C 272.1 (left panel; Laing & Bridle 1987) at 1.4 GHz showing two-sided conical jet structures which terminates and flares into plumes, stretching to $\sim$ 15 kpc across the galactic centre; and classical double, FR II radio galaxy 3C 47 (right panel; Leahy 1996) at 1.7 GHz showing bright hotspots in the two diffuse radio lobes on either side of the core. Note the one-sidedness of the jet which points towards the south and at least one knotty structure observed on the southern side some distance from the core – (Image credit: 3CRR Atlas of DRAGNs).

Kembhavi & Narlikar 1999). The back-flow of the jets from the hotspots expands, giving rise to over-pressured cocoons (huge radio lobes) observed as diffuse radio emission (e.g. Kuligowska 2017).

c) The tail bending narrative

It has been well established that the ICM is a turbulent system with discrepancies in temperature gradients, and density distributions among others (e.g. Hayakawa et al. 2006; Bourdin & Mazzotta 2008; McCourt, Quataert & Parrish 2013). Thus, we can logically conclude that tail-bending of radio jets in FR Is which are known to predominantly live in rich clusters and groups is a direct consequence of large-scale motions (scales of tens of kpc and up) due to turbulence in the ICM. In line with this, Jetha et al. (2005) observe that the large scale plumes in WATs for example can be shaped (i.e., bent backwards) by interactions with their environments due to the relative motion of the host galaxy through the ICM. Bird, Martini & Kaiser (2008) essentially draw similarly conclusions that FR I sources may be FR IIs that encountered high-density environments as they arose from turbulent disruption of their lobes and entrainment of ambient gas. Indeed, numerous theories have been postulated to account for this observed phenomenon.

Electrodynamic effects (e.g. Bodo et al. 1985); gravitational bending (e.g. Burns, Eilek & Owen 1982); buoyancy effects (e.g. Worrall, Birkinshaw & Cameron 1995); ram pressure (e.g. Venkatesan et al. 1994); to mention a few are among the proposed theories to account for the tail-bending of these radio jets. However, in spite of the progress made in resolving the origins of bending, WAT sources with their characteristic luminosities near the FR I/FR II break (e.g. Hardcastle & Sakelliou 2004), varied bending angles (i.e., 30–115 degrees) (e.g. O'Donoghue, Eilek & Owen 1993) and collimated jets which often travel several kpc into the ICM before flaring into plumes, present an unusual challenge. In an attempt to resolve this peculiar case of WAT jets, Hardcastle & Sakelliou (2004) in a study of selected WAT samples in the Abell clusters of galaxies concluded that jets in WATs terminate in a variety of ways, further underscoring the complexity of the physical mechanism that initiates the bending in these class of radio sources. For a detailed review on the topic of bending the reader is referred to O'Donoghue, Eilek & Owen (1993) and Pinkney, Burns & Hill (1994).

1.8.5 Jet knots, hotspots, lobes and plumes

It is well established that the internal dynamics of a supersonic jet beam are rich enough to allow the formation of structures such as knots, filaments and wiggles simply through dynamical instabilities associated with the jet itself (e.g. Stone 1997) and these have indeed been observationally confirmed and studied in detail (e.g. Hardcastle et al. 2002; Laing et al. 2006). In spite of the complex morphologies exhibited by extragalactic radio sources, jets, knots, hotspots, lobes and plumes to a large extent appear to be inherent features in these objects – with propagation of the emitted radio jets through the non-uniform ICM thought to predominantly shape the morphology (e.g. Foster 2010).

One of the most prominent features observed in classical AGN jets are the so called bright knots (e.g. Steenbrugge & Blundell 2007; Goodger et al. 2010) which are often seen as blobs of bright features within the moving jet. In spite of the absence of a simple theory to account for the formation of these bright structures, which arise largely from internal processes such as variable fuelling and instability-triggered flow transitions; Shklovskii (1980) proposed a model in which the knots are treated as blobs of magnetised plasma emitted from the central engine and which upon interaction with the ambient medium produce the bright features. Indeed the model has been used by researchers to account for this knotty structure in jets (e.g. Qian et al. 1991; Godfrey et al. 2012). Other models such as "shock model" (Bicknell & Begelman, 1996)

have also been proposed to account for the formation of these structures in jets.

Hotspots are bright components which are neither a core nor part of the main jet structure with peak brightness greater than any nearby structure within the jet (e.g. Leahy et al. 1997). They are the main sites for dissipation of energy carried by the radio jet from the central engine to the termination point with associated shock processes giving rise to synchrotron radiation. Some FR II radio sources are known to show multiple hotspots (e.g. Laing 1982) – which in principle points to a continued outflow of plasma even after the jet termination point. Beam-deflection (see Lonsdale & Barthel 1998 and references therein) and fluid-dynamical interactions (e.g. Hardcastle 2008) are among the proposed models used to explain this observed structure in jets.

Radio lobes are the most common large scale structures observed in typical radio AGNs. They are extended regions of emission either side of the galactic nucleus with filamentary sub-structures (e.g. Leahy 1993). These diffuse structures are sites for the formation of hotspots (jet termination) of the more powerful FR II radio sources and in effect serve as "cavities" where production of intense radiation occurs. In separate studies, Pedelty et al. 1989 and Liu & Pooley (1991), respectively observed that brighter lobes and lobe lengths correlates with a steeper spectral index of host galaxies – and this has indeed been confirmed in more recent studies (e.g. Dennett-Thorpe et al. 1999). The importance of these diffuse structures lies in the fact that they offer good diagnostics into the active phase of AGNs and, thus, have been used by researchers to constrain the physics of radio AGN activity (e.g. Walker et al. 2000; Shulevski et al. 2015).

Plumes are associated with tailed sources of the rather low power FR Is and in many facets a direct consequence of the turbulent environment within which these radio jets propagate. The dynamics of these structures is analogous to that of a steam column from factory chimneys and thus easily affected by turbulence in the surrounding medium. Hardcastle (1998) notes that formation of these structures is often characterised by broadening at bright flare points tens of kpc away from the central engine into the characteristic plumes and tails – giving its name the so called wide-angle tail (WAT) sources. In line with this, Jetha et al. (2005) further assert that the jet-plume transition of WATs is a consequence of the dense cluster environment, with the cluster properties determining the location of the base of the plume.

1.8.6 Particle acceleration and the physics of deceleration

a) Particle acceleration in jets

In spite of the knowledge that radio jets are responsible for the acceleration of high-energy cosmic rays (e.g. Hillas 1984), the underlying physics of where and how particles are accelerated in the hotspots and jet knots remains an open question. Indeed several models have been proposed in the literature with shock waves resulting from interaction of the jets with the ICM/IGM as the basis (e.g. Stawarz 2004). These interactions are thought to produce supersonic shocks allowing the acceleration of the external medium particles and the jet material as they transit the shock regions giving rise to the observed inflated radio lobes or cocoon (e.g. Kuligowska 2017). In a non-relativistic case (e.g. Blandford & Eichler 1987), these strong shocks are expected to be sites of particle acceleration via the first-order Fermi process with typical power law spectral indices, $S(\nu) \propto \nu^{\alpha}$ ($p = 2\alpha + 1$). In principle, the formation of these shocks could arise from intrinsic velocity asymmetries within the jet flow itself (e.g. Rees 1978) or within the knotty structures due to jet reconfinement by the ambient medium (e.g. Sanders 1983), or large-scale instabilities within the jet flow (e.g. Bicknell & Begelman 1996).

Other existing models involve magnetic reconnection processes (e.g. Birk & Lesch 2000) with Bisnovatyi-Kogan (2005) suggesting a possible oscillation-induced strong EM waves as potential particle accelerators at large distances from the nucleus near the jet, as well as at larger radii. Although strong evidence for these shock-induced models of particle acceleration has come from the radio through optical spectra of hotspots (e.g. Meisenheimer et al. 1989), the rare evidence of multiple hotspots in a given lobe suggests that particle acceleration is not restricted to one location in at least some examples (e.g. Hardcastle, Croston & Kraft 2007). Indeed an earlier report by Hardcastle et al. (2004) had indicated that X-ray emission from many hotspots is most likely synchrotron in nature pointing to the concept of on-going particle acceleration in the form of a well-collimated energy input. Observed spectral problems (e.g. Kraft et al. 2007) and spatial offsets (e.g. Hardcastle et al. 2002; Erlund et al. 2007) are further complications that expose the limitations of these current standard models.

b) The physics of deceleration

The mechanism of deceleration from relativistic to sub-relativistic speeds over scales of 1–10 kpc of FR I jets with its attendant flaring and brightening (e.g. Laing et al. 2006) is still an open

question in the field of extragalactic jet physics. As posited by Laing et al. (1999), the observed asymmetries on kpc scales in these jets are consistent with the hypothesis that the jet velocities from the base are mildly relativistic, and that they decelerate further out – with the extent of the deceleration region and residual velocity after the deceleration has taken place, dependent on the total power of the source.

Considerable efforts have been made in attempt to resolve this deceleration puzzle. Notable among them is the concept of entrainment of ambient material which results in changes in the jet flow dynamics from an initially relativistic speed at the jet base to sub-relativistic speed (as they decelerate further out) (e.g. Bicknell 1994) – a scenario in which the initial deceleration is thought to require an entrainment rate that is extraordinarily close to predictions of mass loss by stars within the jet volume (e.g. Laing & Bridle 2002). A second possibility which is linked to the inner jets can be explained in terms of an abrupt deceleration of the jet due to reconfinement shocks – followed by intense interaction with the external medium (e.g. Nalewajko & Sikora 2008).

Unlike in FR Is, Hardcastle, Croston & Kraft (2007) notes that the jets in FR IIs remain relativistic, often out to scales of hundreds of kpc or more, until they decelerate abruptly at shocks which involve the direct interaction of the jet with the relativistic plasma that fills the lobes in which the jets are typically embedded, giving rise to the observed hotspots. Hardcastle, Croston & Kraft (2007) also draw attention to the fact that particle acceleration is directly linked to the deceleration regions of both FR I and FR II sources – suggesting a rather unusual similarity between jets of these two distinct sources. Indeed this is well in agreement with earlier work by Worrall, Birkinshaw & Hardcastle (2001) in which they posited that the rather common X-ray jet detections in powerful FR I sources hints at the likelihood that particle acceleration is always associated with jet deceleration in FR I jets. However, it is noteworthy that based on a photon index analysis, Harwood & Hardcastle (2012) observed that for *bona fide* FR Is, acceleration to higher energies is more likely to be less efficient. In spite of the considerable efforts made, a comprehensive understanding of the ongoing physical processes in the jets of FR Is and the hotspots of FR IIs will be critical to resolving both the physics of particle acceleration and deceleration – and in the present study we will attempt to solve a piece of the puzzle by constraining the physics driving the observed jet structure in FR I radio sources.

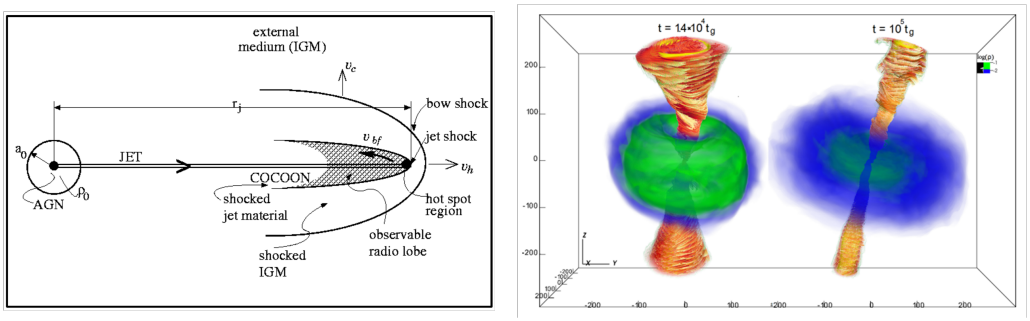

Figure 1.14: Left: A model for extragalactic radio sources as posited by Scheuer, Blandford and Rees since the 1970s (Scheuer 1974; Blandford & Rees 1974). Oppositely directed jets or beams are emitted from the AGN and impact on the external medium. Since the jets are light compared to the external medium, conservation of momentum requires that the flow speed up the jet must be much higher than the advance speed of the contact surface. It follows that conditions are right for the magnetised material to then be redirected away from the head of the source and flow sideways and backwards to form lobes. In the more powerful FR IIs where the jets are supersonic, they can easily drive a shock into the ambient medium. Right: A 3-D volume rendering of density (green and blue) and jet magnetic field colored by magnetic energy (red and yellow) in GRMHD simulations of a tilted disk (Liska et al. 2018).

1.8.7 Numerical simulations of jets

There exist many difficulties in reproducing the observational properties of extragalactic radio sources from simulations even with modestly realistic environments – from the difficulty of accurately modelling particle acceleration, transport and radiative losses, to the presence of relativistic bulk motions and magnetic fields in jets, coupled with the poorly known physical conditions in the lobes and environment of radio-loud AGNs (e.g. Hardcastle & Croston 2020). This notwithstanding, it is noteworthy that numerical modelling and simulations of jets and the large-scale structure of radio sources have long been recognised since the 1980s (e.g. Norman et al. 1982; Williams & Gull 1985; Clarke, Norman & Burns 1986; Lind et al. 1989). Although these early works primarily involved a 2-D MHD simulations, their detailed results essentially confirmed the basic dynamical picture of radio-loud AGNs as posited by Scheuer, Blandford and Rees since the 1970s (Scheuer 1974; Blandford & Rees 1974) – i.e., the jet hotspot picture of a Mach disk, contact discontinuity, and bow shock forming the jet head, with hot post-shocked jet material surrounding the advancing jet (see Figure 1.14–[left panel]).

Despite the complexity of modelling the dynamics of jetted radio sources, pioneering work of relativistic jet formation via General Relativistic MHD simulations (e.g. Koide, Shibata & Kudoh 1998; Mizuno, Hardee & Nishikawa 2008) have shed tremendous insight into the validity and nature of the Blandford-Znajek mechanism (cf. Section 1.8.1). In these 2-D simulations (see Mizuno 2022 and references therein), infalling material unto a thin accretion disk with strong helical magnetic field around a rotating BH loses angular momentum by magnetic breaking and then falls into the BH. A centrifugal barrier near the BH horizon decelerates the infalling material and produces a standing shock. Plasma near the shock is accelerated by the Lorentz force and forms bipolar jets – the shocked jet material forming a downstream nose cone ahead of the original jet. Recent advances in 3-D GRMHD simulations (e.g. Mignone et al. 2010; Mościbrodzka, Falcke & Shiokawa 2016) of a similar situation have found that similar two-layered jets are produced in both co-rotating and counter-rotating black hole magnetospheres, although these helically-magnetized jets develop strong kink instabilities, which inhibits the formation of a nose cone. (e.g. Blandford, Meier & Readhead 2019).

Indeed several mechanisms of jet flow acceleration and collimation have been proposed in the literature, but in the general consensus of relativistic jet formation via MHD processes, two key ingredients – the *poloidal* and *toroidal* magnetic field configurations are essential in GRMHD simulations to investigate the formation and stability of these systems (e.g. Komissarov 2006; Liska, Tchekhovskoy & Quataert 2020). Simulations of jet launching based on accretion flows around rotating BHs have also shown that in radiatively inefficient accretion (sub-Eddington accretion disks – typical of the central engines in low-uminosity AGNs and weaker sources), bipolar jets can be produced from rotating BHs and that the jet power in these systems is an increasing function of the SMBH spin (e.g. McKinney 2006). In the case of super-Eddington accretion disks (with a large, geometrically thick, radiation-pressure dominated disk – typical of the central engines in quasars), 3-D GRMHD simulations have shown that the radiation and jet emerge from a geometrically beamed, bipolar region, with super-Eddington isotropic luminosities (e.g. Sadowski & Narayan 2015).

For further study on the subject, the reader is referred to recent reviews by Blandford, Meier & Readhead (2019); Hardcastle & Croston (2020); Komissarov & Porth (2021) and references therein.

1.9 Scientific rationale

The preceding sections have shed light on how relativistic plasma ejected from SMBHs at the centres of massive galaxies play a leading role in the AGN-feedback cycle, structure formation and black hole growth. This notwithstanding, although sufficient energy input is available from jets, both how feedback is regulated and the processes required to heat the intergalactic medium remain open questions. To resolve them we need to quantify the mass, momentum and energy inputs from jets and map jet interactions with their environment. However, the quantitative study of jet energetics is extremely difficult, based solely on their broad-band synchrotron emission (e.g. Hardcastle 2006) coupled with inverse Compton processes at high energies (e.g. Celotti 2001). Thus, an in-depth appreciation of the physics driving the observed jet structure from these radio-loud AGN populations is very much a work in progress and the need to provide further information serves as the primary motivation for carrying out the present study. It is noteworthy here that major advancements in understanding the physics of these outflows on large scales have demanded a multi-waveband approach (e.g. Worrall et al. 2004). In view of this, in the present study, we aim to use a multi-wavelength (radio to X-ray) approach to construct high sensitivity, high-resolution spectral and polarimetric imaging observations of the jets in six 3CRR sources which show evidence of gas/jet interactions.

Whereas on large ($\sim$ Mpc) scales the huge radio lobes observed in powerful radio sources have been used to constrain the physics of radio-loud AGNs, the corresponding dynamics and kinematics of these outflows on parsec and kpc scales are not well understood, largely due to the varieties of host galaxy environment and properties. As a consequence, several key questions including what initiates the *brightening, flaring and deceleration* of low-power radio jets, what are the magnetic field configurations immediately surrounding jets, and the nature of jet-particle acceleration, among others remain open. To progress we need both sensitivity and image fidelity. With recent advances in instrumentation and new-generation radio telescopes (e.g. LOFAR) and upgrade of existing facilities such as the *e*-MERLIN, we can now get excellent signal-to-noise ratio, at high spatial resolution, with very good coverage of the radio band, working around interference, so can hope to do much better in terms of mapping the structure of the inner jet in our sample to test beaming models of jets and place constraints on the flow dynamics. The results will have implications for our understanding of the physics of jet interactions and associated cosmic outflows.

1.9.1 Goal of the present study

Our science aims require deep, transverse-resolved radio observations. These have, until now, only been feasible on $\sim$ 0.3-arcsec scales with *e*-MERLIN and the VLA at GHz frequencies. In the present study, we extend these techniques to low frequencies where only LOFAR can deliver sensitivity at comparable resolutions. This would be the *first time* the jets and lobes in our radio sample would have been imaged in detail at such low frequencies. These multifrequency radio maps would complement our existing multi-wavelength data at matched resolution, and more specifically allow us to:

i. Study the spectral structure in our sample: We will measure the flux density in discrete regions along the radio structure over different frequency ranges – this will allow us to systematically constrain the synchrotron spectra in order to address key questions in jet-particle acceleration and energy losses. Since our sample is dominated by non-thermal (synchrotron) emission, we expect to obtain negative spectral indices with mean values of about -0.7 in the inner (jet) regions, and $\lesssim -1.0$ further out from the AGN. We estimate $\sim \pm 0.1$ (error) in spectral index in any region with surface brightness $>$10 mJy/beam, which is the case for most of our sample. This is sufficient for good dynamical age estimate (or other) fits, and will allow us to detect spectral flattening and steepening in the inner jets and extended structures at new depth, and possibly, see whether or not older plasma exist near the jets. It will also help us to separate the spectral effects from synchrotron losses and adiabatic expansion, which render many energy-loss studies problematic.

ii. Investigate the magnetic field and rotation measure structures in our sample: We expect RM accuracy per beam better than $\sim \pm$ 1 rad m^{-2}, for a simple external screen in our sample – this will allow us to isolate the range in Faraday space responsible for the small-scale magnetic fields in the inner regions, and so to probe the orientation and degree of ordering of magnetic field structures in the jet (the synchrotron radiation polarisation) and use the RM structures to look into jet boundary layer interactions with the surrounding gas. We have discovered optical and X-ray jets in our sample, and since we know the gas environments from the X-ray, we will get the external B-field to about ± 10 %, and will be able to measure field structures (via RM "banding"). We expect polarisation percentages up to $\sim$ 75 %, close to the theoretical synchrotron value, at the highest spatial resolutions, consistent with previous works (e.g. Perlman et al. 2010).

iii. Test evolutionary models of jet propagation: We will investigate energy deposition in the plumes – where the radio structure most closely traces the environment – by analysing the

radio images using tested MHD codes for modelling the jet kinematics (e.g. Molnar et al. 2017; Musoke et al. 2020), and from conservation-law analysis (e.g. Laing & Bridle 2002) taking external pressure and density profiles from X-ray observations. We will estimate, in addition to energy and mass fluxes, the variation of internal pressure, density, Mach number and entrainment rate along the jets as we have recently done for Cen A (Wykes et al. 2018).

When combined with the numerical simulations, these systematic and comprehensive multi-waveband studies of the electron populations and magnetic field sub-structures will provide new insights into the physics driving the observed jet structure in extragalactic radio sources and allow for new constraints on jet physics. We emphasize here that much of the analysis in the present work is restricted to the multifrequency radio observations.

2

Data and Instruments

As discussed in the preceeding chapter, detailed understanding of jet physics has required a multiwaveband approach. Thus, our science goals require, in addtion to deep transverse resolved radio observations, complementary observations from other wavebands across the EM spectrum. We have therefore made use of high-resolution and high-sensitivity data obtained from multi-configuration, multi-frequency observations of our target sample using the *e*-MERLIN, LOFAR and VLA at radio wavelengths; HST and NICMOS observations at optical and infrared wavelengths respectively; and Chandra observations at X-ray wavelengths. In the sections to follow, I present and discuss our data and instruments, and consider the multiwaveband complementarity of our observations in resolving jet physics.

2.1 Data

2.1.1 Sample selection

In line with our science goals, we have carefully selected six FR I radio sources from the well-defined, flux-limited, low frequency ($\sim$ 178 MHz) LRL sample (Laing, Riley & Longair, 1983), except 3C 371. The sample forms part of the ongoing *e*-MERLIN Jets Legacy programme[5], and they are representative of the range of morphological types in a low-redshift flux-limited survey, including large scale structures with plumes, the brightest example of narrow angle tail (NAT), and bent-double (wide angle tail – WAT) sources. Their high surface brightness should allow us

[5]An *e*-MERLIN survey of a number of well-known bright radio galaxies and quasars with the goal to resolve the jet structures in these objects, and answer key questions in extragalactic jet physics. See `https://jets.extragalactic.info/wiki/index.php/Main_Page` for more details.

to image the jets in detail at radio wavelengths with the *e*-MERLIN and LOFAR at GHz and MHz frequencies respectively. In particular, the characteristic faint but well-collimated inner regions in our selected sample provide reliable means of exploring jet physics on sub-kpc scales. Five objects are low-redshift ($z < 0.05$) Fanaroff-Riley type I sources, but we also include a nearby BL Lac object because such objects are usually related to FR I sources by unification schemes. For all six sources, we are interested in both the spectral structure to measure energy losses and the Faraday rotation measure to probe the magnetic environment. We report the properties of sources in our sample in Table 2.1.

2.1.2 Notes on individual sources

a) 3C 83.1B

3C 83.1B is identified with NGC 1265, an 11.43 mag type-cD galaxy (de Vaucouleurs et al., 1991) which has a redshift of 0.0251 and is a member of the chain of galaxies in the brightest cluster in the X-ray sky – the Perseus cluster (Abell 426). This well-known prominent head-tail radio source has been broadly classified as a narrow-angle tail (NAT; Sijbring & de Bruyn 1998; Sun, Jerius & Jones 2005) radio galaxy in the literature. One of the earliest radio observations of this source dates back to Ryle & Windram (1968) in which Cambridge 1-mile telescope images at 408 and 1407 MHz showed a curved extension of the radio structure to the north-west, and the existence of a weaker unresolved companion 3C 83.1A. Later observations with the WSRT at 49 and 92 cm revealed a large extension of the tail (Sijbring & de Bruyn, 1998) similar to the structures detected in the present study (but with a resolution about an order of magnitude lower than ours). Sijbring and de Bruyn suggested that the tail delineated the orbit of the galaxy through the cluster. Recent VLA 230-470 MHz observations reveal presence of filamentary structures across the entire tail of NGC 1265 (Gendron-Marsolais et al., 2020). HST images reveal a narrow dust lane orthogonal to the radio jet, and oriented along a P.A. of $\sim 171^{\circ}$ (Martel et al., 1999). VLBI observations (e.g. Xu, O'Dea & Biretta 1999) reveal symmetric parsec-scale twin jets which are well aligned with the kiloparsec-scale jets, and deep Chandra observations (e.g. Sun, Jerius & Jones 2005) reveal an absorbed ($N_{\rm H}$ = 1.5–3 $\times$ 10^{22} cm^{-2}) nucleus, and weak X-ray emission from inner radio knots in the jets.

b) 3C 264

The radio galaxy 3C 264 is identified with NGC 3862 [m_v = 13.67, log $P_{\rm tot}$ (408) = 24.85], a large elliptical, located about 8 arcmin off-center in the Leo cluster (Abell 1367). The source has previously been mapped at 5.0 GHz by Baum et al. (1997), Lara et al. (1997) and Lara et al. (1999); at 1.6, 5.0, 22.5 and 43.3 GHz by Lara et al. (2004); at 5.0, 8.4 and 15.3 GHz by Kharb et al. (2009); at 8.5 and 22.5 GHz by Perlman et al. (2010) and more recently at 15 GHz by Boccardi et al. (2019). The VLA 5 GHz map of Lara et al. (2004) has a resolution of 0.8 arcsec and reveals evidence of a faint counterjet emission to the south-west about 5 arcsec from the core. Capetti et al. (2000) have reported that the SED of 3C 264 rises from the radio toward higher frequencies (with an average spectral index $\alpha_{\rm RO}$ = 0.63; see also Lara et al. 1999) and suggested that the SED peak lies in the region 10^{15} – $10^{16.5}$ Hz. At optical wavelengths, a "ring" at a projected radius of $\sim$ 300–400 pc was first reported by Baum et al. (1997) who suggested that the ring is plausibly a manifestation of absorption by a nearly face-on circumnuclear dust disk. Observed variations in the jet collimation, brightness, and polarisation properties as it crosses the outer boundary of the dust ring have been argued to result from interaction between the jet and a dense gaseous region interior to the ring (e.g. Baum et al. 1997; Lara et al. 2004; Perlman et al. 2010).

c) 3C 274

This radio source – a peculiar example of bridged twin-jet radio source – is associated with the giant elliptical galaxy NGC 4486 (aka Messier 87; M 87). With its close proximity (d = 16 Mpc, 78 pc arcsec^{-1}; Tonry 1991), location at the centre of the nearest rich cluster of galaxies (the Virgo cluster), host to one of the largest SMBH discovered so far ($M_{\rm BH} \simeq 6.4 \pm 0.5 \times 10^9 M_{\odot}$; Gebhardt & Thomas 2009) and popularity as the fourth brightest radio source (at m-wavelength) in the northern sky (S_{178} = 1144.5 Jy; Leahy, Bridle & Strom 1996), it is no coincidence that its jets are the most intensely studied features of any radio-loud AGN in the Universe. Detailed observations at radio (e.g. Baade & Minkowski 1954; Perlman et al. 1999; Owen, Eilek & Kassim 2000; de Gasperin et al. 2012), optical and UV (e.g. Boksenberg et al. 1992; Biretta, Sparks & Macchetto 1999; Perlman et al. 1999), infrared (e.g. Shi et al. 2007; Baes et al. 2010) and X-ray (e.g. Bohringer et al. 1995; Wilson & Yang 2002; Forman et al. 2007) wavelengths have previously been made. Efforts at developing theoretical (e.g. Falle & Wilson 1985) and numerical

(e.g. Churazov et al. 2001) models to interpret these observations have also been advanced, and the Event Horizon Telescope Collaboration (2019) have recently imaged the base of the main jet providing the scientific community with the very first glimpse of the central SMBH. The multiwalength (radio to X-ray) observations show a remarkably constant morphology of the M87 jets (e.g. Boksenberg et al. 1992; Forman et al. 2007). The rather striking features in the jets is the well documented multiple bright knots observed in the inner region – the presence of these bright substructures have allowed for proper-motion measurements (direct velocity estimates) in M87 (e.g. Biretta, Zhou & Owen 1995). The knots are highly polarised, plausibly suggesting highly ordered magnetic fields (e.g. Perlman et al. 1999). Junor, Biretta & Livio (1999) reported that the radio jets in M87 is launched within 30 Schwarzschild radii of its central SMBH; the jets are embedded in a halo with diameter extending up to $\sim$ 15-arcmin (e.g. Rottmann et al. 1996).

d) 3C 296

The radio source 3C 296 is coincident with the large elliptical nucleus of NGC 5532, a lenticular (S0) Galaxy that has a redshift of 0.025. The cluster association of this source is a subject of debate in the literature; Colina & Perez-Fournon (1990) reported that it is a member of the Abell cluster A1890 but Leahy, Bridle & Strom (1996) suggest it is in fact more than twice as distant. 3C 296 was first imaged by Birkinshaw, Laing & Peacock (1981) – a classic core-dominated (FR I) radio galaxy with bridged twin jets that are initially relativistic on parsec scales but decelerate to non-relativistic speeds on kpc-scales (e.g. Laing et al. 2006). At radio wavelengths (e.g. Hardcastle et al. 1997) the jets are highly polarized and the inferred magnetic-field direction is longitudinal for the first 6 kpc on the jet side and transverse thereafter; at optical wavelengths (e.g. Martel et al. 1999) the shape of emission from excited gas is roughly conelike with sharp dusty structure centered on its nucleus at a P.A. of $\sim 163^{\circ}$. NGC 5532 has companions to the east and south at a distance of $21''$ and $34''$ respectively; in the infrared, a NICMOS image by Baldi et al. (2010) reveals a bright nucleus with diffuse symmetric emission extending out to $10''$ and at X-ray wavelengths (e.g. Hodges-Kluck et al. 2010), the IGM has a similar shape and orientation to the ISM, albeit distinct in temperature and central position angle.

e) 3C 371

3C 371 is identified with UGC 11130 an 11.39 mag (R-band) strongly polarised and variable BL Lacertae object (e.g. Angel & Stockman 1980). Previously published maps of this source include the VLA maps of Wrobel & Lind (1990); MERLIN map of Akujor et al. (1994); HST maps of Nilsson et al. (1997) and Scarpa et al. (1999); Chandra, HST, and MERLIN maps of Pesce et al. (2001) and Chandra, HST, VLA, and MERLIN maps of Sambruna et al. (2007). The 5 GHz VLA map of Wrobel & Lind (1990) shows low surface brightness twin radio lobes straddling the dominant compact core and a weak component located in the western lobe analogous to radio hot spots; this observation has led Wrobel and Lind to conclude that the morphology of 3C 371 is of a Fanaroff-Riley type II source. Similarly, multiwavelength observations by Sambruna et al. (2007) showed that the core-jet radio morphology resembles that of FR IIs but the jets are less collimated and do not exhibit the typical hard X-ray spectra present in high-power radio sources. Optical jet emission in 3C 371 was first detected by Nilsson et al. (1997); its morphology was later shown to be similar to the radio jet by Scarpa et al. (1999).

f) 3C 465

This archetype of the WAT class of radio sources identified with NGC 7720, is the brightest galaxy in the cluster Abell 2634 and among the best studied WAT sources in the northern sky. Detailed imaging studies in the radio (e.g. Bempong-Manful et al. 2020; Hardcastle & Sakelliou 2004), near-infrared to UV (e.g. Madrid et al. 2006), optical (e.g. Martel et al. 1999; Colina & Perez-Fournon 1990), and X-ray (e.g. Hardcastle, Sakelliou & Worrall 2005) have previously been made. The HST observations of Martel et al. (1999) reveal a companion $12''$ to the north of NGC 7720 (see also the NICMOS image of Madrid et al. 2006). Both NGC 7720 and its companion are large ellipticals, each harbour a spectacular dust structure – a nearly face-on dust ring oriented at a P.A. of $\sim 5^{\circ}$ surrounds the unresolved nucleus of NGC 7720. At GHz frequencies, high resolution imaging reveal multiple bright knotty structures within 4.4 kpc of the radio core (e.g. Bempong-Manful et al. 2020), coincident with the sites of X-ray particle acceleration at the base of the radio jet (Hardcastle, Sakelliou & Worrall 2005).

Table 2.1: Sample properties

	Source name		RA	Dec	Cluster	z	S_{178}	$\log_{10} P_{178}$	α	Size	m_v
IAU	3CRR	Alt. name	(J2000)	(J2000)			(Jy)	(W/Hz/sr)		$''$(kpc)	
(1)	(2)	(3)	(4)	(5)	(6)	(7)	(8)	(9)	(10)	(11)	(12)
J1145+1936	3C 264	NGC 3862	11:45:04.94	+19:36:22.7	A 1367	0.021	28.3	24.30	−0.75	522 (209)	8.56
J0318+4151	3C 83.1B	NGC 1265	03:18:15.70	+41:51:27.9	A 426	0.026	29.0	24.15	−0.60	1216 (409)	11.43
J1416+1048	3C 296	NGC 5532	14:16:52.98	+10:48:27.7	A 1890	0.024	14.2	24.08	−0.67	437 (193)	11.28
J1806+6949	3C 371	UGC 11130	18:06:50.68	+69:49:28.1	—	0.050	5.8*	25.30	−0.30	20 (21)	11.39
J2338+2701	3C 465	NGC 7720	23:38:29.36	+27:01:55.9	A 2634	0.029	41.2	24.79	−0.75	603 (347)	12.17
J1230+1223	3C 274	NGC 4486	12:30:49.40	+12:23:27.8	Virgo	0.004	1144.5	58.79	−0.79	836 (71)	7.19

Notes: Column(1), (2) and (3) – IAU, 3CRR and New/Uppsala catalogue names of the target sample; Column (4) and (5) – core coordinates (J2000); Column (6) – Abell and Virgo galaxy cluster association; Column (7) – redshift; Column (8) and (9) – flux density and logarithm (base 10) of the radio power at 178 MHz; *flux density taken from 7C survey; Column (10) – integrated radio spectral index between 178 and 750 MHz; Column (11) – largest angular size and projected linear size in arcsec and kpc respectively; column (12) – visual magnitude as measured in the visible region of the EM spectrum – (V-band; 3C 83.1B, 3C 264 and 3C 465), (R-band; 3C 371) and (Z-band; 3C 296) – (Adapted from Leahy, Bridle & Strom 1996; redshift measurements taken from Spinrad et al. 1985; visual magnitude taken from NED[6].)

2.2 Instruments

2.2.1 The *e*-MERLIN

The *enhanced* Multi Element Remotely Linked Interferometer Network (*e*-MERLIN) is an upgrade to existing hardware and telescopes of the MERLIN array – a very long baseline interferometry (VLBI) consisting of seven radio telescopes (including: the Lovell Telescope, Mark II, Cambridge, Defford, Knockin, Darnhall and Pickmere – cf. Figure 2.1) spread across the United Kingdom (UK) with an effective maximum baseline of over 217 kilometres. The array is the UK's national facility for radio astronomy and is operated by the University of Manchester from the Jodrell Bank Observatory (JBO) on behalf of the Science and Technology Facilities Council (STFC). Linked remotely, data from each telescope is sent via optical fibres to JBO where a correlator processes them into a single data set. The capabilities of *e*-MERLIN compare with leading ground and space based telescopes. At $\sim$ 5 GHz frequency for example, *e*-MERLIN has a spatial resolution of 40 milliarcsec which is comparable to that of the Hubble Space Telescope at optical wavelengths (e.g. Kukula et al. 1996) and at $\sim$ 1.4 GHz its angular resolution of $\sim$ 200 milliarcsec is much higher than that obtained with the VLA at the same frequency (Biggs & Ivison, 2008). For an in-depth review of the array and its capabilities, the reader is referred to the *e*-MERLIN website (`http://www.e-merlin.ac.uk`). Table 2.2 below shows a summary of the capabilities of the *e*-MERLIN array.

2.2.2 LOFAR

The LOw Frequency ARray (LOFAR) – a pathfinder to the next generation radio telescope, the Square Kilometre Array (SKA) – is an innovative radio telescope optimized for the frequency range from 30 to 240 MHz, but also with the ability to observe down to 10 MHz; for reference, the earth's ionosphere has electron densities $\sim 10^4$ – 10^5 cm^{-3}, which corresponds to a plasma frequency cut-off of $\sim$ 1 – 10 MHz. The antenna distrubution is grouped into 24 core, 14 remote and 14 international stations, with the majority (about 40) of these stations spread over an area roughly 180 km in diameter centered near the town of Exloo in the northeastern Dutch province of Drenthe. Six of the densely sampled, 2-km-wide core stations reside on a 320 m diameter island referred to as the "Superterp" which provides the shortest baselines in the array and can also be reconfigured to effectively form one single, large station. Unlike conventional

Figure 2.1: Left: Location map of the seven radio telescopes of *e*-MERLIN across the United Kingdom. Clockwise from top; Lovell, Mark II, Cambridge, Defford, Knockin, Darnhall and Pickmere. The longest baseline is 217 km, giving resolutions of 150, 40 and 12 mas at 1.3–1.8, 4–8 and 22–24 GHz respectively (see Peck & Fenech 2013). Right: A close-up image of the 76 m diameter Lovell (Mark IA) telescope of the *e*-MERLIN array.

Table 2.2: Technical observing capabilities of the *e*-MERLIN telescope

	1.5 GHz (L-band)	5 GHz (C-band)	22 GHz[5] (K-band)
Resolution[1] (mas)	150	40	12
Field of view[2] (arcmin)	30	7	2
Frequency range (GHz)	1.3–1.7	4–8	22–24
Bandwidth[3] (GHz)	0.4	2	2
Sensitivity[4] (μJy/bm)	5–6	1.8–2.3	$\sim$ 15
Surface brightness sensitivity[4] (K)	$\sim$ 190	$\sim$ 70	$\sim$ 530

Notes: (1) – with uniform weighting, at the central frequency; (2) – FWHM of 25-m dishes; reduced when the Lovell telescope is included; (3) – maximum bandwidth per polarization; (4) – in a full imaging run with the Lovell telescope; (5) – the Lovell telescope is not available at 22 GHz. The Lovell telescope may be included in the array at 1.5 and 5 GHz; this increases the sensitivity by a factor of between 2 and 3, but reduces the field of view – (Adapted from Argo 2015).

"mechanical" parabolic dishes, the LOFAR telescope has no moving parts, and consists of an interferometric array of dipole antenna stations distributed throughout the Netherlands and Europe (Figure 2.2). Signals from individual dipoles are combined digitally into a phased array

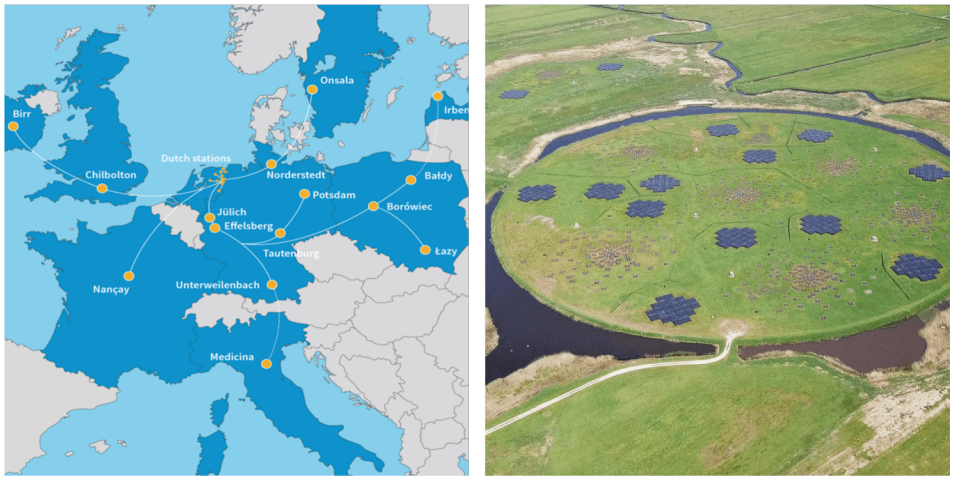

Figure 2.2: Left: Distribution of the international LOFAR stations across Europe with a maximum baseline of $\sim$ 1200 km. Right: Aerial view of the Superterp station which provides the shortest baselines in the array and can also be reconfigured to effectively form one single, large station – (Source: `www.lofar.org`).

Table 2.3: Technical capabilities of the LOFAR array

Frequency ν [MHz]	Wavelength λ [m]	Sensitivity^a [mJy beam^{-1}]	Resolution$^{b(d)}$ [arcsec]	Prim. beam^c [degree]	No. of beams^e
15	20	11	33.00 (3.30)	22.9	50
30	10	2	16.50 (1.65)	11.5	200
60	5	1.65	8.25 (0.83)	5.7	800
75	4	1.30	6.60 (0.66)	4.6	1250
120	2.5	0.070	4.13 (0.41)	2.9	3200
150	2.0	0.065	3.30 (0.33)	2.3	5000
200	1.5	0.063	2.48 (0.25)	1.7	8888
240	1.2	0.076	2.06 (0.21)	1.4	12800

Notes: ^{a} Point source sensitivity given as the rms map noise for 1 hr integration time, 2 polarisations and 4 MHz bandwidth; ^{c} Primary beam size (FWHM) calculated for a 50 m station; ^{e} Number of independent beams needed to cover 2π sterradian; $^{b(d)}$ Resolution scaled to baselines extending to remote (and international) stations – corresponding to $\sim$ 121 (and 1158) km respectively – (Source: `www.lofar.org`).

at station level – i.e. a delay is applied to the relative phases of the signals feeding the dipoles in such a way that the radiation pattern of the array is reinforced in a target direction and suppressed in the sidelobes. A combination of analog and digital beam-forming techniques (e.g.

Thompson, Moran & Swenson 2017) allow for rapid repointing of the telescope as well as the simultaneous observation of multiple, independent areas of the sky (e.g. van Haarlem et al. 2013). There are two main receiver elements – (1) the low-band antennas (LBA), which cover the frequency range 10–90 MHz, and (2) the high-band antennas (HBA), which cover the frequency range 110–240 MHz.These have sufficient sensitivity over the nearly two decades that encompass LOFAR's observing bands. There is currently active preparation for LOFAR2.0 which will be a major upgrade to existing LOFAR capabilities, and with early science expected in 2023. The instrument, designed and constructed by ASTRON, has facilities in several countries, that are owned by various parties (each with their own funding sources), and that are collectively operated by the International LOFAR Telescope (ILT) foundation under a joint scientific policy. For a detailed review of the instrument and its capabilities, see Rottgering et al. 2006; van Haarlem et al. 2013 and references therein, or visit the radio observatory webpage at `https://www.astron.nl/telescopes/lofar/`. We present an overview of the observing capabilities of the LOFAR instrument in Table 2.3.

2.2.3 The VLA

The Very Large Array (VLA) is a relatively compact array of radio telescopes operated by the National Radio Astronomy Observatory (NRAO) in Socorro, New Mexico, United States. The array consists of twenty-seven active antennas (each with a diameter of 25 metres – cf. Figure 2.3) and a maximum baseline of 36 km. By means of rails, the antennas can be easily repositioned and this allows for flexibility in observations in four main configurations (i.e., A, B, C, and D) at frequencies ranging from 1.0 to 50 GHz inclusive. Since commissioning in 1980, its first major upgrade (the Expanded Very Large Array – EVLA) was completed in 2012, and the telescope was subsequently renamed as the Jansky Very Large Array (JVLA). Hereafter I simply refer to the instrument as the VLA. The telescope has in its 4 decades of existence demonstrated capabilities of a cutting edge ground-based astronomical instrument and this is evident in the many discoveries made as well as the numerous citations it has enjoyed in astronomical refereed journals. There is currently ongoing discussions of a future facility: the next generation Very Large Array (ngVLA) with observing frequency up to $\sim$ 100 GHz (twice the maximum

Figure 2.3: Left: Overall view of the VLA, looking south in a compact configuration. The array can be reconfigured by moving the antennas to more distant pads via the rail lines visible in the photograph. Right: A close-up image of one of the 25 m diameter antennas in the array – (Credit: Dave Finley, NRAO/AUI).

Table 2.4: Summary of VLA observing capabilities

	1–2 GHz (L-band)	2–4 GHz (S-band)	4–8 GHz[5] (C-band)	8–12 GHz[5] (X-band)	40–50 GHz[5] (Q-band)
Resolution[a] (arcsec)	1.3–46	0.65–23	0.33–12	0.2–7.2	0.043–1.5
Bandwidth[b] (GHz)	0.7	1.75	3.5	3.8	8
Antenna SEFD[c]	400	350	300	250	1100
Sensitivity[d] (μJy/bm)	5.5	3.9	2.4	1.8	5.6
Sensitivity[e] (mJy/bm)	2.2	1.7	1.0	0.65	1.4

Notes: (a) – approximate synthesized beamwidth, $\theta_{\rm HPBW}$ between A and D-configurations for the central frequency of each band; (b) – an estimate of the effective bandwidth available, free of RFI; (c) – the System Equivalent Flux Density, SEFD = $2kT_{\rm sys}$ /$A_{\rm e}$ is a measure of the antenna sensitivity (i.e., the flux density of a source which doubles the system temperature); (d) and (e) – the expected rms noise in a 1-hour integration at high elevation and under good weather conditions for continuum and line respectively. For the continuum case, the bandwidth utilized is that listed in (b) whereas for the line case, a bandwidth corresponding to 1 km/sec velocity resolution is assumed – (Adapted from Perley et al. 2011).

frequency of the current VLA). For a detailed review of the upgrade and capabilities of the VLA see Perley et al. (2011) or visit the NRAO website at `http://www.vla.nrao.edu/`.

2.2.4 The HST

The NASA/ESA Hubble Space Telescope (HST; Figure 2.5) launched into orbit on April 24, 1990 aboard space shuttle Discovery (STS-31). The HST is 43.5 feet (13.2 meters) long, has a maximum diameter of 14 feet (4.2 m), and weighs 24500 lbs. (11110 kg). Travelling at a speed of 17500 mph (28000 km/h), it takes $\sim$ 97 minutes for the HST to complete one orbit, at an average altitude of 307 nautical miles (569 km, or 353 miles), inclined 28.5 degrees to the equator. The main source of energy/power for the telescope is sunlight via two 25-foot fitted solar panels with 6 nickel-hydrogen (NiH) batteries. The HST as a space-based observatory has two main advantages over ground-based optical telescopes – (1) its angular resolution is limited only by diffraction and telescope optical quality, rather than atmospheric turbulence; and (2) in its early years of operation, could observe both infrared and ultraviolet light, which are strongly absorbed by the earth's atmosphere. The instrument contains primary and secondary mirrors with diameters 2.4 m and 0.3 m respectively and observes in the near UV, visible and near IR wavelengths at high spatial resolution (PSF FWHM at 5000Å reaching $\sim$ 43 milliarcsec) with substantially lower background. In its over three decades of operation, the HST's capabilities have grown immensely and its life span has been extended through five astronaut servicing missions – the last mission occuring in May 2009. Like the VLA at radio wavelengths, the HST at optical wavelength have made numerous and stunning discoveries including determining the rate of expansion of the Universe (e.g. Freedman 2002). The facility is managed by the Space Telescope Science Institute (STScI) which is operated by the Association of Universities for Research in Astronomy, Inc., under NASA contract NAS 5-26555. For a detailed review of the intrument and its capabilities see `https://www.nasa.gov/mission_pages/hubble/`.

2.2.5 Chandra X-ray observatory

The Chandra X-ray Observatory (Figure 2.4) – NASA's flagship mission for X-ray astronomy was launched on July 23 1999 aboard NASA's Space Shuttle Columbia. Chandra is 13.8 m $\times$ 19.5 m (45.3 ft $\times$ 64.0 ft), weigh up to 4800 kg (10560 lbs) and orbits at 10000 km $\times$ 140000 km (6200 $\times$ 86900 miles) at 28.5 degree inclination. The telescope system is powered by two 3-panel silicon solar arrays (2350 W) with three 40 amp-hour nickel hydrogen batteries, and carries four paraboloid and hyperboloid mirrors nested inside each other. The different mirrors have different outer diameters; 0.5 arcsec angular resolution; and weigh up to 956.4 kg (2,104

Table 2.5: Comparison of the imaging capabilities of the HST at near-UV, visible and near-IR wavelengths after Servicing Mission 4 (SM4; May 2009)

Instrument	FoV area (arcsec^2)	Pixel scale (arcsec)	Read noise (e^-)	Dark current (e^-/pix/s)
		Near-UV (200 – 350 nm)		
WFC3/UVIS	$162'' \times 162''$	0.040	3.0–3.1	4.0×10^{-4}
STIS/NUV-MAMA	$25'' \times 25''$	0.025	—	0.005
		Optical (350 – 1000 nm)		
WFC3/UVIS	$162'' \times 162''$	0.040	3.0–3.1	4.0×10^{-4}
ACS/WFC	$202'' \times 202''$	0.049	5	6.2×10^{-3}
		Near-Infrared (800 – 2500 nm)		
WFC3/IR	$123'' \times 136''$	0.13	12.5	—
NIC3	$51'' \times 51''$	0.200	29	—
NIC2	$19'' \times 19''$	0.075	26	—
NIC1	$11'' \times 11''$	0.043	26	—

Notes: ACS – The Advanced Camera for Surveys; NIC – The Near infrared Camera; STIS – The Space Telescope Imaging Spectrograph; WFC – The Wide Field Camera – (Adapted from `https://w.astro.berkeley.edu/~kalas/labs/`).

Table 2.6: Comparison of Chandra main characteristics with other X-ray missions

Satellite	FWHM ($''$)	HEW ($''$)	Energy range (keV)	$A_{\rm eff}$ at 1 keV (cm^2)
Chandra	0.2	0.5	0.1–10	800
ASCA	73	174	0.5–10	350
BeppoSAX	–	75	2–10	150 [a]
ROSAT	3.5	7	0.1–2.4	400
XMM-Newton	6	15	0.15–15	4650

Notes: Col. (2) and (3) is the on-axis point-spread function (PSF) of FWHM and HEW ((Half-Energy Width) for the different instruments; $A_{\rm eff}$ is the effective aperture; [a] at 6.4 keV.

pounds) in total. Four science instruments aboard the spacecraft allow for high-energy astrophysical probes of the Universe. These include; (1) The Advanced Charged Coupled Imaging Spectrometer (ACIS) – consisting of ten CCD chips in 2 arrays for imaging and spectroscopy; angular resolution is 0.492 arcsec over the energy range 0.2 – 10 keV and sensitivity is 4×10^{-15}

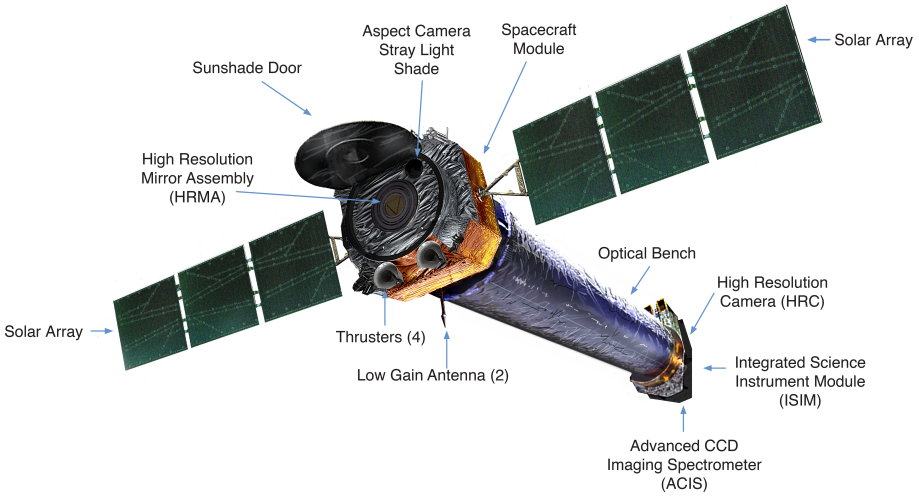

Figure 2.4: An illustration of the Chandra X-ray observatory and spacecraft components – (Image credit: NASA/CXC & J. Vaughan).

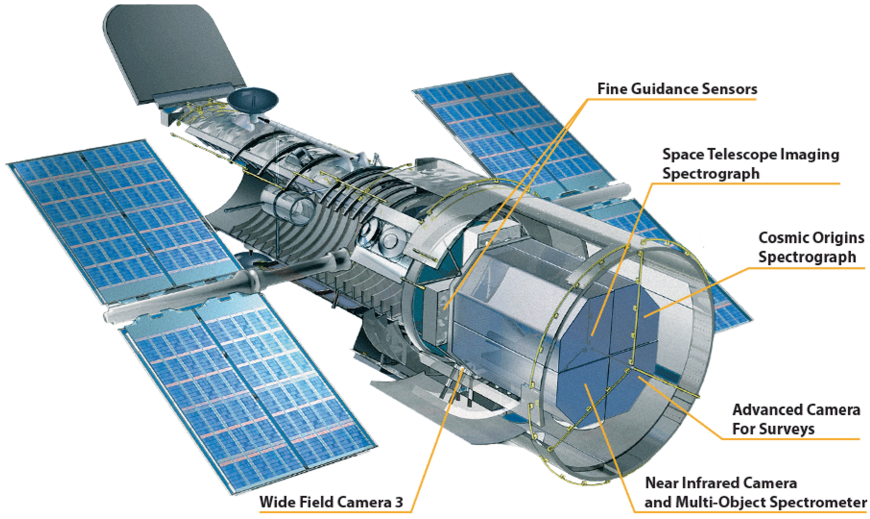

Figure 2.5: A cutaway image of the Hubble Space Telescope showing the three main instruments – cameras, spectrographs and interferometers – aboard the spacecraft – (Image credit: Goddard Space Flight Center, NASA).

ergs cm^{-2} sec^{-1} in 10^5 s . (2) The High Resolution Camera (HRC) – uses large field-of-view micro-channel plates for imaging; angular resolution < 0.5 arcsec at the centre of the FoV (31$\times$31 arcmin); time resolution is 16 micro-sec and sensitivity is 4×10^{-15} ergs cm^{-2} sec^{-1}

in 10^5 s. (3) The High Energy Transmission Grating (HETG) – this provides spectral resolution of 60–1000 over the energy range 0.4 – 10 keV. (4) The Low Energy Transmission Grating (LETG) – this provides spectral resolution of 40–2000 over the energy range 0.09 – 3 keV. The facility is operated and managed for NASA at CXC[7] by the Smithsonian Astrophysical Observatory (SAO), which is part of the Center for Astrophysics, Harvard & Smithsonian located in Cambridge, MA. For a high level review of the Chandra X-ray Observatory and its capabilities, see Wilkes, D'Abrusco & Martínez-Galarza (2019) or visit the observatory website at `https://chandra.harvard.edu/`.

2.3 The multiwaveband complementarity

Notwithstanding the vast array of good existing radio and multi-wavelength data for our selected science targets, the complementarity to VLA observations by *e*-MERLIN (with its broad-bandwidth capabilities) in resolving jet physics on sub-kpc scales cannot be overemphasized. The formation of ERJs on $\lesssim 100$ R_G ($\lesssim 1$ mas) scales implies that direct study is possible only with VLBI techniques, supplemented by coordinated observations of time variability across the EM spectrum. However, detailed exploration of jet flows including; compositions, velocity fields, energetics, particle acceleration, magnetic fields and interactions with the environment can only be gained through *deep, transverse-resolved* radio observations and this until now has only been possible on $\gtrsim 0.25$ arcsec scales with the VLA. We aim to extend these techniques to smaller angular scales by measuring the physical properties of the jets in our sample obtained through the first ever deep, transverse-resolved radio observations using *e*-MERLIN, with complementary observations from the VLA in order to resolve the physics driving the observed jet structure.

With its combination of improved sensitivity, a resolution of ≈ 0.1 arcsec and baselines that lie between those of VLA and EVN, *e*-MERLIN serves as perfect candidate in complementing either array for improved u-v coverage. Our aim therefore is to image L-band observations of the science targets from both the VLA (i.e., A and B configurations) and *e*-MERLIN and as a final step, combine these two observations to construct the highest resolution and sensitivity maps of the science targets to date in order to address our key science goals. The addition of the VLA data will in principle provide the missing short spacings in the *e*-MERLIN data putting the

[7]The Chandra X-ray Center (CXC) operates all aspects of the Chandra mission; `https://cxc.harvard.edu/`

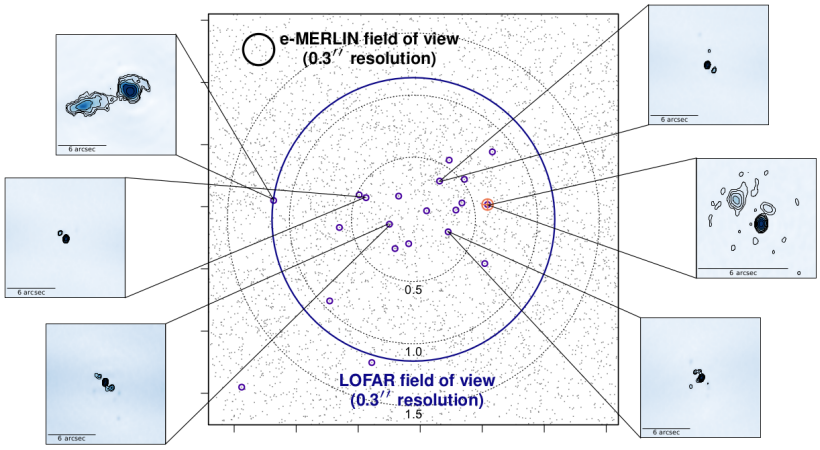

Figure 2.6: Comparison of the sub-arcsec FoV between LOFAR-VLBI and *e*-MERLIN. The dotted lines show radii in increments of 0.5 degrees; the blue line is where 50% intensity losses are expected from bandwidth and time smearing. The orange cross hairs show the position of the in-field calibrator. The cutouts are preliminary LOFAR-VLBI images in the LoTSS P205+55 field generated automatically by current pipeline for International station imaging – see Morabito et al. (2022) for detailed imaging results. Noise levels are shown to reach $\sim$ 100 μJy/beam rms at 0.3 arcsec resolution, as expected – (Image credit: Leah K. Morabito, Durham).

compact structure in context and thus prevent image infidelity which may arise due to spatial frequency gaps. Again we want to take the next (and practically, the *very first step* of its kind) towards lower frequencies and extend these techniques to metre wavelengths, where currently, only LOFAR can deliver sensitivity at comparable resolution (see Figure 2.6). For this reason, we have acquired LOFAR HBA ($\sim$ 150 MHz) observations including international baselines for all our science targets (except M 87). This would provide for good coverage of the radio band and allow for detailed spectral studies to constrain jet-particle acceleration and energy loss processes in our target sample.

Additionally, the optical (HST) data provide important information about the host galaxies and environments of our targets, and will specifically allow us to look for optical emission from the inner jets, and look for dust/gas rings that might help extract the orientation of the jets relative to the plane of the sky (based on associated RM structures, or on the assumption that the rings are perpendicular to the jet ejection direction); whereas the X-ray (Chandra) data will essentially allow us to look at synchrotron and inverse-Compton X-rays – which are tracers of

high-energy particle acceleration in jets, hotspots and lobes, and thermal X-rays – to find out about the external pressure and density affecting the dynamics, and providing the magnetoionic medium for Faraday rotation.

3

Observations and Methods

In this chapter, I present and describe the multiwavelength observations, and methods employed to image our science targets with the required sensitivity and resolution for our science goals.

3.1 Observations

3.1.1 Radio observations

a) *e*-MERLIN observations

All our *e*-MERLIN observations were acquired as part of the ongoing *e*-MERLIN Jets Legacy observing campaign and span the period from March 2015 to the present. The observations include single and multiple epochs for the different sources with all seven antennas operational – except for the second epoch of 3C 465 which did not include the Lovell telescope. The observations were taken in full polarisation, using the bright sources 3C 48 and 3C 286 as flux calibrators with all available antennas in 64 MHz bandwidth centred on 1.51 GHz, in 8 adjacent intermediate-frequencies (IF) and 4 seconds integration time. Each IF had 512 channels which was later averaged to 128 channels per IF. The data were correlated with the *e*-MERLIN correlator at Jodrell Bank Observatory. We report details of the observations in Table 3.1.

b) LOFAR observations

Our targets were co-observed with the LOFAR Two-Metre Sky Survey (LoTSS; Shimwell et al. (2017)) using the LOFAR HBA_Dual_Inner configuration ($\sim$110–190 MHz) with all international stations. The observations were conducted in full polarisation with continuous frequency coverage (120–168 MHz) on the target beams, using a bandwidth of 48 MHz (244 sub-bands). Each sub-band consists of 64 channels, which were averaged in frequency, to 16 channels per sub-band; this reduced the data storage volume and sped up the data reduction process. The shortest and longest baselines recorded correspond to 68 m and 1158 km respectively, and the images have field of view (FOV, primary beam) covering around 3–11 deg^2 full width at half maximum (FWHM) at 144 MHz. The phase centre of each target was set as the pointing centre during the observations, and so we do not expect bandwidth smearing in the outer parts of the FOV, arising from the averaging in frequency, to affect our science goals. The observations were bracketed by observation of appropriate primary flux calibrator sources 3C 48, 3C 196 and 3C 295 for 10 min on either side of an 8 hr target observations with the same frequency setup. The integration time was set to 1 s for both calibrator and target, to facilitate the removal of radio frequency interference. The data were acquired in LOFAR Cycle 11 observations, and span the period from December 2018 to November 2019. Details of the observations are presented in Table 3.2.

c) VLA observations

For two sources in our sample (i.e., 3C 83.1B and 3C 465) we obtained archival EVLA data at L-band ($\sim$ 1.5 GHz) continuum frequencies. The data was taken in both the A-configuration and B-configuration with the new EVLA computer system controlling the array with observations conducted in full polarization mode – using the bright source 3C 48 as flux calibrator with all 27 antennas in 64 MHz bandwidth centred at 1.5 GHz in 16 adjacent spectral windows. Each 64 MHz spectral window had 64 channels 1.0 MHz wide with 1 second and 3 seconds of integration time for A and B-configurations respectively. For all the other sources, we have retrieved historical VLA data from the NRAO data archive (`http://archive.nrao.edu`) at both L-band ($\sim$ 1.5 GHz) and X-band ($\sim$ 8.5 GHz), and in both A and B-configurations including 3C 83.1B and 3C 465. Details of the VLA obsertaions are presented in Table 3.3.

3.1.2 Optical and Infrared observations

Optical and infrared observations for the present study were taken from the Hubble Space Telescope (HST) archive. The data were retrieved from the Multimission Archive at STScI (MAST)[8], and were taken with the Advanced Camera for Surveys (ACS), Wide-Field -and-Planetary Camera (WFC and WFPC) and NICMOS instruments aboard the HST for the optical and infrared data respectively. Exposures were taken predominantly with the F160W, F475W and F606W filters, which corresponds approximately to the H-band, B-band and V-band filters respectively in the Johnson-Cousins BVI system (e.g. Harris 2018). The observations were taken in both General Observer (GO) and 'snapshot' mode programs, and span the period from December 1994 to January 2019. We report details of the observations in Tables 3.4–3.5.

3.1.3 X-ray observations

We acquired X-ray observations for our target sample from the Chandra Data Archive[9]. The observations were taken between 2002 and 2004 inclusive using the ACIS-S instrument on Chandra in both FAINT and VFAINT imaging mode. For all the sources, we have retrieved observations with the longest exposure available from the archive. We present journal of the Chandra X-ray observations in Table 3.6.

3.2 Methods

3.2.1 Data calibration and imaging

The main concept of the radio data calibration strategy is to identify and discard any bad data within the sampled visibilities, derive amplitude and phase corrections, and subsequently, apply these solutions to the data in order to obtain an accurate measure of the true sky brightness distribution of the observed science target.

[8] https://mast.stsci.edu/search/hst/
[9] https://cda.harvard.edu/chaser/

Table 3.1: Summary of *e*-MERLIN observations

		– 3C 83.1B –	
Project ID	LE1005_L_3C83.....[1]	LE1005_L_3C83.....[2]	—
Date(TOS)	21-Dec-2016(133.02)	30-Dec-2016(136.62)	
Flux calibrators	3C 48, 3C 286	3C 48, 3C 286	
		– 3C 264 –	
Project ID	LE1005_L_3C264.....	—	—
Date(TOS)	23-Dec-2018(50.22)		
Flux calibrators	3C 48, 3C 286		
		– 3C 274 –	
Project ID	LG0011_L_M87.....	—	—
Date(TOS)	25-Dec-2016(35.82)		
Flux calibrators	3C 48, 3C 286		
		– 3C 296 –	
Project ID	LE1005_L_3C296.....[1]	LE1005_L_3C296.....[2]	LE1005_L_3C296.....[3]
Date(TOS)	30-Dec-2016(28.62)	02-Jan-2019(64.02)	03-Jan-2019(36.43)
Flux calibrators	3C 48, 3C 286	3C 48, 3C 286	3C 48, 3C 286
		– 3C 371 –	
Project ID	LE1005_L_3C371.....[1]	LE1005_L_3C371.....[2]	LE1005_L_3C371.....[3]
Date(TOS)	28-Mar-2015(94.03)	23-Dec-2016(93.33)	02-Jan-2017(97.02)
Flux calibrators	3C 286	3C 48, 3C 286	3C 48, 3C 286
		– 3C 465 –	
Project ID	EGJ_3C465L.....[1]	EGJ_3C465L.....[2]	—
Date(TOS)	12-Apr-2015(66.53)	13-Apr-2015(65.75)	
Flux calibrators	3C 48, 3C 286	3C 48, 3C 286	
		– L-band Data properties –	
Frequency setup (mean)		1.25–1.77 GHz (1.51 GHz)	
Total bandwidth (IFs)		512 MHz (8 IFs)	
Channel width (Ch/IF)		0.5 MHz (128)	
Integration time		4 s	
Polarization		Full Stokes (R, L)	
UV coverage		$> 0.05\,\mathrm{k}\lambda$	

Notes: [1,2,3] denote the different observing epochs for each source. TOS is the on-source integration time in kiloseconds (scaled to an array with all 7 antennas operational).

Table 3.2: Journal of LOFAR HBA observations

– 3C 83.1B –	
Observation IDs	L691326/30/36
Stations	51 (24 core; 14 remote; 13 int'l)
Pointing centre (J2000)	$03^{\rm h}18^{\rm m}15.^{\rm s}70$, $+41^\circ51'27.''9$
Start / End date (UTC)	14–Dec–2018 (17:00) — 15–Dec–2018 (01:00)
– 3C 371 –	
Observation IDs	L691540–691550
Stations	50 (24 core; 14 remote; 12 int'l)
Pointing centre (J2000)	$18^{\rm h}06^{\rm m}50.^{\rm s}60$, $+69^\circ49'28.''1$
Start / End date (UTC)	23–Dec–2018 (07:19) — 23–Dec–2018 (15:19)
– 3C 465 –	
Observation IDs	L695935/39/45
Stations	50 (24 core; 14 remote; 12 int'l)
Pointing centre (J2000)	$05^{\rm h}42^{\rm m}36.^{\rm s}1$, $+49^\circ51'07.''0$
Start / End date (UTC)	04–Mar–2019 (08:22) — 04–Mar–2019 (16:22)
– 3C 296 –	
Observation IDs	L697489/93/99^a / L708048/52/58^b
Stations	51 (24 core; 14 remote; 13 int'l)
Pointing centre (J2000)	$14^{\rm h}16^{\rm m}52.^{\rm s}90$, $+10^\circ48'27.''7$
Start / End date (UTC)	15–Mar–2019 (00:14) — 15–Mar–2019 (04:14)^a
	10–May–2019 (21:00) — 11–May–2019 (01:00)^b
– 3C 264 –	
Observation IDs	L697475/79/85
Stations	50 (24 core; 14 remote; 12 int'l)
Pointing centre (J2000)	$11^{\rm h}45^{\rm m}05.^{\rm s}00$, $+19^\circ36'22.''7$
Start / End date (UTC)	17–Mar–2019 (19:24) — 18–Mar–2019 (03:24)
– HBA data properties –	
Frequency setup	120–168 MHz (mean 144 MHz)
Total bandwidth	48 MHz (244 sub-bands)
Channel width (Chan/sub-band)	195.3125 kHz (16)
Polarization	Full Stokes
UV coverage	$> 0.05\,{\rm k}\lambda$
Flux density calibrators	3C 48, 3C 196 and 3C 295 (2 scans of 10 min)

Notes: The LOFAR station beams are complex-valued, time and direction dependent, and differ slightly from station to station. $^{(a,b)}$denote two observing epochs for 3C 296.

Table 3.3: Summary of VLA observations

	L-band ($\sim$ 1.5 GHz)		X-band ($\sim$ 8.5 GHz)	
	A-config$*$	B-config$*$	A-config$*$	B-config$*$
		– 3C 83.1B –		
Project ID	12A-195	12A-195	AB0706	AK0403
Date(TOS)	12-Oct-31(3.45)	12-May-28(3.44)	94-Mar-03(4.77)	95-Dec-05(6.83)
Flux calibrators	3C 48	3C 48	3C 286	3C 48
		– 3C 371 –		
Project ID	AB1022	OAK425	AL0695	OAK425
Date(TOS)	02-Mar-17(0.53)	97-Feb-13(3.48)	07-Jun-16(1.32)	97-Apr-14(3.19)
Flux calibrators	3C 48	3C 48, 3C 286	3C 48	3C 48, 3C 286
		– 3C 465 –		
Project ID	12A-195	12A-195	AH0717	TOSR0001
Date(TOS)	12-Oct-31(1.2)	12-May-28(1.2)	01-Jan-15(13.36)	11-Mar-24(5.48)
Flux calibrators	3C 48	3C 48	3C 48, 3C 286	3C 48
		– 3C 264 –		
Project ID	AL0491	AC0135	AP0439	AP0439
Date(TOS)	99-Sep-06(3.42)	85-May-10(2.84)	03-Aug-23(39.67)	02-Jun-23(40.97)
Flux calibrators	3C 138, 3C 147	3C 286	3C 286	3C 286
		– 3C 296 –		
Project ID	AP0418	AL0146	AL0637	AL0637
Date(TOS)	00-Dec-08(5.62)	87-Nov-25(5.83)	04-Dec-12(107.25)	05-Apr-21(195.22)
Flux calibrators	3C 286	3C 286	3C 286	3C 286
		– 3C 274 –		
Project ID	VB0100	AD0305	AO0088	AO0088
Date(TOS)	90-Mar-19(32.07)	93-Mar-14(17.02)	90-Apr-24(40.64)	90-Sep-14(22.59)
Flux calibrators	3C 84, 3C 286	3C 84	3C 286	3C 286

Notes: $*$ denote the VLA observing configuration. TOS is the on-source integration time in kiloseconds (scaled to an array with all 27 antennas operational).

Table 3.4: Summary of HST observations

Source	Instruments	Obs. ID	Filters	Date	T (sec)
(1)	(2)	(3)	(4)	(5)	(6)
3C 83.1B	WFPC2	U2S0150.....	F637N, F702W	1995-Oct-22	600
3C 264	WFPC2, WFC3	U2E67UO1T	F606W, F475W	1995-Apr-16	500
3C 465	WFPC2	U4494W0.....	F555W, F702W	1999-Jan-23	600
3C 296	ACS, WFPC2	J8DA070.....	F606W	2002-Jul-10	2346
3C 371	WFPC2, STIS	U6DK030.....	F555W, MIRVIS	2001-Jun-23	3640
3C 274	WFPC2	U3BE040.....	F450W, F606W	1998-Feb-25	520

Notes: Where data from more than one instrument or filter have been retrieved, we report observational details of the first instrument/filter only. Col. (1), (2), (3), (4) and (5) are self explanatory; Col. (6) – total integration times in seconds.

Table 3.5: Log of NICMOS observations

Source	Obs. ID	Obs. Date	Filter	t_{exp} (sec)
(1)	(2)	(3)	(4)	(5)
3C 83.1B	N90J19010	2005-Mar-12	F160W	1151.836
3C 264	N4OY02040	1998-May-12	F160W	447.722
3C 465	N90J97010	2004-Sep-28	F160W	1151.836
3C 296	N90J57010	2006-Apr-21	F160W	1151.836
3C 371	N90J75010	2005-Jan-29	F160W	1151.836
3C 274	N4K502020	1998-Feb-26	F160W	767.900

Notes: Columns (1), (2), (3) and (4) are self explanatory; Column (5) – total exposure times in seconds.

Table 3.6: Summary of Chandra observations

Source	Instrument	Obs. ID	Obs. Date	t_{exp} (ks)	Evt Counts	Data Mode
(1)	(2)	(3)	(4)	(5)	(6)	(7)
3C 83.1B	ACIS-S	3237	2003-Mar-15	93.89	632034	VFAINT
3C 264	ACIS-S	4916	2004-Jan-24	34.76	35210	FAINT
3C 465	ACIS-S	4816	2004-Aug-31	49.53	498072	VFAINT
3C 296	ACIS-S	3968	2003-Aug-31	49.43	322197	VFAINT
3C 371	ACIS-S	2959	2002-Aug-05	37.06	42317	FAINT
3C 274	ACIS-S	2707	2002-Jul-06	98.66	6370753	FAINT

Notes: Columns (1), (2), (3), (4), (6) and (7) are self explanatory; Column (5) – total exposure times in kiloseconds.

3.2.2 Radio data

The Common Astronomy Software Application (CASA) package was employed as the primary tool for calibration and imaging of the *e*-MERLIN and VLA datasets. A key limitation to dynamic range in synthesis imaging is the well documented – calibration of the instrumental gains – the so called *calibration errors*. Traditional array calibration methods for observations of well-characterised calibration sources have been shown to achieve calibration precision at GHz frequencies of a few percent in amplitude and about 10 degrees of phase (Braun, 2013) – with such gain calibration precision only sufficient to achieve an image dynamic range of $\lesssim$ 1000:1 in full track observations with existing arrays. The required dynamic range in our sample is 4×10^4–4×10^5; and to achieve this, especially at low-frequency (MHz) observations, we have made use of more advanced algorithms, including `PREFACTOR` (Shimwell et al., 2017), `DDFacet` (e.g. Shimwell et al. 2019) and the `LOFAR` $-$ `VLBI pipeline`[10] for the LOFAR data analysis. We emphasize here that other astronomy software applications such as AIPS, DIFMAP and MIRIAD were also employed to further explore the *e*-MERLIN and LOFAR datasets in particular – to gain additional insights into the customary challenges associated with the calibration and imaging of radio data from these two instruments.

Radio data reduction is not an arbitrary process but rather methodical in operation and guided

[10]The LOFAR-VLBI pipeline is a calibration and imaging pipeline which includes all of LOFAR's international stations. The pipeline looks and solves for delays using an in-field calibrator within the FoV of the pointing. See `https://lofar-vlbi.readthedocs.io/en/latest/` for full documentation.

by a distinct philosophy. Against this backdrop and for simplicity, we present here a more general description rather than dataset specifics of the data reduction strategy employed in the present study as implemented in CASA.

a) The calibration process as implemented in CASA

1. Post Correlation RFI Treatment: At L-band ($\sim$ 1.2–1.8 GHz) for example, observations of extra-terrestrial radio sources are considerably affected (usually, $<$20–25%) by radio emissions from GPS, satellites, etc. also emitting at similar frequencies and we need to adequately remove these interfering signals from the actual "true" observations. This is essential for obtaining reasonable calibration solutions during the calibration process – which in turn has direct consequences for image fidelity in the deconvolution stage. Our mitigation strategy for post correlation RFI was executed through the `AOFlagger` algorithm – an automated reduction and RFI-mitigation strategy employing the SumThreshold methodology (see Offringa et al. 2010a for review). Although a daunting task and computationally expensive, we have in addition, manually inspected and flagged bad data from individual IFs, Channels, Baselines and Stokes Parameters (Polarizations) for the individidual observations to further improve our calibration solutions. Approximately 10%, 30% and 12% of the datasets were flagged from the visibilities at $\sim$ 150 MHz, 1.5 GHz and 8.5 GHz respectively.
2. Data Examination and Flagging [tasks: `listobs`, `plotants`, `plotms`, `plotcal`, `flagdata`]: With task `listobs`, we begin by first inspecting basic information on the observing run such as, listing of individual scans, integration time, the frequency setup, channels, source list, spectral windows, etc. Even after executing the automated RFI flagger on the visibilities, the initial stages of data reduction involves examining the data sets and removing any remaining bad data which could originate in a number of factors ranging from bad weather conditions to inaccurate determination of antenna baseline positions during the observation. These bad data were flagged and the visibilities re-examined for absence of major anomalies before calibration. Also, a suitable "reference antenna" is identified at this stage for calibration purposes. Note that the list of tasks specified here were used essentially throughout the calibration process for checking calibration solutions and where necessary removing remaining bad data from the visibilities.
3. A Prior Antenna Position Correction [task: `gencal`]: Since the visibilities are a function of u-v distance, any incorrect baseline position will result in incorrect estimation of u and v,

and consequently errors in the final image. Although in practice this step could be executed at a later stage by a baseline-based calibration, the observer log had information on antennas with no good baseline positions, and thus it was useful (with this prior information) to perform this step in order to incorporate any improved baseline positions prior to the actual calibration.

4. Initial Flux Density Scaling [task: `setjy`]: Here a flux density value (model) which is estimated from an analytical formula for the spectrum of the source as a function of frequency is provided for the amplitude calibrator – and at later stages of the calibration process this scaling information will be transferred to the secondary and polarization calibrators. The idea is to assume a known flux density for a primary calibrator source and, by comparison with the observed data for that calibrator, determine the amplitude antenna gains, g_i.
5. Initial Phase Calibration [task: `gaincal`]: This step involves solving for phase variations as a function of time on the calibrator sources. In particular, considerable gain variations between different scans of the bandpass calibrator may arise when scans happen at much different elevations. Unlike amplitudes, variations in phase can result in de-correlation when vector averaging the data to compute the final bandpass solution during the bandpass calibration step and hence this step is necessary.
6. Bandpass Calibration [task: `bandpass`]: Before deriving the actual bandpass solution, we first solve for the so called antenna-based delays with respect to our chosen reference antenna. These delays introduce phase jumps against frequency channel in each spectral window and therefore must be corrected. Once the delay corrections are obtained, we can form the actual complex bandpass, B_i solution to account for any gain variations with frequency in the visibilities. The bandpass is antenna-specific (and polarisation specific too), but derived from parallel-handed signals.
7. Gain Calibration [task: `gaincal`]: Here we derive corrections for the complex antenna gains – i.e., both amplitude, g_i and phase, θ_i. Time variability arising from instrumental imperfections due to environmental effects often causes fluctuations in the antenna gain. These imperfections can be corrected by repeatedly observing a calibrator source (usually a point source) in order to measure the changes in the visibility amplitudes and phases with time. Since the amplitude of the calibrator is expected to be constant with zero phase, any non-zero phase difference between any two antennas must be due to the antennas themselves, and these must be accounted for. These changes are corrected by interpolating over the

target source scans. The strategy here is to first derive appropriate complex gains for the flux density calibrator, and then obtain the complex gains for a position on the sky close to the target using the phase calibrator, and finally derive the complex gains for the polarisation calibrator source as well. The gain amplitudes are typically of the order $\lesssim 10\%$ amplitude differences, whereas the gain phases are derived over ~ 30 seconds phase soultion times for the calibrator source.

8. Polarisation Calibration [task: `polcal`]: There are primarily two steps involved – (a) solving for the instrumental polarisation (frequency-dependent leakage terms) using an unpolarised source and (b) deriving the polarisation position angles relative to a source with known position angle. First we set a model for our polarisation calibrator using task [`setjy`] and subsequently;

   • Solve for cross-hand delays – which may arise due to residual delay offsets between the R and L terms on the reference antenna.

   • Solve for leakage terms – using the unpolarised calibrator source to solve for the instrumental polarisation (leakage solutions), with Q and U Stokes parameters in the model data set to zero.

   • Solve for R-L polarisation angle – using the unpolarised calibrator (whose position angle was set earlier in task [`setjy`]) to obtain an accurate polarisation position angle for the R-L phase.

9. Scaling the Amplitude Gains [task: `fluxscale`]: Here we obtain the true flux density of the secondary calibrator by deriving the system response to the primary (flux) calibrator and assume that the gain amplitudes for individual antennas for the primary calibrator is equal to that of the secondary calibrator.

10. Applying the Calibration [task: `applycal`]: At this stage we have derived all relevant calibration solutions and our job here is to apply these solutions; firstly to each individual calibrator source using the gain solutions derived on that particular calibrator alone to compute the *Corrected Data Column*, and secondly to the actual science target – linearly interpolating the gain solutions from the secondary calibrator.

11. Imaging/Deconvolution [tasks: `clean`, `tclean`]: Here we split off the calibrated science target from the visibilities with suitable channel averaging (to save computational time) using task [`split`]. Recall from Section 1.2 above that the sampled visibilities are simply a Fourier transform of the sky convolved with a sampling function $V(u, v)$, which has absolute value

of zero where no measurement is made or unity if otherwise. The instrument's point-spread-function $B(x, y)$ is then the Fourier transform of the sampling function;

$$B(x, y) = V^*(u, v) \tag{3.1}$$

where $V^*(u, v)$ is a Fourier transform of the u-v coverage. Since the visibilities do not completely sample Fourier space, $B(x, y)$ contains much grating response structure which affects the appearance of the Fourier-transformed image. The task [`tclean`] in CASA eliminates this structure and can be viewed as interpolating the visibilities to the blank regions of the u-v plane. In practice, the Clark (1980) `CLEAN` algorithm for example adopts two cycles (major and minor cycles) to find approximate positions and strengths of the components using only a small area of the dirty beam. The minor cycle involves;

• Selecting a beam area that includes the highest exterior sidelobe of the beam.

• Selecting points from the dirty image if they have an intensity, as a fraction of the image peak, greater than the highest exterior sidelobe of the beam.

• Performing a list-based Högbom (1974) `CLEAN` using the beam area and the selected points of the dirty image.

The major cycle involves transforming the point source model found in the minor cycle via an FFT, multiplied by the weighted sampling function that is the inverse transform of the beam, transformed back and subtracted from the dirty image. Errors introduced in a minor cycle due to beam area approximation are corrected in subsequent minor cycles.

In view of our science goals, we employed Briggs weighting, with reasonable adjustment of the Briggs robustness parameter ($-2 \leq$ *robust* $\leq +2$) to obtain the highest resolution possible without compromise on sensitivity to large scale structures. After obtaining sufficiently good image of our science target from the first round of deconvolution, we embarked on the so called $\texttt{Self} - \texttt{Calibration}$ process which typically involves using the obtained model image of the target to solve for new and improved complex gain values of the visibilities. This new calibration solution is then re-applied to the science target and the deconvolution process repeated. In principle there is no limit on the number of self-calibration iterations – the goal is simply to correct the visibility phases and amplitudes as well as possible to obtain the highest image quality. Thus, one of the stopping criterion for self-calibration is when the image noise no longer decreases significantly after each cycle. A complete guide on deciding when and how to use the self-calibration strategy to improve image fidelity is presented elsewhere (e.g.

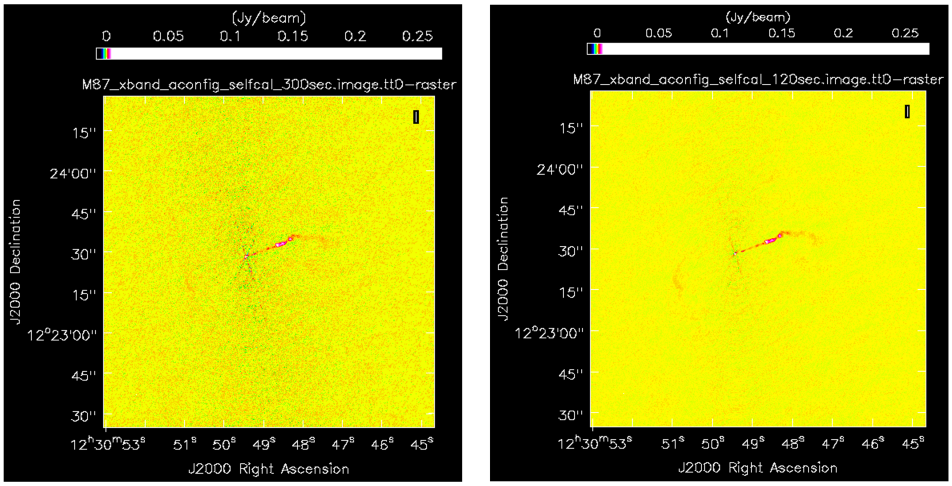

Figure 3.1: An illustration of the usefulness of self-calibration in synthesis imaging in radio astronomy. Both panels show $\sim$ 8.5 GHz VLA maps of M 87 with a total of three self-calibration iterations performed between the two images. The maps are tuned to the same display parameters to show the noise variation across the images. Left panel: image constructed at 300 seconds *phase-only* solution interval; the rms noise at a source free location is 156 μJy. Right panel: image constructed at 120 seconds *phase-only* solution interval; the rms noise at a source free location is 85 μJy. The 4-fold symmetric pattern in the image plane results from the Y configuration of the VLA.

Richards et al. 2022), and we demonstrate in Figure 3.1 the overall usefulness of this step for improving image quality in the present study.

For a comprehensive review of synthesis calibration and imaging using CASA, the reader is referred to the CASA cookbook and documentation webpages hosted by the NRAO at (`https://casa.nrao.edu/`); and for a more detailed review on the broad subject of synthesis imaging in radio astronomy, see Taylor, Carilli & Perley (1999).

b) LOFAR calibration and imaging strategy

The initial steps of the data reduction involved removal of bad data arising from the poor performance of some stations, which causes decorrelation of signals and, especially around 120 MHz, beam-shape deformation effects. This was carried out using the automated observatory New Default PreProcessing Pipeline (NDPPP; Heald et al. 2010), which involved automatic flagging of radio frequency interference (RFI) for each sub-band using the `AOFLAGGER` algorithm as described by Offringa et al. (2010a). The amount of data affected by RFI was typically only a

few per cent and occurred in $\lesssim 8$ stations per observation. In addition, we removed the first and last two channels of each sub-band, due to noise, then averaged the data in time and frequency down to 5 s integration time and 4 channels per sub-band to reduce the data volume for further processing. A visual inspection of the visibilities did not reveal any time-dependent spurious emission from the so called 'A-team' sources: Cassiopeia A, Cygnus A, Taurus A and Virgo A; thus, no *demixing* was required for the datasets in our sample.

1. Part I: Remote station (Dutch) baselines processing

   • *Calibration of the data:* The data calibration involved the use of `ddf − pipeline`. The pipeline performs several iterations of direction-dependent self-calibration on LOFAR continuum observations using KillMS (`kms`; Tasse 2014; Smirnov & Tasse 2015) to calculate the Jones matrices from the visibilities and `DDFacet` (Tasse et al., 2018) to apply these (to the visibilities) during the imaging. The `ddf − pipeline` data processing/calibration strategy has been extensively described elsewhere (see Shimwell et al. 2019). We used the calibrator models and flux densities of 3C 48 (S_{150} = 64 Jy), 3C 196 (S_{150} = 83 Jy), and 3C 295 (S_{150} = 98 Jy) given by Scaife & Heald (2012). Direction-independent (DI) calibration was performed using the `PREFACTOR` pipeline as described by Shimwell et al. (2017); and Direction-dependent (DD) effects (ionosphere and residual clock errors on longer baselines) were solved and corrected for, using the `ddf − pipeline − v2` algorithm as described by Tasse et al. (2021). We corrected the amplitudes of the target visibilities by transferring the derived gain solutions to our science target fields; separately for each sub-band.

   The target visibilities were then self-calibrated in phase only, centred at 150 MHz, using a sky model built from an intial DI and DD self-calibration step. This was done incrementally, using progressively longer baselines (uv distance) to obtain the final (highest) image resolution ($\sim 6''$). We derived the initial phase calibration model from the TGSS catalogue which covers the FOV out to the first null of the station beam; the model contains spectral index information for each source. To maximize the S/N in the target fields, we combined the data into groups of 10 sub-bands each with a bandwidth of $\sim$ 3.5 MHz, while maintaining the 4 channels per sub-band frequency resolution, prior to the initial phase calibration.

   • *Imaging the data*: The first part of the deconvolution involves a series of imaging steps on a set of 60 LOFAR HBA subbands calibrated from Direction-independent effects using `PREFACTOR`. This involves (i) DI initial deconvolution and clustering, followed by (ii) DI calibration and imaging – using the sub-space deconvolution (`ssd`; Tasse et al. 2018)

algorithm which utilises a deconvolution mask automatically generated by `DDFacet` based on a threshold of 15 times the local noise; the mask is re-evaluated at every major cycle throughout the pipeline processing; (iii) Bootstrapping the flux density scale (see Hardcastle et al. 2021) – to both improve accuracy of our flux density estimates and decrease amplitude errors owing to imperfections in the calibration across the bandwidth; (iv) Phase-only DD calibration and imaging – utilising the `ssd` components from the initial DI imaging step to deconvolve deeply with a lowered auto-masking threshold (ten times the local noise); (v) DD calibration and imaging, followed by (vi) DI calibration and imaging – model from the previous cycle is input into `kms` to derive improved DD and DI calibration solutions for each facet and imaged, this time applying both the phase and amplitude calibration solutions.

The second/final part involves using the `ssd` component model produced from the final step of the first part to self-calibrate the entire 240 LOFAR HBA subbands with `kms` and imaged at both low and high resolution in `DDFacet` with the newly derived phase and amplitude solutions applied. The imaging steps follow the same procedure as before, except a much lowered auto-masking threshold (five times the local noise) allows for very much deeper deconvolution than in previous cycles. The steps here include (i) DD calibration; (ii) DI calibration; (iii) DD imaging; (iv) DD calibration; (v) Slow DD calibration; (vi) Final imaging steps; (vii) Facet-based astrometric correction (see Shimwell et al. 2019) – the final images are corrected for astrometric errors in `DDFacet`; from this we selected high-resolution ($\sim 6''$) images not affected by calibration errors for analysis of the kpc-scale jets in our sample (cf. Chapter 4). We selected baselines larger than 0.1 kλ during imaging because when solving for Direction-dependent effects, the extended emission is both difficult to model in the deconvolution step and is seen by only the shortest baselines. Thus, with this inner uv-distance cut along with normalization of the `kms`-estimated Jones matrix we were able to recover the extended emission in our sample which otherwise would be absorbed in the calibration solution on angular scales $\gtrsim$ 30 arcmin. The local rms noise was estimated using a sliding window of 420 arcsec; this suppressed artefacts in the CLEAN components.

2. Part II: International station (Long) baseline processing

   The raw (full) datasets with all international stations were initially preprocessed following standard routine as described above. The LOFAR VLBI processing involves running four parsets – the first two parsets are from the `PREFACTOR` pipeline, and the latter two are from the `LOFAR` − `VLBI` `pipeline` (Jackson et al. 2016; Morabito et al. 2022). For simplicity, I

present a more general description of the steps involved rather than dataset specifics.

• *Pre-Facet-Calibrator:* This involves running the `Pre − Facet − Calibrator.parset` pipeline on the core and remote stations to process the calibrator for direction independent effects. The pipeline can use one calibrator at a time, and so the processing was done separately for the individual calibrators of each observation. The solutions from the pipeline runs were inspected, and for each observation the calibrator with the best solutions was selected for the remainder of the analysis. It is noteworthy here that, for the calibrator 3C 295, the existing component model within `PREFACTOR` although sufficient for studies that only use the core and remote stations, is not suitable for long-baseline analysis. Thus, we have made use of a high-resolution `CLEAN` (Högbom 1974) component model provided by the LOFAR VLBI working group in our analysis. We chose the core station `CS001HBA0` as our reference station. Moderate (typically $\lesssim 30^{\circ}$) phase offsets with respect to this reference station were observed, with the international stations showing the fastest variations with frequency.

• *Pre-Facet-Target:* Here the data are processed through `Pre − Facet − Target.parset` pipeline – this involves flagging the data, removing contributions from bright off-axis sources, and using the *Pre-Facet-Calibrator* solutions to perform phase calibration on the core and remote stations. Following this step, the datasets are ready for international station calibration.

• *Delay-Calibration:* Here, the `Delay − Calibration.parset` pipeline takes the science target and `Pre − Facet` solutions (i.e., the gain solutions from the calibrator pipeline and the phase solutions from the target pipeline) as input. The pipeline automatically determines the best in-field calibrator and phase-shifts the data to the peak component of this position, after applying the `PREFACTOR` calibration solutions. The core station beams are then added coherently to form one single *super* station `ST001`, followed by a phase-only self-calibration of the in-field calibrator against an initial model. The pipeline is optimised to self-calibrate compact calibrators with "simple" structure from the LBCS (see Jackson et al. 2021) and therefore attempts to initialise self-calibration with a point source (Gaussian) model with major and minor FWHM of 0.1 arcsec. We note here that, such a point source model neglects any large-scale structure almost completely and therefore may not suffice for all science cases; a suitable initial model of the whole source can be adopted for improved self-calibration solutions in such instances. All of the calibration solutions are then re-applied to the data.

• *Split-Directions:* This involves running the `Split − Directions.parset` for self-calibration and imaging. The pipeline performs self-calibration using `DIFMAP` which is optimised for VLBI. `DIFMAP` operates on the XX and YY polarisations independently, but the pipeline converts these solutions to an `h5parm`, applies them, and makes a Stokes *I* image from the corrected data using `WSClean`. The final self-calibrated dataset at this point is already corrected for beam effects (including the array factor) and will have TEC-corrected, un-self-calibrated data in the DATA column and TEC + self-cal corrected data in the CORRECTED_DATA column. At this point, the user is free to perform more self-calibration, or re-do the self-calibration, using any tool of their choice. We emphasize here that the challenges/difficulties associated with self-calibration and imaging of LOFAR-VLBI data have prompted us to extensively explore the datasets with other astronomical tools including `AIPS`, `CASA` and `DIFMAP` in addition to the pipeline processing. All our total intensity maps have been produced with the `WSClean` imaging tool which uses both the multiscale clean algorithm (`MSCLEAN`; Cornwell 2008) to improve the diffuse emission fidelity, and multi-frequency synthesis (`MFS`; Rau & Cornwell 2011) to account for spectral variations across the bandwidth.

3.2.3 Data combination and mapping

a) Filling the aperture via array combination

Array combination from different interferometric elements allows for the reconstruction of the true sky brightness distribution of astronomical sources with the combined dataset encompassing the projected baseline spacings of the different arrays thereby providing simultaneous sensitivity and resolution. Although a common practice in radio astronomy, data combination from very different interferometry elements – as is the case in the present study, can be relatively problematic due to fundamental differences in the structure of the visibilities from the different arrays – including differing numbers of intermediate frequencies, frequency channels and channel bandwidths (e.g. Muxlow et al. 2005). In principle, the combination can be achieved via the sky-plane or the u-v plane; and in spite of Muxlow et al. (2005) demonstrating the equivalence of both techniques in reproducing essentially identical images, Biggs & Ivison (2008) observe that combination in the Fourier plane is better able to constrain deconvolution algorithms such as

CLEAN due to the improved u-v coverage in the visibilities making it superior to the sky-plane approach. Against this backdrop, we adopted the Fourier plane combination method in the present work. It is worth mentioning here that the data combination was performed on *e*-MERLIN and VLA datasets at L-band ($\sim$ 1.5 GHz) continuum frequencies.

b) Jet structure reconstruction

To account for differences in the synthesized beam due to differences in baselines, we calibrated and imaged separately the A and B-configurations of the VLA datasets before combining the two configurations with task [concat] into a single dataset. A similar approach was used for the different *e*-MERLIN observing epochs to account for baselines that included the Lovell telescope and the non-Lovell baseline. The resulting datasets from the two interferometry elements were then used to create a complete *e*-MERLIN/VLA dataset at L-band ($\sim$ 1.5 GHz) continuum frequencies for each of our science target, again using task [concat] but this time with appropriate weighting scales for the two array visibilities to account for differences in the weighting schemes for the two arrays. Finding the optimum weighting factor is not a trivial process, and requires both experience and some form of verification by visual inspection. In the present study we varied the weights and formed the dirty beam using CLEAN and/or WSClean to try to find the point where the baselines of the combined dataset were not dominated by that of the VLA. In all cases, we obtained comparable statistical weightings for the two arrays with approximate factor of;

$$\left(\frac{W_{VLA}}{W_{eMLN}} \propto \frac{x}{1}\right), \quad 3 \times 10^{-7} \leq x \leq 2.5 \times 10^{-3} \tag{3.2}$$

This approximation was used to essentially down-weight the VLA data so that its contribution in the combined dataset would be low. This allowed us to reconstruct *total intensity* maps of the jet bases from the combined dataset with a beam size approximately equal to the *e*-MERLIN–only beam ($\sim$ 150 mas) in line with our science goals while retaining information about the more diffuse structure that is represented only in the VLA's visibilities. Deconvolution of the combined *e*-MERLIN/VLA dataset was executed with the Briggs weighting scheme – with Briggs robustness parameter set to -1.5 to give further weighting to the longer baselines contributed by the *e*-MERLIN visibilities.

3.2.4 Optical and Infrared data

The optical data were processed (i.e., flat-fielded, bias-corrected and wavelength calibrated) using STScI's On-The-Fly-Reprocessing (OTFR) pipeline and standard techniques with STSDAS in IRAF – using the best available flat field images and dark count corrections. The pipeline processing software is able to produce calibrated datasets in which minimal further user intervention is necessary. Since our target sample is predominantly located in complicated fields (i.e., rich clusters and groups), we have performed cosmic-ray rejection on the datasets by combining individual exposures at each wavelength to remove the cosmic-ray events – this helped to achieve the best possible dynamic range required for our science goals. To map the optical jets and lobes in our sample, we further performed galactic subtraction on the datasets in IRAF following the procedure described in Perlman et al. (2001). We first masked out the optical jet and lobes as indicated by our GHz frequency radio images. The IRAF task `ELLIPSE` was then used to fit isophotes of the galaxy image, and a model image constructed with task `BMODEL`. The optical synchrotron emission in our sample was derived by subtracting the model image from the original image with task `IMCALC`. We repeated the above procedure several times until the final galaxy-subtracted images did not exhibit any ring-like features. The outputs of each filter were then combined, and the final image rotated to put north at the top and east to the left. We note here that offsets such as core shifts (e.g. Lara et al. 1994) can result in misalignment of the radio-optical reference frames; however, these are of the order 0.1–0.2 mas – about an order of magnitude smaller than the scales of the present study.

3.2.5 X-ray data

Calibration and imaging of the Chandra X-ray data was carried out following standard procedure in NASA's Chandra Interactive Analysis of Observations [`CIAO`][11] software package with the most recent version of the Calibration DataBase [`CALDB`] – version 4.8.5. We first imported the raw data into `CIAO` and reprocessed them by following the "science threads" in `CIAO` version 4.11 to generate new level 2 events files, separately for each observation. Following the automatic procedures[12], the event data were recalibrated. The `dmextract` tool was used to extract light curves in the 0.5 – 7.0 keV energy range from background regions (excluding sources) for inspection, and time intervals affected by flares from soft protons were removed from the

[11] `https://cxc.harvard.edu/ciao/`
[12] `https://cxc.harvard.edu/ciao/threads/createL2/`

data using the `deflare` tool with the `lc_clean` routine. In the case where observations have used detectors with back illuminated chip(s), we extracted light curves for each chip separately and then on all the chips together. Good time intervals [`gti`] for each observation were merged into a single file, which was then applied to the original event file using the `dmcopy` tool with `@combined.gti` task to create final "clean" event files for analysis.

We present in Appendix A–D, a complete multiwavelength gallery of our multi-frequency, multi-configuration radio (*e*-MERLIN, LOFAR and VLA), optical (HST), infrared (NICMOS) and X-ray (Chandra) images obtained from our observations and analysis in the present work.

3.2.6 Numerical simulations

To test evolutionary models of jet propagation in the dense ICM/IGM, we have acquired the `FLASH`[13] (Magneto-)Hydrodynamics code (Fryxell et al. 2000) and with this, we attempt to model the jet kinematics by performing numerical MHD simulations that include particle acceleration and synchrotron losses, and from conservation-law analysis with external pressure and density profiles from the X-ray data. The `FLASH` code is a Eulerian finite-volume, Godunov-based numerical code that utilizes parallel adaptive mesh refinement (AMR). If one assumes that the flow dynamics of AGN jets are governed by thermal plasma rather than the jet magnetic fields, and neglect relativistic effects; then the evolution of the jet flow can be described by the time-dependent non-relativistic Euler equations. `FLASH` solves the Euler equations in conservation form. In Cartesian geometry, the mass density ρ, momentum $\vec{v}$, and energy E conservation equations can be expressed by the Euler equations as;

$$\frac{\partial \rho}{\partial t} + \nabla . \left(\rho \vec{v}\right) = 0 \,, \tag{3.3}$$

$$\frac{\partial \rho \vec{v}}{\partial t} + \nabla . \left(\rho \vec{v} \vec{v}\right) + \nabla P = \rho \vec{g} \,, \tag{3.4}$$

$$\frac{\partial E}{\partial t} + \nabla . \left[\left(E + P\right) \vec{v}\right] = \rho \vec{v} . \vec{g} \,, \tag{3.5}$$

where P is the gas pressure and $\vec{g} = -\nabla \Phi$ is the gravitational acceleration, which can be derived from an external gravitational potential Φ. The total energy per unit volume is defined by

[13]FLASH is a publicly available and extensively tested Eulerian parallel code developed at the University of Chicago; `http://flash.uchicago.edu/site/flashcode/`

$E = \rho\left(\epsilon + (1/2)v^2\right)$, where ϵ is the internal energy density. Equation 3.5 neglects energy loss terms from radiative cooling, and the set of Equations 3.3–3.5 is closed by using the ideal gas equation of state;

$$P = (\gamma - 1)\,\rho\epsilon\,, \tag{3.6}$$

where γ is the adiabatic index.

Here, we conduct a 2-D/3-D axisymmetric simulation of the remarkable kpc-scale flow in 3C 83.1B (cf. Section 4.2.1), to investigate the large-scale flow dynamics of this system. We have chosen to model the outer structures of this particular source for two reasons – (1) our LOFAR HBA observations of this galaxy reveal kpc-scale features of the radio morphology never seen before in this detail which are not fully understood, and thus require further investigation, and (2) the inner jets of this source have been well modelled in previous studies (e.g. O'Dea & Owen 1987; Pfrommer & Jones 2011) and the generic behaviour is pretty well known.

To progress, we have chosen physical parameters of our jet system to match those derived for 3C 83.1B based on our radio (LOFAR HBA; present study), and X-ray (Chandra; Fabian et al. 2006) observations. Detailed analysis and interpretation of results from the numerical simulations will be published elsewhere (Bempong-Manful et al., in prep).

4

LOFAR HBA observations of the kpc-scale jets

We present here a first look at the kpc-scale jets obtained from LOFAR HBA direction-dependent calibrated total intensity and spectral images (Figures 4.1–4.5) and observed parameters (Table 4.2) in order of increasing right ascension, and use these to determine the source morphological properties in our sample being exhibited further out into the envelopes of the radio emission than has been possible before. Our radio images provide the highest sensitivity, and resolution maps to date for the sources in our sample at low frequencies. The dynamic range (defined as peak surface brightness $S_{\rm pk}$ to the rms off source, $\sigma_{\rm rms}$) varies from 10^4:1 to better than 10^5:1.

4.1 LOFAR HBA data analysis

4.1.1 Component fitting

Due to the complex morphology exhibited in our sample on the plane of the sky, we have carefully computed flux densities of all the components in our sample by constructing polygonal regions that trace the likely trajectory of the radio plasma and extracted flux densities of the regions of interest using the CASA tasks `IMFIT` and `IMSTAT` for the compact components and large tails respectively. The flux density uncertainties result from the fitting procedure, and flux calibration due to inaccuracies in the existing LOFAR beam models. The uncertainties are added in quadrature to a 5 per cent flux density bootstrapping uncertainty for LOFAR data (Hardcastle et al., 2021). For three sources in our sample (3C 83.1B, 3C 264 and 3C 465) which show the

most complex extended diffuse structure, we find our estimates for the integrated flux density to be of the order of $\sim$ 13–40% higher when compared with the flux density values of LRL. This is after we have applied the correction factor 1.09 (Laing & Peacock, 1980) needed to bring the LRL flux densities on to the absolute scale of Baars et al. (1977).

3C 83.1B was partially resolved in the revised 3C survey and so its flux density at 178 MHz which have been determined by interpolation or extrapolation in the LRL sample could well have been underestimated. The 178 MHz flux densities of 3C 264 and 3C 465 in the LRL sample were taken from the revised 3C catalogue of Bennett (1962); where the angular diameters of extended sources were unresolved from the total power observations, with an E-W beam width of $13'.6$, then 469λ interferometer observations were used (Laing, Riley & Longair 1983) and the results interpreted in terms of a Gaussian brightness distribution. However, such measurements were still found to be partially resolved and so flux densities from the 2200λ spacing of the Jodrell Bank interferometer were adopted. A general consequence of such high resolution system is that some extended sources were either not observed, or observed as having reduced flux density. Thus, we argue here that our flux measurements are probably better estimates given the unrivalled sensitivity and resolution in our LOFAR HBA ($\sim$ 144 MHz) observations. We report the integrated flux density values and associated uncertainties in Table 4.1.

4.1.2 Radio spectra

As a supplementary analysis, we have estimated the in-band radio spectra in our sample. This allows us to compare and contrast the observed metre wave spectrum in our sample with the cm-wave spectral index. We first split the LOFAR band into three separate subbands – each with a width of 16 MHz, in order to create an in-band spectral index image using a `python` code that fits power laws to pixels in each map. Since the spectra are flux density dependent, we initially performed a "quality" check on our data to test validity of the correction factors applied to the flux densities for the individual subbands – by directly comparing with NVSS, since it is the most suitable high-frequency survey which is sensitive to the large-scale structures in our sample. We matched our sample with NVSS using a 30 arcsec match radius, and determined the NVSS flux density for each source by extrapolating the flux densities from NVSS to LOFAR frequencies. This step allows for accurate measure of the flux scale between NVSS and LOFAR – to better constrain the intrinsic spectral index distribution in our sample (see Hardcastle et al. (2016) for detailed flux scale tests). The extrapolated median flux ratio of LOFAR/NVSS revealed

marginal flux offsets of $\lesssim 10\%$. The individual subbands were then scaled by multiplying the corresponding image by a `reference_factor` parameter which makes use of the median flux scale ratio between LOFAR and NVSS. To derive the spectra in our sample, we fitted power laws in frequency to the total flux densities for each source in the corresponding *scaled* subband images. Background noise was estimated across the images using a circle of radius 60 arcsec.

At 150 MHz the LOFAR HBA band is narrow ($\sim$ 48 MHz), and thus, our in-band spectra are likely to be biased by a few per cent owing to an imperfect HBA beam model – due to sensitivity to even the slightest calibration errors. To ensure that our calculations are robust, we require that the difference across the band is at least 3 $\times$ the off-source noise level, and thus, removed all spectral index values for pixels with a flux density below this threshold. As a sanity check, we have evaluated the spectra for known point sources in our field of view and we find this to be *statistically* consistent with the radio spectra reported in the literature. We also find the in-band metre wave spectral index values for the detected components in our sample to be within ± 5 % of the 2-point radio spectral index at high frequencies – indicating that our results are robust. We report the median spectral indices in Table 4.2 along with derived physical quantities and the corresponding maps showing the metre-wave spectral index distribution in Figures 4.1–4.5.

4.1.3 Physical parameters

In Table 4.2, we present a first order approximation of the synchrotron lifetime (for the electrons radiating in the LOFAR band at $\sim$ 150 MHz) of relativistic particles derived from minimum-energy assumptions along with some physical parameters for all the sources that can be derived from spectral data. We also provide estimates of the physical parameters for the bright and faint parts of the tail of 3C 83.1B separately, although these are crude estimates due to the complex geometry of the source.

We used the 144 MHz flux densities (Table 4.1), and assumed – i) a filling factor of unity for the emitting regions, ii) cylindrical geometry in our calculation of the volumes in our sample, iii) equal energies in relativistic electrons and heavy particles, and iv) the electron population to be bounded by low- and high-energy cut-offs ($10 \leq \Gamma \leq 10^9$) in our estimate of the physical parameters. In order not to underestimate the physical quantities in our sample, we have adopted an injection index $\alpha_{\rm inj} = -0.6$; except the complex tail in 3C 83.1B where we have assumed a slightly flatter index $\alpha_{\rm inj} = -0.55$, and steeper index $\alpha_{\rm inj} = -1.10$ for the bright and faint parts respectively. Using equation (57) in Worrall & Birkinshaw (2006) (cf. Section 5.6) which

is an analytical treatment of the minimum energy condition, we derive equipartition magnetic field strength in our sample and use these to calculate radiation lifetimes of the electrons from synchrotron and inverse-Compton losses as:

$$\tau_{\rm syn} = \frac{1.6 \times 10^{4}\ B^{0.5}}{(U_{\rm B}\ +\ U_{\rm CMB})}\ [(\nu_{\rm br}\,(1+z)]^{-0.5}\ \ {\rm yr}\,, \tag{4.1}$$

where B (in Tesla) is the magnetic field strength, $U_{\rm B}$ (J m^{-3}) is the energy density in the magnetic field, $U_{\rm CMB}$ = 4.2$\times$10^{-14} $(1+z)^4$ J m^{-3} is the equivalent energy density of the cosmic microwave background radiation at redshift z, and $\nu_{\rm br}$ is expressed in units of Hz.

4.2 Kiloparsec scale jet properties

4.2.1 3C 83.1B

Our high dynamic range LOFAR observation of this source (Figure 4.1) shows an extension of the radio structure to the NW and reveals an intricate web of filamentary structures across the entire tail of 3C 83.1B. Two distinct morphologies are exhibited by the source on the plane of the sky in our radio maps; (1) a bright part that curves towards the NW and (2) a faint part that has a more constant surface brightness distribution towards the east. At the tail end of the bright part, a tight loop arising from interaction of the radio plasma (plausibly in rough pressure balance) with the surrounding medium can be seen to the west. The very large scale structure seen to the east of the tail – which has an almost shell-like appearance, is particularly striking. This is an important observation because it suggests a longer period of activity, and a larger source volume, than previous images, indicating that more energy (by a factor of a few) must have been supplied by the radio source than given in previous estimates – compare our derived quantities (Table 4.2) with those of Sijbring & de Bruyn (1998). We obtain radiative ages of 290 and 280 Myr for the bright and faint parts – this is about a factor 3 higher than values reported by Sijbring & de Bruyn (1998) and suggests that the low surface brightness extension of the tail must have formed during the very early stages of the radio source evolution. The total energy supplied by the faint part to the ICM is about an order of magnitude higher compared with the bright part. Zhang et al. (2020) have reported high ambient pressure ($> 1.6 \times 10^{-13}$ Pa) at about 1 Mpc from the centre of the Perseus cluster. Comparing this with our estimates ($U_{\rm min}$ = 0.047 pJ m^{-3}) for the internal energy density in 3C 83.1B would suggest that, a considerable fraction of the

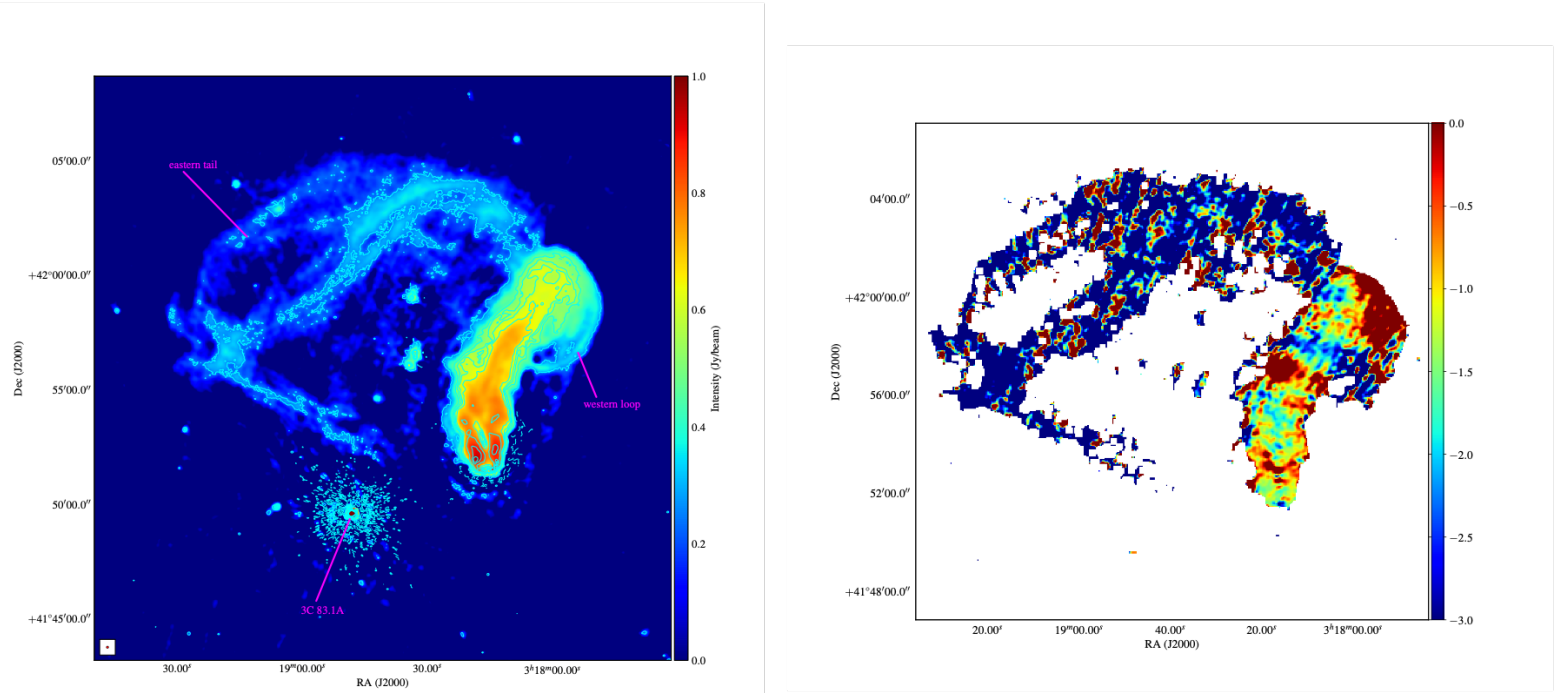

Figure 4.1: Left: Full synthesis image of the radio galaxy 3C 83.1B constructed at 144 MHz with a beam size of $6''$; the peak surface brightness is 3565 mJy beam^{-1}, the rms noise at a source-free location is 80 μJy beam^{-1}, and the contour levels are $1.0 \times (-10, -5, -1, 1, 5, 10, 15)$ mJy beam^{-1}. The small filaments near the compact component (3C 83.1A) south-east of NGC 1265 are instrumental artifacts. The red solid circle in the lower left hand corner indicates the FWHM of the beam. Right: False-colour plot of in-band radio spectral index showing the metre wave spectral index distribution in 3C 83.1B. The map is constructed at a resolution of 6–arcsec FWHM and at 3σ rms noise cut-off in total intensity.

large-scale total energy content in the Perseus cluster is contributed by NGC 1265, consistent with a type-cD galaxy.

At 6 arcsec resolution the compact core is not visible in our radio maps; it could well be affected by self-absorption. Following the formalism of McKean et al. (2016), we used the 144 MHz flux density to determine at which frequency the synchrotron spectrum of the core would be expected to peak. We find the peak frequency to be as high as $\sim$ 9 GHz. The inferred magnetic field strength ($\sim$ 15 μG) at this frequency is about 80 per cent higher than our estimate from minimum energy assumptions (i.e. $\sim$ 3 μG). We measure a total flux density of 45.4 Jy; this is $\sim$ 40 per cent higher compared with measurements reported by Laing, Riley & Longair (1983) at 178 MHz. The metre wave radio spectrum of 3C 83.1B seems to be rather steep. The overall spectrum is also rather steep, $\alpha = -1.2$ (Figure 4.1). This implies that radiative losses dominate in this source, and the break frequency is lower than our observed frequency ($<$ 150 MHz). To put stronger limit on any spectral break, we have made use of literature data at 38 and 74 MHz from NED; we find the spectral shape to steepen at lower frequencies with an index of $\alpha_{38}^{78} = -2.55 \pm 0.99$ and $\alpha_{78}^{144} = -1.23 \pm 0.05$ above a certain spectral break likely occurring below 38 MHz. This puts a lower limit on the source age ($\gtrsim$ 1 Gyr) if the electrons are assumed to have been in the same volume and magnetic field over their lifetimes. In the magnetic field we estimated, this would raise radiative lifetimes by a factor of about two for the lowest-frequency electrons. Our derived metre-wave spectral index, $\alpha = -1.17$ is about 15 per cent higher compared with the integrated spectral index between 49 and 92 cm reported by Sijbring & de Bruyn (1998). Overall, our radio images of this galaxy shows features including some tight loops never seen before in this detail which are not fully understood, and thus require further investigation. Higher resolution spectral and polarimetric (expecting the loop to be magnetic in origin) studies would be particularly useful to see if there exist substructure, and to check whether or not the spectrum is flatter than other regions if this is a locally shocked region, or simply an absorption feature arising from a foreground free-free absorber.

4.2.2 3C 264

Our radio image (Figure 4.2) shows a head-tailed morphology of 3C 264 with a prominent core and a roughly *S*-shaped wiggling trail extending in the direction northeast that terminates in a plume-like feature at 16.5 arcmin and 430 kpc (projected) from the core. A close look at our radio map reveals five distinctive bends (B1–B5) downstream of the core. The first bend occurs

at a projected distance of 33 kpc from the core – here the twin-jet morphology is distinct and parallel, with the NNE jet showing enhanced surface brightness compared with the NE jet. The second bend in the direction NE occurs at 112 kpc – here, the two jets still look distinct, but appear to flow into each other (or superimposed on one another) with downstream distance. At projected distances of 181 kpc and 251 kpc the third and fourth bends in the direction N and NE respectively are evident; at this point the two jets can no longer be distinguished. The final bend in the direction northward occurs at a projected distance of 351 kpc and the trail continues in this direction until the eventual termination of the jet – there is mild evidence for a backflow at the termination point indicating that the jet must have impacted a higher density medium. This complex kpc-scale morphology exhibited on the plane of the sky by 3C 264 suggests that the plume is injected by the jets, encounters the ram pressure of the external medium that bends it back, decelerates (via drag forces and entrainment), and then moves buoyantly. The kpc-scale radio morphology of 3C 264 closely resemble that of the narrow-angle-tail type (as seen in our radio maps), but as shown in high resolution imaging (e.g. Lara et al. 2004), the morphology is of a WAT on the smallest scales. The rather striking observation here is the compact bright feature (or possibly merger of features) in the jets, C2 in the inner 120 arcsec of 3C 264. At a separation of 12 kpc, this steeper-spectrum feature at the bend in the main jet from the core at C1, must lie well outside the prominent dusty region reported by Baum et al. (1997) of the 3C 264 system. Such a blob of radio emission could be interpreted as the signature of shocks arising from interactions between magnetised plasma in the moving jet and the ambient medium (e.g. Bicknell & Begelman 1996).

At 150 MHz and 6-arcsec resolution, there is no evidence of the counterjet in our radio maps. Moderate variability (~ 20 % increase) from 2016 to 2018 of the radio core at 15 GHz has been reported by Boccardi et al. (2019). Our estimate of 0.93 Jy for the core flux density is about a factor 5 higher compared with the core flux density reported by Lara et al. (2004) at 1.6 GHz using the VLA; and we find our estimates for the total flux density to be about 20 per cent higher compared with measurements at 178 MHz (see Table 4.1). The metre wave spectrum, displayed in Figure 4.2 shows slight variations around a mean value of -0.80, and provides marginal indications for a low-frequency steepening in the outer tails. Comparison with the broad band radio spectral index, $\alpha_{\rm r} = -0.58$ at higher frequencies (e.g. Lara et al. 2004) shows the presence of older plasma in the more diffuse parts of the source.

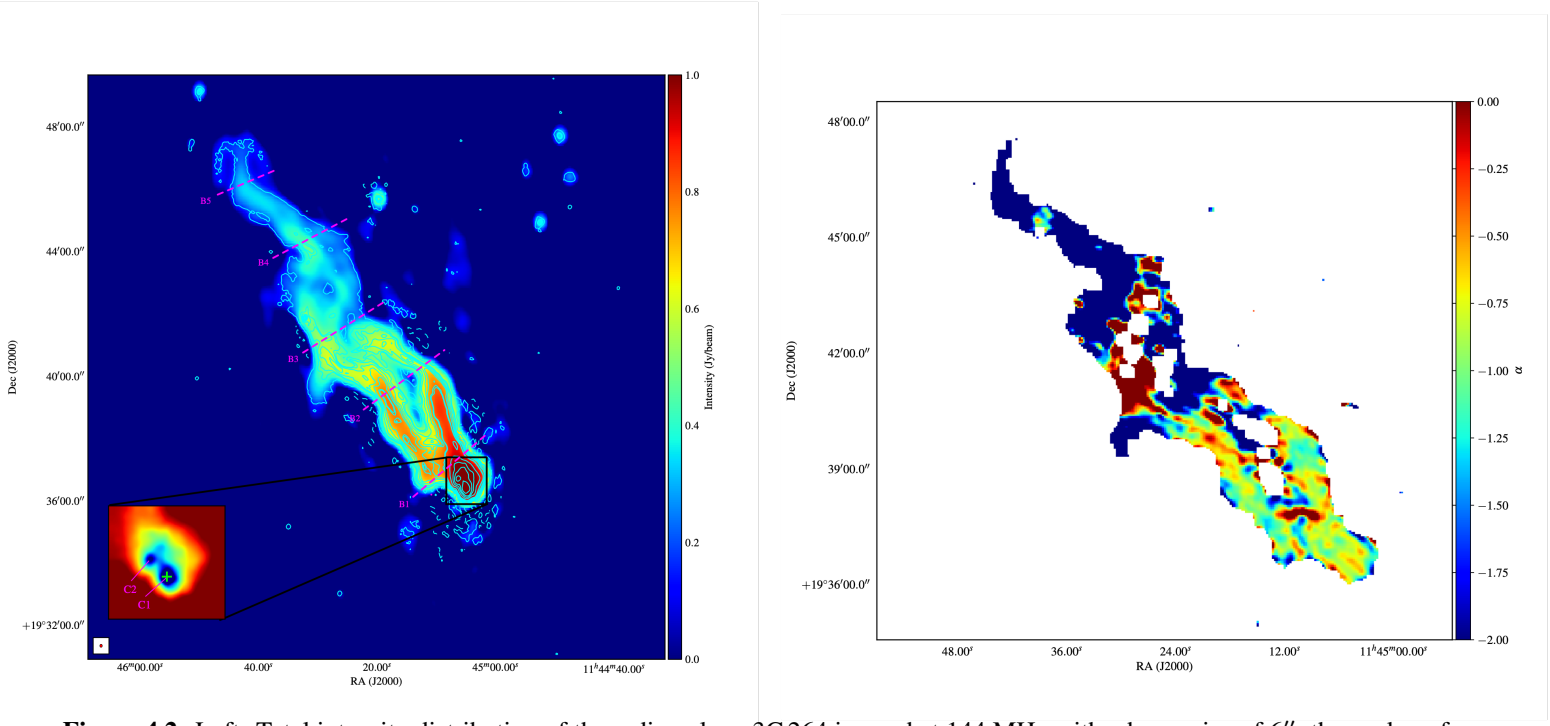

Figure 4.2: Left: Total intensity distribution of the radio galaxy 3C 264 imaged at 144 MHz with a beam size of 6″; the peak surface brightness is 725 mJy beam^{-1}, the rms noise at a source-free location is 86 μJy beam^{-1}, and the contour levels are 1.0 $\times$ ($-$15, $-$10, $-$5, $-$1, 1, 5, 10, 15, 20, 30) mJy beam^{-1}. The CLEAN beam FWHM is shown as a red solid circle in the lower left hand corner. The broken magenta lines (B1–B5) represent distinctive kpc-scale bends downstream the jet trajectory. Insert: the inner 120″ ($\sim$ 52 kpc) of 3C 264 showing the radio core, C1 and a compact bright feature (blob) in the jet, C2 which has integrated flux density of 0.28 Jy. The green cross symbol indicates the position of the VLA C-band core from Lara et al. (2004). Right: In-band metre wave spectral index distribution in 3C 264.

4.2.3 3C 296

Our image of this source (Figure 4.3) shows an elongation of the radio morphology in the direction NE-SW. The radio jets are antiparallel, symmetric about a compact core, and flow into well-defined outer boundaries (lobes). The lobe materials show extension towards the east, and this is particularly the case in the NE lobe. As noted by Laing et al. (2006) it is plausible that the jets propagate (almost) entirely within the lobes. Laing et al. (2006) further report morphological differences between brightness distributions (substructure) in the main and counter-jets and interpret this as an effect of relativistic aberration. The rather striking observation here is the confinement of the radio structures. Based on well accepted conclusions from observations (e.g. Ledlow & Owen 1996) and theory (e.g. Bicknell 1995), if low-luminosity radio sources must reside predominantly in rich clusters, then 3C 296 is one of the few exceptions as the radio structure suggests it lies in a low density environment or poor group. This assertion is reasonably supported by the work of Miller et al. (2002) in their systematic study of radio-selected poor clusters which concluded that 3C 296 exists in a "poor" group of 21 members with velocity dispersion of 428 km/s.

The core flux density remains constant over a broad frequency range whereas the total flux density shows a gradual increase towards lower frequencies (see Table 4.1) with our estimate of 15.18 Jy for the total flux density $\sim$ 17 per cent higher compared with measurements at 178 MHz. The metre wave spectral index distribution (Figure 4.3) confirms synchrotron radio emission with a mean value of -0.71 and provide evidence for marginal steepening at the tail end of the NE lobes. Also, the spectrum appears steeper in the jet region than in the lobes suggesting that more efficient acceleration occurs away from the fastest parts of the flows. Using high frequency VLA observations, Laing et al. (2006) have shown that the sheath of diffuse emission surrounding the flat-spectrum jets has a steeper spectrum. We note that 3C 296 has the lowest signal-to-noise ratio among the sources studied here and there are residual imaging issues to resolve (cf. Figure 4.3).

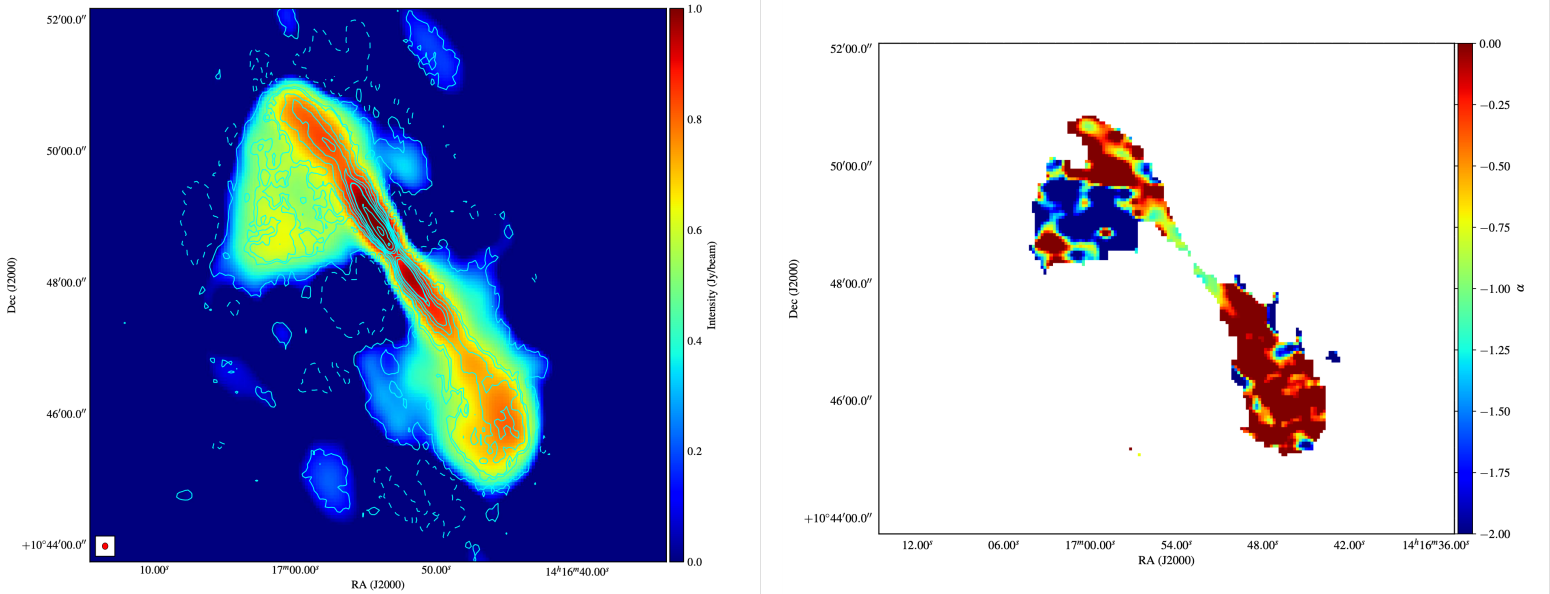

Figure 4.3: Left: Full synthesis image of the radio galaxy 3C 296 made at 144 MHz with a beam size of $6''$; the peak surface brightness is 705 mJy beam^{-1}, the rms noise at a source-free location is 92 μJy beam^{-1}, and the contour levels are 1.0 $\times$ (-15, -10, -5, -1, 1, 5, 10, 15, 20, 30) mJy beam^{-1}. The FWHM of the beam is indicated as a red solid circle in the bottom left hand corner. Right: In-band metre wave spectral index distribution in 3C 296.

4.2.4 3C 371

Our map of this source (Figure 4.4) shows the compact unresolved component with strong emission from the central source, and a large-scale halo component with circular, smooth low surface brightness that extends outwards to 271″ in diameter (measured from west to east). Within the inner 80″ ($\sim$ 85 kpc projected) two diagonal jets reminiscent of those in 3C 296 can easily be seen emanating from the active galactic nucleus in the NE and SW directions – the jets are antiparallel, symmetrically arranged about the compact core and embedded in the diffuse halo component, with the jet presumably pointing towards us (WJ1) showing high surface brightness with a peak flux of 120 mJy beam^{-1} compared with the counterjet, EJ1 (peak; 21 mJy beam^{-1}). There is no sign of a distinct hotspot in our radio maps. The jet and counterjet each have scale lengths of 40″ either side of the compact core – this plausibly suggests a uniform field distibution across the large-scale halo component since field disparity would be expected to cause varying degree of disruption in the jets. Our high dynamic range LOFAR HBA image provides the best radio map of this source to date at low frequencies that reveal for the first time both the jet and counterjet emission in 3C 371 as well as showing the diffuse kpc-scale halo extension out to 285 kpc – this is $\sim$ 22 $\%$ larger compared with the best available physical size estimates for 3C 371 at radio wavelengths (see Drake et al. 2003 and references therein). Based on our observations (i.e., presence of twin jets, and absence of a distinct hotspot), we argue that the morphology of 3C 371 is that of a Fanaroff-Riley class I source, although we do not rule out the possibility of an intermediate source between those of FR Is and FR IIs.

The central component has a flux density of 2.04 Jy and contributes approximately 35 per cent of the source total flux density measured in the present study, and is about a factor 2 higher compared with measurements by Akujor et al. (1994) at 1.6 GHz using MERLIN. The overall metre wave spectrum of 3C 371 is rather flat (Figure 4.4). This implies that the source is "core-dominated", and the break frequency is at our observed wavelength ($\sim$ 150 MHz). We find our calculated metre wave flat spectrum, $\alpha = -0.69$ to be consistent with the broadband (radio to X-ray) spectral indices reported by Sambruna et al. (2007) for the jets in 3C 371.

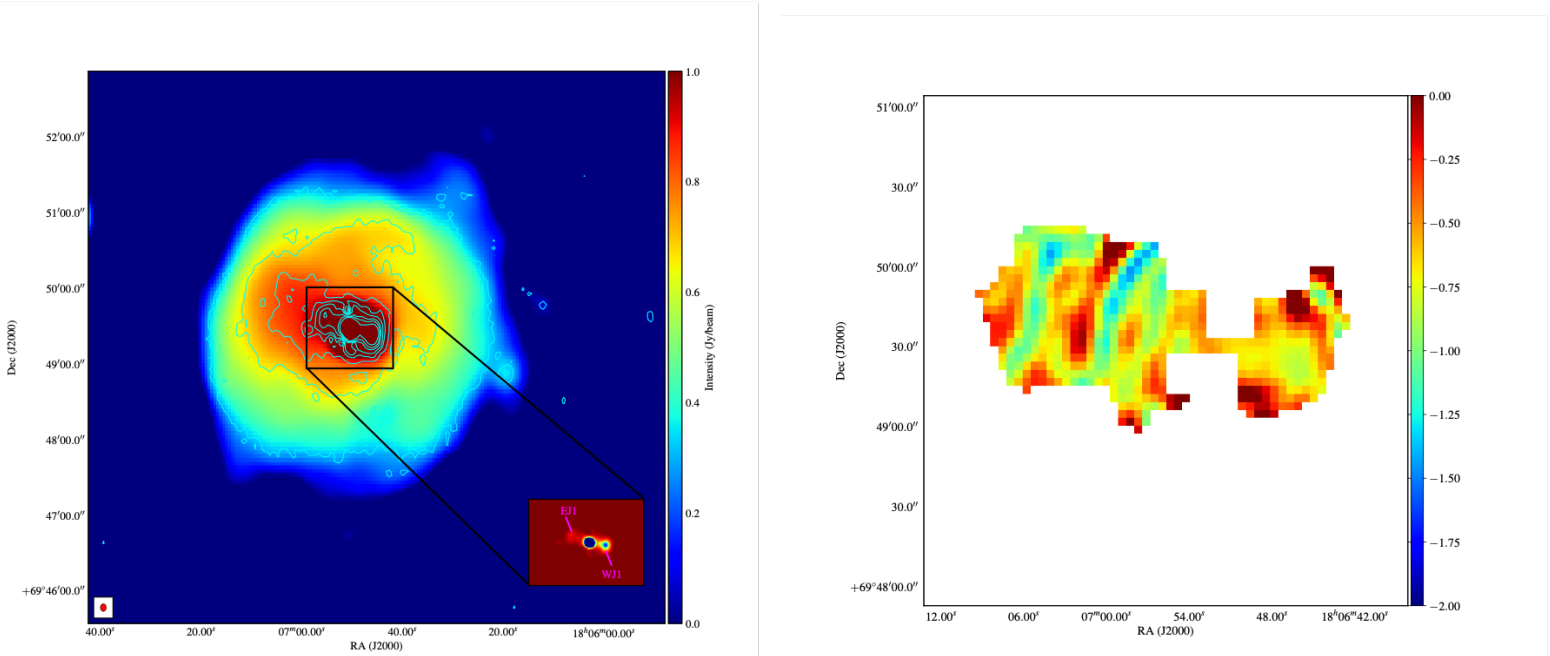

Figure 4.4: Left: Full synthesis image of 3C 371 created at 144 MHz with a beam size of 6″; the peak surface brightness is 1659 mJy beam^{-1}, the rms noise at a source-free location is 75 μJy beam^{-1}, and the contour levels are 0.5 $\times$ ($-$15, $-$10, $-$5, $-$1, 1, 5, 10, 15, 20, 30, 40, 60) mJy beam^{-1}. The CLEAN beam FWHM is shown as a red solid circle in the lower left hand corner. Insert: the inner 80″ ($\sim$ 85 kpc) of 3C 371 showing two jets emanating from the active galactic nucleus in the NE and SW directions – note the asymmetry in brightness distribution between the jet and counterjet emission. Right: In-band metre wave spectral index distribution in 3C 371.

4.2.5 3C 465

The radio map here (Figure 4.5) shows the characteristic U or C-shape morphology exhibited by the WAT class of radio sources – with bent-double radio tails arising from ram pressure due to motion of the host galaxy relative to the cluster. Our map shows an elongation of the radio structure in the NW-SE directions and provides evidence of enhanced surface brightness distribution over almost the entire source. At a projected distance of 170 and 187 kpc in the NW and SE plumes respectively, the change in direction of the radio tails is particularly obvious – both plumes begin to flow towards each other. The NW plume changes direction from west to south-east, and the SE plume from south towards the north-west. The tail ends are separated on angular scale of $63''$ – this corresponds to 38 kpc in linear scale at the redshift of the source. Given this relatively short separation between the lobes and considering the trajectory of the radio plasma, an open question is whether or not it is plausible for the continuous injection of relativistic plasma into the base of the plume materials (see Bempong-Manful et al. 2020) to inflate the lobes and lead to the eventual coalescence of the plumes into a single flow downstream. Our map of this source provides the fullest picture of the large scale-structure of 3C 465. Our estimate of $610''$ for the largest angular size (projected on the sky) about 2 $\%$ higher compared with measurements at 178 MHz from the revised 3C survey reported by Leahy, Bridle & Strom (1996). In Bempong-Manful et al. (2020) we assign the striking asymmetry in physical size and shape of the lobes to 2-D projection effects. An interesting observation here is the $\sim 130''$ unrelated radio trail source (integrated flux = 2.44 Jy; peak surface brightness =15.3 mJy beam^{-1} at P.A. of $126.^{\circ}9$) to the north of 3C 465. We have observed traces of this component in an earlier VLA total intensity map at 1.5 GHz, and for this additional evidence, we cautiously argue that this component is plausibly a low-luminosity radio trail from the nearby elliptical companion NGC 7720A.

At high (GHz) frequencies, the spectrum of 3C 465 steepens with distance from the AGN (e.g. Bempong-Manful et al. 2020). However, the metre wave spectral index distribution (Figure 4.5) suggests a rather flat radio spectrum for 3C 465 with marginal indications for steepening at the tail ends of the plumes. The relatively constant core flux density between 150 MHz and 5 GHz (see Table 4.1) further indicates a flat-spectrum radio source, and is consistent with our observed metre wave spectral distribution. Such spectral behaviour can be interpreted as showing that the relativistic electron energy distribution in the inner (parsec-scale) AGN is *initially* similar to those in the extended ($\sim$ kpc-scale) structures in 3C 465 at low frequencies. Our

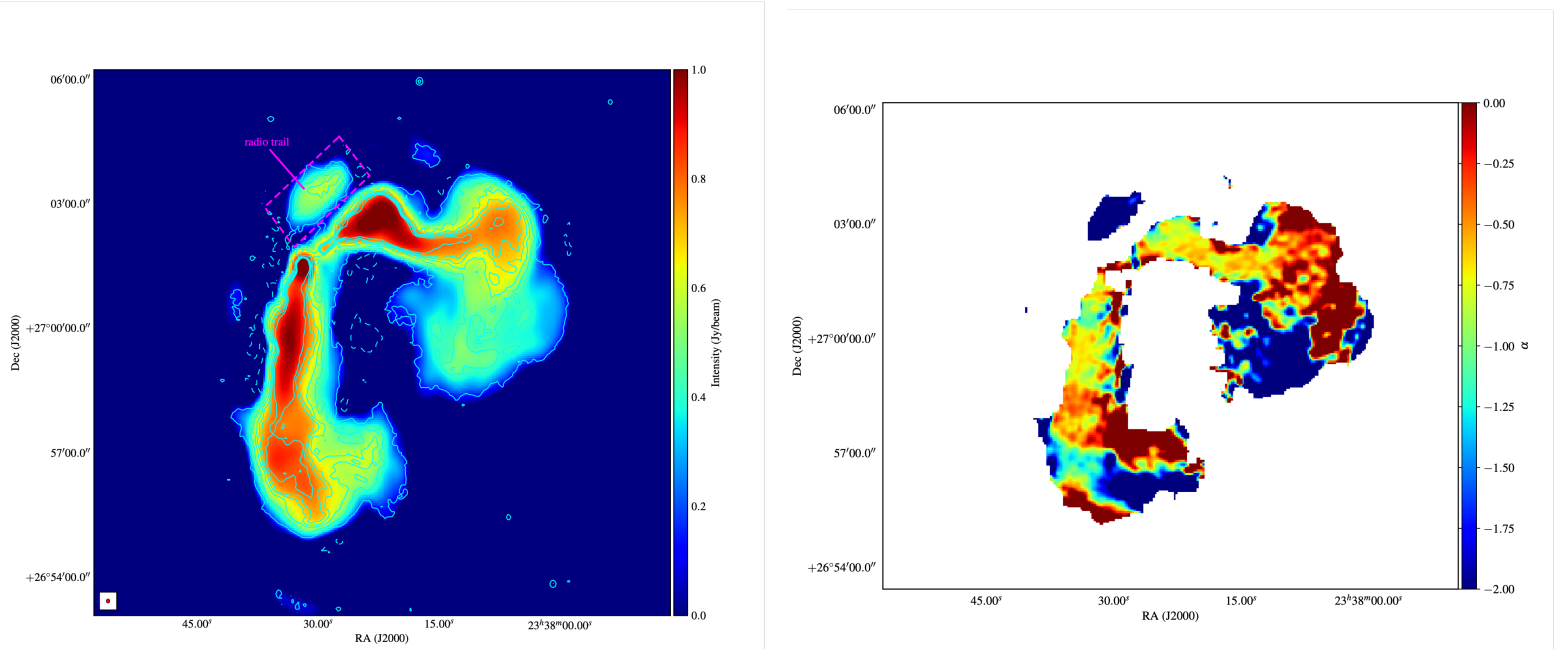

Figure 4.5: Left: Total intensity distribution of the radio galaxy 3C 465 constructed at 144 MHz with a beam size of 6″; the peak surface brightness is 1375 mJy beam^{-1}, the rms noise at a source-free location is 80 μJy beam^{-1}, and the contour levels are 1.0 $\times$ (-15, -10, -5, -1, 1, 5, 10, 15, 20, 30) mJy beam^{-1}. The synthesised beam size is shown in the bottom left hand corner of image. Note the unrelated radio trail source to the north of NGC 7720. Right: In-band metre wave spectral index distribution in 3C 465.

Table 4.1: Archival and measured (integrated) flux densities, S_ν in our sample

	144 MHz*	178 MHz	320 MHz	750 MHz	1450 MHz	5000 MHz
			– 3C 83.1B –			
$S_{\nu,\,\mathrm{core}}$	—	—	—	—	0.25 [b]	0.04
$S_{\nu,\,\mathrm{total}}$	45.45 ± 0.01	26.60	26.47	12.00	8.20	3.53
Ref.	This work	4, 6	11	1, 11	1, 11	1
			– 3C 264 –			
$S_{\nu,\,\mathrm{core}}$	0.93 ± 0.01	—	—	—	0.21	0.17
$S_{\nu,\,\mathrm{total}}$	36.86 ± 0.01	26.00	18.06	9.20	5.80	2.00
Ref.	This work	1, 4, 6	3	1	1, 5, 13	1, 13
			– 3C 296 –			
$S_{\nu,\,\mathrm{core}}$	0.40 ± 0.03	—	—	—	0.40 [b]	0.08
$S_{\nu,\,\mathrm{total}}$	15.18 ± 0.36	13.00	—	5.20	4.30	1.71
Ref.	This work	1, 4, 6	—	1	1, 8, 10	1
			– 3C 371 –			
$S_{\nu,\,\mathrm{core}}$	2.04 ± 0.01	—	—	—	1.22	0.47
$S_{\nu,\,\mathrm{total}}$	5.88 ± 0.01	3.70	4.02 [a]	2.40	2.60	1.74
Ref.	This work	1, 6	WENSS	1	1, 9	1, 7, 12
			– 3C 465 –			
$S_{\nu,\,\mathrm{core}}$	0.24 ± 0.02	—	—	—	0.21	0.27
$S_{\nu,\,\mathrm{total}}$	50.79 ± 0.01	37.80	27.83	13.40	7.70	2.80
Ref.	This work	1, 4, 6	3	1	1, 2, 14	1

Notes: A line indicates that the flux density value is not available in the literature.

REFERENCES – [⋆]This paper; [a](WENSS; Rengelink et al. 1997); [b](NVSS; Condon et al. 1998); (1) Kellermann et al. (1969); (2) Miley & van der Laan (1973); (3) Kuehr et al. (1981); (4) Laing, Riley & Longair (1983); (5) O'Dea & Owen (1985); (6) Spinrad et al. (1985); (7) Wrobel & Lind (1990); (8) Leahy & Perley (1991); (9) Akujor et al. (1994); (10) Hardcastle et al. (1997); (11) Sijbring & de Bruyn (1998); (12) Gómez & Marscher (2000); (13) Lara et al. (2004); (14) Bempong-Manful et al. (2020).

estimate, $\alpha = -0.79$ for the entire source is comparable with the radio spectral index, -0.75 determined between 178 and 408 MHz (see Madrid et al. 2006 and references therein). The low-luminosity trail component has a steep spectrum ($\alpha = -2.12$) as common for radio remnants at low frequencies (e.g. Giacintucci et al. 2007). This suggests the component plasma must have been radiatively cooled due to cutoff in high energy electrons from the host galaxy of the companion, NGC 7720A.

Table 4.2: Measured physical quantities of the kpc-scale jets in our sample

Source name	α	Vol.	$U_{\rm min}$	$P_{\rm min}$	$E_{\rm min}$	$B_{\rm eq}$	$\tau_{\rm rad}$	L_{150}	$D_{\rm L}$	$D_{\rm z}$
		($\rm cm^3$)	(pJ $\rm m^{-3}$)	(pPa)	(J)	(nT)	(Myr)	(W $\rm Hz^{-1}$)	(Mpc)	$''$(kpc)
(1)	(2)	(3)	(4)	(5)	(6)	(7)	(8)	(9)	(10)	(11)
3C 83.1B	-1.17	1.60×10^{71}	0.082	0.027	1.32×10^{52}	0.322	290	9.02×10^{26}	131	1193 (644)
bright part	-0.90	8.91×10^{70}	0.113	0.038	1.01×10^{52}	0.377	290	7.95×10^{26}	131	662 (357)
faint part	-1.80	1.41×10^{72}	0.004	0.001	6.23×10^{51}	0.075	280	1.13×10^{26}	131	1080 (583)
3C 264	-0.80	4.77×10^{70}	0.122	0.041	5.84×10^{51}	0.392	310	3.23×10^{26}	87	988 (431)
3C 296	-0.71	1.94×10^{69}	0.727	0.242	1.41×10^{51}	0.956	270	3.02×10^{26}	131	440 (219)
3C 371	-0.69	1.38×10^{71}	0.057	0.019	7.89×10^{51}	0.268	260	3.21×10^{26}	222	271 (285)
3C 465	-0.79	1.87×10^{70}	0.455	0.152	8.52×10^{51}	0.756	290	10.03×10^{26}	131	610 (367)

Notes: $L_\nu = (1+z)^{\alpha-1} S_\nu 4\pi \rm D_L^2$, assuming isotropic emission. Col.(1) and (3) – is self explanatory; Col.(2) – in-band radio spectral index measured between 120 and 168 MHz; Col.(4), (5) and (6) – minimum energy density, pressure and total energy supplied by the radio source respectively; Col.(7) – equipartion magnetic field; Col.(8) – radiative lifetime of electrons at 144 MHz from synchrotron and inverse-Compton losses; Col.(9), (10) and (11) – the observed $\sim$150 MHz radio luminosities, distances, and largest angular scales and the corresponding linear scales respectively, as measured in the present work. Adopted redshift values are as indicated in Table 2.1.

4.3 Summary

We have presented high-sensitivity and high-resolution LOFAR HBA images of the kpc-scale jets of 5 sources in our sample. These LOFAR HBA images allow us to characterize the source morphological properties with high precision, and draw conclusions on the host galaxies and their environment. We also detect special features such as loops, and report for the first time, the detection of a compact lobe (blob) within the moving jet in the radio galaxy 3C 264. Our derived 150-MHz radio luminosities suggests that the sources studied here lie close to the FR I/FR II luminosity break.

5

The jet bases in 3C 83.1B

In the present chapter, and the next two chapters that follow, I present and discuss results on the *energetics of the jet bases* in our sample derived from high-resolution multifrequency multiwaveband analysis. Hereafter we adopt a cosmology with $\Omega_{\rm m}$ = 0.286, Ω_{Λ} = 0.714, and H_0 = 69.6 km s^{-1} Mpc^{-1} (Spergel et al., 2007), and we define spectral indices, α, in the sense $S \propto \nu^{\alpha}$. At the current best known redshift of 3C 83.1B (z = 0.026), one arcsec is equivalent to a projected length of 0.54 kpc.

We emphasize here that all flux density measurements have been obtained from maps convolved with the same restoring beam size and shape (i.e., a circular Gassian FWHM) using polygonal regions. Where necessary we used polygons slightly wider than regions of *real* emission to reduce sensitivity to any residual misalignments between the maps. Background was taken from the rms errors in total intensity I from circle of radius 10.55 arcsec fixed in position. A key challenge in calibration and synthesis imaging is that, the absolute position information is lost particularly during the phase self-calibration stage as described in Chapter 3. This has the potential to introduce small spatial shifts in the maps. We have therefore performed a pixel alignment procedure (e.g. Harwood, Vernstrom & Stroe 2020) by fitting a Gaussian to the radio core in our multifrequency maps using `CASA`. We used the mean pixel co-ordinates of the core, and shifted and aligned all the maps to this reference position. This step is particularly useful for spectral index and spectral age fitting on resolved scales. From here on, except where otherwise stated, 1.5 GHz map refers to our combined L-band *e*-MERLIN plus VLA map.

5.1 Multiwaveband images

We present here (Figures 5.1–5.7), new high-resolution and high-sensitivity maps of the inner jets in the WAT radio galaxy 3C 83.1B obtained from multi-frequency, multi-configuration radio (*e*-MERLIN, LOFAR and VLA) observations with complementary observations from optical (HST) and X-ray (Chandra). Note the distinct symmetrical radio to X-ray jets in our multiwaveband imaging. We report the properties of the radio maps in Table 5.1.

5.2 Morphology and flux densities

A multi-frequency comparison of the inner jets of 3C 83.1B at radio wavelength is shown in Figure 5.6. This shows the characteristic bent-double radio jets arising from ram pressure due to motion of the host galaxy relative to the cluster as seen in earlier observations. Our radio images reveal a limb-brightened jet which emanates from a compact core. At optical and X-ray wavelengths (Figure 5.7), 3C 83.1B shows two distinct morphologies – our HST image shows a giant elliptical with a central dominant emission and close interaction with the companion galaxy 3C 83.1A; whereas the Chandra map reveals diffuse X-ray gas around the nuclear component along with visible X-ray jets and knots as seen at radio frequencies.

Within the inner 28-arcsec radius, two visible radio knots separated by 2.5 kpc in the eastern jet and a third knot in the west jet which lies at a distance of 3.5 kpc from the core can easily be seen at all three radio observing frequencies. These knots hints at sites of shock signatures between magnetised plasma within the moving jets and the surrounding medium (e.g. Bicknell & Begelman 1996). Using our 0.1-arcsec resolution *e*-MERLIN-only map, we measure a largest angular separation of $55.8''$ ($\sim$ 30 kpc) between the inner bent jets in 3C 83.1B. At a projected distance of 25 kpc from the radio core, the two jets are seen to expand albeit distinguishable, but appear to overlap at $\sim$ 80 kpc. Beyond this point, the radio trail show a single flow downstream the jet trajectory and bends to the northwest. Our multi-frequency observations reveal no evidence of a radio hotspot as common for Type-I radio sources. Our combined 1.5 GHz *e*-MERLIN/VLA map (Figure 5.4) reveal the inner jet structure out to an angular extent of $89''$ ($\sim$ 48 kpc at the redshift of 3C 83.1B), whereas at low frequencies, a combination of LOFAR's sensitivity along with our calibration and imaging strategy allow us to map the sub-arcsecond structure at metre-wavelength out to $604''$ ($\sim$ 326 kpc). This is about 20% lower than estimates

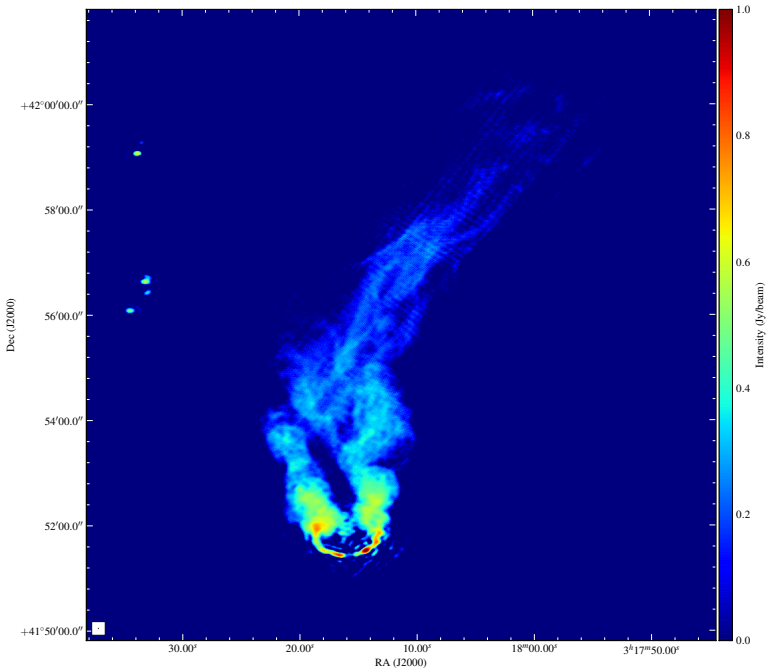

Figure 5.1: Full synthesis image of the inner jets in 3C 83.1B constructed at 144 MHz using LOFAR HBA array.

reported by Leahy, Bridle & Strom (1996) at 1.4 GHz using the VLA in its C and D-configurations (but with a resolution about a factor of 40 lower than ours). While the compact radio core at sub-arcsecond resolution is easily detectable at 1.5 and 8.5 GHz with flux densities of 13.69±0.09 mJy and 4.22±0.02 mJy respectively, there is no such detection at 144 MHz due to synchrotron self-absorption (cf. Section 4.2.1). The total radio flux densities of the inner jets from 144 MHz to 8.5 GHz differ by about three orders of magnitude. We report the integrated flux densities with the associated errors derived from these maps along with a 2-point spectral index estimate for the source and its component in Table 5.2.

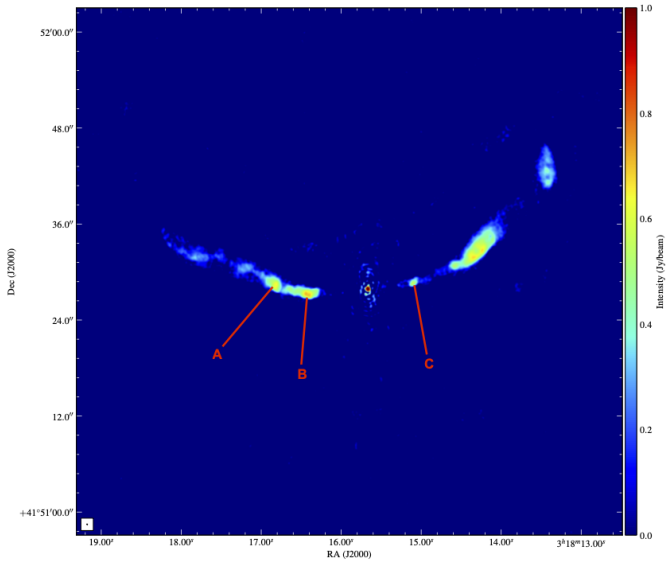

Figure 5.2: Full synthesis image of the inner jets in 3C 83.1B constructed at 1.5 GHz using the *e*-MERLIN array.

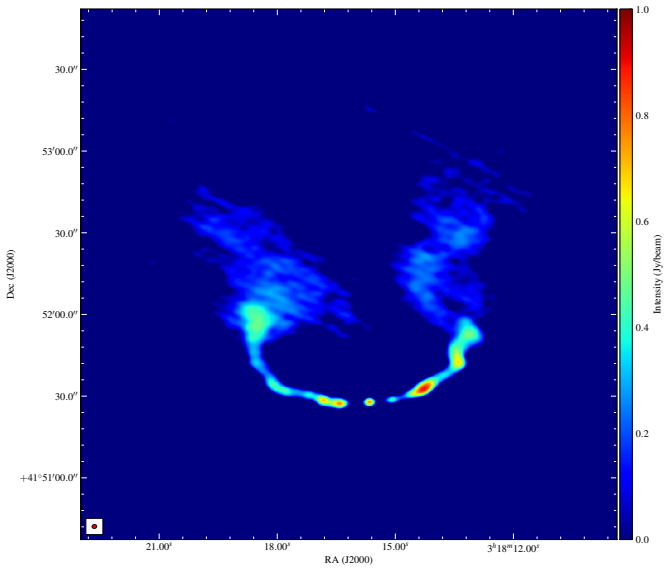

Figure 5.3: Full synthesis image of the inner jets in 3C 83.1B constructed with the VLA at L-band ($\sim$ 1.5 GHz) in A and B-configurations.

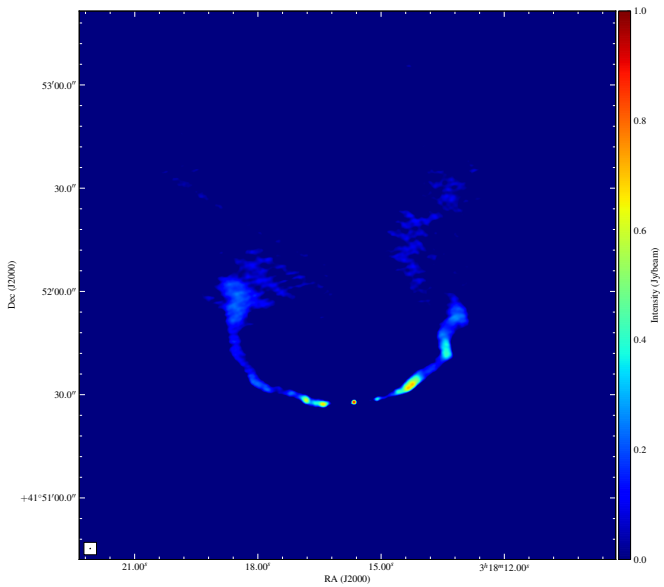

Figure 5.4: Full synthesis image of the inner jets in 3C 83.1B obtained from 1.5 GHz combined *e*-MERLIN plus VLA dataset.

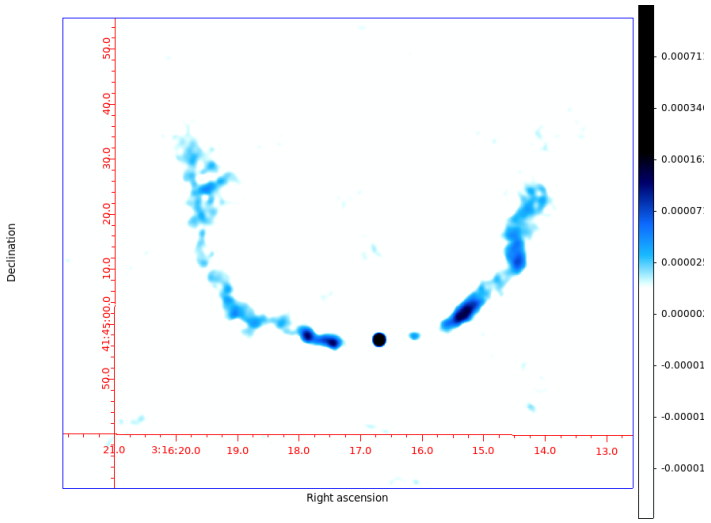

Figure 5.5: Full synthesis image of the inner jets in 3C 83.1B constructed with the VLA at X-band ($\sim$ 8.5 GHz) in A and B-configurations.

Table 5.1: Properties of radio maps presented

Map	Restoring beam			Peak flux	Off-source	Figure
	Major axis	Minor axis	Pos. angle		noise	number
	(arcsec)	(arcsec)	(deg)	(mJy)	(μJy)	
LOFAR	0.41	0.28	-14.40	21.10	70.28	Fig.5.1
$\mathrm{VLA}^{\mathrm{L,AB}}$	1.43	1.32	-17.20	13.91	76.42	Fig.5.3
$\mathrm{VLA}^{\mathrm{X,AB}}$	0.48	0.25	-73.91	4.58	18.43	Fig.5.5
e-$\mathrm{MERLIN}^{\mathrm{L}}$	0.12	0.11	56.15	16.11	30.19	Fig.5.2
e-$\mathrm{MERLIN}^{\mathrm{L}}$ + $\mathrm{VLA}^{\mathrm{L,AB}}$	0.21	0.14	122.45	13.78	33.09	Fig.5.4

Notes: The superscripts L and X respectively denote $\sim$ 1.5 GHz and $\sim$ 8.5 GHz observing frequency deployed in our present study; A & B represent the array configuration of the VLA observations.

Table 5.2: Radio jet properties of 3C 83.1B

Component	$S_{150\ \mathrm{MHz}}$	$S_{1.5\ \mathrm{GHz}}$	$S_{8.5\ \mathrm{GHz}}$	$\alpha_{150\ \mathrm{MHz}}^{1.5\ \mathrm{GHz}}$	$\alpha_{1.5\ \mathrm{GHz}}^{8.5\ \mathrm{GHz}}$
	(mJy)	(mJy)	(mJy)		
Core.....	—†	13.69±0.09	4.22±0.02	—†	−0.68±0.01
Jet total.....	17273.40±10.05	2760.32±5.00	20.31±0.08	−0.78±0.02	−2.84±0.03
Jet west.....	11215.60±8.43	1434.22±3.76	8.26±0.02	−0.88±0.02	−2.98±0.04
Jet east.....	6057.79±5.47	1312.41±3.29	7.89±0.01	−0.65±0.01	−2.96±0.04
West jet knot-1.....	10.47±0.17	2.53±0.06	0.13±0.01	−0.60±0.01	−1.73±0.03
East jet knot-1.....	30.17±0.15	6.48±0.06	0.52±0.02	−0.65±0.01	−1.46±0.02
East jet knot-2.....	27.34±0.16	5.01±0.06	0.46±0.02	−0.72±0.02	−1.38±0.02

Notes: †The radio core is undetected at our LOFAR HBA observing frequencies due to synchrotron self-absorption (cf. Chapter 4). Flux density values have been computed from maps deconvolved with equivalent restoring beam size (i.e., 0.5″ resolution) across all three frequencies (see Figure 5.6).

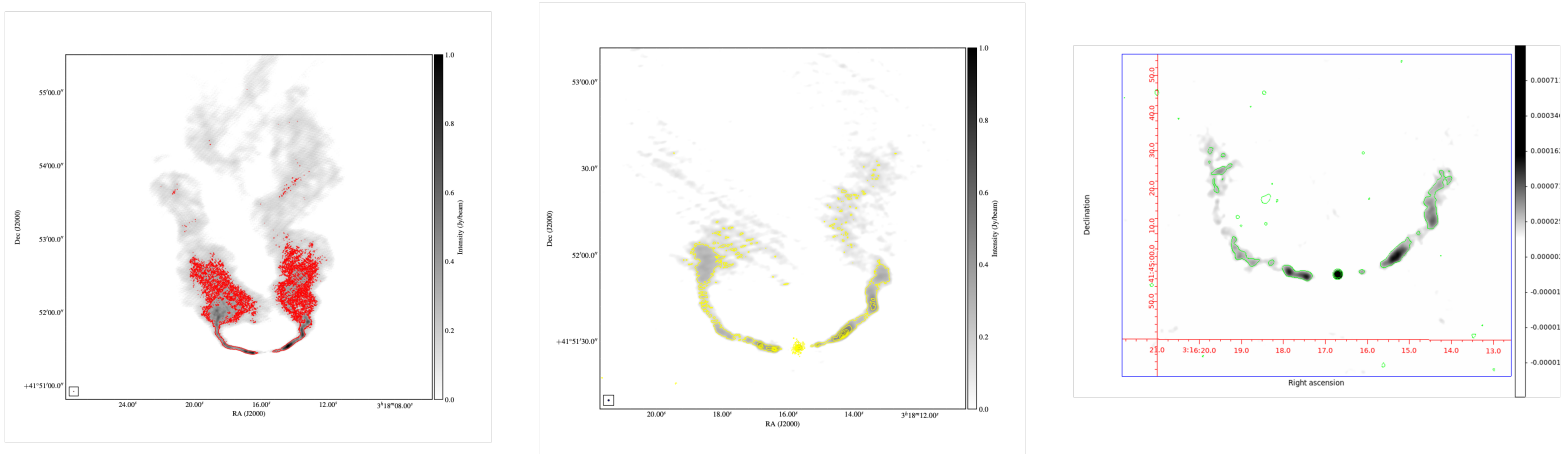

Figure 5.6: High resolution multi-frequency multi-configuration radio imaging comparison of the inner jets in 3C 83.1B. The radio images have been corrected for primary beam response and deconvolved with the same circular beam size of 0.5-arcsec resolution – the synthesised beam size is shown in the bottom left hand corner of image. Left: LOFAR image at 150 MHz – contours start at $6\sigma_{\rm rms}$ and are spaced by $\sqrt{2}$. Middle: Combined *e*-MERLIN plus VLA map at 1.5 GHz – contours start at $6\sigma_{\rm rms}$ and are spaced by $\sqrt{2}$. Right: VLA map at 8.5 GHz – contours start at $6\sigma_{\rm rms}$ and are spaced by $\sqrt{2}$.

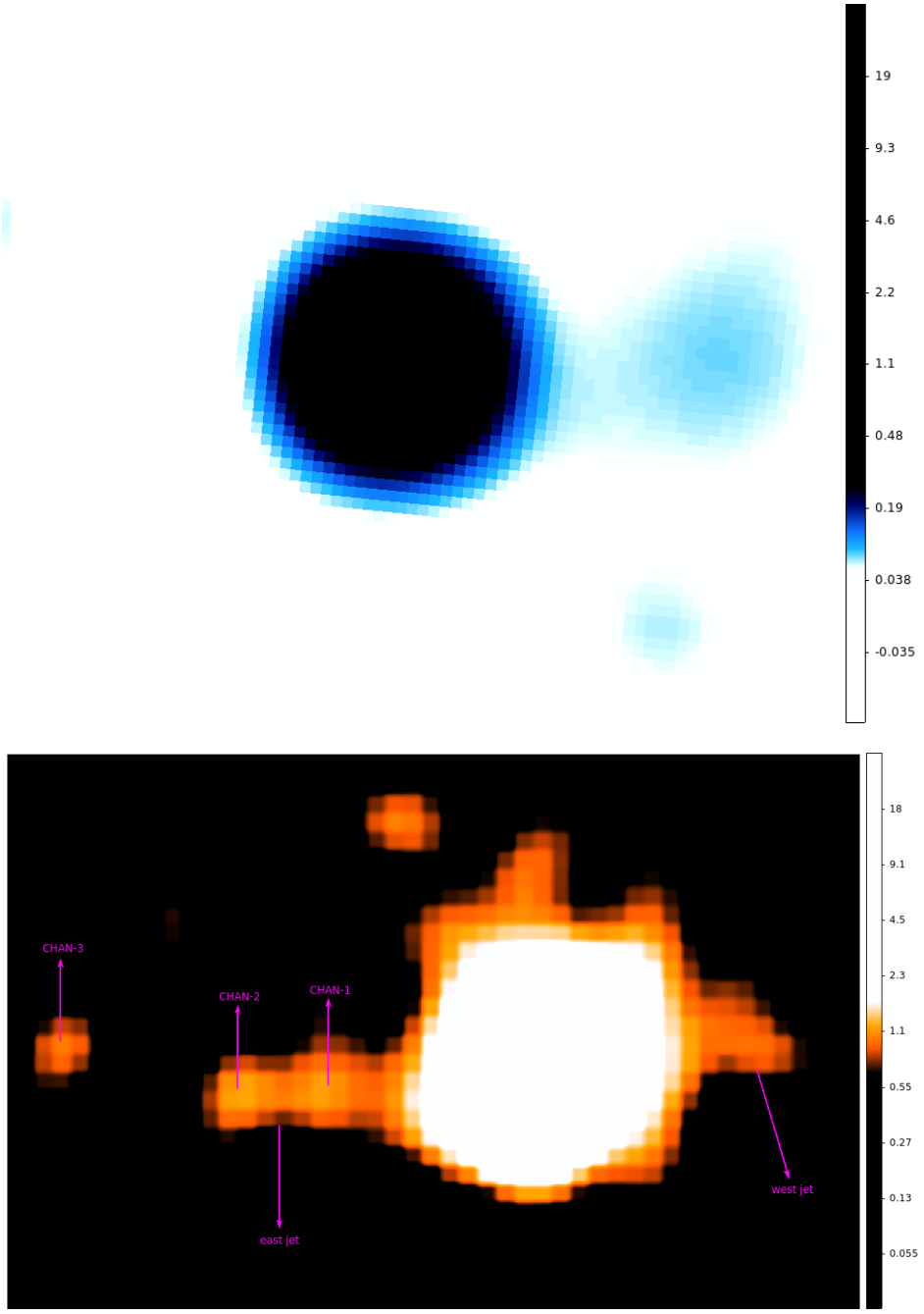

Figure 5.7: Optical (HST) and X-ray (Chandra) images of 3C 83.1B showing extension of the inner jet in the east -and- west directions along with jet-knots as observed at radio wavelengths. Top: HST image at $\sim 0.5''$ resolution. Bottom: Chandra image at $\sim 0.5''$ resolution.

5.3 Orientation, velocity and Lorentz and Doppler factors

It is generally believed that all extragalactic relativistic jets possessing optical (and X-ray) counterparts are significantly beamed (e.g. Stawarz 2004 and references therein). Although the observed symmetrical radio to X-ray jets in our selected sample do not necessarily suggest beaming, usually jets that are morphologically similar sizes but different brightnesses across the core can be interpreted in terms of differential relativistic beaming. Thus, if we make the simplified assumption that the jets in 3C 83.1B (including the other sources in our sample) are light, relativistic, and dynamically dominated by electron-positron plasma, then in the rest frame of the jet, the bulk Lorentz factor, $\Gamma_{\rm jet}$ and Doppler factor, $\delta_{\rm jet}$ are respectively given by;

$$\begin{aligned} \Gamma_{\rm jet} &= \left(1-\beta_{\rm jet}^2\right)^{-1/2}, \quad \text{and} \\ \delta_{\rm jet} &= \left[\Gamma_{\rm jet}\left(1-\beta_{\rm jet}{\rm cos}\theta\right)\right]^{-1}. \end{aligned} \tag{5.1}$$

For a jet propagating with velocity $\beta_{\rm jet}$, the brightness asymmetry R, between the jet and counterjet can be approximated by;

$$R \equiv \frac{S_{\nu\,,\rm jet}}{S_{\nu\,,\rm cjet}} = \left(\frac{1+\beta_{\rm jet}\cos\theta}{1-\beta_{\rm jet}\cos\theta}\right)^{\delta}, \tag{5.2}$$

where, $\beta_{\rm jet}.c$ is the speed of the jet, which is inclined at an angle, $\theta \in$ [0, π/2] to our line of sight, and $\delta = m + \alpha$; the constant m = 2 for a continuous jet (see Scheuer & Readhead 1979 for review). α is the spectral index, which is taken to be -0.6 in the present study. Equation 5.2 assumes intrinsic isotropy of the synchrotron emission (e.g. Giovannini et al. 1994). Thus, we assume here that the jets are intrinsically symmetrical and that the observed jet flux asymmetries are due to relativistic beaming effects. This allows us to constrain the characteristic beaming speed, $\beta_{\rm jet}$, and angle it makes with our line of sight, θ, by re-writing Equation 5.2 in terms of the sidedness ratio as;

$$\beta_{\rm jet} = \frac{R^{1/(2+\alpha)}-1}{R^{1/(2+\alpha)}+1}\,\frac{1}{\cos\theta}, \tag{5.3}$$

Hence, with the known parameter R from observations, one can derive the required advanced velocity of the jet as a function of the jet viewing angle. We note here that Equation 5.3 gives lower limits on both $\beta_{\rm jet}$ and $\cos\theta$ since $0 < \beta_{\rm jet} < 1$, and, $0 < \cos\theta < 1$.

Using our 0.5-arcsec resolution LOFAR HBA map, we measure flux densities of 114.65 $\pm$ 0.18 mJy and 44.34 $\pm$ 0.19 mJy within 2.5 arcsec radius over a length of 7.58 arcsec ($\sim$ 4 kpc)

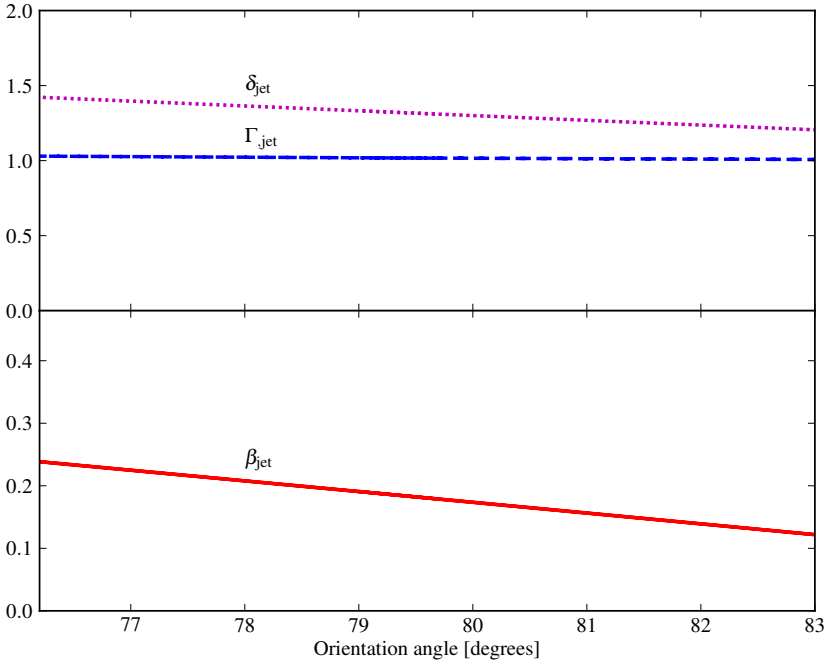

Figure 5.8: Intrinsic jet velocity $\beta_{\rm jet}$ (solid red line), Lorentz factor $\Gamma_{\rm jet}$ (dashed blue line) and Doppler factor $\delta_{\rm jet}$ (dotted magenta line) of the inner jets in 3C 83.1B, as a function of the angle θ between the jet and the line of sight.

of the east and west jet (where the jets are straight) and obtain a sidedness ratio of 2.59 ± 0.01. This corresponds to $\beta_{\rm jet} = 0.2c$ and $\theta = 79.7°$. From Equation 5.3 we constrain the possible values of the product $\beta_{\rm jet} \cos\theta$ measured at different positions along the jet – the results are shown in Figure 5.8.

5.4 Transverse vs longitudinal structures

Although models that describe the acceleration and collimation zones in relativistic jets are currently open to debate in the literature (e.g. Beskin & Nokhrina 2006; Boccardi et al. 2017; Casadio et al. 2021), investigating the transverse jet size and velocity structure at the jet bases provide reliable means of exploring this parameter space. High-resolution imaging of the inner geometry and velocity structures deep in the inner regions of the jets (as in the present study) are particularly useful to test models of jet expansion and recollimation shocks – which serves as diagnostic tools for particle re-acceleration sites and plasma instabilities associated with the

jet propagation on larger scales.

Since both the kinematics and collimation profiles are associated with changes in the brightness intensity distribution within the moving jet, we examine the inner jet structure of 3C 83.1B and the other sources in our sample by analysing their brightness intensity profiles across the jets and comparing with their longitudinal structures. The analysis was performed separately on the individual maps for each of the three observing frequencies (Figure 5.6) of the present study, created after aligning the three maps as described above. The images were sliced pixel-by-pixel (1 px = 0.5 arcsec) using the `AIPS` task `SLICE` in the transverse direction. Then, the transverse intensity distributions of each slice were fitted with Gaussian profiles using the task `SLFIT`. This task was ran twice for the entire length of the jets, first fitting a single Gaussian and then fitting two Gaussian profiles. In Figure 5.9 we present profiles of the surface brightness distribution taken perpendicularly to the jet ridge line at several positions along the inner jets in 3C 83.1B.

5.5 Physical parameters

Here, we derive estimates of the physical parameters in 3C 83.1B (and for the other sources in our sample) that can be derived from spectral data using the python interface to synchrotron libraries [`pysynch`][14] code. We assume isotropic distibution; $L_\nu = (1+z)^{\alpha-1} S_\nu 4\pi \mathrm{D}_\mathrm{L}^2$ of the relativistic particles and magnetic field energy densities over the source volume and in energy equipartition. Following the formalism of Hardcastle, Birkinshaw & Worrall (1998), we adopt a low-energy cut-off of $\Gamma_{\rm min}$ in the energy distribution of the radiating electrons, rather than frequency cut-offs (e.g. Myers & Spangler 1985) normally used in the standard equipartition assumptions. This allows us to account for the contribution from low-energy electrons to the synchrotron *"energy"* spectrum which otherwise would have been neglected under a frequency cut-off assumption. With a power-law spectrum and minimum electron energy given by $E_{\rm min} = \Gamma_{\rm min} m_{\rm e} c^2$, we take $\Gamma_{\rm min}$ = 10; this corresponds to an energy cut-off of $\sim$ 5 MeV (e.g. Brunetti, Setti & Comastri 1997). We adopt an injection index, $\alpha_{\rm inj} = -0.6$ and further assume i) a filling factor of unity for the emitting regions, ii) cylindrical geometry in our calculation of volumes, and iii) equal energies in relativistic electrons and heavy particles. Since electron ageing is less relevant at lower frequencies, we have used our 1.5 GHz flux density measurements (Table 5.2)

[14] pysynch provides an interface to the C synchrotron libraries used by Hardcastle et al (1998) and in subsequent work, and python wrappers for some basic functions. The source code is available at `https://github.com/mhardcastle/pysynch`

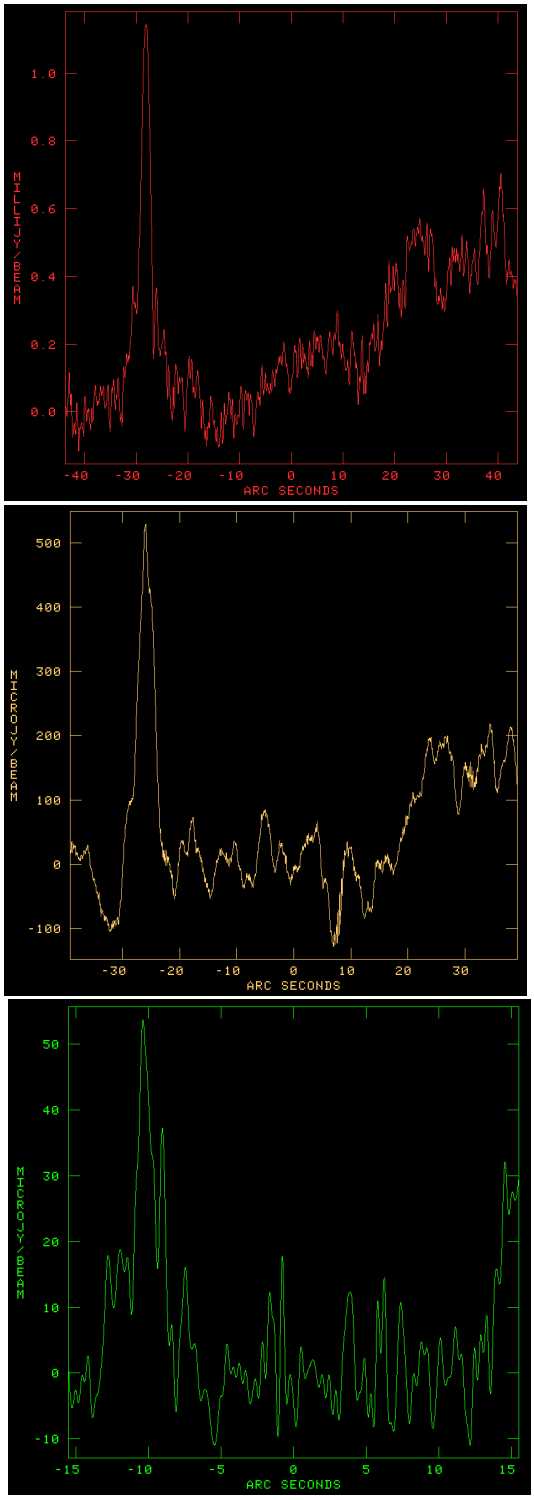

Figure 5.9: Brightness intensity profiles of the inner jets in 3C 83.1B derived from maps convolved with a circular beam of size 0.5 arcsec FWHM. Top: profile at 144 MHz. Middle: profile at 1.5 GHz. Bottom: profile at 8.5 GHz.

Table 5.3: Measured physical parameters of the inner jet in 3C 83.1B and its components

Component	$B_{\rm eq}$ (μG)	$P_{\rm min}$ (10^{-12} dyn cm^{-2})	$U_{\rm min}$ (10^{-11} ergs cm^{-3})	$E_{\rm min}$ (10^{55} ergs)
Jet total.....	5.82	0.91	0.27	402.07
Jet west.....	14.30	5.43	1.63	88.24
Jet east.....	23.65	14.83	4.45	50.53
West jet knot-1.....	49.76	65.69	19.71	0.06
East jet knot-1.....	63.26	106.17	31.85	0.09
East jet knot-2.....	59.22	93.01	27.90	0.08

Notes: Physical quantities derived from 0.5″ resolution radio map constructed at 1.5 GHz using our combined *e*-MERLIN plus VLA datasets.

in our calculation of the physical quantities. The equipartition magnetic field $B_{\rm eq}$ computed in this way along with the minimum energy density $U_{\rm min}$, pressure $P_{\rm min}$, and total energy $E_{\rm min}$ for the source and its components is presented in Table 5.3.

5.6 Spectrum, age and energetics

The electron distribution arising from shock acceleration of a synchrotron emitting population of relativistic plasma is assumed to be a broken power-law in momentum: $n(p) \propto p^{-s}$, $p_{\rm min} < p < p_{\rm c}$; and $n(p) \propto p^{-(s+\Delta s)}$, $p_{\rm c} < p$; where s is governed by the injection process, and Δs = 1 for synchrotron ageing with ongoing injection in a constant B-field (see Eilek 1996 and references therein). Since the synchrotron and inverse-Compton fractional energy loss rates are proportional to gamma, this injection spectrum develops a break where the losses become important. The break shifts to lower energies over time, so that the break frequency would be expected to decrease over time, in the absence of strong reacceleration of the electrons. The synchrotron lifetime, $\tau_{\rm syn}$ of the electron population as a whole can be extracted from the break frequency, $\nu_{\rm br}$, and the observed radiation spectrum in a given frequency range will be observed to steepen as $\nu_{\rm br}$ passes through that frequency range. Here, we set some limits on the inner jet properties from a simple kinematic model for the synchrotron lifetime.

Since the synchrotron spectrum of an emitting relativistic plasma depends on both electron energy and field strength, a knowledge of the field strength, together with the spectral index and

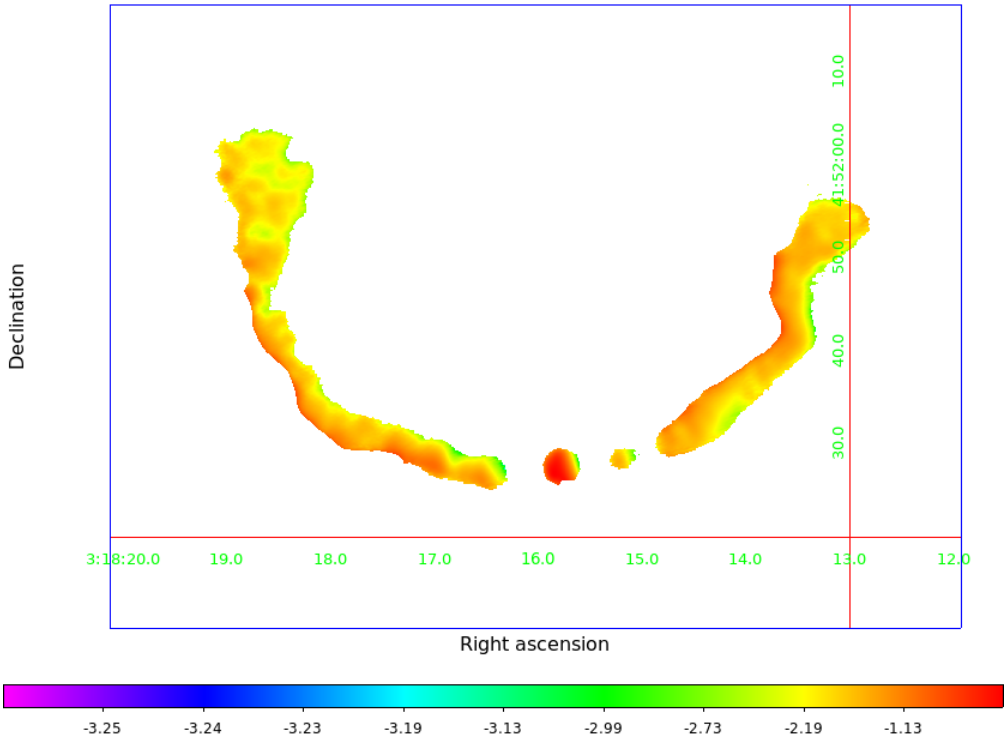

Figure 5.10: A false colour image showing the spectral index, α distribution within the inner jets of 3C 83.1B. The map is constructed across two frequencies ($\sim$ 1.5 GHz and $\sim$ 8.5 GHz) at 1.5–arcsec resolution. α is in the range -0.4 to -2.5 and is plotted at 3σ rms noise cut-off in total intensity.

break frequency are essential parameters for estimating the flow timescale of the synchrotron plasma. To progress, we assume minimum energy conditions, and estimate the magnetic field strengths for the inner jets in 3C 83.1B (along with the other sources in our sample) using the formalism of Worrall & Birkinshaw (2006), which is an analytical treatment of the minimum-energy magnetic field;

$$B_{\rm me} = \left[\frac{(\alpha+1)\,C_1}{2C_2} \frac{(1+\kappa)}{\eta V} L_\nu \nu^\alpha \frac{\left(\gamma_{\rm max}^{1-2\alpha} - \gamma_{\rm min}^{1-2\alpha}\right)}{(1-2\alpha)} \right]^{1/\,(\alpha+3)} \tag{5.4}$$

where C_1 and C_2 are constants that depend on α and field inclination, L_ν is the spectral luminosity in the emission region, of volume, V, at frequency, ν. The parameters κ, $\gamma_{\rm min}$, $\gamma_{\rm max}$ and η have their usual meaning and are defined in Section 5.5 where their adopted values are also given. The field strength (here taken as the minimum energy value, $B_{\rm me}$) together with $\nu_{\rm br}$, then

Table 5.4: Fitting results from minimum energy for synchrotron emitting electrons in the inner jets of 3C 83.1B

$B_{\rm eq}$	$\nu_{\rm b}^{*}$	$\tau_{\rm syn}$
(nT)	(MHz)	(10^7 yrs)
(1)	(2)	(3)
69.80	150	15.0
80.00	1500	4.2
30.50	8500	3.7

Notes: Col.(1): derived equipartition field strength. Col.(2): adopted break frequency. Col.(3): radiative lifetime of synchrotron emitting electrons.

allow us to determine the radiative lifetime of the electrons from Equation 4.1. The synchrotron loss timescale computed this way, along with the spectral index distribution within the inner jets of 3C 83.1B are presented in Table 5.4 and Figure 5.10 respectively.

5.7 Discussion

The inner jets in 3C 83.1B is well resolved in both our radio and X-ray images and show clear evidence of multiple bright knotty structures at the jet base. Our derived radio spectrum for the source and its components (see Table 5.2) provide evidence of spectral steepening towards higer frequencies with a total radio spectral index ($\alpha_{150\,\rm MHz}^{1.5\,\rm GHz} = -0.78 \pm 0.02$) consistent with a synchrotron emission mechanism. The two knots (labelled A and B; Figure 5.2) in the east jet are connected by an edge-brightened bridge and have a marginally steeper spectra ($\alpha = -0.65 \pm 0.01, -0.72 \pm 0.02$) than the knot C in the west jet ($\alpha = -0.60 \pm 0.01$); nevertheless, the knots are flatter than the rest of the jets. Overall, the east jet has a slightly flatter spectral index compared with the west jet with little or no evidence of significant spectral curvature from $\sim$ 150 MHz to 8.5 GHz (see also Figure 5.10). The observed wiggles in the jet morphology can be explained in terms of dynamical instabilities in the flow propagation (e.g. O'Dea & Owen 1987), and we interpret the mild spectral differences across the source and its components as a direct consequence of ageing and expansion effects of the radio plasma as it traverses the ICM. There is good correspondence between features of the jet observed at all three frequencies. At $0.5''$ resolution the transverse total intensity structure of the inner jets (Figure 5.9) is very

asymmetric; the profiles show the knots are brighter in the east jet. O'Dea & Owen (1986) have reported similar asymmetry of the transverse total intensity structure and jet knots in 3C 83.1B at $0.45''$ resolution with the VLA at 5 GHz. Such transverse gradient in the intensity (and velocity) structure indicate that the jets are formed by a fast central spine and a slower outer sheath (e.g. Ghisellini, Tavecchio & Chiaberge 2005). Our derived transverse jet profiles suggests that the edge-brightening characterising the jets in 3C 83.1B are consistent with instability patterns, or simply a direct consequence of the jet formation mechanism.

Our estimate of mildly relativistic speeds ($\beta_{\rm jet} = 0.2c$) for the inner jets in 3C 83.1B although lower than the range of values (0.3 – 0.7)c reported by Jetha et al. (2005) in their study of jet speeds in a sample of 30 WAT radio galaxies, is in general agreement with typical values found for weaker Type-I radio sources, whose properties are consistent with the hypothesis that the jets slow down from relativistic to sub-relativistic velocities on scales of 1$\sim$2 kpc (e.g. Parma et al. 1994). The allowed range of θ is $76^\circ \lesssim \theta \lesssim 83^\circ$ for 3C 83.1B; this is fully consistent with the unified schemes that predict FR I radio galaxies to be at angles $\gtrsim 30^\circ$ (e.g. Ghisellini et al. 1993). If we assume the jets have a constant orientation angle on all scales, then the observed deceleration of the radio plasma (see Figure 5.8) away from the AGN is as expected and consistent with variation of the jet-counterjet brightness ratio. Entrainment of ambient material have been suggested as the main trigger of jet deceleration in FR Is (e.g. Laing 1996). The fact that the host galaxy NGC 1265 resides in a rich/dense environment (i.e., Perseus cluster – e.g. Fabian et al. 2006) supports this interpretation. For an orientation, $\theta = 80^\circ$ and intrinsic jet speed, $\beta_{\rm jet} = 0.2$, we derive a Lorentz factor, $\Gamma_{\rm jet}$ of 1.0 which corresponds to a Doppler factor, $\delta_{\rm jet} = 1.3$. These values are consistent with a bulk deceleration of the flow speeds within the inner jets and hints at plausibly ongoing particle acceleration – at least in the regions close to the inner core where the knots are visible – most likely via steady velocity shear parallel to the jet axis (e.g. Rieger & Duffy 2004). It is noteworthy here, that the first-order Fermi process in mildly relativistic shocks have been suggested as the main acceleration mechanism at the jet bases in low power radio galaxies (e.g. Laing & Bridle 2013).

The physical characteristics of 3C 83.1B and its components are listed in Table 5.3 and the corresponding radiative lifetimes obtained at different frequencies in Table 5.4. The values we find suggest the total energy input from the west jet is about 40% higher than the east jet although the energy budget of the knots are comparable. The minimum pressure magnetic field we measure is 5.82 μG for the total source and typically of the order of a few tens ($\approx$ 10–60 μG) over the

jets and knots. Our derived $P_{\rm min}$ over the length of the jets and knots differ by one order of magnitude, with the highest recorded value, $P_{\rm min}$ = 1.0×10^{-10} dyn cm^{-2} corresponding to knot-1 in the east jet. We measure average minimum pressure of 0.91×10^{-12} dyn cm^{-2} for the source. Pfrommer & Jones (2011) have estimated the ram pressure from the ICM to be $P_{\rm ICM}\, r_{\rm gal} \simeq 1.4\times10^{-12}$ dyn cm^{-2} ($r_{\rm gal} \simeq 1.45$ Mpc) at the present position of the galaxy. Comparison with our derived quantities indicates that the inner jets in 3C 83.1B are highly overpressurized compared with the surrounding ICM – consistent with supersonic beams which are more dense than the external medium – an observation which could well have consequences for bulk flow speeds at the jet base. It is however interesting to note here that the ram pressure is only about the averaged pressure estimate for the source, so on the large scale the structure has reached some sort of steady state. For an injection index, $\alpha = -0.6$, we find $U_{\rm min}$ = 1.63×10^{-11} ergs cm^{-3} for the electrons radiating at 1.5 GHz and estimate a synchrotron lifetime of 4.2×10^{7} years. This age is well in agreement with the typical values 4 – 67 Myrs (median age, $\tau_{\rm syn} \simeq 16$ Myrs) derived for currently active galaxies of similar radio power and luminosity (see Parma et al. 1999; 2007). Such lifetime estimates implies that relativistic electrons created in and around the central engine could travel the entire $\sim$ 25 kpc length of the inner jets within their lifetime for bulk velocities of $v_{\rm bulk} > 0.05c$ – if there is no reacceleration or adiabatic losses.

6

The inner jets in 3C 264

The present chapter is an extension to our ongoing work in resolving the physics driving the observed jet structure in powerful radio galaxies, as part of the extragalactic jet legacy project with *e*-MERLIN. For simplicity, we shall refer to discussion of the underlying physics as described in Chapter 5 for the purpose of analysis and interpretation of our results in the present Chapter. At the current best known redshift of 3C 264 (z = 0.021), we measure a luminosity distance of 87 Mpc, from our asssumed cosmology. This corresponds to an angular scale of 0.44 kpc arcsec^{-1}.

6.1 Multiwaveband images

We present here (Figures 6.1–6.7), new high-resolution and high-sensitivity maps of the WAT source 3C 264 obtained from multi-configuration, multi-frequency radio observations with e-MERLIN, LOFAR and VLA, with complementary observations from optical (HST) and X-ray (Chandra).

6.2 Morphology and flux densities

Figures 6.1–6.5 shows the radio images at all three frequencies and at various angular resolutions (cf. Table 6.1). The inner jet structure of 3C 264 presents a head-tailed morphology with a strong core and a wiggled jet directed toward the northeast, and evidence of a weak counterjet extending in the southwest direction. Our HST image (Figure 6.7–[top panel]) shows a well resolved jet symmetrical to the radio jet, and an optical "ring" as seen in earlier observations (e.g. Baum et al. 1997; Perlman et al. 2010). At X-ray wavelength (Figure 6.7–[bottom panel]), our Chandra

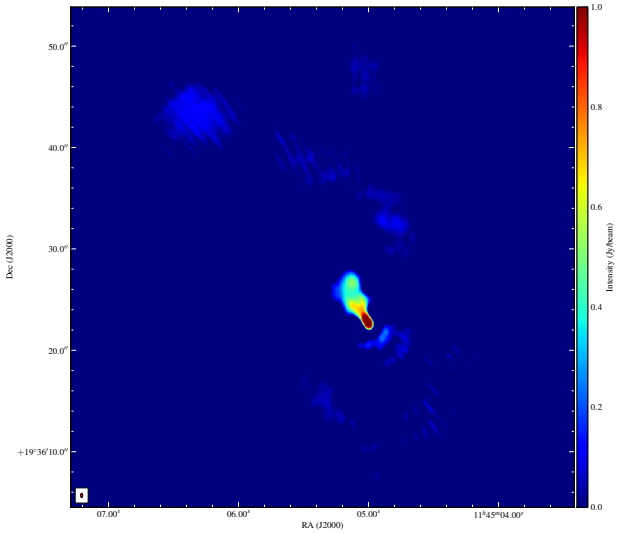

Figure 6.1: Full synthesis image of the inner jets in 3C 264 constructed at 144 MHz using LOFAR HBA array.

observations reveal X-ray emission of the active nucleus covering $\sim 5''$ radius from the core – this extends well beyond the optical jet, but there is no evidence of X-ray jet emission.

Our sub-arcsecond radio images reveal three distinct bends in the inner jets of 3C 264. The main jet emerges from the core with P.A. = 59° in the northeast direction, bends to the northwest at $\sim 5''$ with a large drop in the surface brightness, and bends again to the northeast at about $10''$. At a projected distance of 12 kpc from the core, the third and final bend to the southeast can easily be seen. These sub-arcsecond bends we observe at the jet base are reminiscent of the arcsecond structure – compare the kpc-scale jet morphology (Figure 4.2). While the source (jet-counterjet) is easily detectable at GHz frequencies with a projected linear size of 20 kpc (46.17 arcsec) across, at 144 MHz, the southwest "counter" jet is not visible in our radio image. Thus, to derive the 144 MHz counterjet flux, we have integrated the flux density over the southwest jet area. We note here that this is a crude estimate of the counterjet flux; nonetheless, this approach allows us to put lower limits on the counterjet radio spectrum in 3C 264. There is mild evidence of variability of the radio core flux density, consistent with VLBI observations at 15 GHz from the MOJAVE program reported by Boccardi et al. (2019). Our derived flux density values with the associated errors are presented in Table 6.2 along with a 2-point spectral index estimate for key components of the source.

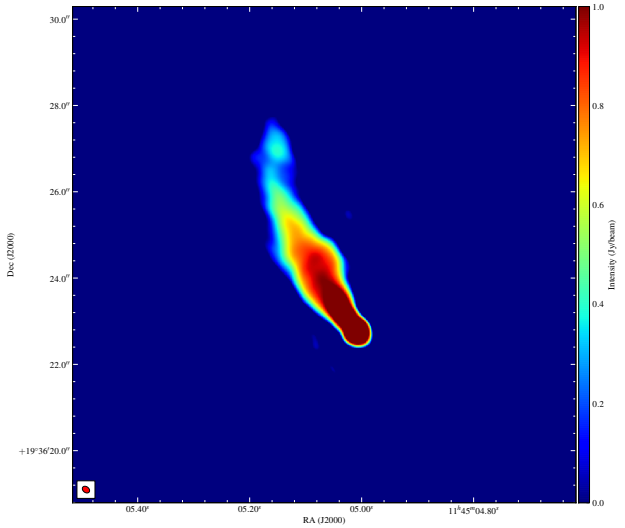

Figure 6.2: Full synthesis image of the inner jets in 3C 264 constructed at 1.5 GHz using the *e*-MERLIN array.

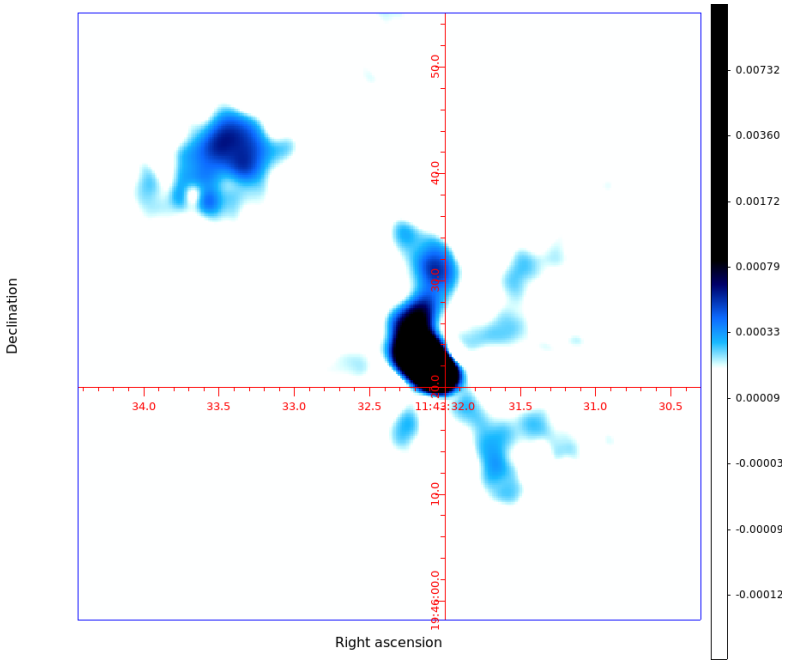

Figure 6.3: Full synthesis image of the inner jets in 3C 264 constructed with the VLA at L-band ($\sim$ 1.5 GHz) in A and B-configurations.

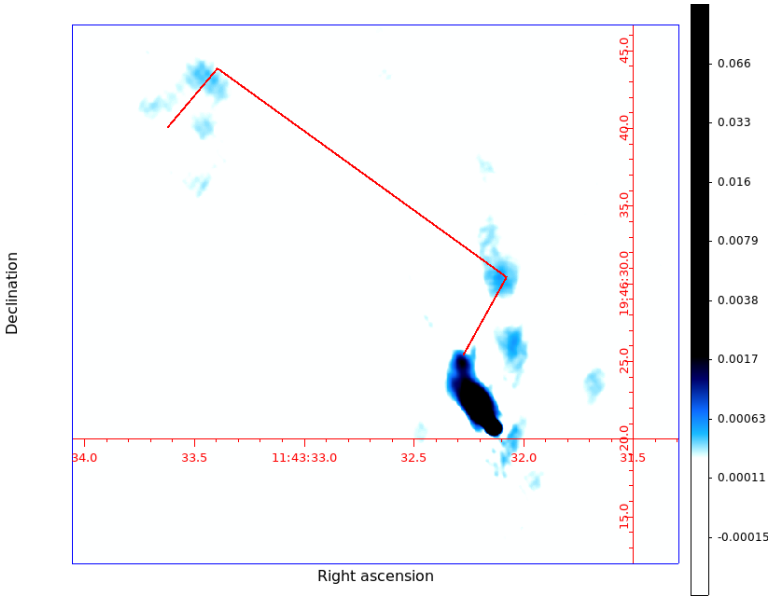

Figure 6.4: Full synthesis image of the inner jets in 3C 264 obtained from 1.5 GHz combined *e*-MERLIN plus VLA dataset. The solid red line traces the inner jet trajectory as seen in the 8.5 GHz map (Fig 6.5).

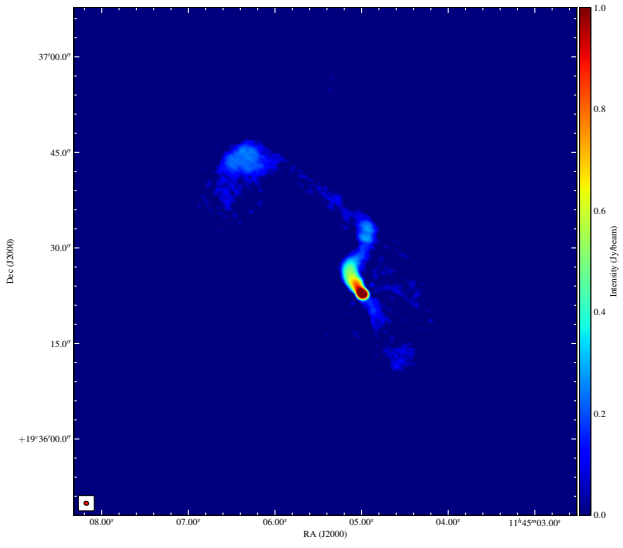

Figure 6.5: Full synthesis image of the inner jets in 3C 264 constructed with the VLA at X-band ($\sim$ 8.5 GHz) in A and B-configurations.

Table 6.1: Properties of radio maps presented

Map	Restoring beam			Peak flux	Off-source	Figure
	Major axis	Minor axis	Pos. angle		noise	number
	(arcsec)	(arcsec)	(deg)	(mJy)	(μJy)	
LOFAR	0.44	0.24	179.26	86.08	258.74	Fig.6.1
VLA$^{\rm L,AB}$	1.87	1.70	55.82	16.57	32.58	Fig.6.3
VLA$^{\rm X,AB}$	0.77	0.63	75.51	20.78	3.35	Fig.6.5
e-MERLIN$^{\rm L}$	0.20	0.14	59.30	186.19	29.52	Fig.6.2
e-MERLIN$^{\rm L}$ + VLA$^{\rm L,AB}$	0.34	0.32	66.25	199.98	32.43	Fig.6.4

Notes: The superscripts L and X respectively denote $\sim$ 1.5 GHz and $\sim$ 8.5 GHz observing frequency deployed in our present study; A & B represent the array configuration of the VLA observations.

Table 6.2: Radio jet properties of 3C 264

Region	$S_{150\ \rm MHz}$	$S_{1.5\ \rm GHz}$	$S_{8.5\ \rm GHz}$	$\alpha_{150\ \rm MHz}^{1.5\ \rm GHz}$	$\alpha_{1.5\ \rm GHz}^{8.5\ \rm GHz}$
	(mJy)	(mJy)	(mJy)		
Core.....	336.59$\pm$0.14	126.86$\pm$0.16	24.96$\pm$0.01	$-$0.42$\pm$0.01	$-$0.94$\pm$0.02
Jet total.....	886.95$\pm$0.79	165.32$\pm$0.70	40.27$\pm$0.11	$-$0.71$\pm$0.01	$-$0.82$\pm$0.02
Jet northeast.....	458.76$\pm$0.67	36.07$\pm$0.61	11.59$\pm$0.10	$-$1.08$\pm$0.03	$-$0.66$\pm$0.01
Jet southwest....	40.37$\pm$0.37	4.41$\pm$0.22	2.41$\pm$0.04	$-$0.94$\pm$0.02	$-$0.42$\pm$0.01

Notes: Flux density values have been computed from maps deconvolved with equivalent restoring beam size (i.e., 0.3$''$ resolution) across all three frequencies (see Figure 6.6).

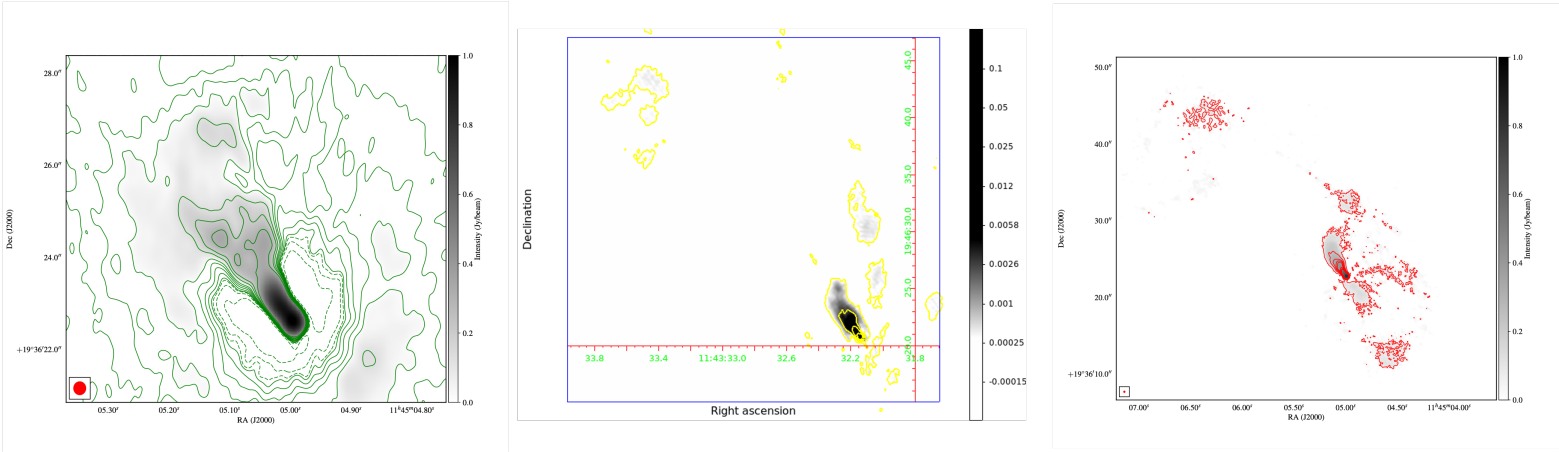

Figure 6.6: High resolution multi-frequency multi-configuration comparison of the total intensity distribution of the inner jets in 3C 264. The images have been corrected for primary beam response and deconvolved with the same circular gaussian beam of size 0.3-arcsec resolution – the synthesised beam size is shown in the bottom left hand corner of image. Left: LOFAR image at 150 MHz – contours start at $6\sigma_{\rm rms}$ and are spaced by $\sqrt{2}$. Middle: Combined *e*-MERLIN plus VLA map at 1.5 GHz – contours start at $6\sigma_{\rm rms}$ and are spaced by $\sqrt{2}$. Right: VLA map at 8.5 GHz – contours start at $6\sigma_{\rm rms}$ and are spaced by $\sqrt{2}$.

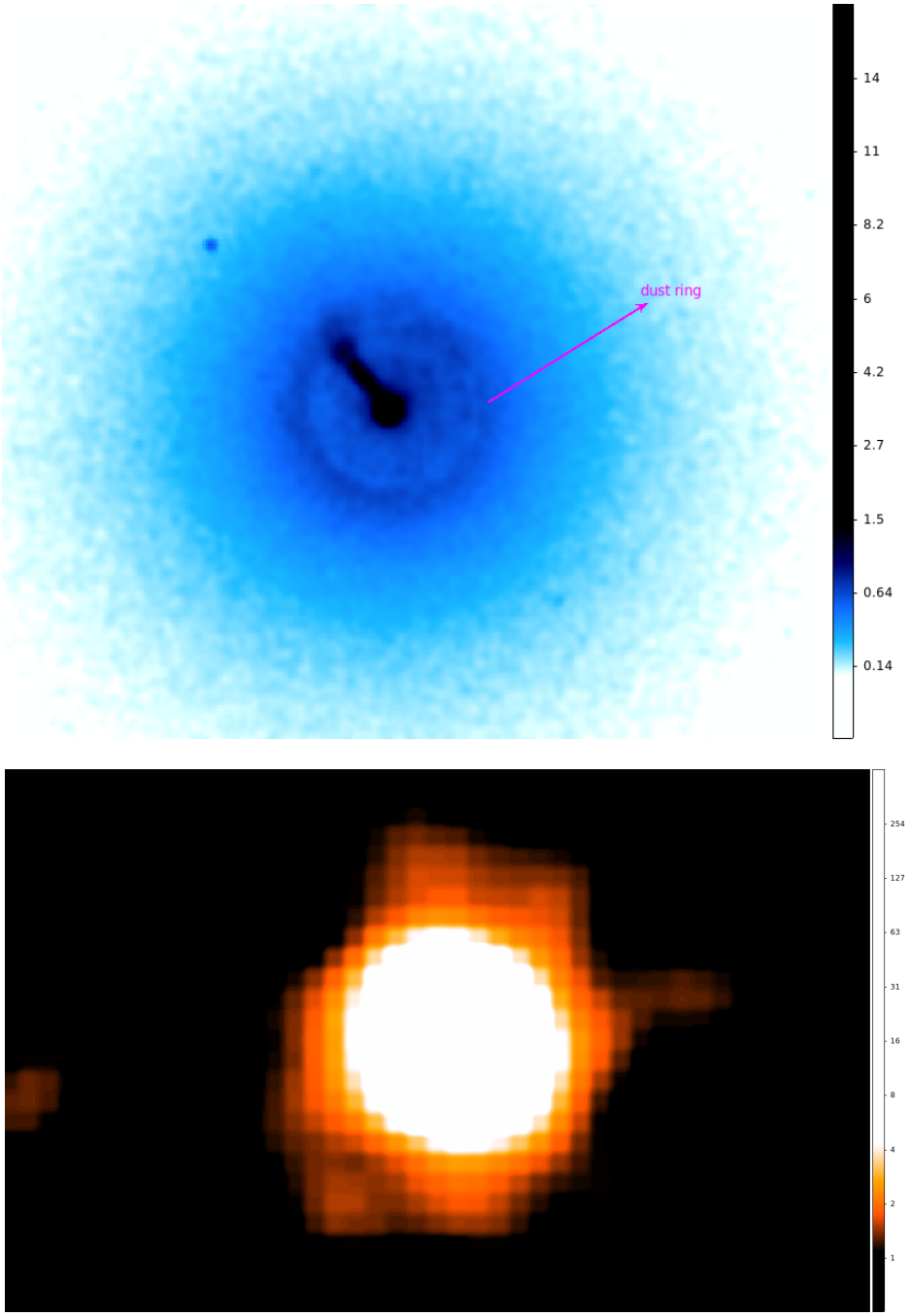

Figure 6.7: Optical (HST) and X-ray (Chandra) images of 3C 264 showing extension of the inner jet in the northeast direction as observed at radio wavelengths. Top: HST image at $\sim 0.5''$ resolution. Bottom: Chandra image at $\sim 0.5''$ resolution.

6.3 Jet sidedness, speed and orientation

Here we put limits on the jet velocity and orientation relative to the line of sight following standard analysis based on the brightness asymmetry (cf. Section 5.3). Since the counterjet is not detected in our 144 MHz map and is also weakly defined in our high resolution 1.5 GHz map; we have used our 8.5 GHz VLA map at $0.3''$ resolution in our estimate of the jet-counterjet brightness ratio in 3C 264. We measure flux densities within the inner $4''$ from the core downstream the jet and counterjet tracjectory (where the jets are bright and straight), and use these to calculate the sidedness ratio. For our assumed spectral index, $\alpha = -0.6$ for the jet emission, we derive $R = 14.33 \pm 0.03$, which yields $\beta_{\rm jet} \cos\theta = 0.42$. From Equation 5.3 we constrain possible values for the angle θ between the jet and the line of sight, and the intrinsic jet velocity $\beta_{\rm jet}$ for 3C 264. The results are shown in Figure 6.8.

6.4 Transverse vs longitudinal structures

In Figure 6.9 we present spatial profiles of intensity for the inner jets in 3C 264 taken perpendicular to the jet ridge line. As described in Section 5.4 we have analysed the individual maps for each of the three observing frequencies separately; the maps used here have a Gaussian beam of size $0.3''$ FWHM.

6.5 Physical parameters

Estimation of physical parameters for the total source and its components in 3C 264 were derived following the procedure described in Section 5.5. We used the standard formulae of synchrotron radiation (e.g. Hardcastle, Birkinshaw & Worrall 1998) along with the aforementioned assumptions to calculate the minimum energy density, $U_{\rm min}$ and the corresponding effective equipartition magnetic field strength, $B_{\rm eq}$. The total pressure here is assumed to be that of equipartition between relativistic particles and magnetic field, $P_{\rm min} = 0.67 U_{\rm min}$ and the total energy, $E_{\rm min}$ depends on the slope of the synchrotron spectrum and the limiting energy cut-off used. We report the derived quantities in Table 6.3.

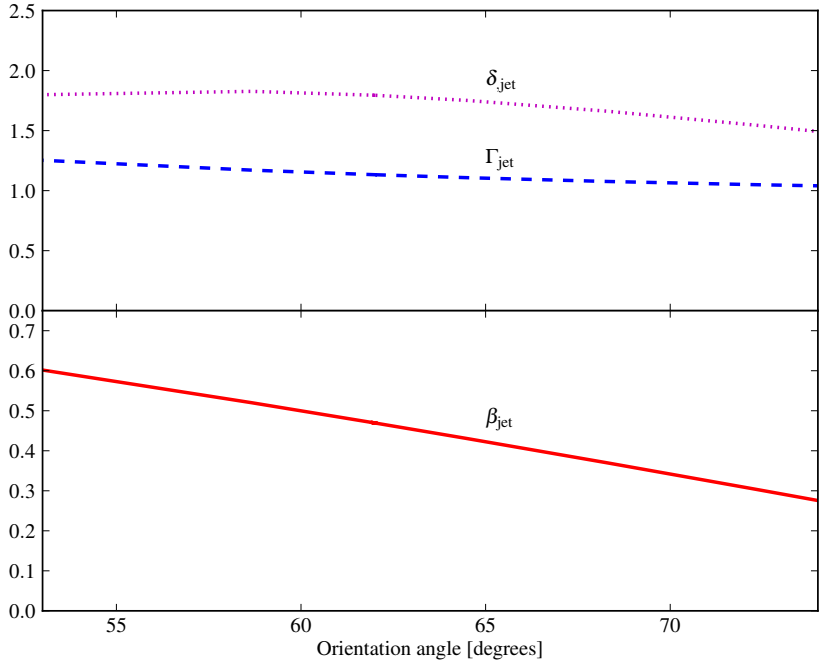

Figure 6.8: Intrinsic jet velocity $\beta_{\rm jet}$ (solid red line), Lorentz factor $\Gamma_{\rm jet}$ (dashed blue line) and Doppler factor $\delta_{\rm jet}$ (dotted magenta line) of the inner jets in 3C 264, as a function of the angle θ between the jet and the line of sight.

6.6 Spectrum, age and energetics

Here, we follow the analytic model of Worrall & Birkinshaw (2006) for the minimum energy conditions (cf. Section 5.6) and place limits on the radiative age of relativistic electrons at the jet bases in 3C 264. The results obtained for the three different observing frequencies in the present study are listed in Table 6.4; and displayed in Figure 6.10 is a radio spectral index ($\alpha_{144\ \rm MHz}^{1.5\ \rm GHz}$) distribution within the inner jets of 3C 264. As in Section 5.6, we interpret the radio spectrum in terms of radiative ageing of the relativistic electrons by both synchrotron and inverse-Compton processes.

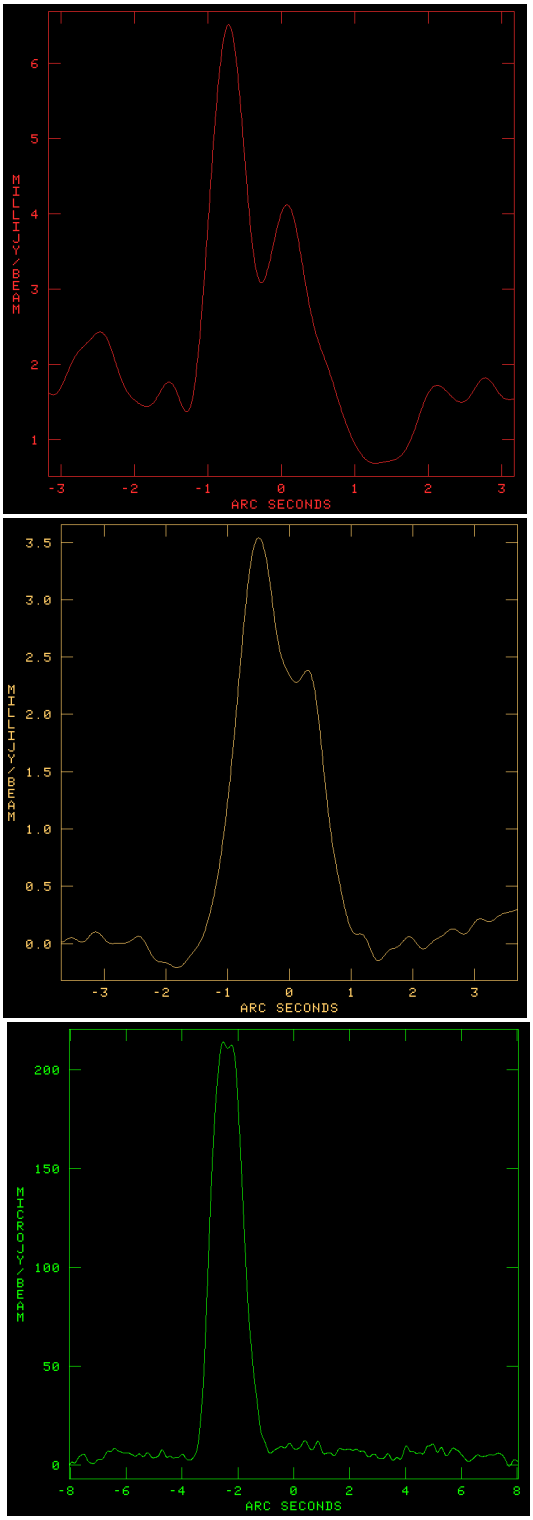

Figure 6.9: Brightness intensity profiles of the inner jets in 3C 264 derived from maps convolved with a circular beam of size 0.3 arcsec FWHM. Top: profile at 144 MHz. Middle: profile at 1.5 GHz. Bottom: profile at 8.5 GHz.

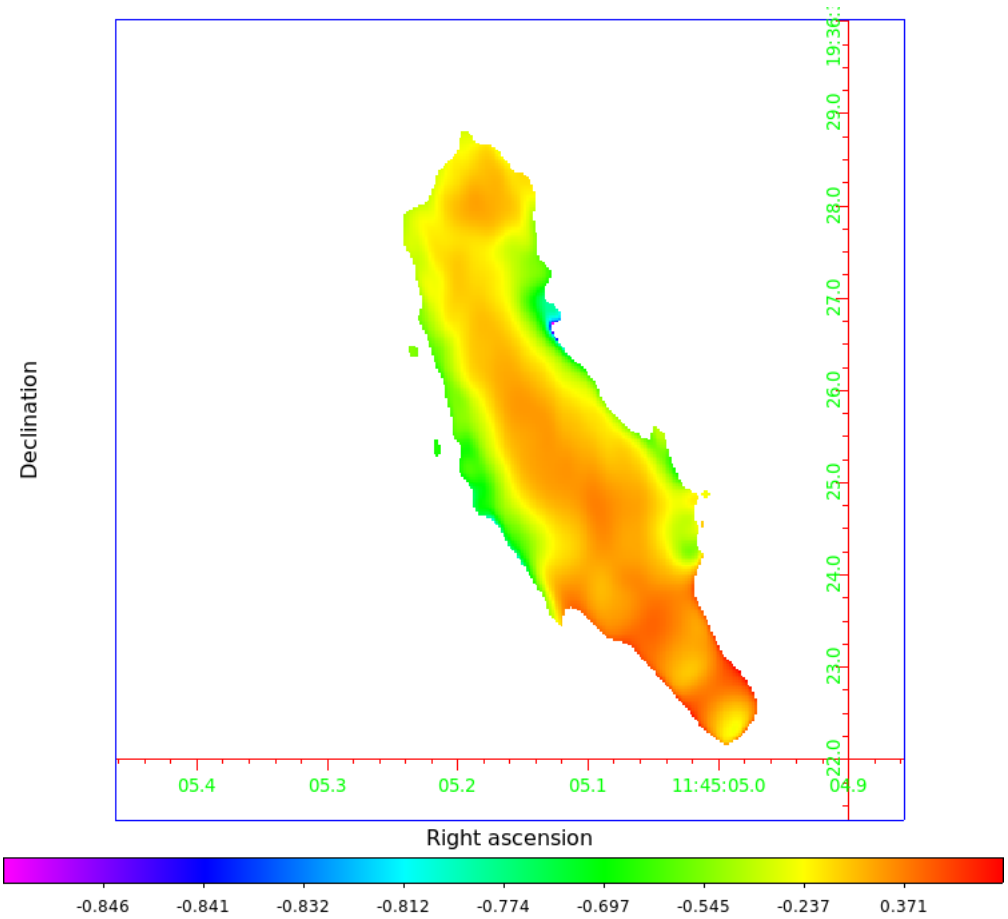

Figure 6.10: Map of spectral index, α of the inner jets in 3C 264 constructed from maps made at two frequencies ($\sim$ 150 MHz and $\sim$ 1.5 GHz) at 0.3–arcsec resolution. α is in the range -0.2 to -0.7 and is plotted at 5σ rms noise cut-off in total intensity.

Table 6.3: Measured physical parameters of the inner jet in 3C 264 and its components

Component	$B_{\rm eq}$ (μG)	$P_{\rm min}$ (10^{-12} dyn cm^{-2})	$U_{\rm min}$ (10^{-11} ergs cm^{-3})	$E_{\rm min}$ (10^{54} ergs)
Jet total.....	19.04	9.61	2.88	14.54
Jet northeast.....	16.16	6.93	2.08	7.83
Jet southwest.....	12.71	4.29	1.29	1.93

Notes: Physical quantities derived from 0.3″ resolution radio map constructed at 8.5 GHz using the VLA in A and B-configurations.

Table 6.4: Fitting results from minimum energy for synchrotron emitting electrons in the inner jets of 3C 264

$B_{\rm eq}$	$\nu_{\rm b}^{*}$	$\tau_{\rm syn}$
(nT)	(MHz)	(Myr)
(1)	(2)	(3)
9.59	150	3.8
6.19	1500	2.3
2.70	8500	3.4

Notes: Col.(1): derived equipartition field strength. Col.(2): adopted break frequency. Col.(3): radiative lifetime of synchrotron emitting electrons.

6.7 Discussion

The sub-arcsecond morphology of 3C 264 as shown in our multiwaveband imaging (Figures 6.1–6.7) is consistent with the class of radio galaxies termed head-tail radio sources. The brightness distribution appears dominated by a very compact component, to which we can assign an upper limit on the size of 0.6 arcsec and a flux density of 126.86 $\pm$ 0.16 mJy at 1.5 GHz. The jet is well collimated and brightest within the first $1''$ ($\sim$ 400 pc). This region coincides with the radius of the dust ring around the host galaxy core (e.g. Baum et al. 1997). Our multifrequency radio images show the jets stay collimated beyond the confines of the dusty ring; but begin to expand beyond the first $2''$ ($\sim$ 0.9 kpc) from the core. The jet width increases from $0.7''$ to $2''$ over a distance of about 1.3 kpc in linear scale before tilting at an angular distance of $5''$ to the N-W (cf. Section 6.2). Jet expansion on sub-kpc scales and its related impact over large volumes of the host galaxy ISM is well documented in the literature (e.g. Sutherland & Bicknell 2007; Mukherjee et al. 2016; Murthy et al. 2022); and as noted by Sutherland & Bicknell (2007), the jet at this stage, while maintaining a more or less single direction, is unstable – the jet momentum here spread over a region that is wider than the original jet diameter.

Our estimate of 126.9 mJy for the sub-arcsecond core at 1.5 GHz is consistent with the VLBI core flux density (126.2 mJy) reported by Lara et al. (2004) using the EVN at 1.6 GHz. The total radio jet spectrum between 150 and 1.5 GHz ($\alpha = -0.71 \pm 0.01$) although marginally steeper than the radio spectral index, $\alpha_{\rm r} = -0.58$ reported by Lara et al. (2004) from a least squares fitting approach is well in agreement with a synchrotron emission mechanism. The southwest

jet has a marginally flatter spectrum compared with the northeast jet (see Table 6.2).

The transverse intensity distribution of the inner structure (Figure 6.9) confirms differences in the brightness distribution of the jet as reported by Lara et al. (2004) (see also Lara et al. 1999). At 1.5 GHz, the brightness profile of the jet appears centrally peaked. This feature is consistent with a spine-brightened jet when considering only the longitudinal structures obtained at the smallest scale of $0.''2 \times 0.''1$ (Figure 6.2). Lara et al. (2004) have reported similar transverse profiles for the inner ($\lesssim 100$ pc) jets in 3C 264 and an edge-brightened jet beyond, and interpret this as evidence of a transverse jet velocity structure. If the jets in 3C 264 were sufficiently misaligned, then such limb-brightening is expected due to differential boosting of the main filaments of the flow, or to the de-boosting of the fast central spine. In this scenario a spine-sheath velocity structure would give rise to distinct velocity components at different angles. There is remarkable consistency of the bends in the inner jets at sub-arcsecond scales with those of the kpc-scale jet, and could be something dynamical in the surrounding medium or gravitational interaction with close companion galaxy, IC 2955. We are by this conclusion not ruling out the possiblity of Kelvin-Helmholtz instabilities in this flow regime (e.g. Birkinshaw 1991) and/or a combination of different mechanisms altogether.

From the brightness asymmetry, we have computed the intrinsic velocity $\beta_{\rm jet}$ for the inner jets in units of the speed of light c. The results are plotted in Figure 6.8 – and provide evidence of a steady decline in the jet velocities to vlaues $\lesssim 0.1c$ at larger distances from the core. For our adopted isotropic case (i.e., no preferred direction for the B-field), we obtain an intrinsic speed of $0.42c$ which constrains the jet viewing angle θ to assume relatively large values ($52^\circ \lesssim \theta \lesssim 74^\circ$). The corresponding Doppler and Lorentz factors here are respectively $\delta_{\rm jet} = 1.7$ and $\Gamma_{\rm jet} = 1.1$. Our estimates are in good agreement with values reported by Baum et al. (1997) [$\beta_{\rm jet} = 0.4c$, $\theta = 50^\circ$, and $\Gamma_{\rm jet} = 1.1$] for the jets in 3C 264. Higher initial jet velocities of $\sim 0.99c$ ($\Gamma = 7$) for the inner 300–400 pc have been reported in the literature (e.g. Lara et al. 2004). Comparsion with our estimates for the jet velocity on sub-kpc scales suggests a deceleration of the order of a factor 2 from the initial parsec-scale jet. Our results here are consistent with the range of values reported by Jetha et al. (2005) for the jet velocities in a sample of 30 WAT radio galaxies, and reinforce existing conclusions from abundant observational evidence (e.g. Hardcastle et al. 1997; Feretti et al. 1999; Laing & Bridle 2002) that FR I jets must decelerate from an initially relativistic speeds to sub-relativistic speeds on kpc-scales. We note here that the spine-sheath form of the brightness intensity structure along with the observed limb-brightened jet hints at

plausible velocity stratification within the inner relativistic jets (where the jet velocities are high and strongly de-boosted), and is consistent with earlier work by Lara et al. (2004).

Using the 8.5 GHz jet flux density and volume for the source and its component, we derive estimates for the magnetic field strength, electron energy density, pressure and total energy (Table 6.3) under the "equipartition" assumptions. The larger value of the minimum internal pressure, $P_{\rm min}$ in the northeast component compared with the southwest, together with its rather relaxed appearance, suggests that it is essentially in pressure equilibrium with the host galaxy ISM. Such conclusions implies that the two components are lying in different external pressure environments, or they are simply in different dynamical states. The two arms – N-E jet and S-W jet – contribute about 50% of the total energy supplied by the source. We report the radiative lifetime of the source in Table 6.4. The values we find at all three frequencies are very similar, at about 3 Myr; the equipartition field strength here decreasing from 9.59 nT at $\nu_{\rm br}$ = 150 MHz to 2.70 nT at $\nu_{\rm br}$ = 8.5 GHz. This agreement, although could be just a coincidence, shows that the assumed break frequency has about an order-of-magnitude effect on the equipartition calculation, so the derived magnetic field strength are only good to about a factor 3. This implies that the observed variation in the spectrum is likely due to changes in local magnetic fields and/or other loss processes. The spectral index distribution (Figure 6.10) shows a flat spectrum filament embedded in a relatively steep sheath of diffuse emission. Similar observations have been reported in the radio galaxy 3C 296 (Laing et al. 2006) whose radio power and luminosity compares with that of 3C 264. This spectral behaviour could be interpreted as evidence of local reacceleration of relativistic electrons within the inner jets in 3C 264. It is noteworthy here that our derived total spectral index for the two arms (Table 6.2) presents a slightly different picture. The difference could be due to projection effects, but, nonetheless, reflects plausible asymmetry in the process of energy supply from the nucleus in the two directions during the history of the source – compare our derived minimum energy values for the two arms (Table 6.3).

7

The jet bases in 3C 371

This chapter is an extension to our ongoing work in resolving jet physics on pc and kpc-scale in radio-loud AGNs with *e*-MERLIN. As in the preceeding two chapters, much of the analysis here is based on the radio data, and again, for simplicity, we refer to discussion of the underlying physics as described in Chapter 5 for the purpose of analysis and interpretation of our results in the present Chapter. For our assumed ΛCDM cosmology, we obtain an angular diameter distance to 3C 371 ($z = 0.051$) of $D_L = 222$ Mpc; at this distance, $1''$ corresponds to a projected length of 1.05 kpc.

7.1 Multiwaveband images

We present here (Figures 7.1–7.7), new high-resolution and high-sensitivity maps of the inner jets in the BL Lac object 3C 371 obtained from multi-frequency, multi-configuration radio (*e*-MERLIN, LOFAR and VLA) observations with complementary observations from optical (HST) and X-ray (Chandra). Note the distinct symmetrical radio to X-ray jets in our multiwaveband imaging. We report the properties of the radio maps in Table 7.1.

7.2 Morphology and flux densities

Figure 7.6 shows the radio images of 3C 371 at all three frequencies deconvolved with a beam size of $0.3''$ FWHM. The integrated flux densities with the associated errors derived from these maps along with a 2-point spectral index estimate for each component is presented in Table 7.2. Our radio images provide evidence of a core-dominated source, with the central core emitting

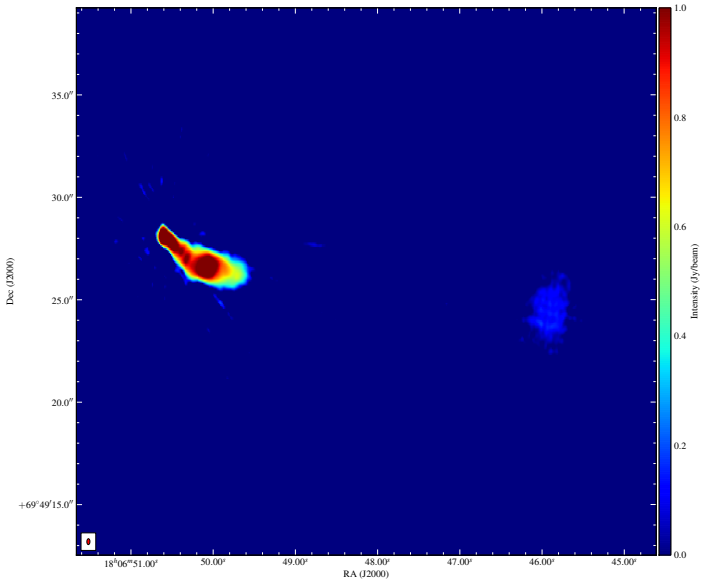

Figure 7.1: Full synthesis image of the inner jets in 3C 371 constructed at 144 MHz using LOFAR HBA array.

$\sim$ 40%, 75% and 93% of the total 144-MHz, 1.5-GHz and 8.5-GHz flux respectively. The total radio spectral index of the inner jets is flatter compared with its components. Continuum variability in 3C 371 at cm-wavelengths is well documented in the literature (e.g. Wrobel & Lind 1990 and references therein). Our radio observations confirm cm-wavelength variability, and as well provide evidence of moderate ($\sim$ 23%) variability at metre-wavelength. At optical and X-ray wavelengths (Figure 7.7), our images show a central dominant nuclear emission with extension of the optical and X-ray jets in the southwest direction – similar to the radio jets.

The jet is one-sided (i.e., no evidence of a counterjet) at all three frequencies and is directed towards the southwest. At a projected distance of 3 kpc from the AGN, there is a $\sim 45^{\circ}$ change in direction of the jet trajectory from southwest to west. Within the inner $2''$ radius, two visible radio knots can easily be seen at LOFAR (144 MHz) and *e*-MERLIN (1.5 GHz) observing frequencies; the knots are separated by $0.5''$ angular scale. Gómez & Marscher (2000) suggests the knots are stationary features in the jet arising from standing recollimation shocks. Our high resolution imaging confirms the presence of a radio hotspot as reported by Wrobel & Lind (1990) and is located $\sim 3.5''$ from the radio core. Observations of radio hotspots appear to be rather common among the more powerful FR Is (e.g. 3C 465; Bempong-Manful et al. 2020). The VLA

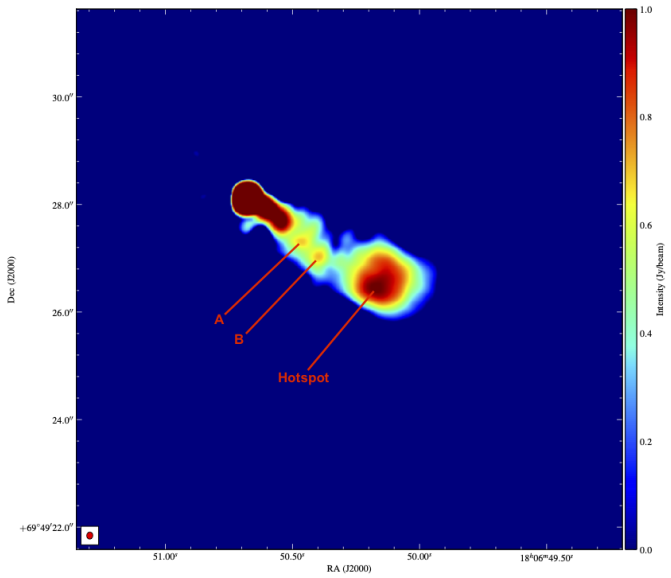

Figure 7.2: Full synthesis image of the inner jets in 3C 371 constructed at 1.5 GHz using the *e*-MERLIN array.

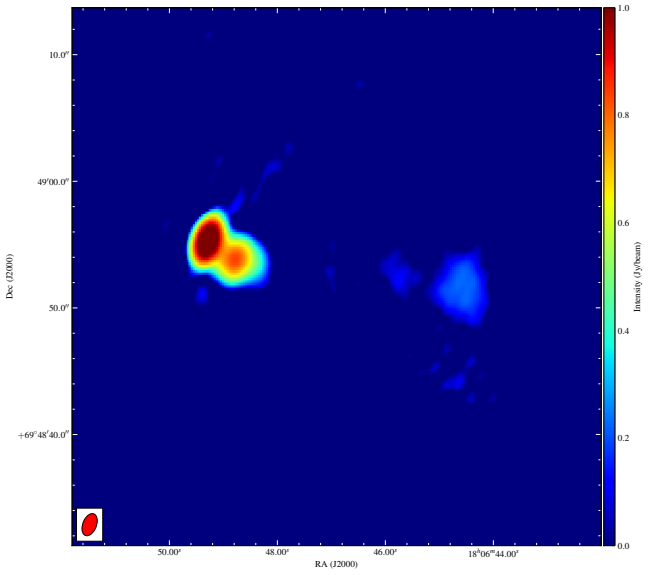

Figure 7.3: Full synthesis image of the inner jets in 3C 371 constructed with the VLA at L-band ($\sim$ 1.5 GHz) in A and B-configurations.

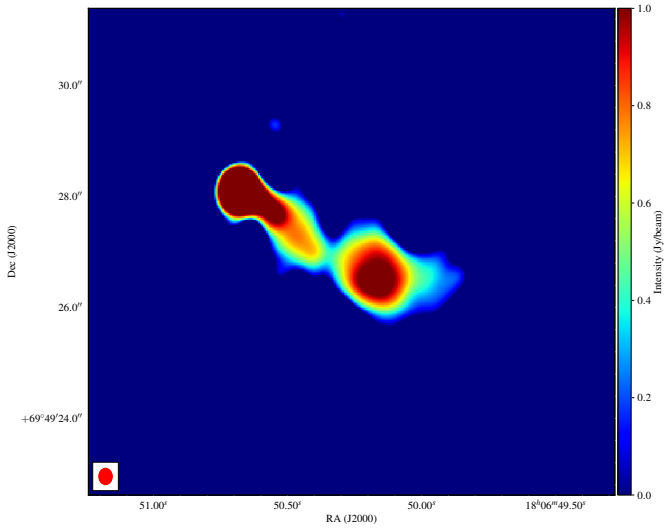

Figure 7.4: Full synthesis image of the inner jets in 3C 371 obtained from 1.5 GHz combined *e*-MERLIN plus VLA dataset.

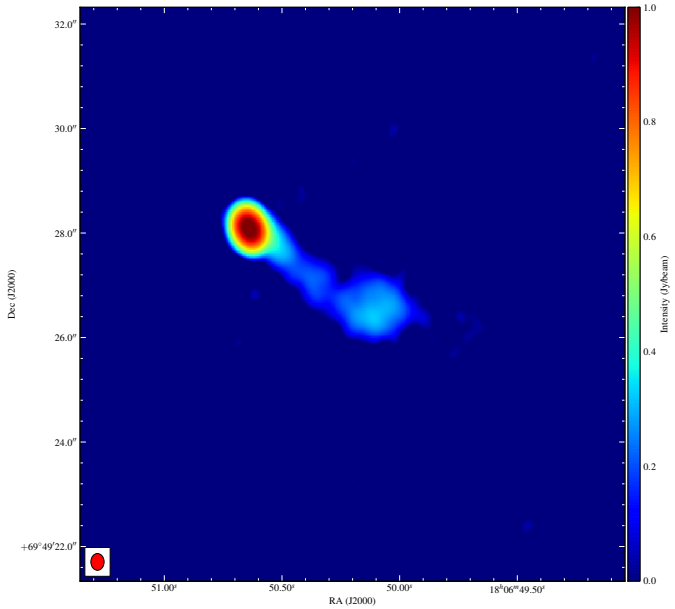

Figure 7.5: Full synthesis image of the inner jets in 3C 371 constructed with the VLA at X-band ($\sim$ 8.5 GHz) in A and B-configurations.

Table 7.1: Properties of radio maps presented

Map	Restoring beam			Peak flux	Off-source	Figure
	Major axis	Minor axis	Pos. angle		noise	number
	(arcsec)	(arcsec)	(deg)	(mJy)	(μJy)	
LOFAR	0.33	0.24	8.12	841.71	49.92	Fig.7.1
VLA$^{\rm L,AB}$	1.95	1.39	153.90	108.91	70.31	Fig.7.3
VLA$^{\rm X,AB}$	0.41	0.30	34.82	109.02	77.65	Fig.7.5
e-MERLIN$^{\rm L}$	0.13	0.13	156.90	914.49	70.42	Fig.7.2
e-MERLIN$^{\rm L}$ + VLA$^{\rm L,AB}$	0.16	0.15	169.60	916.45	96.75	Fig.7.4

Notes: The superscripts L and X respectively denote $\sim$ 1.5 GHz and $\sim$ 8.5 GHz observing frequency deployed in our present study; A & B represent the array configuration of the VLA observations.

Table 7.2: Radio jet properties of 3C 371

Component	$S_{144\ \rm MHz}$	$S_{1.5\ \rm GHz}$	$S_{8.5\ \rm GHz}$	$\alpha_{144\ \rm MHz}^{1.5\ \rm GHz}$	$\alpha_{1.5\ \rm GHz}^{8.5\ \rm GHz}$
	(mJy)	(mJy)	(mJy)		
Core.....	1338.39±0.30	1037.01±0.34	146.55±0.11	−0.11±0.01	−1.12±0.02
Jet total.....	3250.86±1.15	1365.80±0.96	156.97±0.25	−0.37±0.01	−1.24±0.02
Knot A.....	44.25±0.12	12.26±0.16	0.23±0.03	−0.59±0.02	−2.18±0.04
Knot B.....	78.54±0.16	9.99±0.16	0.33±0.03	−0.88±0.02	−1.97±0.03
Hotspot.....	98.52±0.11	21.34±0.13	0.87±0.04	−0.68±0.02	−1.81±0.03

Notes: Flux density values have been computed from maps deconvolved with equivalent restoring beam size (i.e., 0.3″ resolution) across all three frequencies (see Figure 7.6).

L-band image (Figure 7.3) at 1.95×1.39″ resolution show a faint trace of the western lobe, though this is prominent at sub-arcsecond resolutions with LOFAR at 144 MHz (Figure 7.1). The total angular extent of the inner jet measured at 144 MHz is 6.4″ corresponding to 6.7 kpc in linear scale at the redshift of the source. This is about 50% higher than the value reported by Akujor et al. (1994) at a similar resolution with MERLIN at 1.6 GHz.

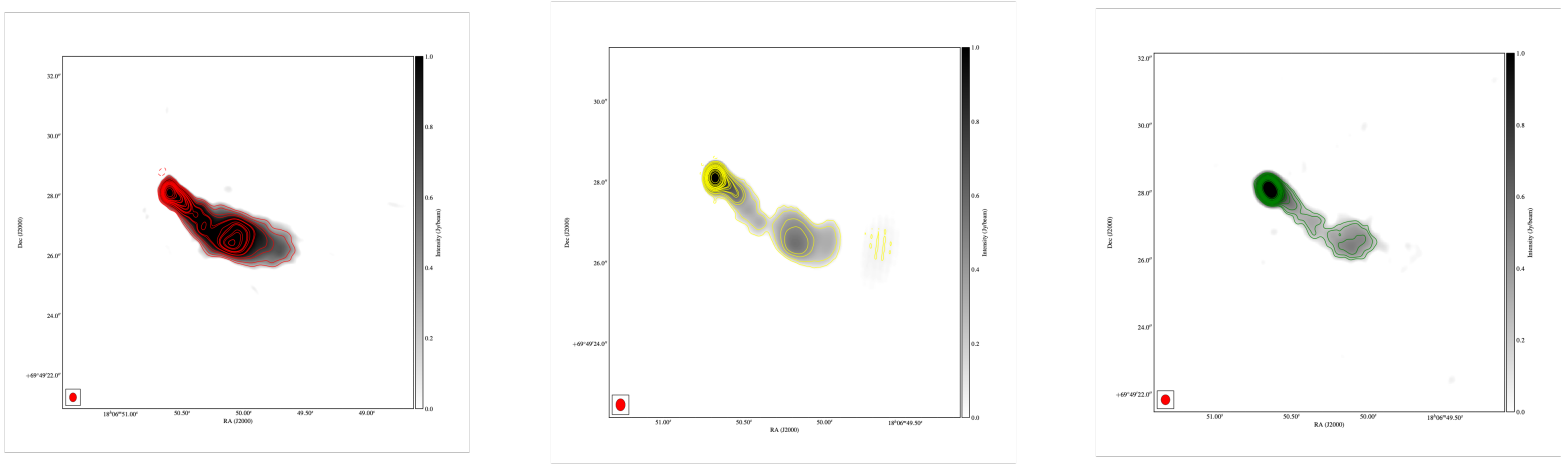

Figure 7.6: High resolution multi-frequency multi-configuration comparison of the total intensity distribution of the inner jets in 3C 371. The images have been corrected for primary beam response and deconvolved with the same circular gaussian beam of size 0.3-arcsec resolution – the synthesised beam size is shown in the bottom left hand corner of image. Left: LOFAR image at 150 MHz – contours start at $3\sigma_{\rm rms}$ and are spaced by $\sqrt{2}$. Middle: Combined *e*-MERLIN plus VLA map at 1.5 GHz – contours start at $3\sigma_{\rm rms}$ and are spaced by $\sqrt{2}$. Right: VLA map at 8.5 GHz – contours start at $3\sigma_{\rm rms}$ and are spaced by $\sqrt{2}$.

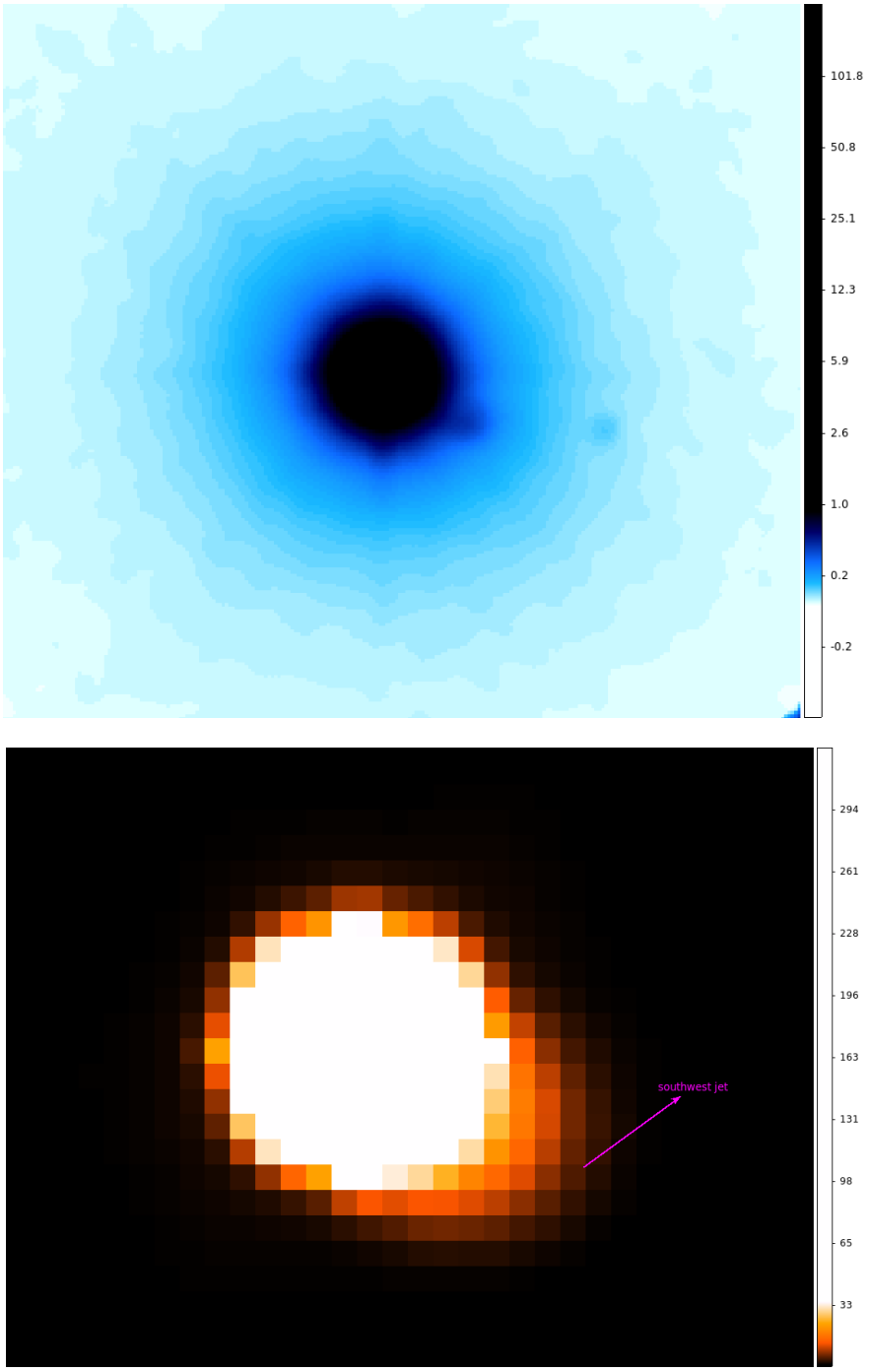

Figure 7.7: Optical (HST) and X-ray (Chandra) images of 3C 371 showing extension of the inner jet in the southwest direction as observed at radio wavelengths. Top: HST image at $\sim 0.5''$ resolution. Bottom: Chandra image at $\sim 0.5''$ resolution.

7.3 Brightness asymmetry, orientation and velocity

The counterjet in 3C 371 is undetected in our observations, thus to derive the jet-counterjet ratio, we follow the formalism of Lara et al. (1997) and assume that the emission from the counterjet is lower than or equal to the off-source noise level of the image, measured over large empty regions of the maps. As noted by Lara et al. (1997) the choice of 1 σ as an upper limit to the counterjet surface brightness is more conservative than other methods found in the literature, such as, for example, the integration of flux density over the counterjet area. Furthermore, the high dynamic range in our radio images should allow for a good approximation of the sidedness ratio in 3C 371 following this approach. Using our LOFAR HBA ($\sim$ 144 MHz) map, we measure flux densities over the region in which a well-defined and straight jet is observable (i.e., the first $\sim 2''$). We measure flux densities of 90.19 $\pm$ 0.06 mJy and 0.21 $\pm$ 0.01 mJy for the jet and counterjet respectively, and obtain a sidedness ratio of 429.48 $\pm$ 22. From Equation 5.3 we constrain the possible values of the product $\beta_{\rm jet} \cos\theta$ – the results are shown in Figure 7.8.

7.4 Transverse vs longitudinal structures

In Figure 7.9 we show distribution of the transverse jet brightness profile derived for all three frequencies following the procedure described in Section 5.4. This allows us to compare and contrast the shapes of the outflows in the inner jets of 3C 371 (cf. Section 7.7).

7.5 Physical parameters

We measure and report the physical quantities in the inner jets of 3C 371 that can be derived from integrated intensity data in Table 7.3. As in Section 5.5, we assume that the relativistic particle and magnetic field energy densities are uniformly distributed over the source volume and in energy equipartition, and adopt a low-energy cut-off of $\Gamma_{\rm min}$ in our calculations.

7.6 Spectrum, age and energetics

A first order approximation of the synchrotron lifetime for the inner jets along with derived values for the equipartion magnetic field strength at all three radio frequencies is presented in

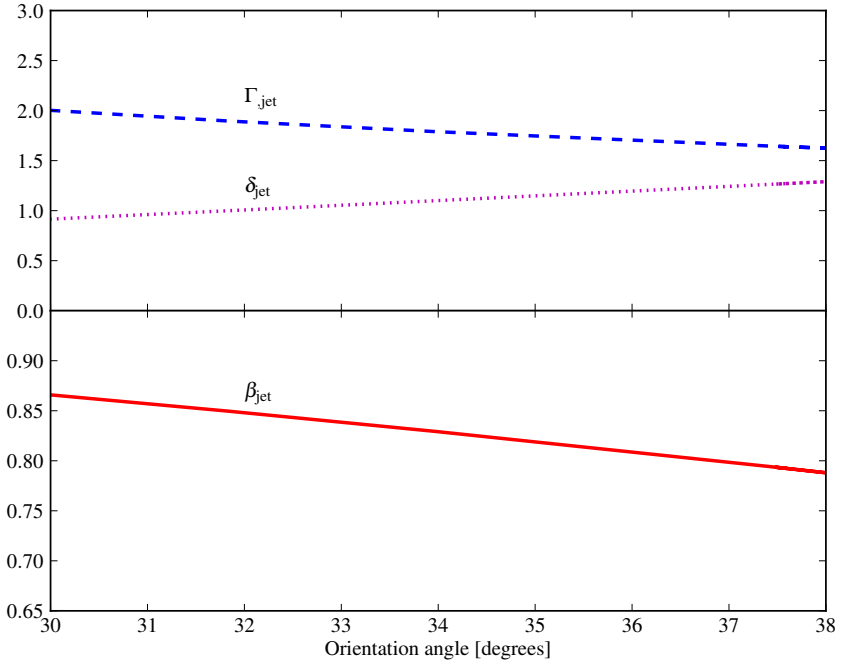

Figure 7.8: Intrinsic jet velocity $\beta_{\rm jet}$ (solid red line), Lorentz factor $\Gamma_{\rm jet}$ (dashed blue line) and Doppler factor $\delta_{\rm jet}$ (dotted magenta line) of the inner jets in 3C 371, as a function of the angle θ between the jet and the line of sight.

Table 7.3: Measured physical parameters of the inner jet in 3C 371 and its components

Component	$B_{\rm eq}$ (μG)	$P_{\rm min}$ (10^{-9} dyn cm^{-2})	$U_{\rm min}$ (10^{-9} ergs cm^{-3})	$E_{\rm min}$ (10^{55} ergs)
Jet total.....	239	1.52	4.55	25.7
Knot A.....	142	0.53	1.60	0.36
Knot B.....	136	0.49	1.46	0.34
Hotspot.....	177	0.83	2.49	1.23

Notes: Physical quantities derived from 0.3″ resolution radio map constructed at 1.5 GHz using our combined *e*-MERLIN plus VLA datasets.

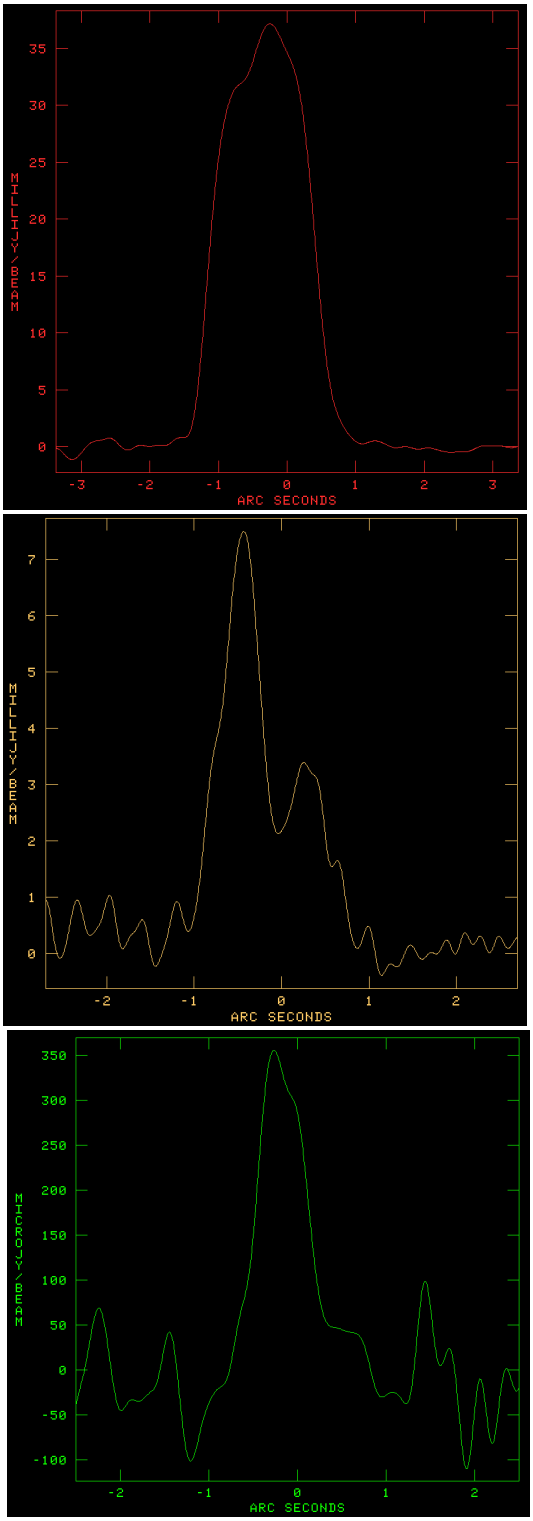

Figure 7.9: Brightness intensity profiles of the inner jets in 3C 371 derived from maps convolved with a circular beam of size 0.3 arcsec FWHM. Top: profile at 144 MHz. Middle: profile at 1.5 GHz. Bottom: profile at 8.5 GHz.

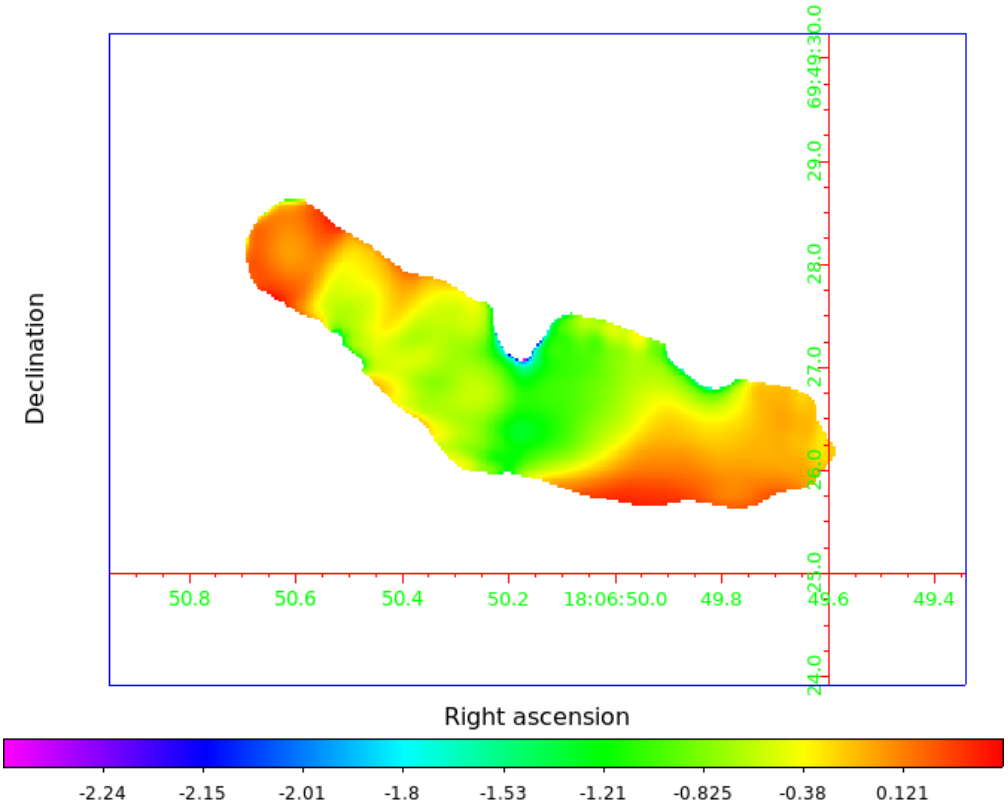

Figure 7.10: Map of spectral index, α of the inner jets in 3C 371 constructed from maps made at two frequencies ($\sim$ 150 MHz and $\sim$ 1.5 GHz) at 0.3–arcsec resolution. α is in the range -0.1 to -1.5 and is plotted at 5σ rms noise cut-off in total intensity.

Table 7.4: Fitting results from minimum energy for synchrotron emitting electrons in the inner jets of 3C 371

$B_{\rm eq}$	$\nu_{\rm b}^{*}$	$\tau_{\rm syn}$
(nT)	(MHz)	(10^5 yrs)
(1)	(2)	(3)
8.26	150	47
12.80	1500	7.8
11.10	8500	4.1

Notes: Col.(1): derived equipartition field strength. Col.(2): adopted break frequency. Col.(3): radiative lifetime of synchrotron emitting electrons.

Table 7.4. The quantities here are obtained from maps created with equivalent resolution (i.e., $0.3''$) following minimum energy assumptions as described in Section 5.6.

7.7 Discussion

Our multiwaveband images show the jet in the BL Lac object 3C 371 to be well resolved from radio to X-rays in a direction perpendicular to the jet axis. There is no detection of a counterjet in our radio images. Our data agree very well with previous works (e.g. Sambruna et al. 2007) and provide strong evidence of a core-dominated source as common for BL Lacs (e.g. Perlman & Stocke 1994). At high resolutions (i.e., $0.13''$ resolution; Figure 7.2), there is very clear evidence of a double asymmetric radio knots located at $1.3''$–$1.8''$ away from the compact core. To put this into context, until now, no detailed sub-arcsecond observations of the radio knots we observe at the jet base have been reported in the literature. Previous works by Wrobel & Lind (1990), Akujor et al. (1994), Nilsson et al. (1997) and others following have rather reported the radio hotspot which is located $\sim 3''$ from the core as a bright knot in 3C 371. We note here that Pesce et al. (2001) have reported features of knot B (but not A); instead, labelling the component at about $3''$ from the core as knot A. It is entirely plausible that their observations may have been affected by limited sensitivity and spatial resolution. For comparison, the knots we observe have been detected by Gómez & Marscher (2000) on milliarcsecond scales using space VLBI observations of 3C 371 at 4.8 GHz. Gómez & Marscher (2000) interpret the knots as being stationary features in the jet such as standing shocks. The spectral index between 144 MHz and 1.5 GHz for the optically thick core is very flat ($\alpha = -0.11 \pm 0.01$), and the components have a relatively steeper spectral index: -0.59 ± 0.02 for knot A, -0.88 ± 0.02 for knot B, and -0.68 ± 0.02 for hotspot, compared with the total radio spectral index of -0.37 ± 0.01 for the jet (see Table 7.2). Using available data from the literature, Nilsson et al. (1997) fitted a slope of -0.81 for the broadband spectrum of the hotspot component.

In Figure 7.8 we show constraints for the product $\beta_{\rm jet}\cos\theta$ of the jets in 3C 371. We infer highly relativistic speeds, $\beta_{\rm jet} = 0.81c$ for the inner jets in 3C 371. Our derived jet-to-counterjet brightness ratio is 430:1, implying an orientation angle $\theta = 35^\circ$ and a Lorentz factor, $\Gamma_{\rm jet} = 1.7$ (Doppler factor, $\delta_{\rm jet} = 1.2$). For comparison, Gómez & Marscher (2000) measured a sidedness ratio of 1700:1, corresponding to $\theta \lesssim 18^\circ$ and $\Gamma_{\rm jet} \gtrsim 3.2$, which is however difficult to reconcile

with our estimates. In the simplest scenario, the observed structure and intermediate classification suggests that 3C 371 is most likely seen at moderate viewing angles, plausibly near our derived upper limit of $\sim 35^{\circ}$. We note that for such an orientation with respect to the observer, a high velocity jet is expected to be strongly de-boosted; $\delta_{\rm jet} \approx [\Gamma_{\rm jet}\,(1 - \beta_{\rm jet}{\rm cos}\theta)]^{-1}$ becoming smaller for increasing velocities. Thus, if the jet were to remain relativistic beyond $2''$ from the core, then differences in $\delta_{\rm jet}$ along the jet could produce apparent brightenings, consistent with velocity structure in the jets as suggested in previous studies (e.g. Chiaberge et al. 2000) to reconcile BL Lacs and FR I radio galaxies in the unification scheme. In this regime, a limb-brightened jet structure consistent with the total intensity structures we observe is expected; where a brighter external lower velocity region of the jet surround an inner high velocity spine such that different velocity components dominate the emission at different angles. Tavecchio, Ghisellini & Guetta (2014) have proposed transversely stratified jets in BL Lacs as possible sources of high-energy (0.1–1) PeV neutrinos. Emission profiles transverse to the jet axis taken at the three different frequencies are shown in Figure 7.9. The main apparent feature is that the jet profiles are resolved at all three frequencies consistent with the longitidunal structures; the FWHM is $\simeq 2''$ at 144 MHz.

We report physical quantitites derived for the inner jets in 3C 371 and its components in Table 7.3. These show that our derived intensity of the equipartition magnetic field in the components are relatively constant, and suggest that the electron energy distribution plausibly does not change considerably along the inner jet, consistent with earlier report by Scarpa et al. (1999). The hotspot is slightly overpressured ($P_{\rm min}$ = 0.83$\times 10^{-9}$ dyn cm^{-2}) compared with the two knots, and the energy supplied by the components altogether ($E_{\rm min}$ = 1.93$\times 10^{55}$ ergs) is about an order of magnitude lower than the total energy budget ($E_{\rm min}$ = 25.73$\times 10^{55}$ ergs) of the source. This supports the conclusion that the bulk of the radio emission in 3C 371 is contributed by the compact and energetic nucleus of the host galaxy. Snyder et al. (1982) have looked at the energy curves (optical to X-ray) in 3C 371 and also find that the light of this BL Lac object is dominated by a central component of nonthermal energy. The values we find for radiative life-times are typically of the order of a few 10^5 years for the electrons emitting at GHz frequencies (see Table 5.4) and increases towards lower frequencies. For comparison, Perley & Johnston (1979) reported a radiative lifetime of 5.0$\times 10^5$ yrs for electrons radiating at 5 GHz in 3C 371. Since ageing is less relevant at lower frequencies, and considering our estimates ($\tau_{\rm syn} \approx 10^5$ yrs at GHz frequencies) for the inner jets, indicate that, 3C 371 is ralatively young when compared

with both the sources studied here and other low luminosity radio galaxies in previous works (e.g. Parma et al. 1999; 2007). The radio spectral index distribution obtained between 150 MHz and 1.5 GHz (Figure 7.10) is fairly flat, consistent with a core-dominated source. In the standard model, constant injection of a fresh population of relativistic electrons near the core is expected. These young electron-emitting populations have the tendency to flatten the synchrotron spectrum, and is qualitatively in agreement with our observed spectral index distribution in 3C 371.

8

Summary, conclusions and future work

8.1 Summary

We have presented the highest resolution and sensitivity maps of a sample of six extragalactic radio sources, derived from multifrequency, multiwavband observations with *e*-MERLIN, LOFAR and VLA (at radio wavelengths); HST (at optical wavelength); and Chandra (at X-ray wavelength). There is clear evidence of distinct symmetrical radio to X-ray jets in our sample. Total intensity and spectral images at metre wavelength (constructed at 6-arcsec resolution) and cm-wavelength (constructed at sub-arcsecond resolutions) for the sources are also presented. The metre wavelength images we show here are the first ever made for these sources at such low frequencies (144 MHz) and resolutions ($\sim$ 0.3 arcsec). A comprehensive description of the kpc-scale jet properties of the individual sources (except M 87) has also been presented (cf. Chapter 4). These have allowed us to characterize the configuration of old radio-emitting plasma in our sample with high precision, and draw conclusions on the host galaxies and their environment; we also report detection of several new features such as loops and blobs. For three of the sources in our sample (i.e., 3C 83.1B, 3C 264 and 3C 371) we have also examined jet physics, orientation effects and energetics of the inner jets (cf. Chapters 5–7). The data are particularly relevant for exploring the dynamics and kinematics of radio jets in the vicinity of the AGN, and testing models of jet deceleration in FR Is from relativistic to sub-relativistic speeds on scales of $1\sim10$ kpc. We emphasize here that much of the analysis in the present work is based on the radio data. Detailed multiwaveband analysis of the complete sample will be presented in future work

(Bempong-Manful et al., in progress). Preliminary results from our ongoing numerical simulation efforts are also presented in Appendix E. Altogether, these systematic and comprehensive multiwaveband studies of the electron populations and magnetic field sub-structures when combined with the state-of-the-art numerical simulations, will provide new insights into the physics driving the observed jet structure in extragalactic radio sources and allow for new constraints on jet physics.

8.2 Conclusions

The main conclusions from our analysis of the kpc-scale jets (cf. Chapter 4) are as follows:

a) In all cases, our derived minimum energy densities lie in a relatively narrow range [$\Delta_{U_{\rm min}}$ = 0.670 pJ m^{-3}], consistent with a mild variation [$\Delta_{B_{\rm eq}}$ = 0.688 nT] in equipartition magnetic field strength (Table 4.2). If we make realistic assumptions about the ambient gas density and allow for slight deviations from the minimum-energy conditions, then from pressure balance arguments, the work done, $p\Delta V \simeq 10^{51}$ J by the lobes on the environment in our sample is very similar. This plausibly hints at comparable local environment assuming the cluster atmospheres in our sample to be spherical – thus, the derived energetics based on the larger source sizes, and surface brightness at the location of the jet lobes suggest the sources must lie anywhere between a few and a few hundred core radii.

b) Except for 3C 371 which shows an overall flat spectrum, the low-frequency spectral indices of the four radio galaxies in our sample steepen in the outer regions. This is particularly the case for the eastern lobe of 3C 83.1B in which there seems to be a sharp transition in the spectral index (from flat to steep) going into the tail. If the tail were re-excited plasma by the passage of NGC 1265 near it, then in principle, the observed steep spectra is as expected for a radio relic. However, given that the steep spectra of fossil plasma (assuming no re-acceleration from the ICM) make them difficult to observe at low frequencies ($\leq$ 140 MHz; e.g. Vazza et al. 2021), we argue that the eastern lobe of 3C 83.1B plausibly formed from outflow from the source, and that, the observed steep spectrum is a consequence of radiative and adiabatic losses.

c) Our derived radiative ages for relativistic electrons emitting at about 150 MHz are of the order of several 10^7 years. This implies that the bulk flow speeds must be $> 0.05c$ in order to reach the physical scales ($\sim$ 3 Mpc) where age effects become manifest – if there is no

reacceleration or adiabatic losses. These ages appear to correlate with the source linear sizes (a few hundred kpc) except the BL Lac object 3C 371. If the apparent (projected) linear size of a source is a proxy for age, then the radio galaxies studied here reinforce such a relation; although a separate physical interpretation may well be required for the physics of source age and dynamics in BL Lacs.

The principal results from our detailed study of the jet bases (cf. Chapters 5–7) are as follows:

a) 3C 83.1B: The inner jets in 3C 83.1B is well resolved in our radio and X-ray images and show clear evidence of multiple bright knotty structures at the jet base. The observed wiggles in the jet morphology can be explained in terms of dynamical instabilities in the flow propagation (e.g. O'Dea & Owen 1987), and we interpret the mild spectral differences across the source and its components as a direct consequence of ageing and expansion effects. There is good correspondence between features of the jet observed at all three frequencies. The transverse total intensity structure of the inner jets is very asymmetric; the profiles show the knots are brighter in the east jet. Our derived radio spectrum for the source and its components provide evidence of spectral steepening towards higer frequencies with a total radio spectral index ($\alpha_{150\ \mathrm{MHz}}^{1.5\ \mathrm{GHz}} = -0.78$) consistent with a synchrotron emission mechanism. Our estimate of mildly relativistic speeds ($\beta_{\rm jet} = 0.2c$) for the inner jets in 3C 83.1B is in good agreement with typical values found for weaker Type-I radio sources, whose properties are consistent with the hypothesis that the jets slow down from relativistic to sub-relativistic velocities on scales of 1$\sim$2 kpc (e.g. Parma et al. 1994). We suggest entrainment of ambient material as the main trigger of jet deceleration in 3C 83.1B. For an orientation, $\theta = 80^{\circ}$ and intrinsic jet speed, $\beta_{\rm jet} = 0.2$, we derive a Lorentz factor, $\Gamma_{\rm jet}$ of 1.0 which corresponds to a Doppler factor, $\delta_{\rm jet} = 1.3$. These values are consistent with a bulk deceleration of the flow speeds within the inner jets and hints at plausibly ongoing particle acceleration – at least in the regions close to the inner core where the knots are visible – most likely via steady velocity shear. Our derived physical quantities suggests the total energy input from the west jet is about 40% higher than the east jet although the energy budget of the knots are comparable. We measure average minimum pressure of 0.91×10^{-12} dyn cm^{-2} for the source. Comparing our derived quantities with ram pressure estimates from the ICM, $P_{\rm ICM}\, r_{\rm gal} \simeq 1.4\times10^{-12}$ dyn cm^{-2} ($r_{\rm gal} \simeq 1.45$ Mpc) (Pfrommer & Jones 2011) indicates that the inner

jets in 3C 83.1B are highly overpressured compared with the surrounding ICM – an observation which could well have consequences for bulk flow speeds at the jet base. For an injection index, $\alpha = -0.6$, we find $U_{\rm min} = 1.63\times10^{-11}$ ergs cm^{-3} for the electrons radiating at 1.5 GHz and estimate a synchrotron lifetime of 4.2×10^{7} years. This age is well in agreement with the typical values 4–67 Myrs (median age, $\tau_{\rm syn} \simeq 16$ Myrs) derived for currently active galaxies of similar radio power and luminosity (see Parma et al. 1999; 2007). Such lifetime estimates implies that relativistic electrons created in and around the central engine could travel the entire ~ 25 kpc length of the inner jets within their lifetime for bulk velocities of $v_{\rm bulk} > 0.05c$ – if there is no reacceleration or adiabatic losses.

b) 3C 264: Our high resolution multifrequency observations of this source show that the jet is well collimated and brightest within the first $1''$ ($\sim$ 400 pc). This region coincides with the radius of the dust ring aound the host galaxy core reported by Baum et al. (1997). Beyond $2''$ ($\sim$ 900 pc) from the core, the jet begins to expand, with the jet width increasing from $0.7''$ to $2''$ over a distance of about 1.3 kpc in linear scale before bending to the N-W at an angular distance of $5''$. The transverse intensity distribution of the inner structure confirms differences in the brightness distribution of the jet consistent with plausible velocity stratification within the inner relativistic jet as reported in previous studies. We suggest something dynamical in the surrounding medium or gravitational interaction with close companion galaxy, IC 2955 to be responsible for the remarkable sub-arcsecond bends in the inner jets of 3C 264. We measure an intrinsic speed of $0.42c$ which constrains the jet viewing angle θ to assume relatively large values ($52^\circ \lesssim \theta \lesssim 74^\circ$). The corresponding Doppler and Lorentz factors here are respectively $\delta_{\rm jet} = 1.7$ and $\Gamma_{\rm jet} = 1.1$. These estimates are in good agreement with values reported by Baum et al. (1997), and when compared with the higher initial VLBI jet velocities of $\sim 0.99c$ ($\Gamma = 7$) for the inner 300–400 pc (e.g. Lara et al. 2004), a deceleration of the order of a factor 2 from the initial parsec-scale jet can be inferred. The estimates of radiative lifetime of electrons emitting at all three frequencies are very similar, at about 3 Myr. This agreement, although could be just a coincidence, provides a rather complex indication that radiative losses may be less relevant to the physical processes of the inner jets in 3C 264 on sub-kpc scales. Thus, the observed variation in the spectrum is likely due to changes in local magnetic fields and/or other loss processes. Map of the spectral index distribution shows a flat spectrum filament embedded in a relatively steep sheath of diffuse emission. We suggest this spectral behaviour could be evidence of local reacceleration of

relativistic electrons within the inner jets in 3C 264.

c) 3C 371: Our observations are consistent with a core-dominated source, with the central core emitting $\gtrsim 50\%$ of the total flux across all three frequencies. Our high resolution observations reveal evidence of a double asymmetric radio knots located at $1.3''$–$1.8''$ away from the compact core and a radio hotspot $\sim 3''$. These knots could be interpreted in the context of stationary features in the jet such as standing shocks. The radio spectral index between 144 MHz and 1.5 GHz for the optically thick core is very flat ($\alpha = -0.11$), and the components have a relatively steeper spectral index compared with the total source. We find similar magnetic field strengths in all jet components, and suggest that the electron energy distribution plausibly does not change considerably along the inner jet. We infer highly relativistic speeds, $\beta_{\rm jet} = 0.81c$ and an orientation angle, $\theta = 35^{\circ}$ for the inner jets in 3C 371. The values we find for the radiative lifetime of electrons emitting at GHz frequencies is of the order of a few 10^5 years, consistent with previous works and suggests that the jets in 3C 371 are relatively young compared with the other sources studied here.

8.3 Future work

As next step, we aim to complete analysis on the inner jets for the other three sources (i.e., 3C 274, 3C 296 and 3C 465) in our sample, similar to the analysis done in the present work. Time constraints have also not allowed us to make use of the full multiwavelength datasets in the present study. Thus, for future work, we plan to conduct a detailed multiwaveband analysis in our sample. This should help us generate spectral energy distributions for the individual sources in our sample and compare these with their broadband spectral indices to test beaming models of jets as done in previous studies (e.g. Trussoni et al. 2002; Perlman et al. 2010).

We will also fit spectral ageing models to the inner radio jet spectra using the Broadband Radio Astronomy ToolS `BRATS`[15] (Harwood et al. 2013; 2015) software package. For a given age and magnetic field, `BRATS` compute the model fluxes for each region in the radio map and compares them with the observed flux for the same regions at the frequency of the map, producing a set of χ^2 values, and outputting the best-fitting ages for each of the predefined and resolved regions in the map. This should allow us derive a more robust estimate of the synchrotron age

[15]BRATS is a publicly available spectral analysis software package that uses a variety of tools to derive the properties and morphology of a radio source. For more details, visit `http://www.askanastronomer.co.uk/brats/`

for the inner jets in our sample.

Aditionally, to fully address the research questions of the present study, a knowledge of the magnetic field configurations immediately surrounding these jets is required. Clearly, the observed strong synchrotron radio emission from our sample illustrate the presence of intergalactic magnetic field. Thus, as an extension of this work, we will construct polarised intensity maps of our sample and extract the Farady rotation measure structures to investigate the orientation and degree of ordering of magnetic field in the jet bases. This will further reinforce our understanding of the underlying physics driving the evolution of radio jets in extragalactic sources.

Finally to put all of the observational results into perspective, we will complete our ongoing numerical simulations for 3C 83.1B, and do further simulations for 3C 264 and 3C 465. These three sources in our sample reveal remarkable kpc-scale morphologies never seen before in such detail and therefore, modelling their large scale structures should allow us test evolutionary models of jet propagation in the dense ICM/IGM and place better constraints on the flow dynamics.

Appendices

Appendix A

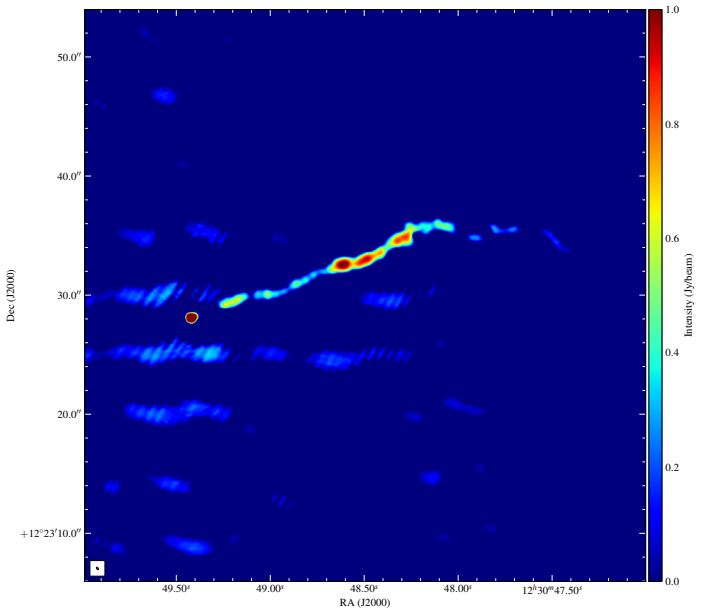

Figure A.1: Full synthesis image of the inner jets in 3C 274 (M 87) constructed at 1.5 GHz using the *e*-MERLIN array.

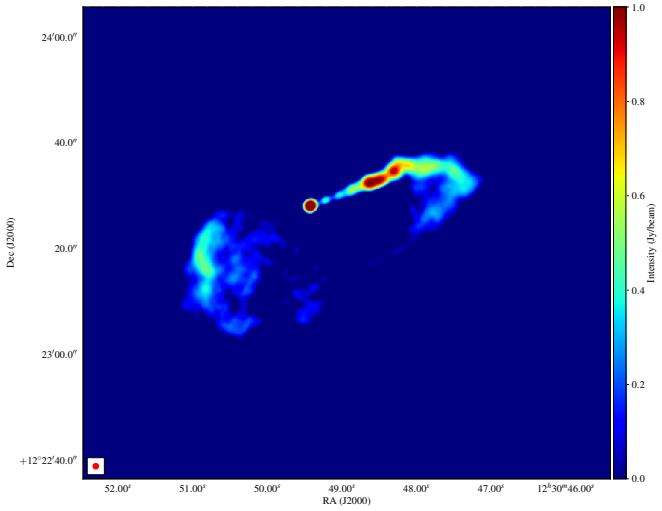

Figure A.2: Full synthesis image of the inner jets in 3C 274 (M 87) constructed with the VLA at L-band ($\sim$ 1.5 GHz) in A and B-configurations.

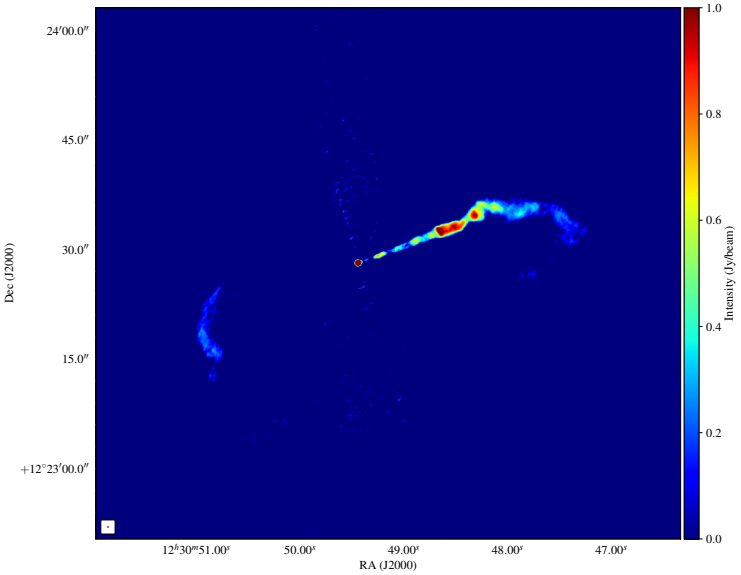

Figure A.3: Full synthesis image of the inner jets in 3C 274 (M 87) constructed with the VLA at X-band ($\sim$ 8.5 GHz) in A and B-configurations.

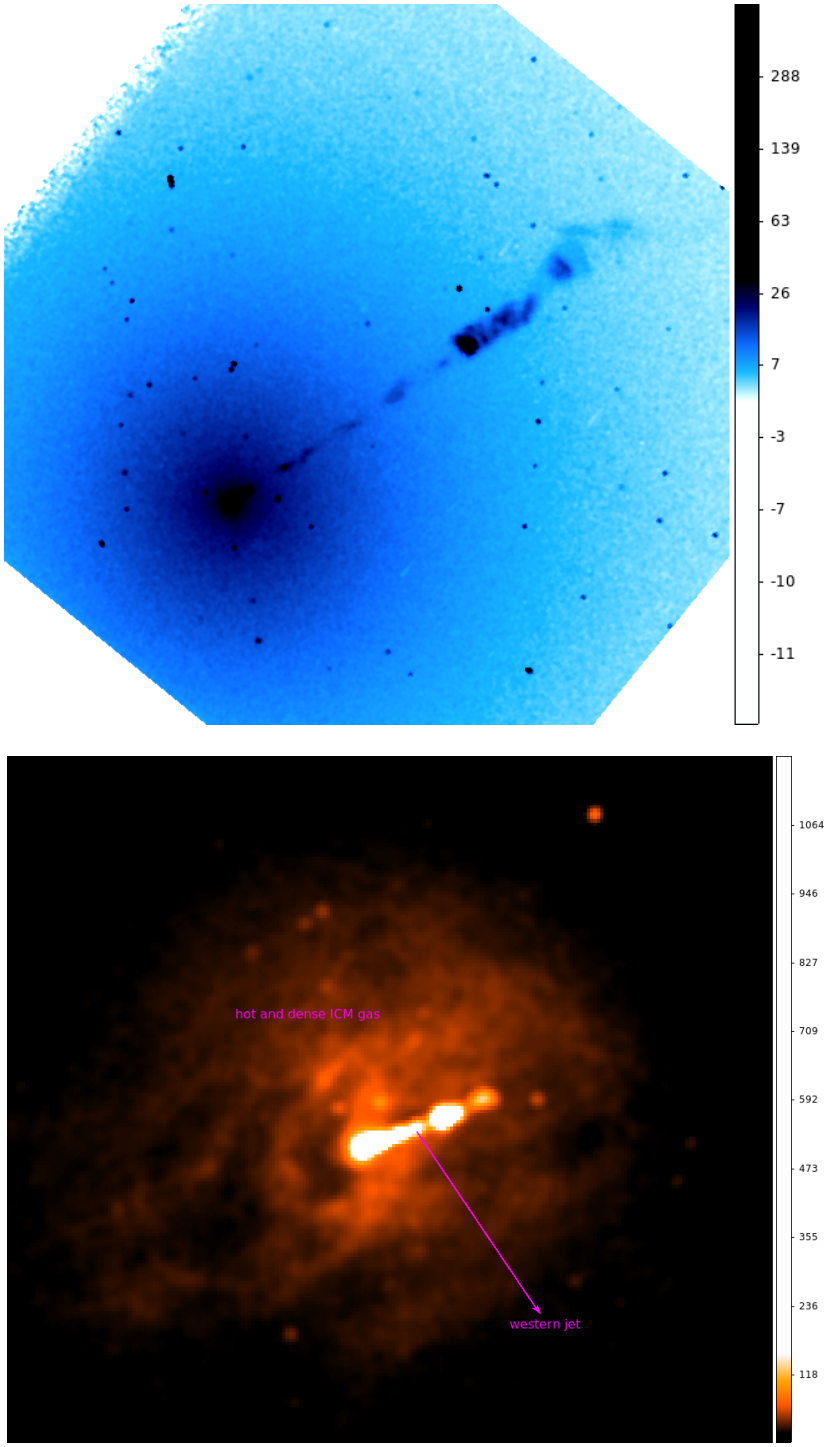

Figure A.4: Optical (HST) and X-ray (Chandra) images of 3C 274 (M 87) showing extension of the inner jet in the southwest direction as observed at radio wavelengths. Top: HST image at $\sim 0.5''$ resolution. Bottom: Chandra image at $\sim 0.5''$ resolution.

Table A.1: Properties of radio maps presented

Map	Restoring beam			Peak flux	Off-source	Figure
	Major axis	Minor axis	Pos. angle		noise	number
	(arcsec)	(arcsec)	(deg)	(mJy)	(μJy)	
VLA$^{\mathrm{L,AB}}$	1.31	1.25	-83.07	310.53	96.43	Fig.A.2
VLA$^{\mathrm{X,AB}}$	0.27	0.24	79.64	301.80	27.93	Fig.A.3
e-MERLIN$^{\mathrm{L}}$	0.23	0.12	30.75	2.43	70.72	Fig.A.1

Notes: The superscripts L and X respectively denote $\sim$ 1.5 GHz and $\sim$ 8.5 GHz observing frequency deployed in our present study; A & B represent the array configuration of the VLA observations.

Appendix B

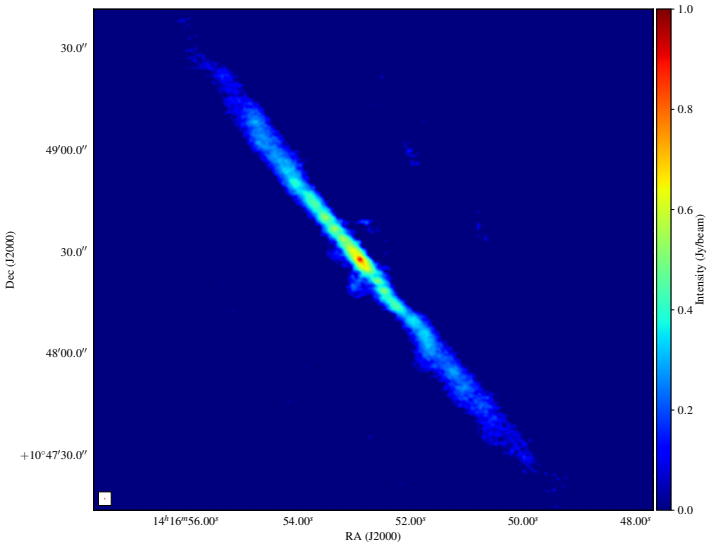

Figure B.1: Full synthesis image of the inner jets in 3C 296 constructed at 144 MHz using LOFAR HBA array.

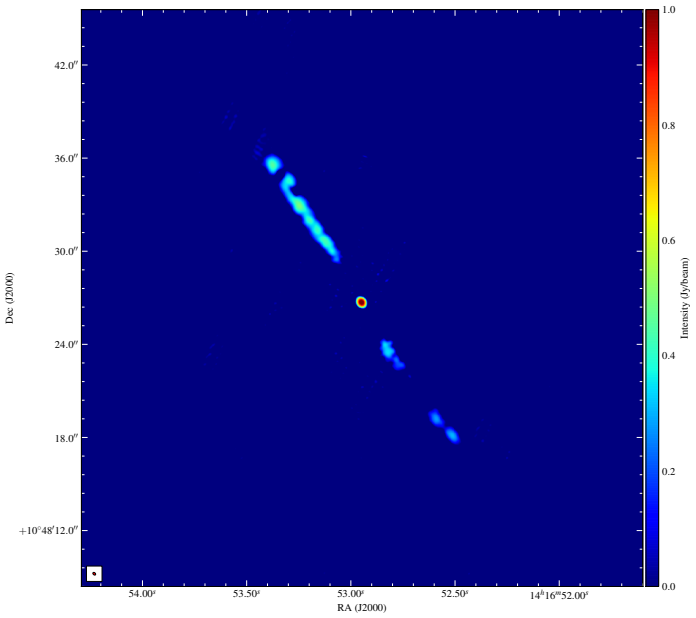

Figure B.2: Full synthesis image of the inner jets in 3C 296 constructed at 1.5 GHz using the *e*-MERLIN array.

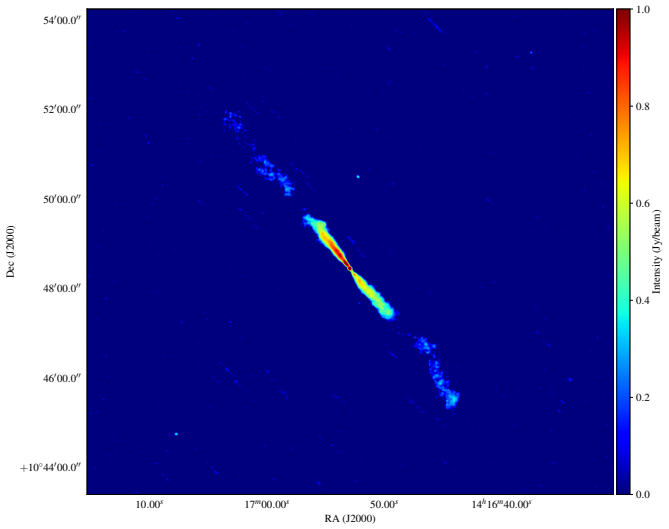

Figure B.3: Full synthesis image of the inner jets in 3C 296 constructed with the VLA at L-band ($\sim$ 1.5 GHz) in A and B-configurations.

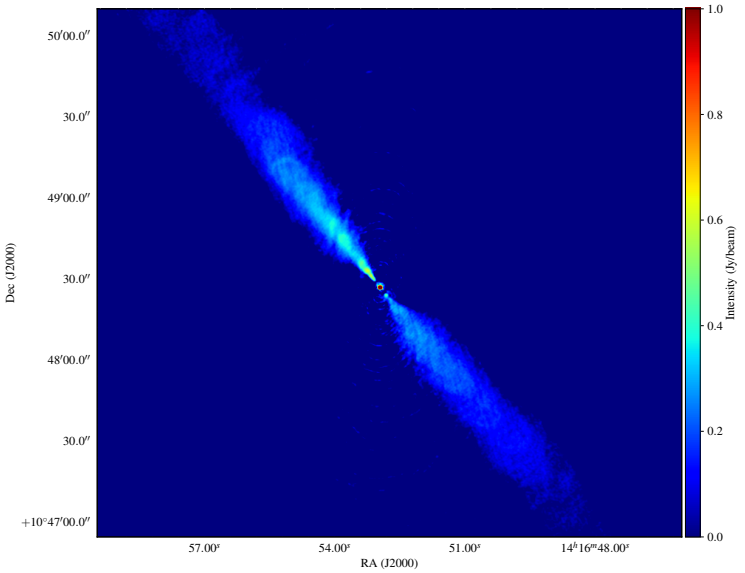

Figure B.4: Full synthesis image of the inner jets in 3C 296 constructed with the VLA at X-band ($\sim$ 8.5 GHz) in A and B-configurations.

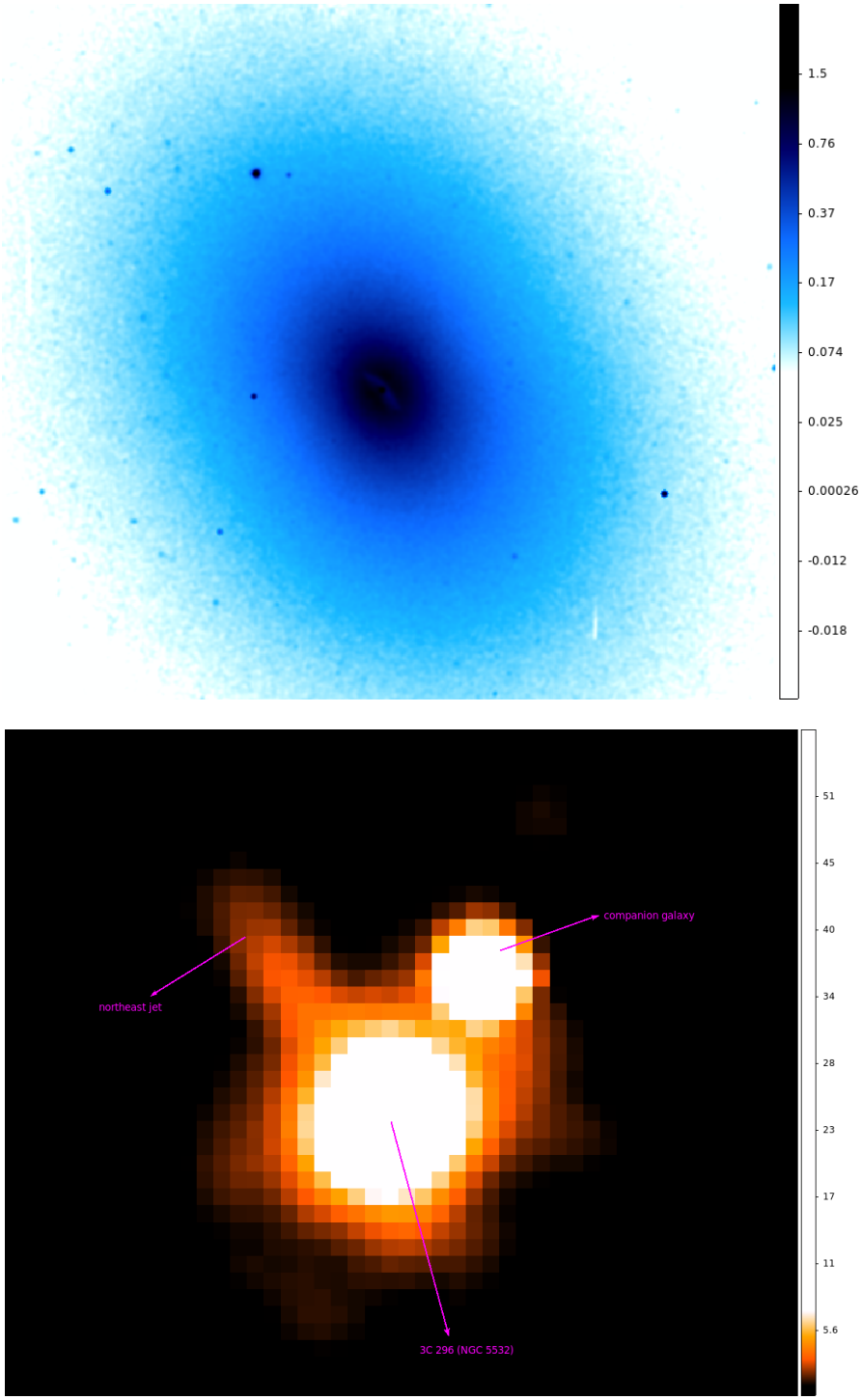

Figure B.5: Optical (HST) and X-ray (Chandra) images of 3C 296 showing extension of the inner jet in the southwest direction as observed at radio wavelengths. Top: HST image at $\sim 0.5''$ resolution. Bottom: Chandra image at $\sim 0.5''$ resolution.

Table B.1: Properties of radio maps presented

Map	Restoring beam			Peak flux	Off-source	Figure
	Major axis	Minor axis	Pos. angle		noise	number
	(arcsec)	(arcsec)	(deg)	(mJy)	(μJy)	
LOFAR	0.52	0.23	10.60	10.13	62.60	Fig.B.1
VLA$^{\mathrm{L,AB}}$	1.56	1.45	124.30	55.89	62.05	Fig.B.3
VLA$^{\mathrm{X,AB}}$	0.45	0.39	62.25	129.64	9.26	Fig.B.4
e-MERLIN$^{\mathrm{L}}$	0.22	0.15	54.64	75.64	20.45	Fig.B.2

Notes: The superscripts L and X respectively denote $\sim$ 1.5 GHz and $\sim$ 8.5 GHz observing frequency deployed in our present study; A & B represent the array configuration of the VLA observations.

Appendix C

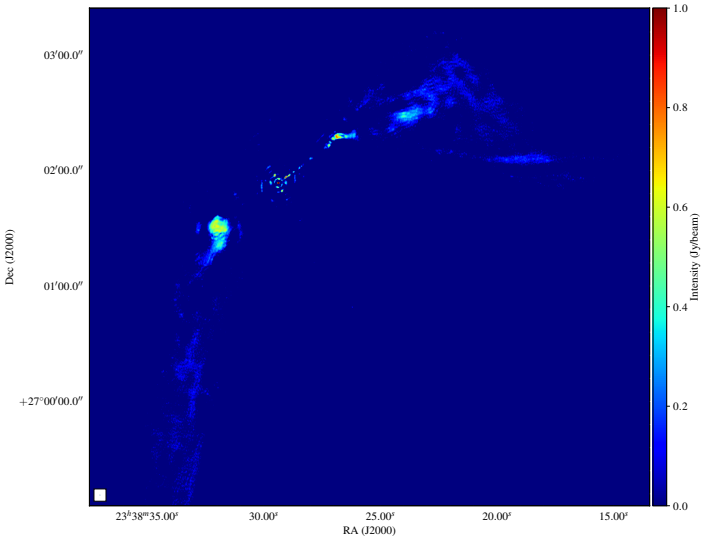

Figure C.1: Full synthesis image of the inner jets in 3C 465 constructed at 144 MHz using LOFAR HBA array.

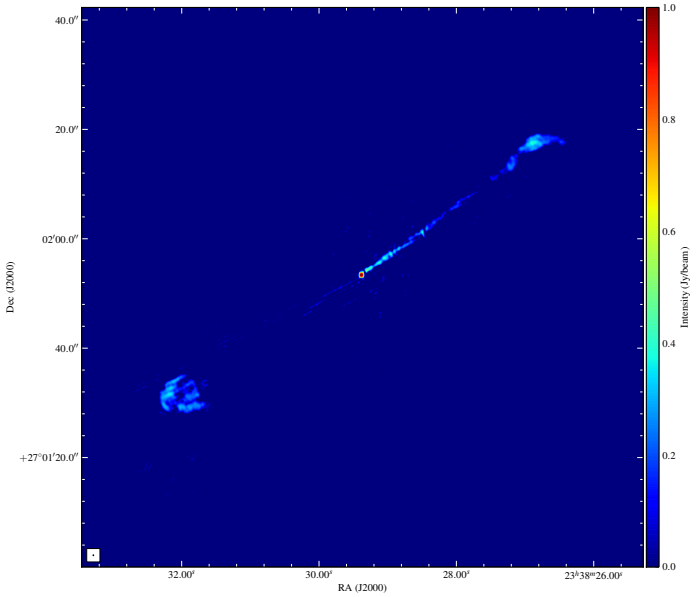

Figure C.2: Full synthesis image of the inner jets in 3C 465 constructed at 1.5 GHz using the *e*-MERLIN array.

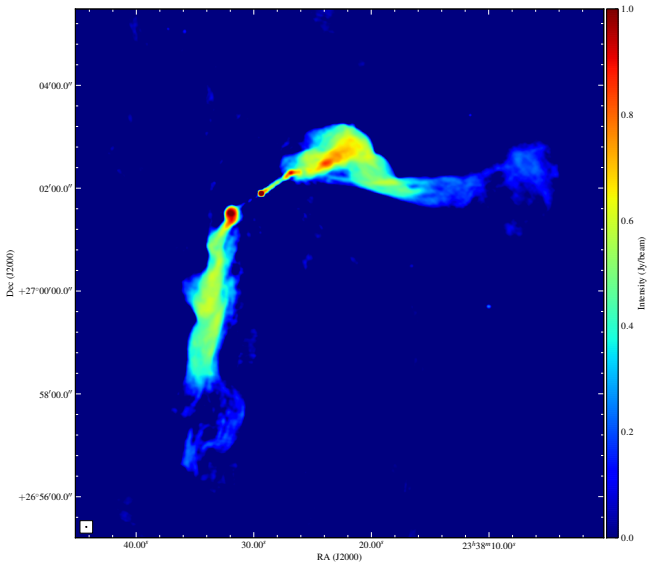

Figure C.3: Full synthesis image of the inner jets in 3C 465 constructed with the VLA at L-band ($\sim$ 1.5 GHz) in A and B-configurations.

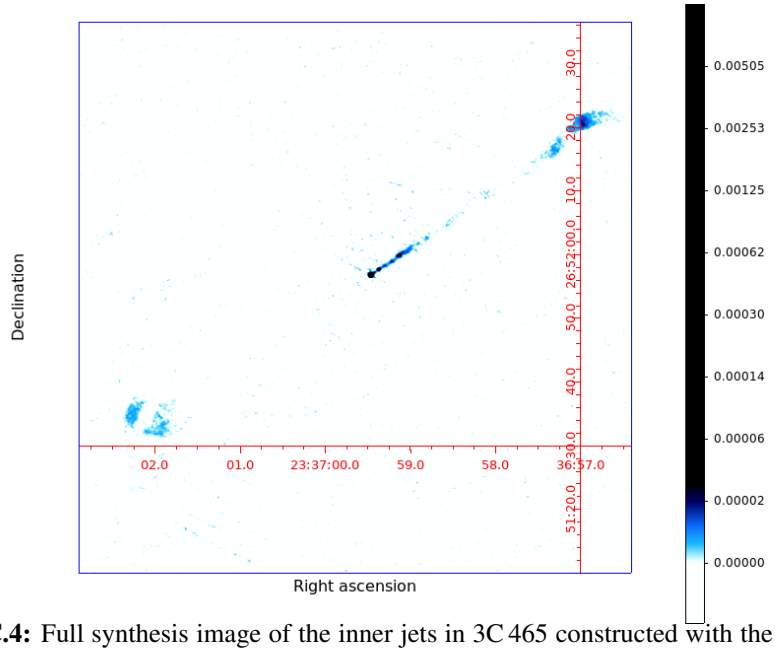

Figure C.4: Full synthesis image of the inner jets in 3C 465 constructed with the VLA at X-band ($\sim$ 8.5 GHz) in A and B-configurations.

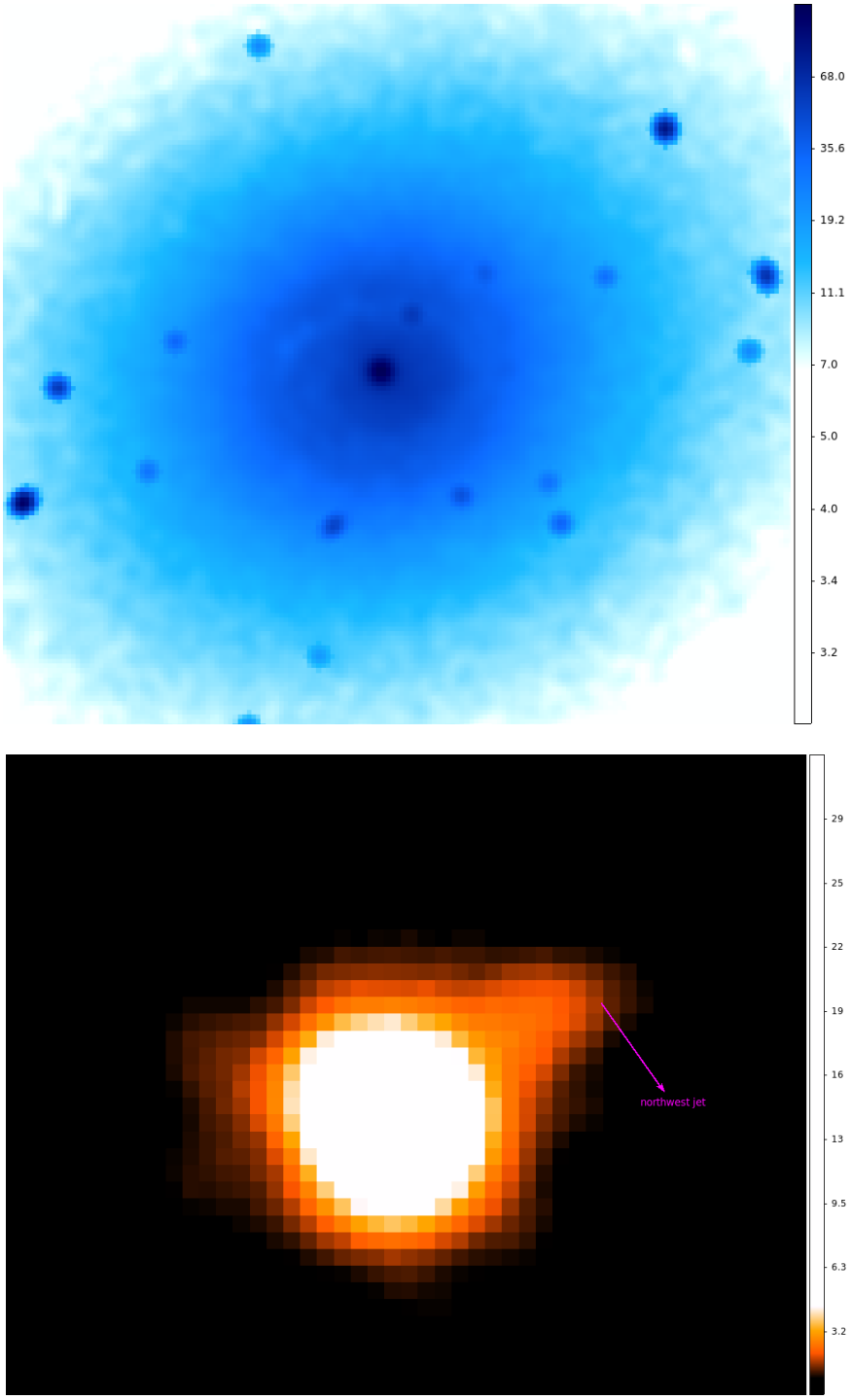

Figure C.5: Optical (HST) and X-ray (Chandra) images of 3C 465 showing extension of the inner jet in the southwest direction as observed at radio wavelengths. Top: HST image at $\sim 0.5''$ resolution. Bottom: Chandra image at $\sim 0.5''$ resolution.

Table C.1: Properties of radio maps presented

Map	Restoring beam			Peak flux	Off-source	Figure
	Major axis	Minor axis	Pos. angle		noise	number
	(arcsec)	(arcsec)	(deg)	(mJy)	(μJy)	
LOFAR	0.41	0.29	5.88	237.02	96.32	Fig.C.1
VLA$^{\rm L,AB}$	1.37	1.13	71.02	206.15	34.64	Fig.C.3
VLA$^{\rm X,AB}$	0.23	0.22	88.09	25.75	2.64	Fig.C.4
e-MERLIN$^{\rm L}$	0.17	0.12	30.71	207.49	31.05	Fig.C.2

Notes: The superscripts L and X respectively denote $\sim$ 1.5 GHz and $\sim$ 8.5 GHz observing frequency deployed in our present study; A & B represent the array configuration of the VLA observations.

Appendix D

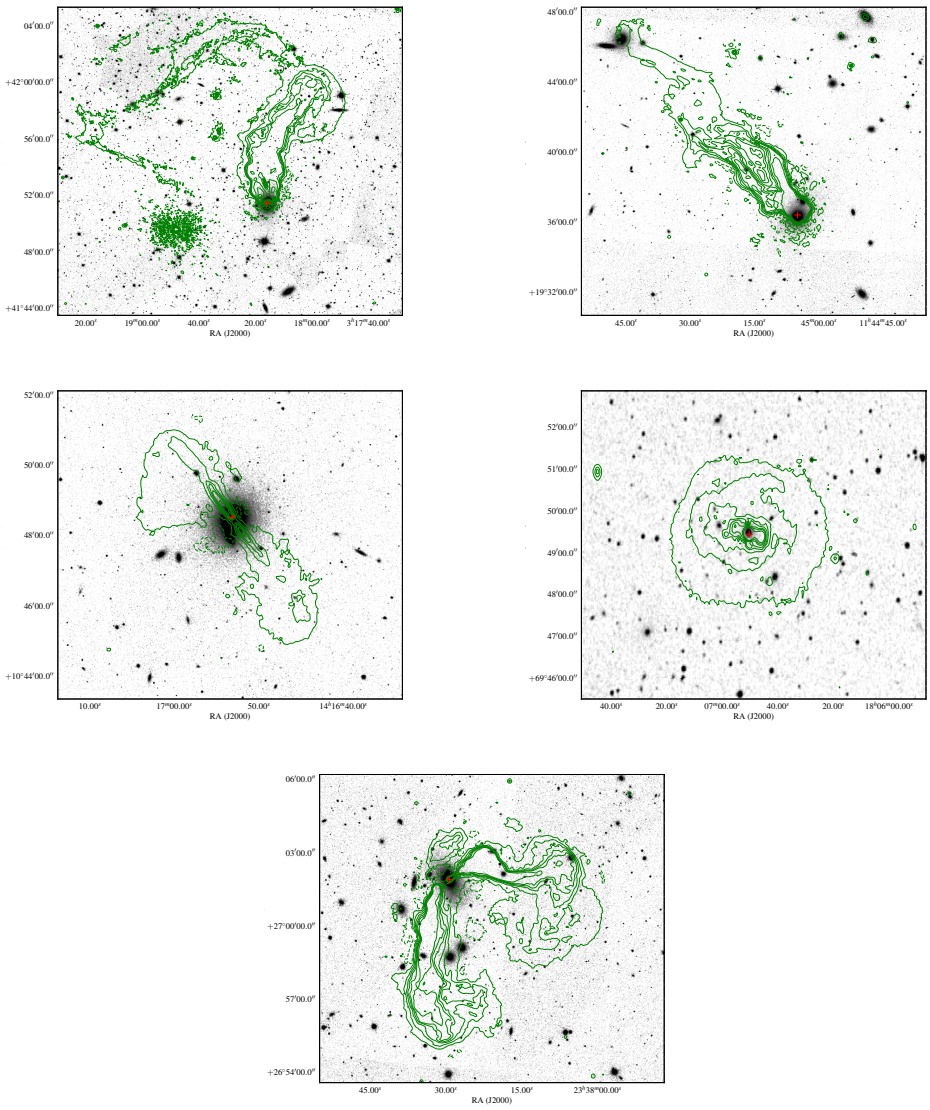

Figure D.1: LOFAR 150-MHz contours of constant radio surface brightness are shown (in green) superposed on the optical images of the individual galaxies from (SDSS z-band; 3C 83.1B, 3C 264, 3C 296, 3C 465) and (DSS; 3C 371) in greyscale. The red cross symbol indicates positions of the radio galaxy core coincident with the optical host galaxy location.

Bibliography

Aab A., Abreu P., Aglietta M., Albuquerque I. F. M., Albury J. M., Allekotte I., Almela A., et al., 2018, ApJ, 868, 4.

Ables J. G., 1974, A&AS, 15, 383.

Akujor C. E., Luedke E., Browne I. W. A., et al., 1994, A&AS, 105, 247.

Alfvén H., 1942, Natur, 150, 405.

Antonucci R., 1993, ARA&A, 31, 473.

Angel J. R. P., Stockman H. S., 1980, ARA&A, 18, 321.

Argo M., 2015, arXiv, arXiv:1502.04936.

Athreya R., 2009, ApJ, 696, 885.

Attridge J. M., Roberts D. H., Wardle J. F. C., 1999, ApJL, 518, L87.

Aversa R., Lapi A., de Zotti G., Shankar F., Danese L., 2015, ApJ, 810, 74.

Baade W., Minkowski R., 1954, ApJ, 119, 215.

Baan W. A., Fridman P. A., Millenaar R. P., 2004, AJ, 128, 933.

Baars J. W. M., Genzel R., Pauliny-Toth I. I. K., Witzel A., 1977, A&A, 500, 135.

Baes M., Clemens M., Xilouris E. M., Fritz J., Cotton W. D., Davies J. I., Bendo G. J., et al., 2010, A&A, 518, L53.

Bahcall J. N., Kirhakos S., Saxe D. H., Schneider D. P., 1997, ApJ, 479, 642.

Baldi R. D., Chiaberge M., Capetti A., Sparks W., Macchetto F. D., O'Dea C. P., Axon D. J., et al., 2010, ApJ, 725, 2426.

Baldi R. D., Capetti A., Giovannini G., 2016, AN, 337, 114.

Barthel P. D., 1989, ApJ, 336, 606.

Bassani L., Dadina M., Maiolino R., Salvati M., Risaliti G., Della Ceca R., Matt G., et al., 1999, ApJS, 121, 473.

Baum S. A., O'Dea C. P., Giovannini G., Cotton W. B., de Koff S., Feretti L., Golombek D., et al., 1997, ApJ, 483, 178.

Baum S. A., O'Dea C. P., Murphy D. W., de Bruyn A. G., 1990, A&A, 232, 19.

Beck R., Krause M., 2005, AN, 326, 414.

Bempong-Manful E., Hardcastle M. J., Birkinshaw M., et al., 2020, MNRAS, 496, 676.

Bennett A. S., 1962, MNRAS, 125, 75.

Benson A. J., Bower R. G., Frenk C. S., Lacey C. G., Baugh C. M., Cole S., 2003, ApJ, 599, 38.

Beskin V. S., Nokhrina E. E., 2006, MNRAS, 367, 375.

Best P. N., Heckman T. M., 2012, MNRAS, 421, 1569.

Bianchi S., Maiolino R., Risaliti G., 2012, AdAst, 2012, 782030.

Bicknell G. V., 1994, ASPC, 54, 231.

Bicknell G. V., 1995, ApJS, 101, 29.

Bicknell G. V., Begelman M. C., 1996, ApJ, 467, 597.

Bicknell G. V., 2002, NewAR, 46, 365.

Biggs A. D., Ivison R. J., 2008, MNRAS, 385, 893.

Bird J., Martini P., Kaiser C., 2008, ApJ, 676, 147.

Biretta J. A., Zhou F., Owen F. N., 1995, ApJ, 447, 582.

Biretta J. A., Sparks W. B., Macchetto F., 1999, ApJ, 520, 621.

Birk G. T., Lesch H., 2000, ApJL, 530, L77.

Birkinshaw M., 1991, MNRAS, 252, 505.

Birkinshaw M., Laing R., Scheuer P., Simon A., 1978, MNRAS, 185, 39P.

Birkinshaw M., Laing R. A., Peacock J. A., 1981, MNRAS, 197, 253.

Birkinshaw M., Rawes J., Worrall D., 2020, IAUGA.

Bîrzan L., McNamara B. R., Nulsen P. E. J., Carilli C. L., Wise M. W., 2008, ApJ, 686, 859.

Bisnovatyi-Kogan G., 2005, Ap&SS, 297, 9.

Blandford R. D., Rees M. J., 1974, MNRAS, 169, 395.

Blandford R. D., Znajek R. L., 1977, MNRAS, 179, 433.

Blandford R. D., Payne D. G., 1982, MNRAS, 199, 883.

Blandford R., Eichler D., 1987, PhR, 154, 1.

Blandford R. D., 2001, PThPS, 143, 182.

Blandford R., Meier D., Readhead A., 2019, ARA&A, 57, 467.

Bodo G., Ferrari A., Massaglia S., Rosner R., Vaiana G. S., 1985, ApJ, 291, 798.

Boccardi B., Krichbaum T. P., Ros E., Zensus J. A., 2017, A&ARv, 25, 4.

Boccardi B., Migliori G., Grandi P., et al., 2019, A&A, 627, A89.

Bohringer H., Nulsen P. E. J., Braun R., Fabian A. C., 1995, MNRAS, 274, L67.

Boksenberg A., Macchetto F., Albrecht R., Barbieri C., Blades J. C., Crane P., Deharveng J. M., et al., 1992, A&A, 261, 393.

Bondi H., 1952, MNRAS, 112, 195.

Bourdin H., Mazzotta P., 2008, A&A, 479, 307.

Braun R., 2013, A&A, 551, A91.

Brentjens M. A., de Bruyn A. G., 2005, A&A, 441, 1217.

Bridle A. H., Hough D. H., Lonsdale C. J., Burns J. O., Laing R. A., 1994, AJ, 108, 766.

Briggs F. H., Bell J. F., Kesteven M. J., 2000, AJ, 120, 3351.

Brunetti G., Setti G., Comastri A., 1997, A&A, 325, 898.

Burn B. J., 1966, MNRAS, 133, 67.

Burns J. O., Eilek J. A., Owen F. N., 1982, IAUS, 97, 45.

Cackett E. M., Horne K., 2006, MNRAS, 365, 1180.

Camenzind M., 2005, MmSAI, 76, 98.

Capetti A., Macchetto F., Axon D. J., Sparks W. B., Boksenberg A., 1995, ApJL, 452, L87.

Capetti A., Axon D. J., Macchetto F. D., Marconi A., Winge C., 1999, ApJ, 516, 187.

Capetti A., Trussoni E., Celotti A., Feretti L., Chiaberge M., 2000, MNRAS, 318, 493.

Casadio C., MacDonald N. R., Boccardi B., Jorstad S. G., Marscher A. P., Krichbaum T. P., Hodgson J. A., et al., 2021, A&A, 649, A153.

Celotti A., 2001, ASPC, 227, 105.

Cheung C. C., Harris D. E., Stawarz Ł., 2007, ApJL, 663, L65.

Chiaberge M., Celotti A., Capetti A., Ghisellini G., 2000, A&A, 358, 104.

Ching J. H. Y., Croom S. M., Sadler E. M., Robotham A. S. G., Brough S., Baldry I. K., Bland-Hawthorn J., et al., 2017, MNRAS, 469, 4584.

Churazov E., Brüggen M., Kaiser C. R., Böhringer H., Forman W., 2001, ApJ, 554, 261.

Cirasuolo M., Celotti A., Magliocchetti M., Danese L., 2003, MNRAS, 346, 447.

Clark B. G., 1980, A&A, 89, 377.

Clark B. G., 1999, ASPC, 180, 1.

Clarke D. A., Norman M. L., Burns J. O., 1986, ApJL, 311, L63.

Clarke D.A., Macdonald N.R., Ramsey J.P., Richardson M., 2008, Astrophysical Jets, La Physique au Canada, Vol. 64, No. 2.

Cohen R. D., 1983, ApJ, 273, 489.

Colina L., Perez-Fournon I., 1990, ApJS, 72, 41.

Collett E., 2005, Field guide to polarization, SPIE.

Condon J. J., Cotton W. D., Greisen E. W., et al., 1998, AJ, 115, 1693.

Cornwell T. J., 2008, ISTSP, 2, 793.

Croton D. J., Springel V., White S. D. M., De Lucia G., Frenk C. S., Gao L., Jenkins A., et al., 2006, MNRAS, 365, 11.

Curtis H. D., 1918, PLicO, 13, 9.

Das T. K., 1999, arXiv, astro-ph/9906113.

Dennett-Thorpe J., Bridle A. H., Laing R. A., Scheuer P. A. G., 1999, MNRAS, 304, 271.

de Gasperin F., Orrú E., Murgia M., Merloni A., Falcke H., Beck R., Beswick R., et al., 2012, A&A, 547, A56.

de Vaucouleurs G., de Vaucouleurs A., Corwin H. G., et al., 1991, rc3..book

Drake C. L., McGregor P. J., Dopita M. A., van Breugel W. J. M., 2003, AJ, 126, 2237.

Dunlop J. S., 1999, ASPC, 193, 133.

Eichler D., 1993, ApJ, 419, 111.

Eilek J. A., 1996, ASPC, 100, 281.

Erlund M. C., Fabian A. C., Blundell K. M., Moss C., Ballantyne D. R., 2007, MNRAS, 379, 498.

Evans D. A., Worrall D. M., Hardcastle M. J., Kraft R. P., Birkinshaw M., 2006, ApJ, 642, 96.

Event Horizon Telescope Collaboration, Akiyama K., Alberdi A., Alef W., Asada K., Azulay R., Baczko A.-K., et al., 2019, ApJL, 875, L1.

Fabian A. C., Rees M. J., 1995, MNRAS, 277, L55.

Fabian A. C., Sanders J. S., Taylor G. B., Allen S. W., Crawford C. S., Johnstone R. M., Iwasawa K., 2006, MNRAS, 366, 417.

Fabian A. C., 2012, ARA&A, 50, 455.

Falcke H., Körding E., Markoff S., 2004, A&A, 414, 895.

Falle S. A. E. G., Wilson M. J., 1985, MNRAS, 216, 79.

Fanaroff B. L., Riley J. M., 1974, MNRAS, 167, 31P.

Feretti L., Perley R., Giovannini G., Andernach H., 1999, MmSAI, 70, 129.

Ferrarese L., Merritt D., 2000, ApJL, 539, L9.

Fiore F., Feruglio C., Shankar F., Bischetti M., Bongiorno A., Brusa M., Carniani S., et al., 2017, A&A, 601, A143.

Forman W., Jones C., Churazov E., Markevitch M., Nulsen P., Vikhlinin A., Begelman M., et al., 2007, ApJ, 665, 1057.

Foster J. M., 2010, AAS.

Freedman W., 2002, A&G, 43, 1.10.

Frey S., Paragi Z., Fogasy J. O., Gurvits L. I., 2015, MNRAS, 446, 2921.

Fryxell B., Olson K., Ricker P., Timmes F. X., Zingale M., Lamb D. Q., MacNeice P., et al., 2000, ApJS, 131, 273.

Garrington S. T., Leahy J. P., Conway R. G., Laing R. A., 1988, Natur, 331, 147.

Gebhardt K., Thomas J., 2009, ApJ, 700, 1690.

Gendron-Marsolais M., Hlavacek-Larrondo J., van Weeren R. J., Rudnick L., Clarke T. E., Sebastian B., Mroczkowski T., et al., 2020, MNRAS, 499, 5791.

Giacintucci S., Venturi T., Murgia M., et al., 2007, A&A, 476, 99.

Giovannini G., Feretti L., Venturi T., Lara L., Marcaide J., Rioja M., Spangler S. R., et al., 1994, ApJ, 435, 116.

Ghisellini G., Padovani P., Celotti A., Maraschi L., 1993, ApJ, 407, 65.

Ghisellini G., Tavecchio F., Chiaberge M., 2005, A&A, 432, 401.

Godfrey L. E. H., Lovell J. E. J., Burke-Spolaor S., Ekers R., Bicknell G. V., Birkinshaw M., Worrall D. M., et al., 2012, ApJL, 758, L27.

Gómez J.-L., Marscher A. P., 2000, ApJ, 530, 245.

Goodger J. L., Hardcastle M. J., Croston J. H., Kraft R. P., Birkinshaw M., Evans D. A., Jordán A., et al., 2010, ApJ, 708, 675.

Goodrich R. W., 2001, sac..conf, 69.

Grupe D., 2004, tivo.conf, 283.

Gutcke T. A., Fanidakis N., Macciò A. V., Lacey C., 2015, MNRAS, 451, 3759.

Hardcastle M. J., Alexander P., Pooley G. G., Riley J. M., 1997, MNRAS, 288, L1.

Hardcastle M. J., 1998, MNRAS, 298, 569.

Hardcastle M. J., Alexander P., Pooley G. G., Riley J. M., 1998, MNRAS, 296, 445.

Hardcastle M. J., Birkinshaw M., Worrall D. M., 1998, MNRAS, 294, 615.

Hardcastle M. J., Worrall D. M., Birkinshaw M., Laing R. A., Bridle A. H., 2002, MNRAS, 334, 182.

Hardcastle M. J., 2004, A&A, 414, 927.

Hardcastle M. J., Sakelliou I., 2004, MNRAS, 349, 560.

Hardcastle M. J., Harris D. E., Worrall D. M., Birkinshaw M., 2004, ApJ, 612, 729.

Hardcastle M. J., Sakelliou I., Worrall D. M., 2005, MNRAS, 359, 1007.

Hardcastle M. J., 2006, ESASP, 604, 627.

Hardcastle M. J., Evans D. A., Croston J. H., 2006, MNRAS, 370, 1893.

Hardcastle M. J., Croston J. H., Kraft R. P., 2007, ApJ, 669, 893.

Hardcastle M. J., 2008, ASPC, 386, 46.

Hardcastle M. J., Ching J. H. Y., Virdee J. S., Jarvis M. J., Croom S. M., Sadler E. M., Mauch T., et al., 2013, MNRAS, 429, 2407.

Hardcastle M. J., Gürkan G., van Weeren R. J., Williams W. L., Best P. N., de Gasperin F., Rafferty D. A., et al., 2016, MNRAS, 462, 1910.

Hardcastle M. J., Croston J. H., 2020, NewAR, 88, 101539.

Hardcastle M. J., Shimwell T. W., Tasse C., Best P. N., Drabent A., Jarvis M. J., Prandoni I., et al., 2021, A&A, 648, A10.

Harris W. E., 2018, AJ, 156, 296.

Harwood J. J., Hardcastle M. J., Croston J. H., Goodger J. L., 2013, MNRAS, 435, 3353.

Harwood J. J., Hardcastle M. J., 2012, MNRAS, 423, 1368.

Harwood J. J., Vernstrom T., Stroe A., 2020, MNRAS, 491, 803.

Hayakawa A., Hoshino A., Ishida M., Furusho T., Yamasaki N. Y., Ohashi T., 2006, PASJ, 58, 695.

Heald G., McKean J., Pizzo R., et al., 2010, arXiv, arXiv:1008.4693.

Heckman T. M., O'Dea C. P., Baum S. A., Laurikainen E., 1994, ApJ, 428, 65.

Hill G. J., Lilly S. J., 1991, ApJ, 367, 1.

Hillas A. M., 1984, ARA&A, 22, 425.

Hine R. G., Longair M. S., 1979, MNRAS, 188, 111.

Ho L. C., Filippenko A. V., Sargent W. L. W., 1997, ApJS, 112, 315.

Hodges-Kluck E. J., Reynolds C. S., Cheung C. C., Miller M. C., 2010, ApJ, 710, 1205.

Högbom J. A., 1974, A&AS, 15, 417.

Holt J., Tadhunter C. N., Morganti R., 2008, MNRAS, 387, 639.

Homan D. C., Ojha R., Wardle J. F. C., Roberts D. H., Aller M. F., Aller H. D., Hughes P. A., 2002, ApJ, 568, 99.

Hopkins P. F., Robertson B., Krause E., Hernquist L., Cox T. J., 2006, ApJ, 652, 107.

Hovatta T., Lister M. L., Aller M. F., Aller H. D., Homan D. C., Kovalev Y. Y., Pushkarev A. B.,

et al., 2012, AJ, 144, 105.

Ineson J., Croston J. H., Hardcastle M. J., Kraft R. P., Evans D. A., Jarvis M., 2015, MNRAS, 453, 2682.

Jackson N., Rawlings S., 1997, MNRAS, 286, 241.

Jackson N., Tagore A., Deller A., Moldón J., Varenius E., Morabito L., Wucknitz O., et al., 2016, A&A, 595, A86.

Jackson N., Badole S., Morgan J., Chhetri R., Prusis K., Nikolajevs A., Morabito L., et al., 2021, arXiv, arXiv:2108.07284.

Jansky K. G., 1933, PA, 41, 548.

Jetha N. N., Sakelliou I., Hardcastle M. J., Ponman T. J., Stevens I. R., 2005, MNRAS, 358, 1394.

Jetha N. N., Hardcastle M. J., Sakelliou I., 2006, MNRAS, 368, 609.

Junor W., Biretta J. A., Livio M., 1999, Natur, 401, 891.

Kadler M., Ros E., Kerp J., Roy A. L., Marscher A. P., Zensus J. A., 2005, MmSAI, 76, 126.

Kaiser C. R., Best P. N., 2007, hvcg.conf, 222.

Kameno S., Inoue M., Wajima K., Sawada-Satoh S., Shen Z.-Q., 2003, PASA, 20, 213.

Kaufman M. J., Wolfire M. G., Hollenbach D. J., Luhman M. L., 1999, ApJ, 527, 795.

Kaviraj S., Schawinski K., Silk J., Shabala S. S., 2011, MNRAS, 415, 3798.

Kellermann K. I., Pauliny-Toth I. I. K., Williams P. J. S., 1969, ApJ, 157, 1.

Kellermann K. I., Sramek R., Schmidt M., Shaffer D. B., Green R., 1989, AJ, 98, 1195.

Kellermann K. I., Kovalev Y. Y., Lister M. L., Homan D. C., Kadler M., Cohen M. H., Ros E., et al., 2007, Ap&SS, 311, 231.

Kembhavi A. K., Narlikar J. V., 1999, qagn.book

Kharb P., Gabuzda D. C., O'Dea C. P., Shastri P., Baum S. A., 2009, ApJ, 694, 1485.

Koide S., Shibata K., Kudoh T., 1998, ApJL, 495, L63.

Koide S., Shibata K., Kudoh T., Meier D. L., 2002, Sci, 295, 1688.

Komissarov S. S., 2006, MNRAS, 368, 993.

Komissarov S. S., Falle S. A. E. G., 1997, MNRAS, 288, 833.

Komissarov S., Porth O., 2021, NewAR, 92, 101610.

Kormendy J., Ho L. C., 2013, ARA&A, 51, 511.

Kraemer S. B., Crenshaw D. M., 2000, ApJ, 544, 763.

Kraft R. P., Nulsen P. E. J., Birkinshaw M., Worrall D. M., Penna R. F., Forman W. R., Hardcastle M. J., et al., 2007, ApJ, 665, 1129.

Kravchenko E. V., Cotton W. D., Kovalev Y. Y., 2015, IAUS, 313, 128.

Krolik J. H., 1999, ApJL, 515, L73.

Kuehr H., Witzel A., Pauliny-Toth I. I. K., Nauber U., 1981, A&AS, 45, 367.

Kukula M. J., Holloway A. J., Pedlar A., Meaburn J., Lopez J. A., Axon D. J., Schilizzi R. T., et al., 1996, MNRAS, 280, 1283.

Kuligowska E., 2017, A&A, 598, A93.

Kundt W., 2014, frap.conf, 25.

Laing R. A., Peacock J. A., 1980, MNRAS, 190, 903.

Laing R., 1982, IAUS, 97, 161.

Laing R. A., 1996, ASPC, 100, 241.

Laing R. A., 1988, Natur, 331, 149.

Laing R. A., Riley J. M., Longair M. S., 1983, MNRAS, 204, 151.

Laing R. A., Bridle A. H., 1987, MNRAS, 228, 557.

Laing R. A., 1993, in Burgarella D., Livio M., O'Dea C. P., eds, STScI Symp. Astrophysical Jets. Cambridge Univ. Press, Cambridge, p. 95

Laing R. A., Jenkins C. R., Wall J. V., Unger S. W., 1994, ASPC, 54, 201.

Laing R. A., Parma P., de Ruiter H. R., Fanti R., 1999, MNRAS, 306, 513.

Laing R. A., Bridle A. H., 2002, MNRAS, 336, 1161.

Laing R. A., Bridle A. H., 2013, MNRAS, 432, 1114.

Laing R. A., Bridle A. H., 2014, MNRAS, 437, 3405.

Laing R. A., Canvin J. R., Bridle A. H., Hardcastle M. J., 2006, MNRAS, 372, 510.

Lannes A., Anterrieu É., Bouyoucef K., 1994, JMOp, 41, 1537.

Lara L., Alberdi A., Marcaide J. M., Muxlow T. W. B., 1994, A&A, 285, 393.

Lara L., Cotton W. D., Feretti L., Giovannini G., Venturi T., Marcaide J. M., 1997, ApJ, 474, 179.

Lara L., Feretti L., Giovannini G., Baum S., Cotton W. D., O'Dea C. P., Venturi T., 1999, ApJ, 513, 197.

Lara L., Giovannini G., Cotton W. D., Feretti L., Venturi T., 2004, A&A, 415, 905.

Lawrence A., 1987, PASP, 99, 309.

Lawrence A., 1999, AdSpR, 23, 1167.

Leahy J. P., Perley R. A., 1991, AJ, 102, 537.

Leahy J. P., 1993, LNP, 1.

Leahy J. P., 1996, VA, 40, 173.

Leahy J. P., Bridle A. H., Strom R. G., 1996, IAUS, 175, 157, IAUS..175

Leahy J. P., Black A. R. S., Dennett-Thorpe J., Hardcastle M. J., Komissarov S., Perley R. A., Riley J. M., et al., 1997, MNRAS, 291, 20.

Ledlow M. J., Owen F. N., 1996, AJ, 112, 9.

Lin Y.-T., Ostriker J. P., Miller C. J., 2010, ApJ, 715, 1486.

Lind K. R., Payne D. G., Meier D. L., Blandford R. D., 1989, ApJ, 344, 89.

Liska M., Hesp C., Tchekhovskoy A., Ingram A., van der Klis M., Markoff S., 2018, MNRAS, 474, L81.

Liska M., Tchekhovskoy A., Quataert E., 2020, MNRAS, 494, 3656.

Lister M. L., Homan D. C., 2005, AJ, 130, 1389.

Lister M. L., Cohen M. H., Homan D. C., Kadler M., Kellermann K. I., Kovalev Y. Y., Ros E., et al., 2009, AJ, 138, 1874.

Lister M. L., Aller M. F., Aller H. D., Homan D. C., Kellermann K. I., Kovalev Y. Y., Pushkarev A. B., et al., 2013, AJ, 146, 120.

Liu R., Pooley G., 1991, MNRAS, 249, 343.

Lonsdale C. J., Barthel P. D., 1998, AJ, 115, 895.

Madrid J. P., Chiaberge M., Floyd D., Sparks W. B., Macchetto D., Miley G. K., Axon D., et al., 2006, ApJS, 164, 307.

Márquez I., Durret F., Masegosa J., Moles M., Varela J., González Delgado R. M., Maza J., et al., 2004, A&A, 416, 475.

Marscher A. P., 2005, MmSAI, 76, 13.

Martel A. R., Baum S. A., Sparks W. B., et al., 1999, ApJS, 122, 81.

McCourt M., Quataert E., Parrish I. J., 2013, MNRAS, 432, 404.

McCready L. L., Pawsey J. L., Payne-Scott R., 1947, RSPSA, 190, 357.

McKean J. P., Godfrey L. E. H., Vegetti S., Wise M. W., Morganti R., Hardcastle M. J., Rafferty D., et al., 2016, MNRAS, 463, 3143.

McKinney J. C., 2006, MNRAS, 368, 1561.

Meier D. L., Koide S., Uchida Y., 2001, Sci, 291, 84.

Meisenheimer K., Roser H.-J., Hiltner P. R., Yates M. G., Longair M. S., Chini R., Perley R. A., 1989, A&A, 219, 63.

Middelberg E., Bach U., 2008, RPPh, 71, 066901.

Mignone A., Rossi P., Bodo G., Ferrari A., Massaglia S., 2010, MNRAS, 402, 7.

Miley G. K., van der Laan H., 1973, A&A, 28, 359.

Miller J. S., Antonucci R. R. J., 1983, ApJL, 271, L7.

Miller L., Peacock J. A., Mead A. R. G., 1990, MNRAS, 244, 207.

Miller N. A., Ledlow M. J., Owen F. N., Hill J. M., 2002, AJ, 123, 3018.

Mingo B., Croston J. H., Hardcastle M. J., et al., 2019, MNRAS, 488, 2701.

Mizuno Y., Hardee P. E., Nishikawa K.-I., 2008, ASPC, 386, 410.

Mizuno Y., 2022, Univ, 8, 85.

Molnar S. M., Schive H.-Y., Birkinshaw M., Chiueh T., Musoke G., Young A. J., 2017, ApJ, 835, 57.

Morabito L. K., Jackson N. J., Mooney S., Sweijen F., Badole S., Kukreti P., Venkattu D., et al., 2022, A&A, 658, A1.

Morganti R., Killeen N. E. B., Tadhunter C. N., 1993, MNRAS, 263, 1023.

Morganti R., 2010, agnf.book, 63.

Mortlock D. J., Warren S. J., Venemans B. P., Patel M., Hewett P. C., McMahon R. G., Simpson C., et al., 2011, Natur, 474, 616.

Mościbrodzka M., Falcke H., Shiokawa H., 2016, A&A, 586, A38.

Mukherjee D., Bicknell G. V., Sutherland R., Wagner A., 2016, MNRAS, 461, 967.

Murgia M., Parma P., Mack K.-H., de Ruiter H. R., Fanti R., Govoni F., Tarchi A., et al., 2011, A&A, 526, A148.

Murthy S., Morganti R., Wagner A. Y., Oosterloo T., Guillard P., Mukherjee D., Bicknell G., 2022, NatAs.tmp.

Mushotzky R. F., 1982, ApJ, 256, 92.

Musoke G., Young A. J., Molnar S. M., Birkinshaw M., 2020, MNRAS, 494, 5207.

Muxlow T. W. B., Richards A. M. S., Garrington S. T., Wilkinson P. N., Anderson B., Richards E. A., Axon D. J., et al., 2005, MNRAS, 358, 1159.

Myers S. T., Spangler S. R., 1985, ApJ, 291, 52.

Nalewajko K., Sikora M., 2008, AIPC, 1085, 483.

Narayan R., Yi I., 1994, ApJL, 428, L13.

Nelson C. H., MacKenty J. W., Simkin S. M., Griffiths R. E., 1996, ApJ, 466, 713.

Nilsson K., Heidt J., Pursimo T., Sillanpää A., Takalo L. O., Jäger K., 1997, ApJL, 484, L107.

Norman M. L., Winkler K.-H. A., Smarr L., Smith M. D., 1982, A&A, 113, 285.

O'Dea C. P., Owen F. N., 1985, AJ, 90, 954.

O'Dea C. P., Owen F. N., 1986, ApJ, 301, 841.

O'Dea C. P., Owen F. N., 1987, ApJ, 316, 95.

O'Dea C. P., 2001, EAS, 1, 97.

O'Donoghue A. A., Owen F. N., Eilek J. A., 1990, ApJS, 72, 75.

O'Donoghue A. A., Eilek J. A., Owen F. N., 1993, ApJ, 408, 428.

Offringa A. R., de Bruyn A. G., Biehl M., Zaroubi S., 2010a, in Proc. Conf. RFI mitigation workshop, 29–31 March 2010, Groningen, The Netherlands (PoS), id.36.

O'Sullivan S. P., Gaensler B. M., Lara-López M. A., van Velzen S., Banfield J. K., Farnes J. S., 2015, ApJ, 806, 83.

Owen F. N., Rudnick L., 1976, ApJ, 203, 307.

Owen F. N., Ledlow M. J., 1997, ApJS, 108, 41.

Owen F. N., Eilek J. A., Kassim N. E., 2000, ApJ, 543, 611.

Panessa F., Bassani L., 2002, A&A, 394, 435.

Park J., Algaba J. C., 2022, Galax, 10, 102.

Parma P. et al., 1992, in Burgarella D., Livio M., O'Dea C., eds, Astrophysical Jets, Poster Papers, STScI Symp. Baltimore, p. 30.

Parma P., de Ruiter H. R., Fanti R., Laing R., 1994, ASPC, 54, 241.

Parma P., de Ruiter H. R., Fanti R., 1996, IAUS, 175, 137.

Parma P., Murgia M., Morganti R., Capetti A., de Ruiter H. R., Fanti R., 1999, A&A, 344, 7.

Peck L. W., Fenech D. M., 2013, ascl.soft. ascl:1312.001.

Pedelty J. A., Rudnick L., McCarthy P. J., Spinrad H., 1989, AJ, 98, 1232.

Peng C. Y., Impey C. D., Ho L. C., Barton E. J., Rix H.-W., 2006, ApJ, 640, 114.

Pérez E., Márquez I., Marrero I., Durret F., González Delgado R. M., Masegosa J., Maza J., et al., 2000, A&A, 353, 893.

Perley R. A., Johnston K. J., 1979, AJ, 84, 1247.

Perley R. A., Dreher J. W., Cowan J. J., 1984, ApJL, 285, L35.

Perley R. A., Chandler C. J., Butler B. J., Wrobel J. M., 2011, ApJL, 739, L1.

Perlman E. S., Stocke J. T., 1994, AJ, 108, 56.

Perlman E. S., Biretta J. A., Zhou F., Sparks W. B., Macchetto F. D., 1999, AJ, 117, 2185.

Perlman E. S., Biretta J. A., Sparks W. B., Macchetto F. D., Leahy J. P., 2001, ApJ, 551, 206.

Perlman E. S., Padgett C. A., Georganopoulos M., Worrall D. M., Kastner J. H., Franz G., Birkinshaw M., et al., 2010, ApJ, 708, 171.

Pesce J. E., Sambruna R. M., Tavecchio F., Maraschi L., Cheung C. C., Urry C. M., Scarpa R., 2001, ApJL, 556, L79.

Peterson B. M., 2014, SSRv, 183, 253.

Pfrommer C., Jones T. W., 2011, ApJ, 730, 22.

Pinkney J., Burns J. O., Hill J. M., 1994, AJ, 108, 2031.

Polatidis A. G., Wilkinson P. N., 1998, MNRAS, 294, 327.

Popović L. Č., 2005, MmSAI, 76, 43.

Pracy M. B., Ching J. H. Y., Sadler E. M., Croom S. M., Baldry I. K., Bland-Hawthorn J., Brough S., et al., 2016, MNRAS, 460, 2.

Pudritz R. E., Ouyed R., Fendt C., Brandenburg A., 2007, prpl.conf, 277.

Pushkarev A., Kovalev Y., Lister M., Savolainen T., Aller M., Aller H., Hodge M., 2017, Galax, 5, 93.

Qian S. J., Quirrenbach A., Witzel A., Krichbaum T. P., Hummel C. A., Zensus J. A., 1991, A&A, 241, 15.

Rau U., Cornwell T. J., 2011, A&A, 532, A71.

Rees M. J., 1966, Natur, 211, 468.

Rees M. J., 1978, MNRAS, 184, 61P.

Reid R. I., 2006, MNRAS, 367, 1766.

Rengelink R. B., Tang Y., de Bruyn A. G., et al., 1997, A&AS, 124, 259.

Richards A. M. S., Moravec E., Etoka S., Fomalont E. B., Pérez-Sánchez A. F., Toribio M. C., Laing R. A., 2022, arXiv, arXiv:2207.05591.

Rieger F. M., Duffy P., 2004, ApJ, 617, 155.

Rodrigo C., Solano E., 2020, sea..conf, 182.

Rothstein D. M., Lovelace R. V. E., 2008, ApJ, 677, 1221.

Rottgering H. J. A., Braun R., Barthel P. D., van Haarlem M. P., Miley G. K., Morganti R., Snellen I., et al., 2006, arXiv, astro-ph/0610596.

Rottmann H., Mack K.-H., Klein U., Wielebinski R., 1996, A&A, 309, L19.

Rowan-Robinson M., 1977, ApJ, 213, 635.

Rybicki G. B., Lightman A. P., 1986, rpa..book, 400.

Rybicki G. B., Lightman A. P., 2008, Wiley & Sons.

Ryle M., Windram M. D., 1968, MNRAS, 138, 1.

Sadowski A., Narayan R., 2015, MNRAS, 453, 3213.

Saikia D. J., Jamrozy M., 2009, BASI, 37, 63.

Sambruna R. M., Donato D., Tavecchio F., Maraschi L., Cheung C. C., Urry C. M., 2007, ApJ, 670, 74.

Sanders R. H., 1983, ApJ, 266, 73.

Sanders D. B., Soifer B. T., Elias J. H., Madore B. F., Matthews K., Neugebauer G., Scoville N. Z., 1988, ApJ, 325, 74.

Sanders D. B., Phinney E. S., Neugebauer G., Soifer B. T., Matthews K., 1989, ApJ, 347, 29.

Scaife A. M. M., Heald G. H., 2012, MNRAS, 423, L30.

Scarpa R., Urry C. M., Falomo R., Treves A., 1999, ApJ, 526, 643.

Schawinski K., Lintott C. J., Thomas D., Kaviraj S., Viti S., Silk J., Maraston C., et al., 2009, ApJ, 690, 1672.

Scheuer P. A. G., 1974, MNRAS, 166, 513.

Scheuer P. A. G., 1987, in Zensus J., Pearson T., eds, Superluminal Radio Sources, Cambridge Univ. Press, Cambridge, p. 104.

Scheuer P. A. G., Readhead A. C. S., 1979, Natur, 277, 182.

Schmidt M., 1963, Natur, 197, 1040.

Schmidt M., 1966, ApJ, 146, 7.

Schoenmakers A. P., de Bruyn A. G., Röttgering H. J. A., van der Laan H., Kaiser C. R., 2000, MNRAS, 315, 371.

Schoenmakers A. P., 2001, ASPC, 250, 408.

Seyfert C. K., 1943, ApJ, 97, 28.

Shi Y., Rieke G. H., Hines D. C., Gordon K. D., Egami E., 2007, ApJ, 655, 781.

Shibata K., Aoki S., 2003, arXiv, astro-ph/0303253.

Shimwell T. W., Röttgering H. J. A., Best P. N., et al., 2017, A&A, 598, A104.

Shimwell T. W., Tasse C., Hardcastle M. J., Mechev A. P., Williams W. L., Best P. N., Röttgering H. J. A., et al., 2019, A&A, 622, A1.

Shklovskii I. S., 1980, SvAL, 6, 107.

Shlosman I., Frank J., Begelman M. C., 1989, Natur, 338, 45.

Shulevski A., Morganti R., Barthel P. D., Murgia M., van Weeren R. J., White G. J., Brüggen M., et al., 2015, A&A, 579, A27.

Sijbring D., de Bruyn A. G., 1998, A&A, 331, 901.

Sikora M., Begelman M. C., Madejski G. M., Lasota J.-P., 2005, ApJ, 625, 72.

Silk J., Rees M. J., 1998, A&A, 331, L1.

Singal A. K., 1993, MNRAS, 262, L27.

Smirnov O. M., Tasse C., 2015, MNRAS, 449, 2668.

Smith P. S., Balonek T. J., Heckert P. A., Elston R., 1986, ApJ, 305, 484.

Smolčić V., 2009, ApJL, 699, L43.

Snios B., Nulsen P. E. J., Kraft R. P., Cheung C. C., Meyer E. T., Forman W. R., Jones C., et al., 2019, ApJ, 879, 8.

Snyder W. A., Wood K. S., Yentis D. J., Meekins J. F., Smathers H. W., Byram E. T., Chubb T. A., et al., 1982, ApJ, 259, 38.

Spergel D. N., Bean R., Doré O., et al., 2007, ApJS, 170, 377.

Spingola C., McKean J. P., Massari D., Koopmans L. V. E., 2019, A&A, 630, A108.

Spinrad H., Djorgovski S., Marr J., Aguilar L., 1985, PASP, 97, 932.

Spruit H. C., 1996, ASIC, 477, 249.

Spruit H. C., 2013, arXiv, arXiv:1301.5572.

Stawarz Ł., 2004, ApJ, 613, 119.

Steenbrugge K. C., Blundell K. M., 2007, Ap&SS, 310, 321.

Stokes G. G., 1852, RSPT, 142, 463.

Stone J. M., 1997, IAUS, 182, 323.

Sun M., Jerius D., Jones C., 2005, ApJ, 633, 165.

Sun M., Trump J. R., Brandt W. N., Luo B., Alexander D. M., Jahnke K., Rosario D. J., et al., 2015, ApJ, 802, 14.

Sutherland R. S., Bicknell G. V., 2007, ApJS, 173, 37.

Tadhunter C., 2006, AN, 327, 180.

Tadhunter C., 2008, NewAR, 52, 227.

Tadhunter C. N., Ramos Almeida C., Morganti R., Holt J., Rose M., Dicken D., Inskip K., 2012, MNRAS, 427, 1603.

Tasse C., 2014, A&A, 566, A127.

Tasse C., Hugo B., Mirmont M., Smirnov O., Atemkeng M., Bester L., Hardcastle M. J., et al., 2018, A&A, 611, A87.

Tasse C., Shimwell T., Hardcastle M. J., O'Sullivan S. P., van Weeren R., Best P. N., Bester L., et al., 2021, A&A, 648, A1.

Tavecchio F., Ghisellini G., Guetta D., 2014, ApJL, 793, L18.

Taylor A. R., Young G., Peracaula M., Kenny H. T., Gregory P. C., 1996, A&A, 305, 817.

Taylor G. B., Carilli C. L., Perley R. A., 1999, ASPC, 180.

Taylor G. B., Zavala R., 2010, ApJL, 722, L183.

Terlevich R., Tenorio-Tagle G., Franco J., Melnick J., 1992, MNRAS, 255, 713.

Thompson A. R., Moran J. M., Swenson G. W., 2017, isra.book.

Tonry J. L., 1991, ApJL, 373, L1.

Tribble P. C., 1991, MNRAS, 250, 726.

Trimble V., 2015, IAUS, 309, 1.

Trussoni E., Ferrari A., Zaninetti L., 1983, ASSL, 103, 281.

Trussoni E., Capetti A., Celotti A., Chiaberge M., 2002, ASPC, 258, 177.

Urry C. M., Padovani P., 1995, PASP, 107, 803.

Urry C. M., Padovani P., Stickel M., 1991, ApJ, 382, 501.

van Haarlem M. P., Wise M. W., Gunst A. W., et al., 2013, A&A, 556, A2.

Vazza F., Wittor D., Brunetti G., Brüggen M., 2021, A&A, 653, A23.

Venkatesan T. C. A., Batuski D. J., Hanisch R. J., Burns J. O., 1994, ApJ, 436, 67.

Vlahakis N., 2015, ASSL, 414, 177.

Voit G. M., Donahue M., 2015, ApJL, 799, L1.

Walker R. C., Dhawan V., Romney J. D., Kellermann K. I., Vermeulen R. C., 2000, ApJ, 530, 233.

Wardle J. F. C., Homan D. C., Ojha R., Roberts D. H., 1998, Natur, 395, 457.

Weber R., Faye C., Biraud F., Dansou J., 1997, A&AS, 126, 161.

Wiaux Y., Jacques L., Puy G., Scaife A. M. M., Vandergheynst P., 2009, MNRAS, 395, 1733.

Wiita P. J., 2001, arXiv, astro-ph/0103020.

Wilkes B. J., D'Abrusco R., Martínez-Galarza R., 2019, cxro.book, 2.

Williams A. G., Gull S. F., 1985, Nature, 313, pp.34-36.

Williams W. L., Calistro Rivera G., Best P. N., Hardcastle M. J., Röttgering H. J. A., Duncan K. J., de Gasperin F., et al., 2018, MNRAS, 475, 3429.

Wilson A. S., Yang Y., 2002, ApJ, 568, 133.

Worrall D. M., Birkinshaw M., Cameron R. A., 1995, ApJ, 449, 93.

Worrall D. M., Birkinshaw M., Hardcastle M. J., 2001, MNRAS, 326, L7.

Worrall D. M., Hardcastle M. J., Pearson T. J., Readhead A. C. S., 2004, MNRAS, 347, 632.

Worrall D. M., 2005, MmSAI, 76, 28.

Worrall, D.M., Birkinshaw, M., 2006, in Alloin D., Johnson R., Lira P., eds, LNP, 693, SpringerVerlag, Berlin, p. 39.

Wrobel J. M., Lind K. R., 1990, ApJ, 348, 135.

Wykes S., Taylor A. M., Bray J. D., Hardcastle M. J., Hillas M., 2018, NPPP, 297-299, 234.

Xu C., O'Dea C. P., Biretta J. A., 1999, AJ, 117, 2626.

Xu C., Sulentic J. W., Tuffs R., 1999, ApJ, 512, 178.

Zernike F., 1938, Phy, 5, 785.

Zhang C., Churazov E., Dolag K., Forman W. R., Zhuravleva I., 2020, MNRAS, 498, L130.

Zhang Y., An T., Frey S., Gabányi K. É., Sotnikova Y., 2022, ApJ, 937, 19.

Zubovas K., King A., 2016, MNRAS, 462, 4055.